Sea ice tracking from SAR in the Arctic

Jennifer Ann King

Department of Geography

University of Sheffield

A thesis submitted in fulfilment of the requirements for the degree of Doctor of Philosophy

November 12, 2012

Abstract

Satellite observations play an important role in ice identification services because they are cost effective and efficient compared to extensive field campaigns. Radar data are extensively used to derive information about sea ice extent and movement. In the first part of this thesis I adapt a semi-automated algorithm, originally developed by Silva (2006) to track large icebergs in Antarctic waters, to track the movement of ice in the Northern Hemisphere. In addition to the move from Antarctic to Arctic waters, the algorithm is adapted to track sea ice rather than icebergs, with an attendant change in the shape of the tracked objects and their radar backscatter characteristics. The algorithm development is focused on the identification of appropriate image segmentation, brightness thresholding, and shape parameters appropriate to the identification and tracking of sea ice floes throughout the year. These developments are tested on images from a variety of locations, and from different SAR sensors.

Recent literature documents the warming of the Arctic region (Alexandrov et al., 2004; Serreze et al., 2007) with an accompanying decline in sea ice cover (Kwok and Rothrock, 2009). The identification of ice extent and movement is an important tool in the study of climate variability (Spreen et al., 2006; Bochert, 1999); for example the magnitude of the sea ice flux through the Fram Strait is a measure of net ice production in the Arctic Ocean (Widell et al., 2003). The Fram Strait is of key importance for the export of ice from the Arctic (Kwok and Rothrock, 1999; Kwok et al., 2004) and well known for the presence of strong surface currents (Dickson et al., 2007; Fahrbach et al., 2001). In the second part of the thesis I investigate the competing influences of atmospheric and oceanographic forcings on ice export through the Fram Strait. The focus is on the western (Greenland) side of the strait between 79 - 81 °N. This area is within the East Greenland Current and also covers the boundary between fast ice and drift ice. The East Greenland Current, coupled with the prevailing northerly wind, is the main driver for ice export through the Fram Strait. On shorter temporal resolution ice movement is seen to be governed by the winds. Where the temporal resolution is greater than 1-2 days the influence of the East Greenland Current becomes more dominant and overall movement is towards the south. My results suggest that the prevailing wind speed and direction have a key impact on the rate of ice export through the Fram Strait. A period in which the wind forcing is in agreement with the East Greenland Current will see greater ice export than a period in which the two are acting in opposite directions.

Acknowledgements

This work was supported by a PhD studentship funded by Kongsberg Satellite Services, who also provided the radar data: ENVISAT data are courtesy of European Space Agency (ESA); RADARSAT data courtesy of the Canadian Space Agency (RADARSAT-2 Data and Products copyright MacDONALD, DETTWILER AND ASSOCIATES LTD (2010) All Rights Reserved); and Cosmo Sky Med data courtesy of Italian Space Agency (ASI) COSMO-SkyMed Product copyright ASI (2010) processed under licence from ASI - Agenzia Spaziale Italiana. All rights reserved. Distributed by e-GEOS. Cosmo Sky Med data from April 2010 were originally acquired for Conoco Phillips, to whom I extend my thanks for permission to include this work in the thesis.

I am extremely grateful for the encouragement and support of my supervisors, Grant Bigg and Richard Hall, without whom this thesis could not have taken shape.

Extra special thanks are due to Daniel Money and Richard King; whose support has kept me sane. Thank you for listening without judgement, for believing in me even when I did not believe in myself, for dragging me out into the fresh air when I needed it, and for the endless proofreading!

I would also like to thank my family for their love and support, and for encouraging the appetite for learning that has led me down this road. I am grateful also to all of my friends, in particular to Kiri, my 'study-buddy', for keeping me focused in these final months, to Helen, Pete and the doggies for providing the perfect retreat, to Kate for pummelling the tension out of my poor shoulders, to Rosie, Tom and Sarah for Munro bashing with me when I needed a break, and to Theresa, Elka, Angela, Amelie, Andy & Mishca, Alex, and Julie for good listening ears and sound advice.

Table of Contents

List of Figures

List of Tables

Abbreviations and Acronyms

ITSARI - Ice Tracking from SAR Images

RADAR - RAdio Detection And Ranging

SAR - Synthetic Aperture Radar

ROA - Ratio of Averages

CSM - Cosmo Sky Med

Chapter 1

Introduction

1.1 Arctic Sea Ice and climate

Recent literature documents the warming of the Arctic region (Alexandrov et al., 2004; Serreze et al., 2007) with an accompanying decline in sea ice cover (Kwok and Rothrock, 2009). The Arctic is highly susceptible to climate warming and changes to the Arctic sea ice cover are used as an early indicator of climate trends (Bochert, 1999; Serreze and Francis, 2006; Comiso, 2006). The identification of ice extent and movement is an important tool in the study of climate variability (Spreen et al., 2006; Bochert, 1999), for example, the magnitude of the sea ice flux through the Fram Strait is a measure of net ice production in the Arctic Ocean (Widell et al., 2003). Sea ice movement is both influenced by, and in turn has an influence on, the climate of the Polar regions. The movement of sea ice and icebergs can give us information about the ocean surface currents and near surface atmospheric flow.

The earliest measurements of sea ice movement in the Arctic come from early explorers such as Herbert (1969), who established camp on the ice and drifted with it recording progress and location. Records of iceberg sightings from ships date back over a century (Gladstone and Bigg, 2002; Jacka and Giles, 2007). More recently digital cameras have been deployed to record ice conditions throughout a voyage (Weissling et al., 2009; Hall et al., 2002). Ice charting has moved to take

advantage of developments in technology, for example Russian ice charts, dating back to 1933, were at first hand drawn from aerial reconnaissance, but now make use of airborne and satellite instruments (Mahoney et al., 2008). With the advent of modern technology, observations of ice movement fall into two camps: those from equipment used within the ice environment, and those from air or space-borne observation platforms. In the first category is equipment such as drift buoys released into the ice pack, that transmit their location as they travel, and upward looking sonars moored in the passages through which ice is known to travel (Vinje, 2001; Widell et al., 2003). Several Arctic drift buoy projects have been established since 1980 with data archived by the International Arctic Buoy Programme (Inoue and Kikuchi, 2007).

In the second category, satellite observations play an important role in ice identification services, being cost effective and efficient compared to extensive field campaigns. Radar is extensively used to derive information about sea ice extent and movement. Information that can be retrieved from radar data includes the location of the ice edge, direction of movement, classification of different types of sea ice and the location of icebergs held within the pack, and in the open ocean (Walker et al., 2006; Karvonen et al., 2007; Lane et al., 2004; Silva and Bigg, 2005). Ice services around the world aim to classify different ice types within the pack, and also to follow the movement of hazardous objects such as areas of thicker ice and ridges within the pack, or pieces of sea ice or icebergs in open water that may enter shipping lanes (Maillard et al., 2005; McClintock and McKenna, 2007). SAR has also been used to observe the snow water equivalent (Yackel and Barber, 2007), establish the presence and geometry of melt ponds (Yackel et al., 2001; Yackel and Barber, 2000; Tschudi et al., 2008), and to estimate the frequency of pressure ridges (Haas et al., 1999; Melling, 1998).

Ice movement can be measured in two ways. The first is to take a fixed point, or flux gate, and measure the movement of the ice past that point (speed and volume of ice). This measures the Eulerian motion. The second method is to identify specific ice objects, and track the movement of those objects over time, generating a

Lagrangian motion track. This second method is most commonly used to track the movement of icebergs, while the first is used, for example, to monitor the movement of the sea ice pack as a whole through outlets such as the Fram Strait.

Sea ice and icebergs present a hazard to shipping and to oil platforms, and can be of importance to submarine manoeuvres. The need for timely and reliable information on the movement of sea ice and icebergs in Arctic waters has become more pressing because:

- Exploration for oil and gas is pushing further into Arctic regions,
- the expansion of Arctic tourism has brought an increasing number of cruise ships into Arctic waters,
- there has been an increase in commercial shipping due to the north-west and north-east passages becoming navigable for longer periods each year.

In the future, as the Arctic sea ice retreats, greater exploration of the regions resources and increased navigation will bring increasing numbers of people into contact with the hazards associated with sea ice.

1.2 About the thesis

In this thesis I take a semi-automated algorithm, originally developed by Silva (2006) to track large icebergs in Antarctic waters, and further develop and adapt this to track the movement of ice in the northern hemisphere. The algorithm is known as 'ITSARI', which stands for: Ice Tracking from SAR Images. Tracking is achieved by matching size and shape characteristics of objects identified in successive Synthetic Aperture Radar (SAR) images by using a one dimensional shape representation (described in Silva and Bigg (2005) and Silva (2006)). In addition to the move from Antarctic to Arctic waters the algorithm is adapted to track sea ice rather than icebergs, with an attendant change in the shape of the tracked objects, and their radar backscatter characteristics. The algorithm development is focused on the identification of appropriate image segmentation, brightness thresholding and

also shape parameters appropriate to use to identify and track sea ice floes. These developments are tested on images from a variety of locations, and from different SAR sensors; to show the potential for applying this method in a commercial setting, and to contribute to Polar oceanography and meteorology.

The main study area is the Fram Strait. This is an interesting region because it is the main flux gate through which sea ice exits the Arctic Ocean (Kwok and Rothrock, 1999; Kwok et al., 2004). An increase in the volume of ice exiting through the Fram Strait may be a contributing factor to recent loss of ice in the Arctic Ocean. Ice movement in the western Fram Strait identified using ITSARI is compared to a) known ocean currents in the region, b) local pressure gradient and resulting wind speed and direction. The algorithm works well for tracking ice movement in the summer months when the ice is separated into individual floes.

1.3 Thesis Structure

This thesis has two distinct parts: algorithm development, and application to my chosen study area, the Fram Strait. The first part deals with the adaptation of the algorithm for use in the Arctic, with sea ice floes as well as icebergs, and with different sensors. Chapter 2 provides a literature review describing the use of remote sensing to derive information about sea ice. Chapter 3 discusses the method used in the ITSARI algorithm and the various modifications made to that algorithm for its use in the work presented here. Chapters 4 and 5 present a series of case studies designed to illustrate the testing of the algorithm with information from different areas (chapter 4) and from different sensors (chapter 5). Section 4a takes a first look at adapting the algorithm to track the movement of sea ice floes in the Fram Strait using Envisat wide swath data from February 2008 while section 4b expands this study to cover the full year 2008 at 3 - 10 day intervals. Section 4c uses Envisat wide swath data from the Barents Sea to demonstrate that the technique development carried out for sections 4a and 4b is applicable to other areas of the Arctic outside the Fram Strait. Section 5a looks at adapting the technique to use data from Radarsat,

another C band sensor, while section 5b investigates the use of the technique with data from the Cosmo Sky Med constellation, a move to X band data.

The second part of the thesis is concerned with using the results to investigate the competing influences of climate and oceanography on ice movement in the Fram Strait. The focus is on the western (Greenland) side of the strait between 79 - 81 °N. This area is within the East Greenland Current and also covers the boundary between fast ice and drift ice. The Fram Strait is of key importance for the export of ice from the Arctic (Kwok and Rothrock, 1999; Kwok et al., 2004) and well known for the presence of strong surface currents (Dickson et al., 2007; Fahrbach et al., 2001). Chapter 6 introduces the study area in more detail: explaining the oceanography and climate of the region and its importance for sea ice export from the Arctic. Chapter 7 describes the results of performing tracking on a series of images from the Fram Strait between 3 and 10 days apart over the whole year 2008. These results are related to the oceanography and synoptic conditions of the area by comparison with surface ocean currents, air pressure charts, and wind speed and direction vectors from reanalysis data. The strength of the algorithm is revealed to be tracking the movement of ice floes in open conditions in the summer months, a time when tracking techniques based on cross correlation can fail. Chapter 8 focuses on tracking in later summer at a shorter temporal resolution: ice movement in the Fram Strait in August and September 2010 from images acquired 1 or 2 days apart. This period is interesting because it stands at the end of summer melting, but prior to the the onset of freeze up and the beginning of a new ice year. Because the ice is open and floes are able to move individually this is the ideal time to compare the competing effect of ocean and climate factors. Chapter 9 concludes the thesis with a summary of what we have learnt about a) the use of the algorithm on sea ice and b) the competing effects of ocean and climate factors on sea ice movement in the Fram Strait region; and suggestions for future research directions.

Chapter 2

Radar Remote Sensing of Sea Ice and Icebergs

2.1 Introducing Remote Sensing

Remote sensing is the process of gaining information about the earth's surface from sensors mounted on air- and space- borne platforms. Remote sensing allows us to view vast areas of the earth's surface at once, and at less cost than a field survey, thus it has an important role to play in the pursuit of knowledge about our world. The sensors mounted on various satellites in the earth's orbit image the earth at different wavelengths, some working in the visible and near infrared (e.g. ASTER, Landsat), and some working in the microwave part of the spectrum. Remote sensing in the microwave part of the spectrum is commonly used in polar regions because it is neither daylight dependent nor adversely affected by cloud. This makes it appropriate for use in an environment where it is dark for months at a time and where cloudy weather can be common. Microwave remote sensing can be passive (recording the microwave radiation emitted from the earth's surface) or active (emitting a pulse of electromagnetic radiation and recording the reflected signal once those waves have interacted with the surface and returned to the sensor). Radar (RAdio Detection And Ranging) is a form of active microwave remote sensing.

2.2 Synthetic Aperture Radar

A Synthetic Aperture Radar (SAR) instrument emits a pulse of electromagnetic radiation in one of the bands described in Table 2.1. This pulse is absorbed, scattered, or reflected by the surfaces it encounters, and the returned signal is measured by the sensor (Rees, 2001; Woodhouse, 2006). In the case of SAR sensors a series of observations along a flight track is combined to appear as if they came from one larger antenna. SAR instruments emit coherent radiation at a single frequency and polarisation. The returning signal has the same frequency, but phase and polarisation vary depending on the way the incident radiation interacts with the earth's surface (Haykin et al., 1994; Woodhouse, 2006). Table 2.2 gives some examples of satellite-borne SAR instruments.

Table 2.1: Radar Bands

Band	Wavelength (mm)	Frequency (GHz)
L	150-300	1-2
S	80-150	2-4
C	40-80	4-8
X	25-40	8-12
Ku	16 - 25	12-18
K	11-16	18 - 27

Table 2.2: Radar Sensors

Sensor	Band	Resolution (m)	Swath Width (km)
Envisat (ESA)	C	30/150/1000	100- 400
ERS1 & 2 (ESA)	C	30	100
Radarsat 1 & 2 (Canada)	C	8-100	45-500
ALOS Palsar (Japan)	L	2.5/10/10-100	35-70/7/350
TerraSAR X (Germany)	X	1/2/3/18	5-10/10/30x50/100x150
COSMOSKYMED (x4) (Italy)	1/3-15/30/100/15	10/40/100/200/30	

2.2.1 Radar Geometry

The pulse of electromagnetic radiation emitted by a SAR instrument interacts with the earth's surface at a range of incidence angles (defined as the angle between the propagation direction of the radiation and the local vertical). The incidence angle at any given point on the illuminated surface depends on the pointing of the instrument and the relative position of the sensor with respect to that point. The redirection of incident electromagnetic radiation by an object is known as scattering

(Woodhouse, 2006). Surface scattering refers to a return from the surface of an object, while volume scattering refers to returns from within an object, caused by internal inhomogeneities. How much is absorbed depends on the dielectric properties of the target material.

Incident radiation may be scattered in any direction. To gain information about the earth's surface one must be able to quantify that which is scattered in the direction of the sensor - the returning signal, or 'backscatter'. In an active system we control how much power is incident upon the target area. To quantify the power scattered back in the direction of the sensor from a target located at range R, one first makes the simplification of defining a radar cross sectional area, σ, as follows: (Woodhouse, 2006)

$$\sigma = \frac{I_{received}}{I_{incident}} 4\pi R^2 \qquad [m^2] \tag{2.1}$$

where σ is a target area that one would infer based on the measured intensity, $I_{received}$, by assuming the target area, σ, intercepted the power transmitted ($I_{incident}$) and then scattered that power isotropically (Woodhouse, 2006). However, the intensity of the returning signal (σ) depends on the target's geometry and electromagnetic characteristics, and is normally described for a given area of the earth's surface by the backscattering coefficient (σ^0):

$$\sigma^0 = \frac{\sigma}{A} \tag{2.2}$$

where σ is the scattering cross section described above and A is the area on the ground surface (Woodhouse, 2006). The backscattering coefficient is conventionally expressed on a logarithmic scale for ease of visualisation:

$$[\sigma^0]dB = 10.log10(\sigma^0) \tag{2.3}$$

The backscattering coefficient describes the intensity of the radar signal that is

returned to the sensor by the target surface area, normalised to account for the transmitted power, antenna gain and distance to target (Woodhouse, 2006; Haykin et al., 1994). If the radar pulse penetrates into the target, the radar return may come from inhomogeneities within the target, or from the interface between different materials at the bottom or at the back side of the target.

The interaction with a given target may result in a different response from the incident radiation at different incidence angles and wavelengths. At lower incidence angles surface roughness can increase the radar cross section of the target by allowing more of the pulse to interact with the sides of ridges in the surface. Smaller features, such as the individual ridges of a rough surface, will also have a greater interaction with shorter wavelengths than longer ones. Incidence angle varies from one side of an image to the other, with the effects of this becoming more noticeable the wider the swath of the image is. The strength of the return from a surface with strong geometrical features will depend on the imaging geometry, and could be either weaker or stronger. Figure 2.1 illustrates different scenarios for the scattering of incident radiation upon interaction with a target.

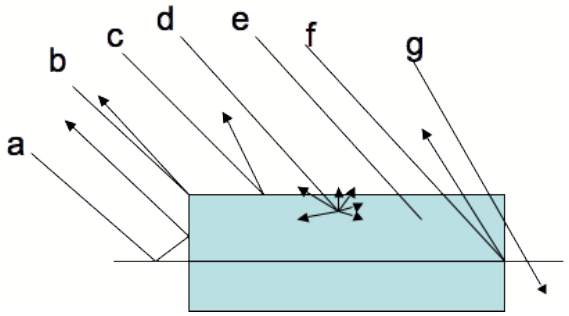

Figure 2.1: Possible fate of radar signal and different sources of backscatter a) double bounce from surface in front of object followed by side of object, b) direct return from corner of object, c) direct return from surface of object, d) volume scattering from inhomogeneities within an object, e) absorption (no return) f) return from back side of object g) passage through object (no return).

2.3 Radar Detection of Ice

The SAR backscatter of ice is determined by the dielectric constant (which is linked to the brine content of the ice), incidence angle, and surface roughness (compared

to the scale of the radar wavelength) (Haykin et al., 1994; Maillard et al., 2005). Strong radar returns occur when there is an abrupt change in the dielectric constant within a wavelength, for example at the air-ice interface, the ice-water interface and the ice-air interface at the back surface of an iceberg (Haykin et al., 1994). Radar is also sensitive to inhomogeneities in the ice volume, such as cracks and air bubbles, and to changes in the dielectric properties of the ice (Dierking and Dall, 2007). To compound these sensitivities, the physical properties of ice and snow vary enormously by type, age, season, time of day and region, posing difficulties for accurate characterisation.

Sensitivity to changes of incidence angle depends on the scattering medium (Dierking and Dall, 2008). For example, the backscatter from water varies greatly with incidence angle, and also in relation to the wind direction, and wave crest angle, relative to the incidence angle (Carlstrom and Ulander, 1993; Williams et al., 1999; Walker et al., 2006). This can cause problems if the images used are wide swath (around 400 km across) because areas of water on one side of the image will appear much brighter than areas of water on the other side of the image, making classification of that image more complex (Haarpainter and Solbo, 2007; Dierking and Dall, 2007). This complicates the separation of ice from water because the contrast between the two is not constant from one time or place to the next (Williams et al., 1999; Walker et al., 2006).

2.3.1 Detection of Sea Ice over a Seasonal Cycle

Seasonal variations in the backscatter of sea ice arise from the physical processes of sea ice growth, ageing, and decay over an annual cycle (Gill and Valeur, 1999; Haykin et al., 1994; Nghiem and Bertoia, 2001). To confuse matters it is possible for regions with different ice types to have the same SAR signatures - and different SAR signatures may be found for the same ice type (Bochert, 1999). As new ice begins to form, SAR can be used to monitor the formation of frazil ice crystals as they group together in Langmuir plumes (Drucker et al., 2003). During freeze-up in the autumn, new ice forms and the freezing horizon in the old ice descends, with loss of

liquid in the upper layers. First year ice has a high dielectric constant because of its high brine content, which makes it quite lossy, and leads to low returns. But if frost flowers form on the surface this cause strong returns that may lead to first year ice being mistaken for multi-year ice. During freeze up, the ice surface temperature and liquid water content both decrease. This changes the dominant mechanism for radar returns from surface to volume scattering (Carlstrom and Ulander, 1993).

Spring melt can enhance surface roughness in a variety of different ways, rough super-imposed ice may form, or snow may melt completely revealing a rough wet ice surface. This increased surface roughness increases the backscatter (Ulander et al., 1995; Gill and Valeur, 1999). The backscatter of refrozen brash ice is also dependent on its surface roughness (Dierking et al., 1997). In the summer melt season continuous or intermittent ablation takes place, with flood/drain cycles, and the opening of brine drainage channels. Ice that survives the melt is desalinated, with a coarse grained bubble structure on the high points, and ponds in the lows. Yackel and Barber (2000) show that Radarsat is sensitive to the development of melt water ponds, particularly on windy days when the surface of the ponds is roughened.

Ice dynamics may also impact on the backscatter by changing the surface roughness. Ridges develop within pack ice due to the effects of wind and ocean currents. Total backscatter from an area increases with ridge frequency (Haas et al., 1999; Marko et al., 2003). Enhanced weathering gives ridges lower salinity and higher backscatter (Haas et al., 1999). Leads may be confused with ridges as both contain bright corner reflectors (Melling, 1998; Dierking and Dall, 2007).

Ice that survives the summer melt season becomes second year or multi-year ice. The uppermost layers of multi-year ice floes have a complicated, highly variable, density and air void structure that strongly affects the radar backscatter (Carlstrom and Ulander, 1993; Nystuen and Garcia, 1992). Multi-year ice is also less saline than younger ice, therefore volume scattering is more important (Dierking and Dall, 2008; Carlstrom and Ulander, 1995). Frost flowers on young ice can mimic this

highly variable structure, causing confusion with older ice (Nystuen and Garcia, 1992).

The presence of snow cover on the ice surface has its own influence on the radar backscatter. The electromagnetic properties of snow are dependent on temperature and density, ice crystal size distribution, and liquid water inclusions (Langlois and Barber, 2007). Snow decreases the dielectric discontinuity at the ice surface and reduces the surface component of the radar reflectivity of the ice. Radar wavelengths comparable to the scale of ice crystals or water incursions will be affected by volume scattering. Dry winter snow allows penetration to the ice beneath therefore the backscatter will reflect the ice properties rather than the snow (Marko et al., 2003). In the early melt season extensive snowpack re-crystallisation takes place. The snow cover contribution to the backscatter may become stronger as individual scatterers (snow grains and liquid water pockets) increase in size. Alternatively if the increased scattering is mainly directed away from the sensor this will have the opposite effect (Gill and Valeur, 1999; Ulander et al., 1995). Damp snow has low penetration at most radar frequencies, may have low surface reflection, and also acts as a wave absorber.

2.3.2 SAR signatures for ice type

A SAR 'signature' is the backscatter associated with a particular surface type at a given band, polarisation, and incidence angle (Livingstone et al., 1987; Carlstrom and Ulander, 1993; Dierking et al., 1997). Ice type signatures under cold conditions are quite stable in the high Arctic and major ice classes can be readily identified (Livingstone et al., 1987). The variation in ice signatures is largest during the melt season. Under warmer conditions the signatures change with the structure, moisture content of the snowpack, and with free water in the surface layers of underlying ice (Livingstone et al., 1987). Figures 2.2 and 2.3 show the SAR backscatter signatures associated with different ice types in summer (Figure 2.2) and winter (Figure 2.3). These figures are not included in the eThesis to avoid copyright infringement, the reader is referred to the original: Onstott and Shuchman (2004), page 92.

2.3.3 Iceberg Detection

Icebergs produce different radar returns to those from sea ice due to the different structure and salinity of the ice. Icebergs stand out from a background of sea ice because they have a higher backscatter coefficient (Williams et al., 1999). Surface and volume scattering can both be significant (Willis et al., 1996). The edges of icebergs (where the ice freeboard stands proud of the water surface) can act as strong corner reflectors. Icebergs are non-saline, therefore volume scattering is more dominant than it is in sea ice (Power et al., 2001). A double bounce mechanism may create strong returns from the iceberg edges while an iceberg shadow is found in the lee of the berg (Haykin et al., 1994). Penetration to the bottom of an iceberg is possible at L band, but is unlikely at C band, due to increased sensitivity to surface roughness and internal inhomogeneities at shorter wavelengths. Icebergs are expected to stand out from sea ice as brighter areas, however, snow on the surrounding sea ice or water on the surface of the iceberg can lower the contrast between the two (Gladstone and Bigg, 2002; Williams et al., 1999). In some cases iceberg signatures may become confused with those from multi-year ice floes from which the brine has drained (Land et al., 2002).

2.3.4 The use of different bands and polarisation to identify sea ice and icebergs

The backscatter from sea-ice and icebergs varies with wavelength. C band shows greater variation between young and old ice than L band does because of its greater sensitivity to the surface roughness in relation to the wavelength (Dierking and Dall, 2007). At an even shorter wavelength, X band shows an even greater sensitivity to surface roughness, i.e. the brightness of returns from an ice object will be very dependent on the roughness of that objects surface. If the penetration depth exceeds the thickness of the medium, the next lower layer interface receives significant energy to contribute to the returns. This is common for dry snow over sea ice in winter and for icebergs at L band (Dierking and Busche, 2006).

The backscatter of sea ice and icebergs also varies at different polarisations (Alexandrov et al., 2004; Nghiem and Bertoia, 2001). Polarisation can be vertical (V) or horizontal (H), normally denoted by a two letter code with the first letter indicating the polarisation of the transmitted pulse in and the second letter denoting the polarisation of the received backscatter. A cross polarised radar cross section contains information not found in a like polarised cross section. Strong cross polarised returns are seen from volume scatterers such as snow and cold, old ice and for geometric reflections at dihedral interfaces e.g. rafts, fractures, and ridges. Significant improvements in sea ice mapping may be made by combining bands and polarisations (Rignot and Drinkwater, 1994).

At C band, HH has been shown to produce better ice discrimination at low windspeed, while VV produces better results in high wind speeds, at a range of incidence angles (Williams et al., 1999). C band backscatter differs more between like and cross polarisation than L band does because of increased sensitivity to surface roughness. Backscatter coefficient and VV to HH ratio are highly correlated with ice thickness at L band (Wakabayashi et al., 2004). At L band, cross polarisation (HV or VH), produces better discrimination between ice and water than like polarisation (Dierking and Dall, 2008). Dierking and Dall (2008) and Dierking and Busche (2006) recommend an L band SAR system for mapping the deformation state of sea ice, because frost flowers and ice crystals within surface snow pack can result in high returns of vertically polarised radiation but low returns of horizontally polarised radiation at C band, while maintaining low returns to L band in either polarisation.

2.4 Commercial use of Radar data

Radar data is used by ice identification services around the world to map the ice edge, estimate ice concentration, and identify different ice types (McClintock and McKenna, 2007; Druckenmiller et al., 2009; Mahoney et al., 2008). SAR is also used to track individual icebergs within an operational setting, for example, the

Grand Banks iceberg management program has used RADARSAT data since 2003 to identify icebergs that may pose a hazard to oil installations (McClintock and McKenna, 2007). Ice services aim to provide a comprehensive identification and prediction service; plotting the ice motion and concentration, mean ice thickness, ridged ice thickness, ridge concentration, compression regions and deformed ice fraction (Karvonen et al., 2007). Ice charts are generated by trained analysts using a combination of satellite images, observations and a forecast model, with the previous week's ice chart and meteorological data (Walker et al., 2006; Maillard et al., 2005; Kwok et al., 1990). The segmentation of satellite imagery and classification of different ice types may be carried out by automated image processing algorithms (Kwok et al., 1990; Fetterer et al., 1994; Kwok et al., 1992). Because human interpretation is time consuming substantial effort has gone into the automation of image processing for commercial use; but unfortunately no automated classification method is completely reliable (Haarpainter and Solbo, 2007). Common problems encountered by automated classification include accommodating the range of backscattering signatures from different ice types and the effect of wind on open water (Sephton et al., 1994; Haarpainter and Solbo, 2007; Maillard et al., 2005). C band radar is widely used for all season capability, this represents a compromise: a longer wavelength (L band) would be better in summer and for mapping deformation features, while a shorter wavelength (X- and Ku bands) would be better in winter (Dierking and Busche, 2006). It is possible that as data from various different sensors becomes more affordable and more widely available the use of a combination of different bands will become more common place.

2.5 Tracking ice movement

Use of automatic ice motion tracking techniques began in the late 1980s (Sun, 1996). Methods for the derivation of sea ice movement vectors from passive microwave data rely on cross correlation between pairs of images (Kwok and Rothrock, 1999; Spreen et al., 2006; Haarpainter, 2006). Cross correlation techniques have also been applied to data from SAR sensors such as Radarsat and Envisat (Sun, 1996; Kwok et al.,

2004; Karvonen et al., 2007), and the Quikscat scatterometer (Walker et al., 2006). Cross correlation techniques are based on convolution: finding the same pattern of pixels in two images. Attempts to track the motion of sea ice are complicated by the similarity of the ice edge in different places and by similarities between individual floes (Karvonen et al., 2007). Almost all studies using cross correlation technique exclude the summer months as these techniques are not suited to tracking movement where the pack is dispersed rather than moving together.

An alternative to cross correlation techniques is feature based or object based tracking, where the same individual 'objects' are identified in consecutive images. Kwok et al. (1990) and Liu et al. (1997) describe the use of one such feature based tracking system at the Alaska SAR Facility. Automatic identification of individual sea ice floes or leads is achieved by segmentation of the satellite image. The boundaries of individual segments are then vectorised to form one-dimensional data structures consisting of ordered pairs representing the boundary image co-ordinates (Kwok et al., 1990). A transformation is then applied to these co-ordinate pairs to generate a rotationally invariant curvilinear representation that can be matched to the same representation of objects in subsequent images.

A significant volume of work aims to identify and tracking of individual icebergs from remotely sensed data (Power et al., 2001; Willis et al., 1996; Lane et al., 2004; Sun, 1996; Silva and Bigg, 2005; Silva, 2006; Gill, 2001; Williams et al., 1999). Large tabular Antarctic icebergs were the first objects to be tracked on satellite images. The national ice centre in Washington DC has been monitoring the movement of giant bergs since 1977. Manual identification of the same objects in a series of images from the SSM/I passive microwave sensor (Phillips and Laxon, 1995) was superseded by automated identification techniques. In the Antarctic; Williams et al. (1999), Gladstone and Bigg (2002), and Silva and Bigg (2005), demonstrate the identification of icebergs using automated or semi automated methods, based on edge detection and thresholding of radar images from ERS 1 SAR. Success is also reported in similar techniques applied to Radarsat and ERS 1 and 2 images, and later Envisat images, from Arctic regions including the Newfoundland coast and

the European high Arctic (Willis et al., 1996; Power et al., 2001; Lane et al., 2004; Howell et al., 2004). The automation or semi automation of iceberg identification tools is well documented. Less well documented is the successful automation of the matching of objects between one image and the next. Gladstone and Bigg (2002) applied a simple matching algorithm that looked for similarities in the length, width, and perimeter of objects, while Silva and Bigg (2005) took this concept a stage further by calculating a one dimensional shape representation for each iceberg object. The shape representation is obtained by following the object's contour and recording at 5° intervals the direction and distance from the objects central point. All pairs of geometrically similar objects are then compared by shifting one of the contour vectors until a maximum correlation is obtained. Using this method, named the ITSARI algorithm (Silva and Bigg, 2005; Silva, 2006), the tracking of tabular Antarctic icebergs was successfully semi-automated. The ITSARI algorithm (Silva and Bigg, 2005; Silva, 2006) is similar to the method (described in the previous paragraph) used by the Alaska SAR facility to track sea ice movement (Kwok et al., 1990; Liu et al., 1997) in that they both begin with image segmentation and perform object matching based on a shape representation. There is no indication in Silva and Bigg (2005) or Silva (2006) that the ITSARI algorithm built on the work of the Alaska SAR facility. I am informed (Bigg - personal communication) that any similarity is coincidental.

Larger icebergs are detected more consistently (Power et al., 2001; Gladstone and Bigg, 2002; Silva and Bigg, 2005; Silva, 2006). The smallest icebergs that can be detected are of the order of a pixel in an image (Land et al., 2002), but objects this small cannot be tracked as they have no individual shape. Silva and Bigg (2005) successfully tracked bergs as small as 200m diameter on high resolution SAR of the Southern Ocean. Icebergs in the Southern Ocean are easier to identify using radar data than those in the Arctic as they have consistently stronger backscatter than the background of sea ice and water (Gladstone and Bigg, 2002). Icebergs in the Arctic tend to be smaller and more easily confused with multi-year sea ice (Lane et al., 2004). The bergs produced in the Arctic are smaller than those of the Antarctic, being 100-300m in diameter, because the glaciers of the area are narrow

and fast flowing, therefore heavily crevassed. Many of the fjords that Arctic glaciers calve into have a shallow sill at seaward end on which icebergs become grounded. Here they may remain trapped for months before advancing into the open ocean. Those that drift into shipping lanes tend to be the smaller ones that are harder to detect; so considerable effort has gone into detecting small icebergs against a background of sea clutter (Gill, 2001; Panagopoulos and Soraghan, 2004; Leung et al., 2002). Unfortunately higher wind speeds, generating greater sea clutter, may lead to icebergs being missed altogether in automatic detection (Howell et al., 2004; Land et al., 2002; Power et al., 2001).

Chapter 3 describes the adaptation of the ITSARI algorithm for use in the Arctic.

Chapter 3

Methods

3.1 Introduction to the ITSARI algorithm

The identification and tracking of individual sea ice floes in this thesis is carried out using the ITSARI (Ice Tracking from SAR images) algorithm. The ITSARI algorithm was developed by Tiago Silva to track large tabular icebergs in the Antarctic (Silva and Bigg, 2005; Silva, 2006). A detailed description of the development of the original algorithm can be found in Silva (2006). Further development by Alex Giorgianis and 'Genesys' (a software company based at the University of Sheffield) improved the usability and linked various blocks of code together to form a workflow. The focus of this project was testing the algorithm in different geographical areas, and with data from different sensors, in line with the research aims of my sponsors, Kongsberg Satellite Services. During the course of this project modifications to the workflow were made to suit the new uses to which it was being put, for example, to facilitate the handling of different images. It should be understood that the core of the algorithm has not been modified from the original.

ITSARI is implemented as a series of functions in Matlab, using a text based interface operating from the Matlab command line. The algorithm is divided into three parts: importing an image into Matlab, identifying ice objects within that image, and matching objects from one image to the next. The basic workflow is

presented in Figure 3.1. The image-processing machine is configured with two 64-bit Intel Xeon E5450 CPUs running at 3 GHz, giving a total of 8 processing cores, and 4GB of RAM.

3.2 Image pre-processing and import into Matlab

In any remote sensing endeavour the accuracy of the pre-processing of the raw satellite data to create the image that is then subject to analysis can be as important as the analysis itself. If pre-processing is not accurate then an image may be difficult to analyse or provide misleading information. The original code (Silva, 2006) was written to process N1 data obtained from ESA (European Space Agency). N1 data are data supplied at the most basic level, following any corrections for instrument bias at the time. The pre-processing of this data is carried out using the Basic Envisat SAR Toolbox (BEST) that is supplied by ESA (downloaded from the ESA website at http://earth.esa.int/best/). The ITSARI script creates a template that is then passed to BEST with the following instructions: BEST must read the header file from the N1 data, and then read in the N1 data, determining the output image size. The image is read both as a quicklook and as a full scene. The BEST tools perform an amplitude to power conversion, a rough range calibration, and conversion to backscatter (σ^0) values. In the earlier versions of ITSARI BEST was used to generate a band-interleaved image file with accompanying text file storing the information from the original header. The band-interleaved file was read into Matlab and the image was rotated depending on the orbit direction.

One of the updates made for this thesis was a move towards working with Geotiff files. The reason for this was linked to the aim of separating the pre-processing from the rest of the workflow to enable the processing of images from different radar sensors. Geotiff was chosen as a commonly used image format, convenient for operational uses. In the modified code, where data are supplied in N1 format supplied BEST is used to convert these to Geotiff rather than band-interleaved

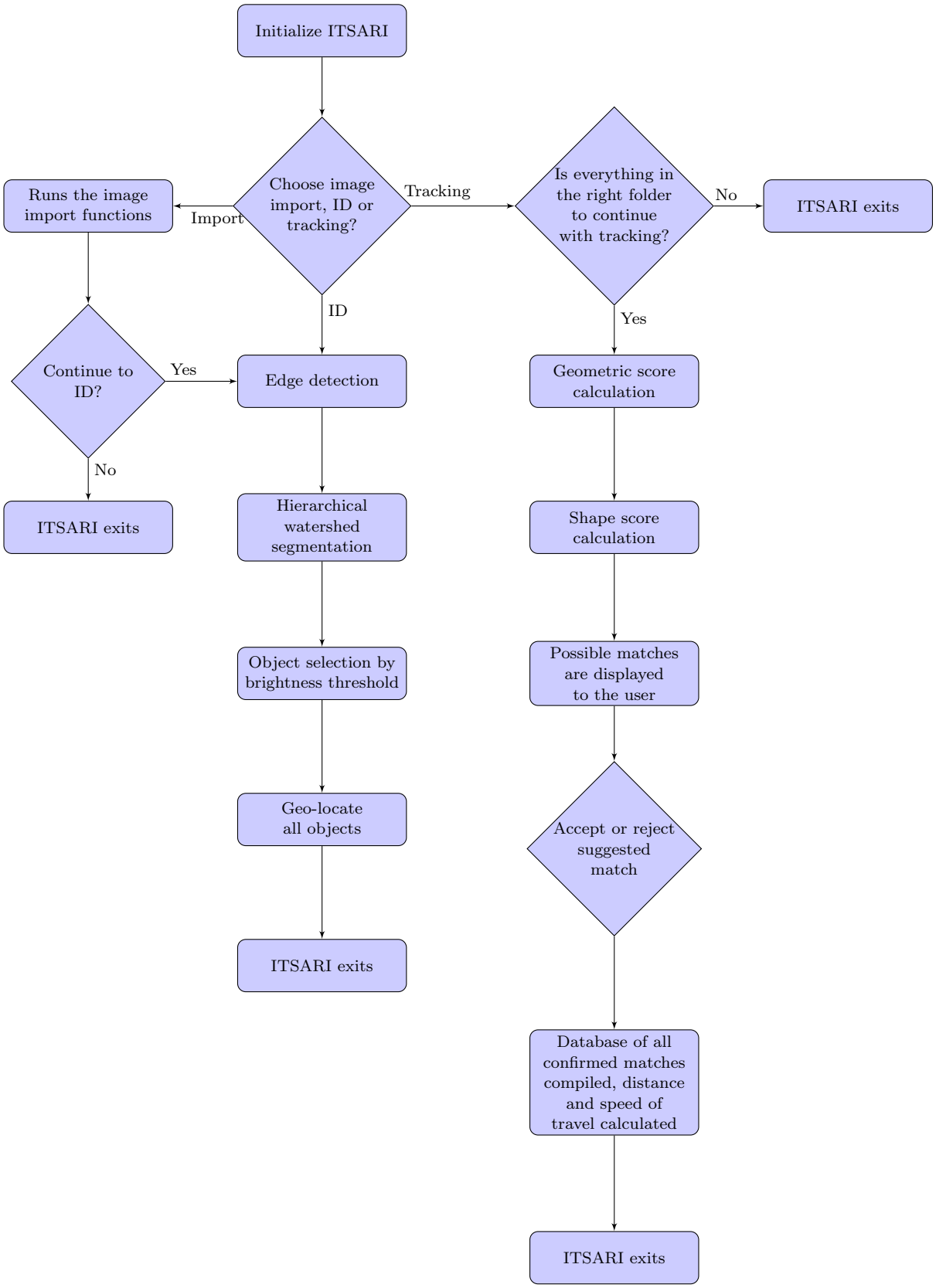

Figure 3.1: The ITSARI algorithm in its most basic form

images. The image is rotated by the BEST toolbox and a referencing matrix is supplied to convert each pixel from x - y co-ordinates into latitude - longitude (alongside the image in the geotiff file). ITSARI has been adapted to read into Matlab geotiff files generated elsewhere containing data from different sensors and their accompanying referencing matrices. Where no referencing matrix is supplied ITSARI will generate one from the corner tie-points supplied, but it should be noted that this is not as accurate as using the referencing matrix. Once read into Matlab the image and referencing matrix are saved in internal Matlab format for further processing.

In all cases the input to ITSARI must be a single band image with pixel values in dB. To use information from sensors with multiple bands, these must be combined into a single grey-scale image as part of their pre-processing (an example using band mathematics to combine two bands is included in Section 5:1).

3.3 Image Segmentation

The first stage of the processing is to segment the image into homogeneous regions. The image segmentation has two stages. The first stage is to find edges within the images using a multi-resolution Ratio Of Averages (ROA) filter. The second stage is to join the edges to create closed regions using Hierarchical Watershed Segmentation (Silva and Bigg, 2005; Silva, 2006).

3.3.1 Coast Masking

Where appropriate it is possible for the operator to mask out areas of land from further analysis to avoid 'false alarms' caused by strong radar returns from the land. This occurs after the ROA filter has been used to create the edge map, but before the hierarchical segmentation. The coastline is delineated using a semi-automated process: the user must draw two polygons onto the image: one within the boundaries of the coast and one within the boundaries of open water. A hierarchical watershed

segmentation is used on the edge map created by the ROA filter to find the one strongest edge within the area of the image that lies between the two polygons defined by the user. The user then defines which polygon (left or right of the strongest edge) should be used as a 'landmask' excluding the part of the image containing land from the following processing.

3.3.2 Ratio of Averages filter

A Ratio of Averages (ROA) filter is used to detect edges within the SAR image. Per-pixel segmentation of SAR images is inefficient because of the large variation in grey tones caused by speckle, (Touzi et al., 1988). The ROA filter is designed to detect edges using the ratio of average pixel brightness values in non-overlapping neighbourhoods defined either side of a given point (Touzi et al., 1988; Sephton et al., 1994; Silva and Bigg, 2005; Silva, 2006). The ROA filter passes a filter window over the image. For each pixel the filter window is split into two parts (subwindows), not including the central pixel. The average brightness of pixels in each of these subwindows is calculated and the ratio of the averages between each subwindow is calculated as follows:

$$\tau = min\{\frac{\hat{\mu_1}}{\hat{\mu_2}}, \frac{\hat{\mu_2}}{\hat{\mu_1}}\} \tag{3.1}$$

where μ_1 and μ_2 are the average values calculated for the two subwindows either side of the central pixel (Silva and Bigg, 2005). This is a test for the presence of an edge in the space between (that is, the central pixel under consideration) with low values indicating the presence of an edge (Figure 3.2). An ROA is calculated for each of the four possible edge directions - horizontal, vertical and two diagonals - and the minimum pixel value for the four orientations is taken and used for the central pixel in the edge map. A detailed description of the ROA filter used here is available in Silva (2006). It is important to keep in mind that the following stage, hierarchical watershed segmentation, is applied to the edge map not to the image itself.

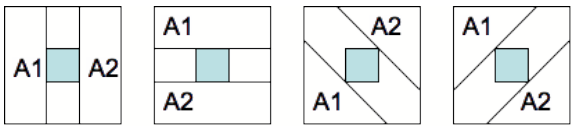

Figure 3.2: Figure showing four orientations for ROA. For each direction the ROA is the ratio of the average for each subregion, A1 and A2 (after Silva (2006))

Using a larger filter window gives greater noise suppression; but unfortunately also reduces the size of objects that can subsequently be detected. The multi-resolution ratio of averages filter used in ITSARI applies the filtering window at 3 x 3 and 5 x 5, then normalises it and for each pixel takes the higher brightness value, independently of the window size from which it was obtained (Silva, 2006; Fjortoft, 1999). This results in more noise reduction in homogeneous areas of the image without reducing the detail in heterogeneous areas. Using a larger filter window is appropriate for sea ice identification because of the small contrast between adjacent segments or between objects of interest and the background (Williams et al., 1999).

3.3.3 Hierarchical Watershed Segmentation

Following edge detection using the ROA, a hierarchical watershed segmentation is used to find closed regions within the edge map created for the image. A watershed segmentation can be said to consider a greyscale image as a topographical surface; the pixel brightness values of which are interpreted as heights. The segmentation algorithm finds watersheds and basins within the image. A hierarchical watershed segmentation joins or divides regions based on the 'height' of the watershed walls separating different basins. The user must select a threshold value for the segmentation. Only watersheds taller or deeper than this threshold will be created as segments. A higher threshold value therefore produces fewer segments. To put it another way, if the difference in brightness values of two adjacent pixels is lower than the threshold, those two pixels will belong to the same image segment. If the difference is above the threshold, they remain separate. Non-closed contours are eliminated from the segmentation, because the algorithm is ultimately looking for discrete objects. To assist with the selection of a threshold value the user is presented with an example showing the possible segmentation results on a sub-section of the image.

3.4 Selection of ice objects using a brightness threshold

Following segmentation of the image both bright and dark objects will have been identified. The next stage is for the operator to select a brightness value that can be used to separate ice objects from open water, or where both are present, to distinguish between icebergs and sea-ice floes. Figure 3.3 shows two objects, with their brightness (σ^0 in dB) profiles across the centre of the objects alongside, demonstrating that in these winter images the brightness of the objects can be up to -16 dB against a background of -20 to -24 dB. Brightness is not consistent across an object, therefore ITSARI calculates the average brightness of each of the objects segmented, and thus can select all objects with an average brightness above the brightness threshold defined by the operator.

ITSARI computes the geometric properties for each of the selected objects: perimeter, area, length of each of three axes, and x and y co-ordinates of the centre pixel, and stores this information in a database.

The original ITSARI workflow contained the following options within the identification stage:

- Manual removal of individual objects from the selection to remove obvious 'false alarms';
- Further narrow down the selection of objects using a size and shape threshold that was optimised for the identification of tabular icebergs using the following parameters: ratio of perimeter to square root of the area, ratio of minimum and major axis length, and total area (object size). This option is not used in this thesis as the parameters did not apply to sea ice floes;
- Merge adjacent objects based on their brightness values (to remove over-segmentation).

In the course of work for this thesis the following additional options have been developed:

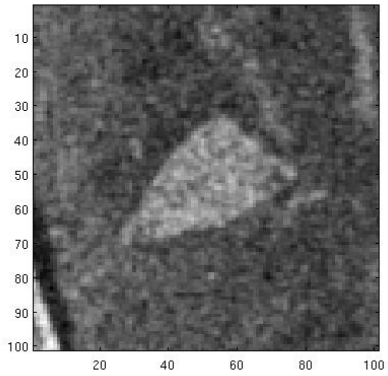

(a) Object in centre of 100 pixel subimage

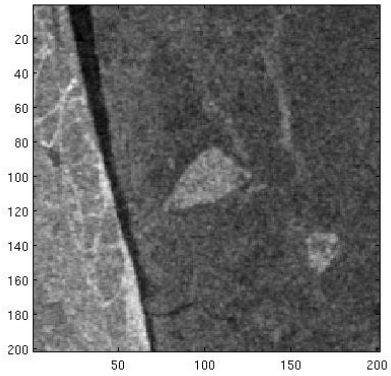

(b) Object in centre of 200 pixel subimage

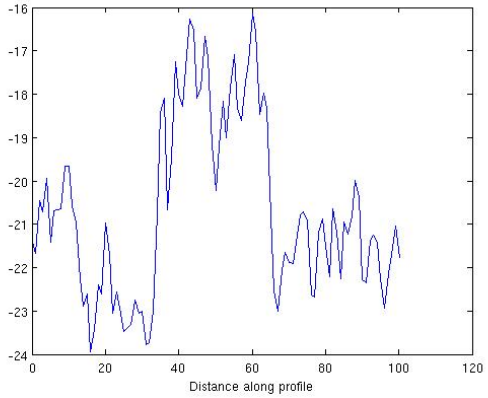

(c) Vertical brightness profile through centre of 100 pixel subimage (a)

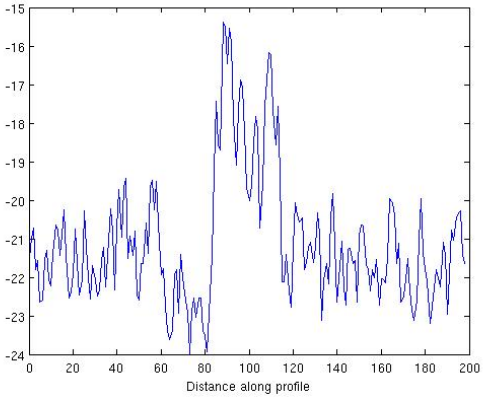

(d) Vertical brightness profile through centre of 200 pixel subimage (b)

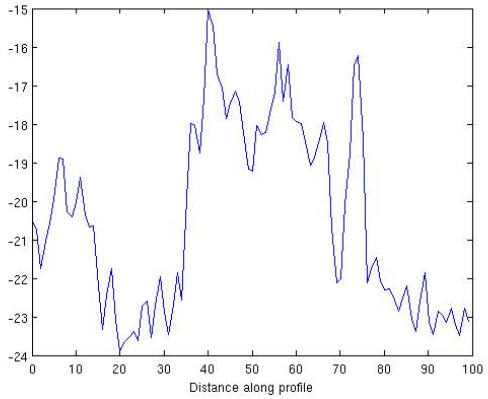

(e) Horizontal brightness profile through centre of 100 pixel subimage (a)

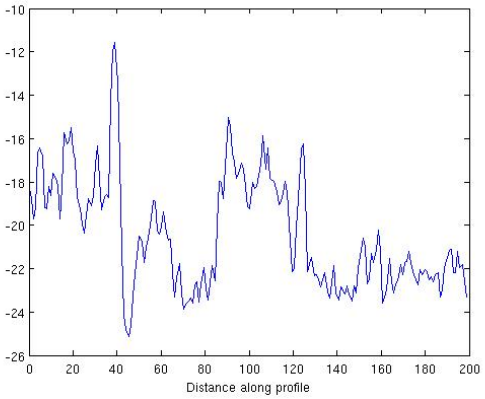

(f) Horizontal Brightness profile through centre of 200 pixel subimage (b)

Figure 3.3: Brightness of an ice object on February 18th 2008.

- Select only the largest objects by number of pixels contained therein using a size threshold defined by the user;
- Manually select the wanted objects as opposed to excluding the unwanted ones;
- Edge mapping used to locate the sea ice edge in the same fashion as it is used to delineate the coast and thus mask out land masses.

The work that led towards the inclusion of these extensions is described in the case studies contained within chapters 4 and 5.

3.5 Location of ice objects

ITSARI carries out all of the image processing in image row - column co-ordinates. To geolocate the objects the original ITSARI relied on the BEST toolbox to convert the row-column (x and y) co-ordinates of the centre pixel of each object to latitude and longitude, taking into account the rotation that took place on import to Matlab. ITSARI was modified in the course of work for this thesis to call instead on the referencing matrix imported (or generated on import) with the image.

3.6 Tracking the movement of ice objects using shape matching

The third and final section of the ITSARI algorithm tracks the movement of ice objects by matching their shape in one image to the same shape in the next image - an 'object pair'. The shape matching occurs in three stages: an initial match, shape vector creation and testing, and confirmation of 'true' matches by the operator

3.6.1 Initial match

In the first stage ITSARI performs an initial shape match on objects not prohibited from matching by the following parameters: ITSARI prevents the matching of shapes from the same image and from images less than an hour apart; prevents small objects from being included in the match; and imposes a limit on the speed at which the ice object can move, to prevent wildly inaccurate matches being suggested. This limit is currently hard coded at 0.5 ms^{-1}, as an absolute upper limit on how far an object could physically travel, however, in reality the rates of movement are much lower than this.

For each possible object pair the original algorithm first checked the metadata associated with the images to ensure that the orbit and frame identifiers for the two images were different, then looked up the acquisition time in the header (stored as a text file) and eliminated matches less than an hour apart. This procedure has been simplified to simply check the date and time as not all images used in this project were identified by orbit and frame. The distance the object would have to travel for the match to be true is calculated from the two latitude / longitude positions. This plus the time difference is used to calculate speed and eliminate those matches that would require the object to be travelling at greater than 0.5 ms^{-1}. The inclusion of a speed threshold is another innovation for this thesis.

For each possible pairing that passes the above checks a geometric score is calculated. The geometric score is the reciprocal of the euclidean distance between two feature vectors consisting of the square root of the area and the minor axis length of each object (Silva, 2006).

$$Geometric\ Score = \frac{1}{|\vec{a} - \vec{b}|} \tag{3.2}$$

where: $\vec{a} = \sqrt{area_{object\ a}} : minoraxis_{object\ a}$ and $\vec{b} = \sqrt{area_{object\ b}} : minoraxis_{object\ b}$

In the earlier version of ITSARI this value is compared to a geometric threshold set

by the user. Possible matches that exceed this threshold pass to the second test. One of the objectives of the case studies that follow in chapters 4 and 5 was to ascertain whether the introduction of a geometric match threshold was meaningful when looking at sea ice. It was discovered that successful matches fell into a broad range of geometric match values so in later tests this stage was dropped altogether.

3.6.2 Shape Vector creation and testing

The second stage performs a more detailed analysis of those object pairs that pass the initial match test. For each object that has a possible match, ITSARI creates a shape vector based on the distance from the centre to all points on the perimeter of the object for each object in a pair. First, a raster file is created for each individual object that has a possible match. In this raster file areas within the object are given the value 1 and areas outside the object are 0. From each mini raster file the shape vector is created as follows (Silva and Bigg, 2005; Silva, 2006): the centre of the object has already been defined in the identification stage; from this centre the algorithm steps out left until the edge of the object or the end of the image is found. The algorithm then follows the object's contour and records, for each pixel, the distance and direction from the object's centroid (Silva and Bigg, 2005). The resulting distance/ direction vector is then interpolated linearly and resampled every 5° to yield a shape vector that describes the distance from the edge to the centroid for 72 regularly distributed directions (Silva and Bigg, 2005; Silva, 2006). All pairs of geometrically similar objects are then compared by shifting one of the contour vectors until a maximum correlation is obtained. This eliminates the effect of rotation on object matching (Silva and Bigg, 2005). Finally, the reciprocal of the euclidean distance between the two shape vectors is calculated (in a similar manner to the method used to compare the two vectors for the geometric score above) as a measure of the two objects similarity (referred to from here on in as the 'shape match score' and those pairs whose similarity falls below a threshold defined by the user are discarded.

Whereas in the original version of ITSARI (Silva, 2006) a possible match goes forward to be presented to the user if the shape match score is above a threshold set by the user; it became apparent in the case studies in the following two chapters that for application to sea ice the most efficient option is calculating all possible shape matches that fall within acceptable speed of travel, and looking first at those with the best scores when presenting matches to the operator for approval.

3.6.3 Confirmation of 'True' matches by the operator

Once shape vectors have been created and their correlation tested for all possible matches, ITSARI prints to screen a subsection of each image showing the objects that are a possible match, alongside a map showing the locations of the two sets of objects. The user must confirm whether a match is correct. If the match is correct then both objects are removed from future possible matches, otherwise the possible matches are re-sorted, and the next option is displayed. When all possible matches have been accounted for the list of confirmed matches is saved in a database, and the tracks plotted on a map. For this thesis the algorithm was extended to calculate the distance travelled and speed of travel and output these to the database along side the match identifiers and object location at each end of the track.

3.6.4 Export of vectors as shapefiles

A significant development for this project was the introduction of a function to export the information as shape files that can be read into and used with other mapping software such as ArcGIS.

3.7 Demonstration of the identification and tracking of two ice objects from an Envisat WS image

This example works through the identification and tracking of two ice objects located just outside the fast-ice area off the Greenland coast. Figure 3.4 shows the location of these objects in an image from 16 February 2008.

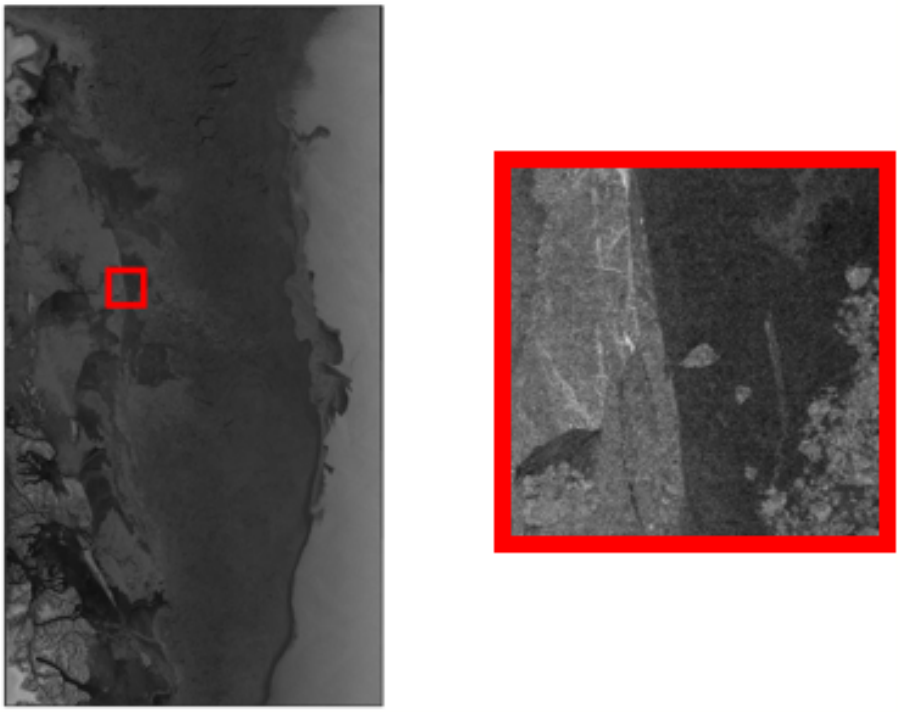

Figure 3.4: Location of ice objects in the example described in section 3.7 on 18 February 2008.

The image segmentation begins by using the multi-resolution ratio of averages filter to identify edges within the images; and hierarchical watershed segmentation to find closed regions within the edge map (as described in section 3.3). It is up to the user to define how fine the segmentation should be. What will be identified at different segmentation levels is displayed to the user to help with this selection (Figure 3.5). In this case a segmentation threshold of 12 was chosen, this segments the two objects as shown in Figure 3.6.

Segments are assigned to the ice object's class using a brightness threshold (dB) defined by the user. The user is presented with a histogram showing the brightness

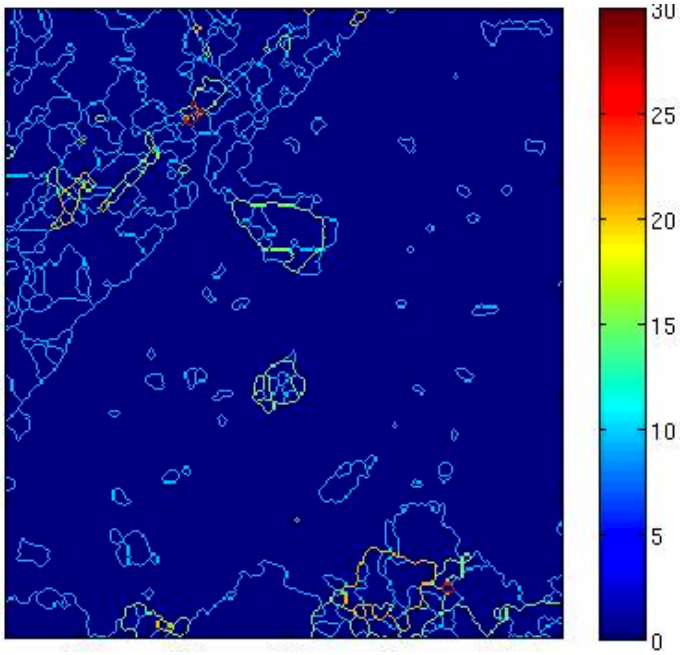

Figure 3.5: Showing the possible segmentation of the image at different segmentation thresholds.

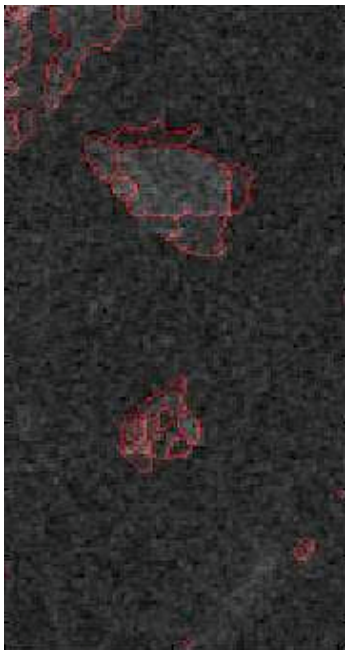

Figure 3.6: Showing the segmentation of part of the image using a threshold of 12. The red lines indicate the segments. The smaller object can be seen to be over-segmented.

of all segments in the image to help them choose. Objects with an average brightness less than the threshold are rejected. In this case a threshold of -18 dB was chosen. The user must then use the option to manually select individual objects to select the two objects used in this example from the full set identified by the algorithm.

At the end of the identification process a database is created, listing the geometric properties of the ice objects located, and their location in row-column co-ordinates. These row-column co-ordinates are converted to latitude-longitude values. A map is produced showing the location of the identified objects within an outline showing the geo-location of the images.

To match between pairs of images the two lists of identified objects, the two latitude-longitude location files, both images, both accompanying text files containing the date and the two object label files are passed to the matching algorithm which matches object pairs using the method described above. Two examples of matches suggested by ITSARI for this example are presented in Figure 3.7

3.8 Identification of the sea ice edge

The ITSARI algorithm has also been adapted (for this thesis) to map the sea ice edge using a similar semi-automated method to that used to delineate the coast for the coast masking. In order to do this the operator must draw two polygons onto the image one within the boundaries of the sea ice and one within the boundaries of open water. A hierarchical watershed segmentation is used on the edge map created by the ROA filter to find the one strongest edge within the area of the image that lies between the two polygons defined by the operator (Figure 3.8).

3.9 Further examples of the algorithm at work

Chapters 4 and 5 present a series of case studies designed to explore the possibilities for using ITSARI to track ice movement in different areas, at different times of year (with associated differing ice conditions) and with data from different instruments.

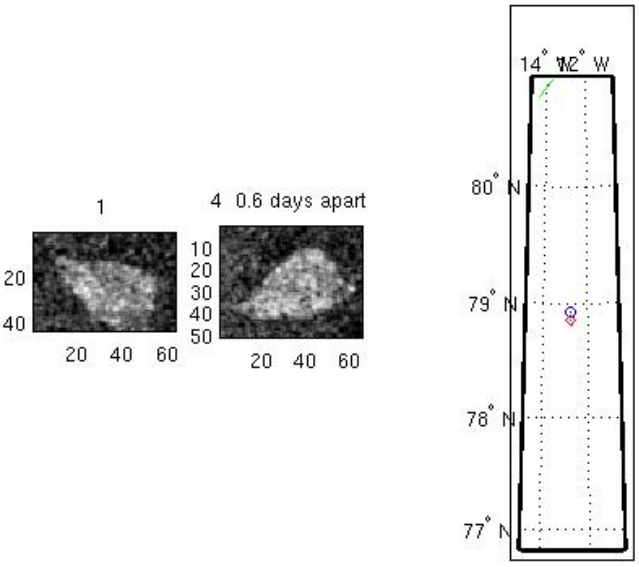

(a) Matching the first object

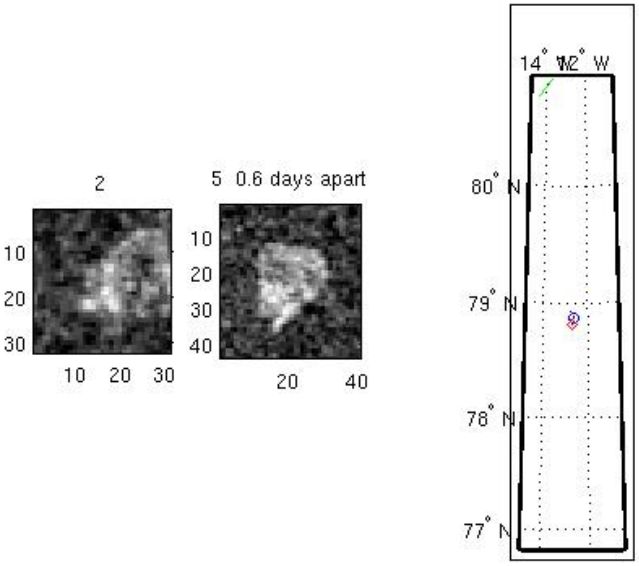

(b) Matching the second object

Figure 3.7: Two screen shots showing how possible matches (in this case the two objects from the case study described in section 3.7 are displayed by ITSARI for approval by the user.

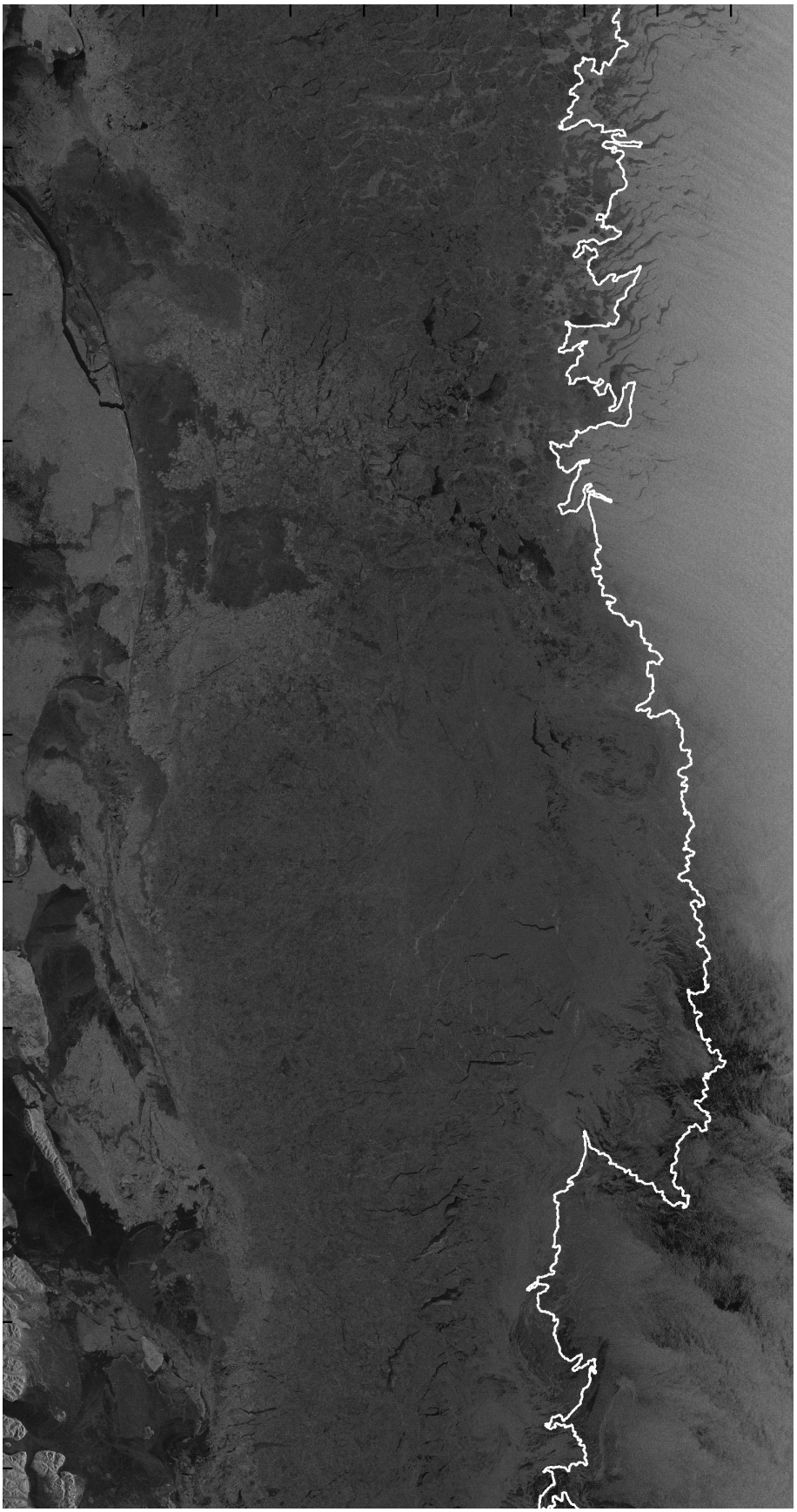

Figure 3.8: Sea ice edge (strongest edge found by ITSARI between two polygons drawn by the operator) on 18 February 2008.

Due to the flexibility of the ITSARI algorithm, the following case studies may include a short methodology section that describes the options and configuration in use.

Chapter 4

Envisat Wide Swath images of the Arctic

This chapter details three case studies, the aim of which was to adapt the use of the algorithm to tracking sea ice movement in the Arctic. In the first instance the algorithm was tested with Envisat images, these being the logical follow on from the ERS 1 and 2 images the algorithm was originally developed to process. The first case study looks at tracking ice movement in the Fram Strait in February 2008 from images acquired at 2 or 3 day intervals. The second case study expands the temporal resolution to study images of the Fram Strait over a whole year at up to 10 day intervals. The third case study was a test of whether the methodologies used for the Fram Strait could be easily applied to other areas of the Arctic; for this images from the Barents Sea were used.

4.1 Identification and tracking of individual sea ice floes in the Fram Strait from Envisat Wide Swath images; February 2008

The work discussed in this section appears in Hall et al. (2012). The aim of this first case study was to ascertain whether the ITSARI algorithm could be adapted

from use as an iceberg tracking tool to be used successfully in Arctic conditions for monitoring sea-ice object movement. An additional change was the switch from ERS-1 images to Envisat wide swath images. The reason for testing the ITSARI algorithm with wide swath imagery was that the routine imaging of polar regions using Envisat is scheduled to continue in Wide Swath mode into the future, generating a longer term time series of comparable images at between 3 to 10 day intervals (Vogel et al., 2010). Wide swath images are economical, covering a large area on a regular repeat track.

The Fram Strait was chosen as a study area because it is of key importance for the export of ice from the Arctic (Kwok and Rothrock, 1999; Kwok et al., 2004; Spreen et al., 2006) and well known for the presence of strong surface currents (Fahrbach et al., 2001; Dickson et al., 2007). Twenty images centred on the western (Greenland) side of the strait were obtained (Table 4.1). All were acquired in N1 format and imported into Matlab using the BEST toolbox and ITSARI's import routine. The images cover an area between 77-81 degrees N. The study area is within the area of the East Greenland current, and also covers the fast ice / drift ice boundary.

This case study is in two parts: part one tracking two specific pieces of ice and part 2 looking at tracking over the wider area covered by the images using fixed parameters. This example represents the first attempt at using the ITSARI algorithm to identify sea ice movement in the Arctic. Individual sea ice floes are tracked within the ice pack in the Fram Strait.

4.1.1 Tracking two specific pieces of ice

We begin with the adventures of the two pieces of ice introduced at the end of Chapter 3. This exercise demonstrates how the algorithm could be used to identify and track specific objects of interest. The two pieces of ice are triangular in shape, and travelling together adjacent to the fast ice edge. These two pieces of ice were identified in a total of 10 images, travelling almost 100 km between the 13th and 25th of February with speeds varying between 0.01 m s $^{-1}$ and 0.19 m s $^{-1}$ (Figure 4.1).

Table 4.1: Envisat WS ASAR Images acquired for use in the Feb 08 case study.

Identifier	Acquisition Date	Acquisition Time (UTC)
30973_3618	01/02/2008	20:54:19
30982_3619	02/02/2008	12:06:05
31016_3620	03/02/2008	21:00:48
31030_3621	04/02/2008	20:29:50
31073_3622	08/02/2008	20:35:28
31116_3623	11/02/2008	20:41:06
31145_3624	13/02/2008	21:17:12
31154_3632	14/02/2008	12:28:35
31188_3633	16/02/2008	21:22:55
31211_3635	18/02/2008	12:03:12
31231_3636	19/02/2008	21:28:40
31245_3637	20/02/2008	20:57:16
31254_3638	21/02/2008	12:08:51
31288_3641	23/02/2008	21:02:57
31296_3639	24/02/2008	12:14:33
31317_3646	25/02/2008	21:40:02
31331_3647	26/02/2008	21:09:14
31340_3648	27/02/2008	12:20:16
31374_3649	29/02/2008	21:14:50

The movements between the 16th and 18th February and between the 21st and 23rd (at 0.15 m s $^{-1}$ and 0.19 m s $^{-1}$ respectively) are the most rapid, with the speed of movement between the 24th and 25th almost as high(Table 4.2).

Table 4.2 also details the brightness values (dB) of each object; and shape and geometric scores for the object pair (defined in Chapter 3), for the matched pairs of objects. In this exercise the brightness threshold used was -20 dB. The average brightness of the two objects varies over time, as do the shape and geometric scores. This is due to the shape identified not remaining constant due to edge effects and brightness changes caused by the changing orientation of the sensor in relation to the objects. The geometric scores vary between 0.05 and 0.38, while shape scores varied between 0.009 and 0.08. The lowest shape scores are lower than would be ideal for routine matching, because they are low enough that a large number of false matches would inevitably by presented to the user in the final stage, which would be time consuming.

The two objects have not rotated around their centres', being held in their orientation by the pack. However, it must be borne in mind that ITSARI is looking at the images in image co-ordinates during the matching stage, and it can be seen that

Table 4.2: Distance and speed of travel, geometric and shape scores, and average brightness values in db for two ice objects tracked in the case study described in Section 4.1.1

Start date	End date	Distance (km)	Speed (m/s)	Geometric Score	Shape Score	Average brightness first image	Average brightness second image
Object One							
13/02/2008	14/02/2008	1.39	0.03	1.5476	0.0530	-18.84	-18.59
14/02/2008	16/02/2008	6.05	0.03	0.1398	0.0500	-18.59	-18.36
16/02/2008	18/02/2008	20.2	0.15	0.1292	0.0098	-18.36	-18.29
18/02/2008	19/02/2008	0.88	0.01	0.4669	0.0091	-18.29	-18.35
19/02/2008	20/02/2008	3.22	0.04	0.1646	0.0267	-18.35	-18.64
20/02/2008	21/02/2008	3.01	0.06	0.1428	0.0142	-18.64	-18.51
21/02/2008	23/02/2008	38.83	0.19	0.1352	0.0145	-18.51	-19.13
23/02/2008	24/02/2008	6.47	0.12	0.1471	0.0372	-19.13	-18.6
24/02/2008	25/02/2008	21.96	0.18	0.3853	0.0360	-18.6	-18.82
Object Two							
13/02/2008	14/02/2008	1.64	0.03	0.5562	0.0822	-19.25	-18.91
14/02/2008	16/02/2008	6.75	0.03	0.1364	0.0265	-18.91	-18.98
16/02/2008	18/02/2008	21.23	0.15	0.0520	0.0514	-18.98	-18.22
18/02/2008	19/02/2008	0.65	0.01	0.1314	0.0322	-18.21	-18.86
19/02/2008	20/02/2008	3.8	0.04	0.0892	0.0352	-18.86	-19.47
20/02/2008	21/02/2008	3.3	0.06	0.0844	0.0352	-19.47	-18.82
21/02/2008	23/02/2008	39.56	0.19	0.0585	0.0210	-18.82	-18.45
23/02/2008	24/02/2008	6.84	0.12	0.0592	0.0211	-18.45	-19.03
24/02/2008	25/02/2008	23.01	0.19	0.1666	0.0515	-19.03	-19.07

there are two different orientations on the ascending and descending orbits. ITSARI has coped with this effective rotation of the objects and successfully matched them anyway.

4.1.2 Tracking over the wider area covered by the images

The next exercise was to identify and track as many objects as possible between each consecutive pair of images. Each of the images listed in Table 4.1 was processed using the ITSARI algorithm to identify distinctive ice objects. Following a period of experimentation, the following thresholds were chosen for the processing of each image. The segmentation threshold was set at 14, the brightness threshold at -19 dB, and an additional size threshold prevented the inclusion of any object measuring less than 150 pixels in total. This was necessary to avoid hundreds of small, similarly shaped objects made up of a small handful of pixels going forward to the matching stage, and so increasing the number of false matches and the time taken for this latter stage.

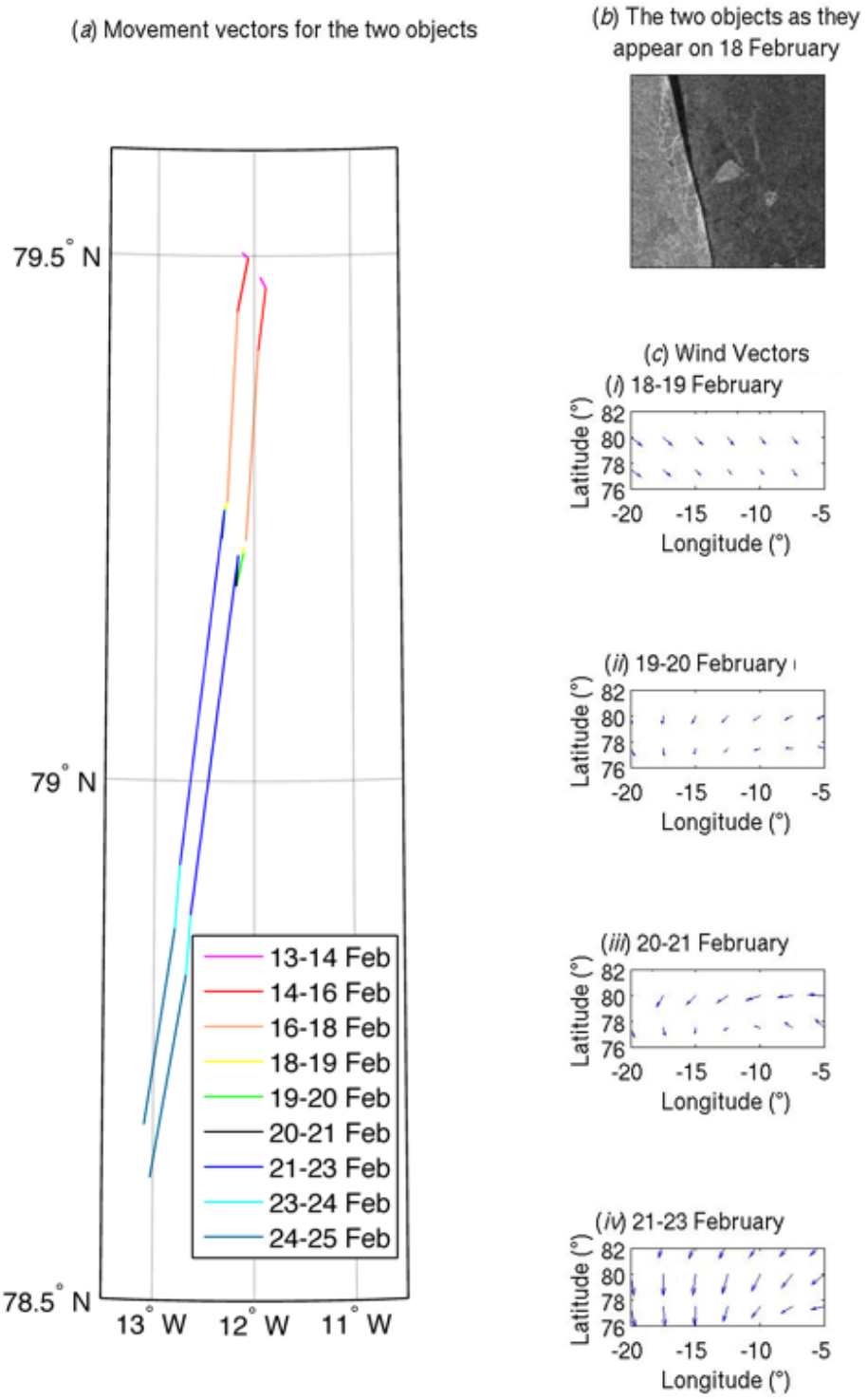

Figure 4.1: a) Tracking the movement of two pieces of sea ice over 12 days in winter conditions. b) how the objects appear in the intensity image c) wind direction between the 18th and 23rd February, which can be seen to impact on the direction of movement of the 2 pieces of ice at this time.

Table 4.3 shows a summary of the number of matches, and average speed, bearing and distance traveled for the objects identified in each of the 17 consecutive image pairings. The number of matches possible in each pairing varied from 2 to 15. The average speed of movement for the objects successfully matched varied between 0.01 and 0.42 m s^{-1} (Figure 4.2). Within an image pairing, the greatest variation is between 0 and 0.48 m s^{-1} between the 2nd and 3rd of February. The distance travelled between images varies from 0.35 km to 73 km. The direction of travel is consistently towards the south or southwest (Figure 4.3 and Figures 4.4, 4.5, 4.6). Several of the ice objects have been tracked over more than one pairing. Geometric scores for the pairings in this exercise varied between 0.12 and 0.75. Shape scores varied between 0.02 and 0.08 (Figure 4.7). Where it was possible to identify either the fast ice edge or the outer limit of the pack ice theses are also located in the figures.

4.1.3 The effect of changing the geometric and shape score thresholds.

To look at the effectiveness of different thresholds in the geometric and shape scores, the first three images in the series were taken and the matching algorithm run with a series of thresholds. These are listed in Table 4.4. With thresholds set low, the number of matches is higher, but the time taken to perform the matching may be prohibitive (over 2hrs). There is no point at which almost all matches become correct, instead, for all thresholds the majority of matches are incorrect with approximately 30% correct. Beyond a geometric threshold or shape threshold of 0.5 all matches produced are incorrect. In other words the level of similarity the algorithm is being asked to look for higher than the level of similarity that any of the true matches achieve. This test indicated that these thresholds may not be an appropriate method for processing matches between sea ice objects. Instead the algorithm was adapted to discard the geometric score altogether, and to rank all possible matches by their shape score then present to the operator the top x percent, instead of those over a certain threshold, where x can be defined by the operator.

Table 4.3: Minimum, maximum and average speed and distance travelled in each set of matches, with average bearing relative to true north.

Pair No	Start Date	End Date	No of Matches	Average Speed (m s^{-1})	Max Speed (m s^{-1})	Min Speed (m s^{-1})	Average Bearing (°)	Average Distance (km)	Max Distance (km)	Min Distance (km)
1	01/02/2008	02/02/2008	7	0.1	0.19	0	130.8	5.59	10.59	0.11
2	02/02/2008	03/02/2008	6	0.15	0.48	0	162.96	31.38	98.71	0.07
3	03/02/2008	04/02/2008	14	0.14	0.3	0	127.3	11.55	25.45	0.16
4	04/02/2008	08/02/2008	5	0.1	0.18	0	196.72	27	45.86	0.05
5	08/02/2008	11/02/2008	0	-	-	-	-	-	-	-
6	11/02/2008	13/02/2008	2	0.42	0.45	0.39	184.75	73.46	79.46	67.46
7	13/02/2008	14/02/2008	15	0.09	0.34	0.02	156.69	4.8	18.5	1.24
8	14/02/2008	16/02/2008	5	0.02	0.04	0	250.62	4.77	7.33	0.87
9	16/02/2008	18/02/2008	9	0.23	0.49	0.14	198.36	32.67	67.71	19.37
10	18/02/2008	19/02/2008	8	0.06	0.12	0.02	185.63	7.38	13.87	2.24
11	19/02/2008	20/02/2008	4	0.05	0.1	0	166.4	4.36	8.36	0.33
12	20/02/2008	21/02/2008	5	0.04	0.06	0	245.64	1.99	3.46	0.23
13	21/02/2008	23/02/2008	2	0.12	0.24	0	277.38	24.64	48.8	0.48
14	23/02/2008	24/02/2008	12	0.16	0.24	0	175.24	18.86	28.7	0.05
15	24/02/2008	25/02/2008	4	0.11	0.21	0	204.16	5.81	11.57	0.06
16	25/02/2008	26/02/2008	3	0.07	0.21	0	163.88	5.98	17.51	0.04
17	26/02/2008	27/02/2008	3	0.1	0.27	0	168.93	5.2	14.78	0.14
18	27/02/2008	29/02/2008	2	0.0016	0.002	0.0014	174.74	0.35	0.41	0.28

This test also shows that when attempting to track sea ice in winter conditions this algorithm is always going to give a large number of false alarms; regardless of the thresholds chosen. This is time consuming for the user. This problem of an excessive number of false alarms is improved slightly by taking the top x percent rather than using a threshold, but not solved. The only way to lower the number of false alarms in winter conditions is to limit the objects that are put forward to the matching stage, for example by being very strict with the brightness threshold. The problem of false alarms is lower in the summer months when the ice objects become more distinctive shapes and are better separated. I would suggest that this algorithm is simply not well suited to tracking where sea ice conditions are such that many similar shaped floes are present in close proximity.

Table 4.4: Time taken & success of matching exercises at different thresholds.

Geometric Score	Shape Score	Time Taken (mins)	No of matches found by ITSARI	No of Matches approved by operator
Pairing A: 1st and 2nd Feb 2008				
0.01	0.01	65	106	25
0.05	0.01	47	102	20
0.1	0.01	10	76	9
0.25	0.01	4	39	4
0.5	0.01	2	15	0
0.75	0.01	.5	16	1
0.01	0.02	18	79	17
0.01	0.05	2	5	0
Pairing B: 2nd and 3rd Feb 2008				
0.01	0.01	182	191	13
0.05	0.01	87	182	8
0.1	0.01	31	160	6
0.25	0.01	10	101	3
0.5	0.01	3	35	0
0.01	0.02	59	155	14
0.01	0.05	2	14	1
Pairing C: 3rd and 4th Feb 2008				
0.01	0.01	77	205	53
0.05	0.01	19	183	32
0.1	0.01	18	155	22
0.25	0.01	5	86	7
0.5	0.01	2	29	1
0.01	0.02	35	146	30
0.01	0.05	3	10	1

The first thing apparent in this example was that tracking sea ice objects from within the pack is not as straightforward as tracking icebergs in the Southern Ocean. Success relies not only on finding an object with a distinctive shape, but also that

object must be seen against a background of a different brightness value, and must remain distinctive against its background for the duration of its tracking life. This does not prevent the tracking of objects that leave the pack to enter open water, as long as the shape remains distinct and there is contrast with both backgrounds. It has been demonstrated that with a fixed set of parameters for the identification of ice objects it is possible to select the same objects in consecutive images, and thus to perform tracking of those objects.

The greatest number of matches was possible where the images were one or two days apart, with a similar orbit and incidence angle. The lowest number of matches occurred where images were a longer time apart or where the incidence angle varied significantly, leading to problems with edge effects. Matches were also low where the images did not have a large area in common.

Speeds varied within each image pairing, and between pairings. The two pieces of ice tracked in the first exercise demonstrate two distinct flow regimes; that may be linked to the interaction of ocean and wind currents. The ice is essentially travelling south in the East Greenland current, but there is a variability linked to the behaviour of the wind. If the ocean current remains steady then a wind acting in the same direction would act to speed up the movement of the ice, while wind acting in the opposite direction would slow or even reverse the travel. The movement of the two pieces of ice was compared to surface wind vectors obtained from the NCEP / NCAR Reanalysis data available at http://www.esrl.noaa.gov/psd/data/composites/day/. This comparison appears to show that changes in the wind velocity may have an influence of the movement of the two floes, but it is not the only factor at play here, the movement of the ice also reveals the influence of ocean currents (Figure 4.1). In Chapters 7 and 8 I further explore the interplay between the wind forcing and the ocean currents in the area.

The tracking of the two objects over 10 images / 12 days demonstrates that it is possible, with the appropriate selection of parameters, to fix on objects of interest and track their progress in time. Successful tracking relies on the object maintaining

a distinctive shape, on that object being seen against a background of a different brightness value, and remaining distinctive against that background for the duration of its tracking life. The objects successfully identified are on the western side of the Strait, closer to the fast ice edge than to the further limits of the pack. This may be due to either the incidence angle illuminating individual objects better on this side of the Strait, (as discussed in Chapter 2 objects illuminated at a shallower angle return a strong signal from their edges) or to a higher proportion of multi-year ice floes (which appear bright against a background of first year ice) travelling on this side of the Strait. It is also of note that the objects identified and tracked are within the pack, not in open water. The scope for following the same identified objects over a series of images makes it possible to identify Lagrangian motion and hence surface ocean currents.

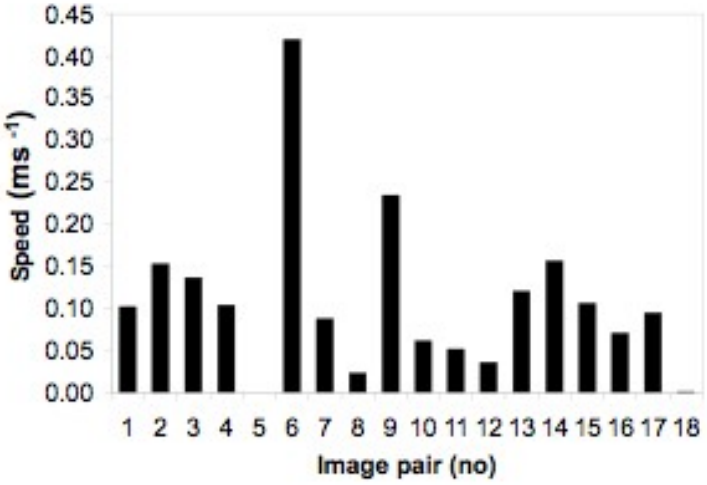

Figure 4.2: Average speed of travel for matches between each of the image pairs listed in Table 4.3.

4.2 Tracking in the western Fram Strait 2008

We now turn to using the algorithm over a full year. The aims of this case study were:

- To establish how the use of the algorithm over a year would affect the choice of brightness & segmentation thresholds;

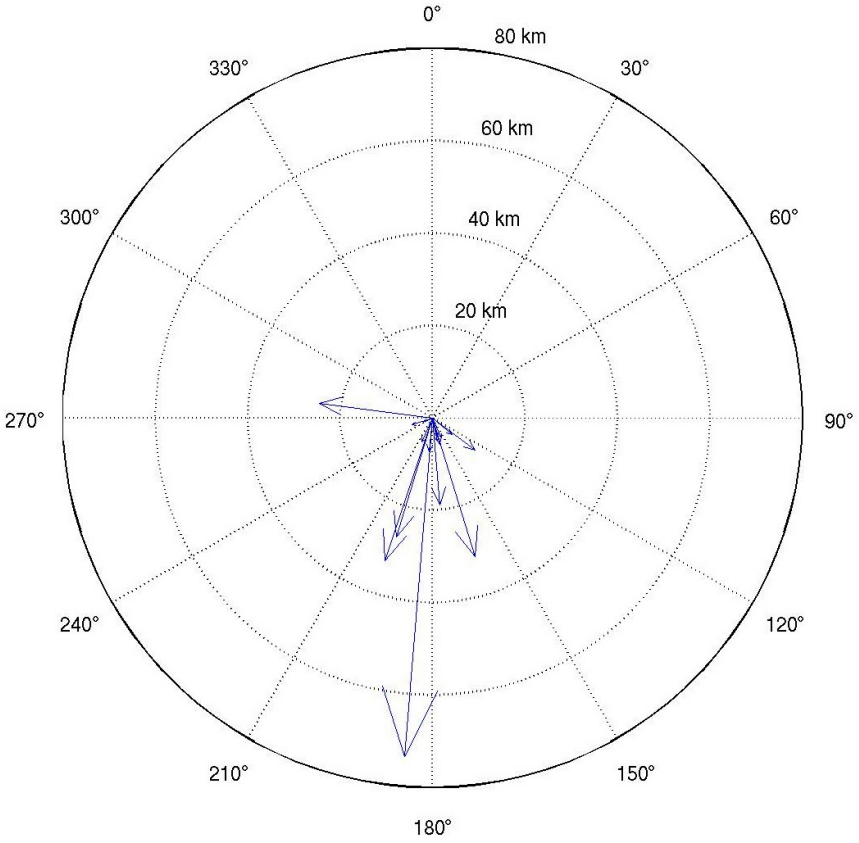

Figure 4.3: Average direction (relative to true north) and distance of travel (in km) for matches between each pair of consecutive images. Note the large number of short movements towards the south, which overlap.

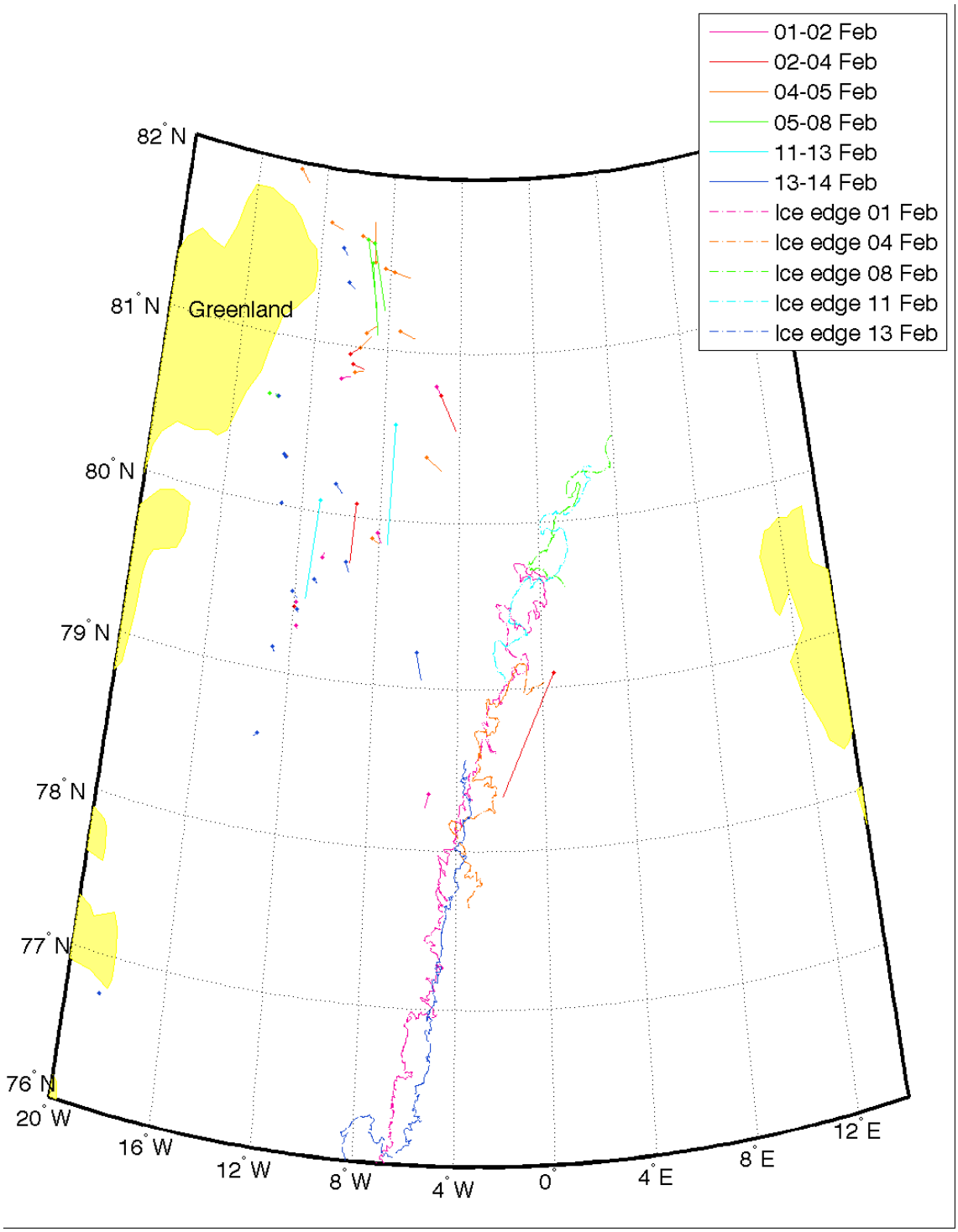

Figure 4.4: Ice movement vectors from tracking exercises between the 1st and 13th February 2008.

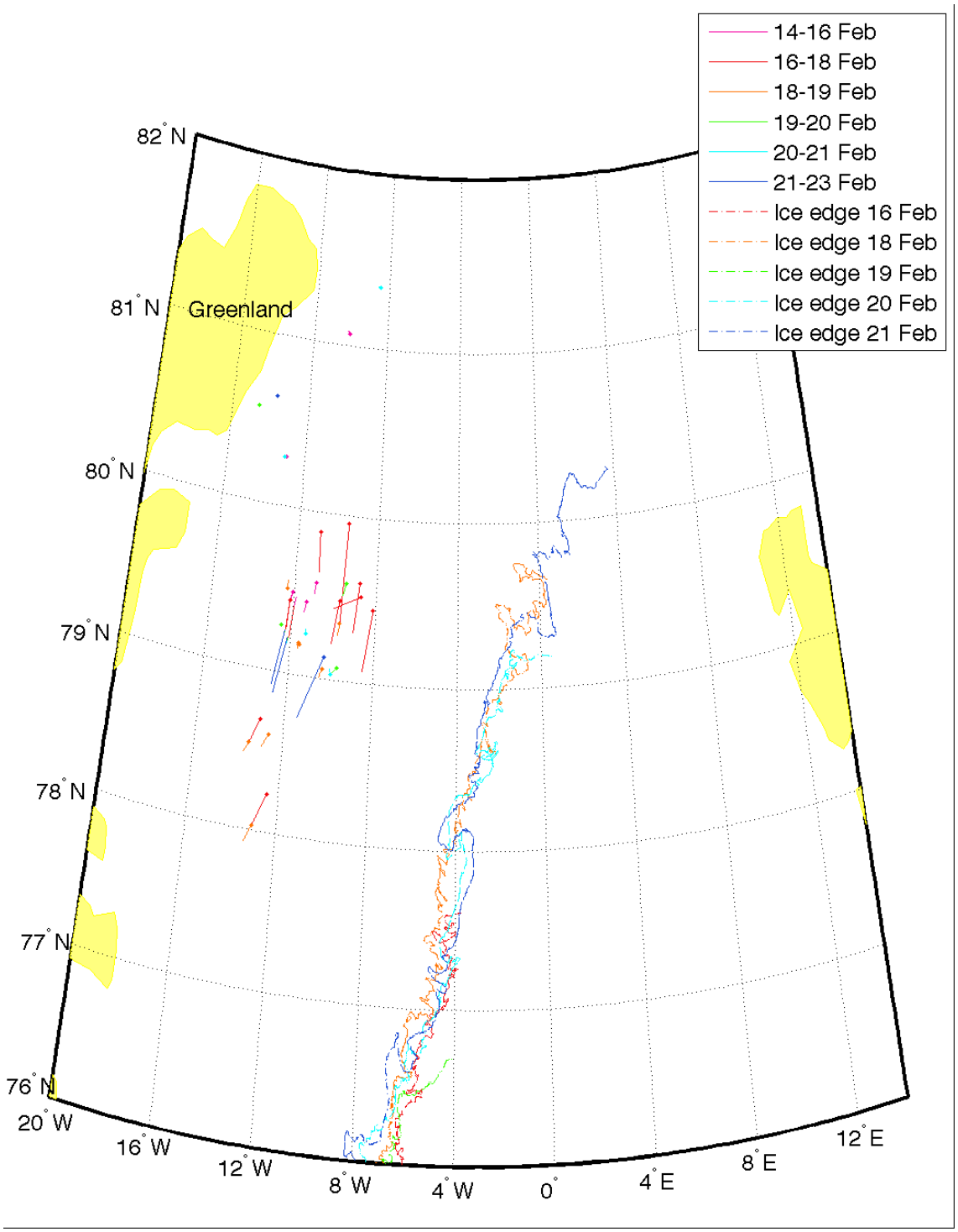

Figure 4.5: Ice movement vectors from tracking exercises between the 14th and 21st February 2008.

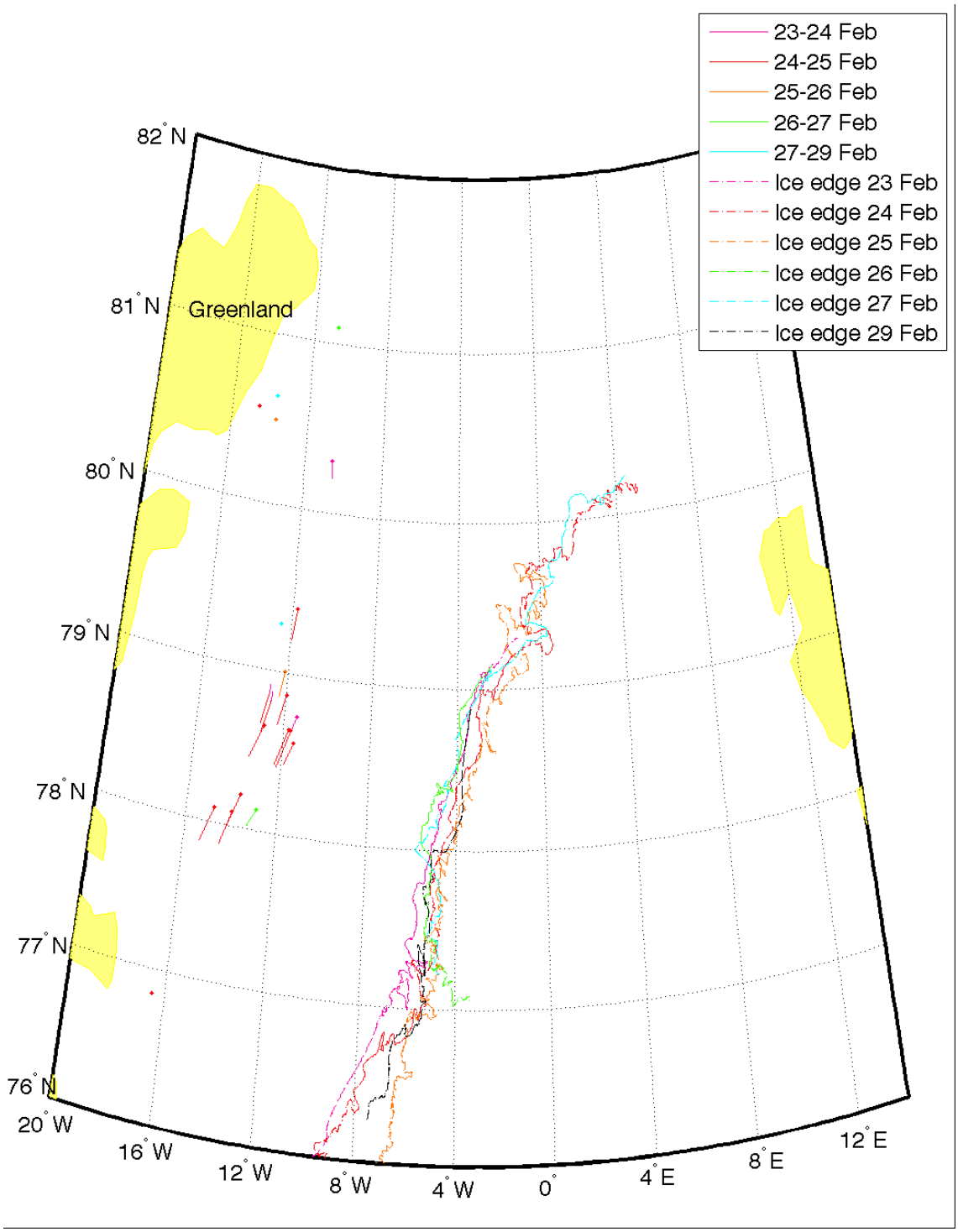

Figure 4.6: Ice movement vectors from tracking exercises between the 23rd and 29th February 2008.

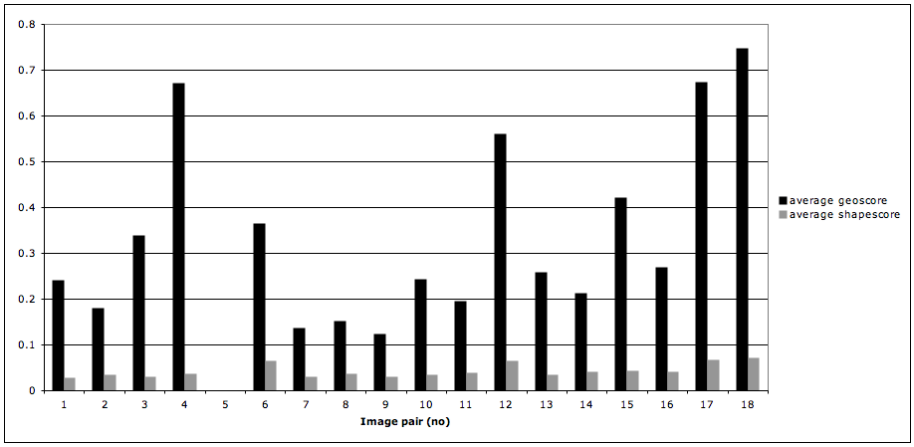

Figure 4.7: Average geometric score & shape score for matches in each pair of consecutive images.

- To ascertain whether it was possible to match objects between images up to 10 days apart.

Fifty three images centred around 80°N 4°W were acquired at intervals of between three and 11 days throughout 2008. The ITSARI algorithm was used to identify a set of ice objects from each image. The segmentation threshold used was between 11 and 14 depending on the image. In some cases the objects were over-segmented so the merging function (described in Chapter 3) was used to restore them. To reduce the number of objects put forward to the matching stage, objects from the first pass were subject to a size threshold preventing any object smaller than 150 pixels going forward to the matching stage. The two sets of ice objects from each consecutive pair of images were then fed into the matching stage of the algorithm. If no successful object matches were made from an image pairing, then an attempt was made to match with the next-image-but-one. For each successful object match the following information was extracted: the location of the centre of the object in both images; the distance between these points and compass bearing for direction of travel; the speed of travel and the time between the images.

4.2.1 Results

In total, 46 tracking exercises were completed, with between one and 21 (average 12) object tracks generated from each image pairing. Five consecutive image pairings generated no matches. For each month a map has been produced showing all of

the object tracks within that month. Four examples of these from January, April, August and November are presented in Figures 4.8 to 4.11. On each map the location of the image acquired that month is shown with a dotted line. Where it was possible to identify the sea ice edge and/or the fast ice edge in the image (using the ITSARI algorithm), these are marked with a dashed line in the same colour as the outline of the image on which they were identified. For simplicity, date and corresponding colour is listed only once in the key. The movement vectors are grouped by image pairing and denoted as such in each key. A month by month discussion of the results and their relation to ocean and atmospheric forcing can be found in Chapter 7.

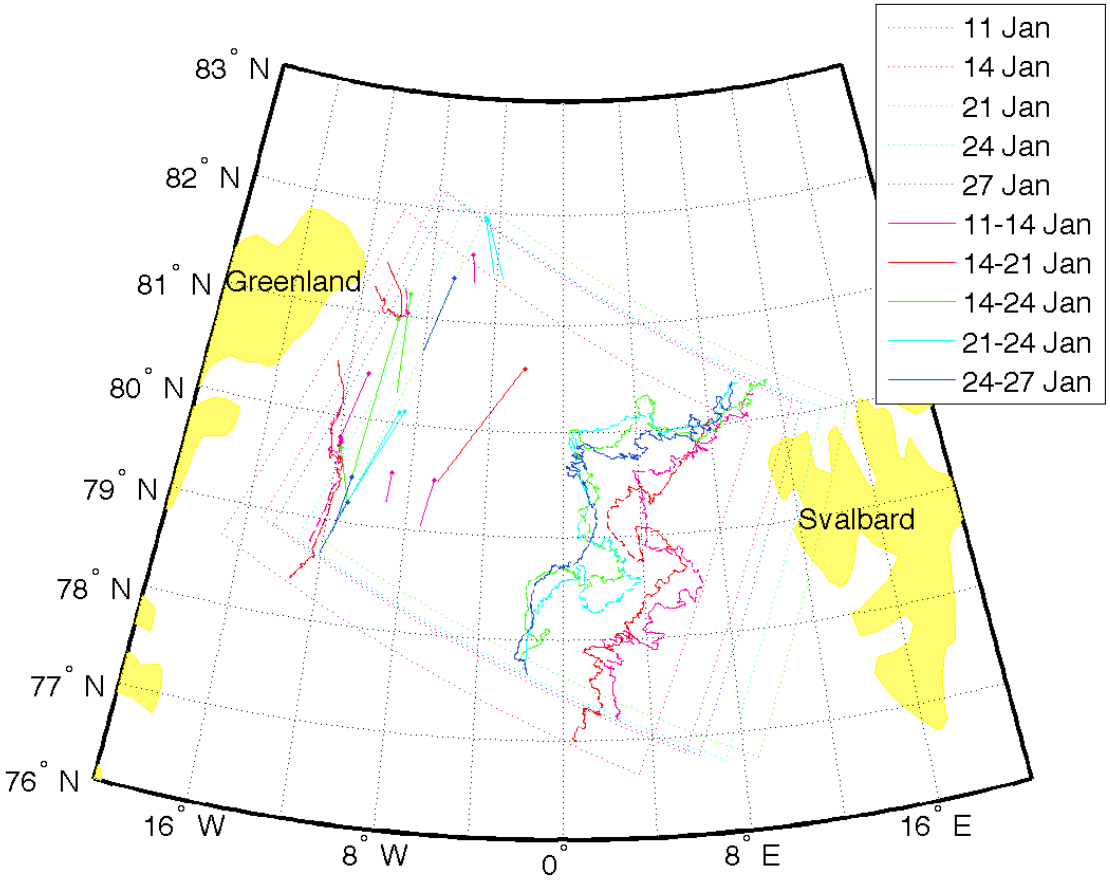

Figure 4.8: Movement of ice objects identified and tracked in images from January 2008. Note fast ice boundary around 10 °W and pack ice boundaries around 4 °E.

Brightness of Identified Objects The objects identified were less bright (below -20 dB) during July, August and September (Figure 4.12). Between January and May and October to December a brightness threshold of -19 dB was used to identify

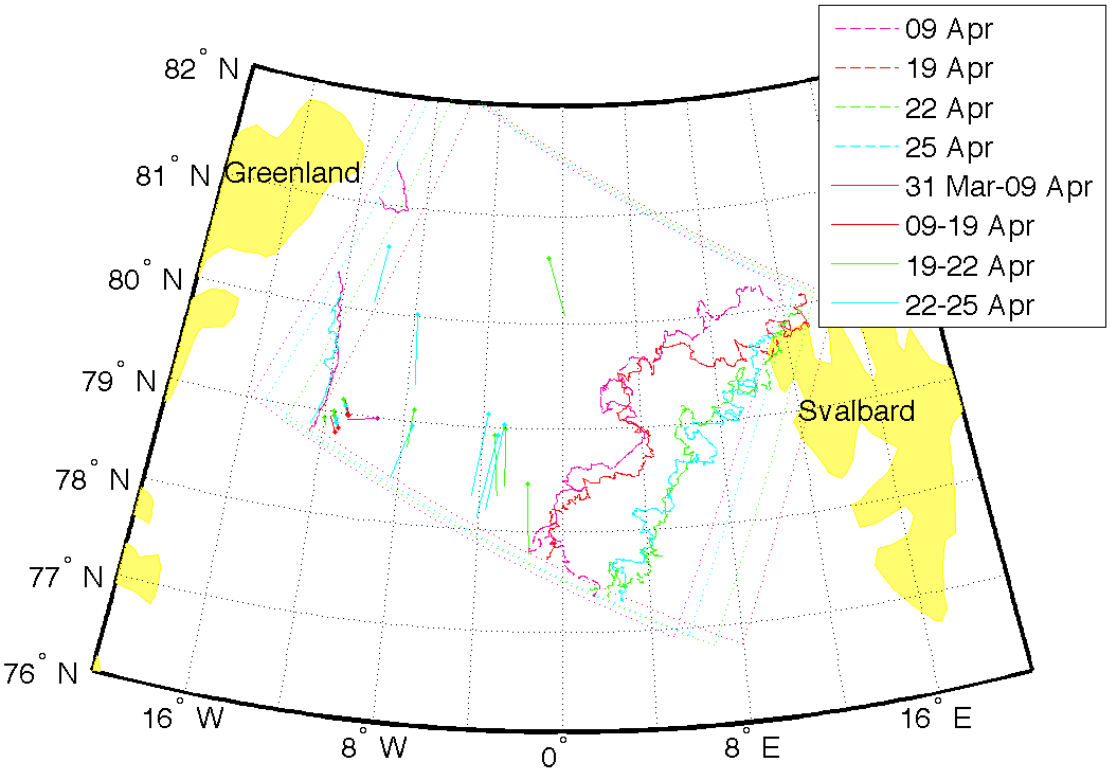

Figure 4.9: Movement of ice objects identified and tracked in April 2008.

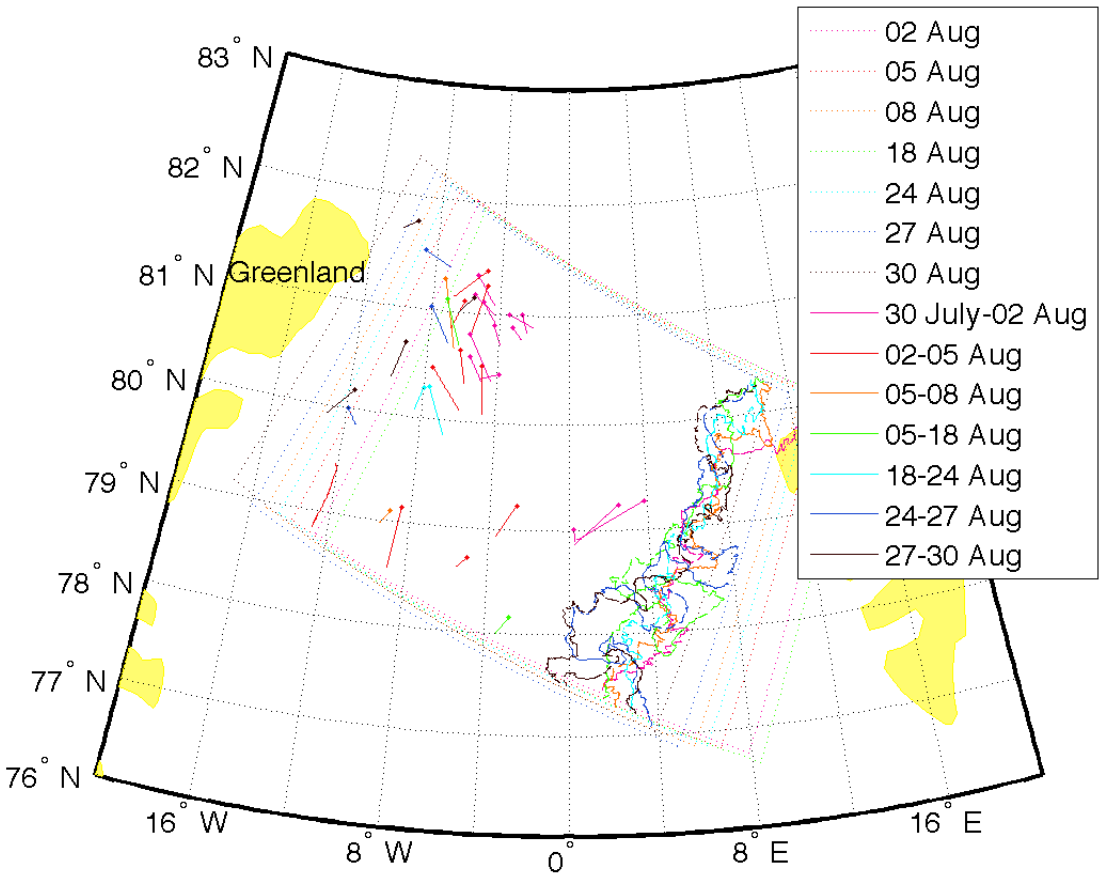

Figure 4.10: Movement of ice objects identified and tracked in August 2008.

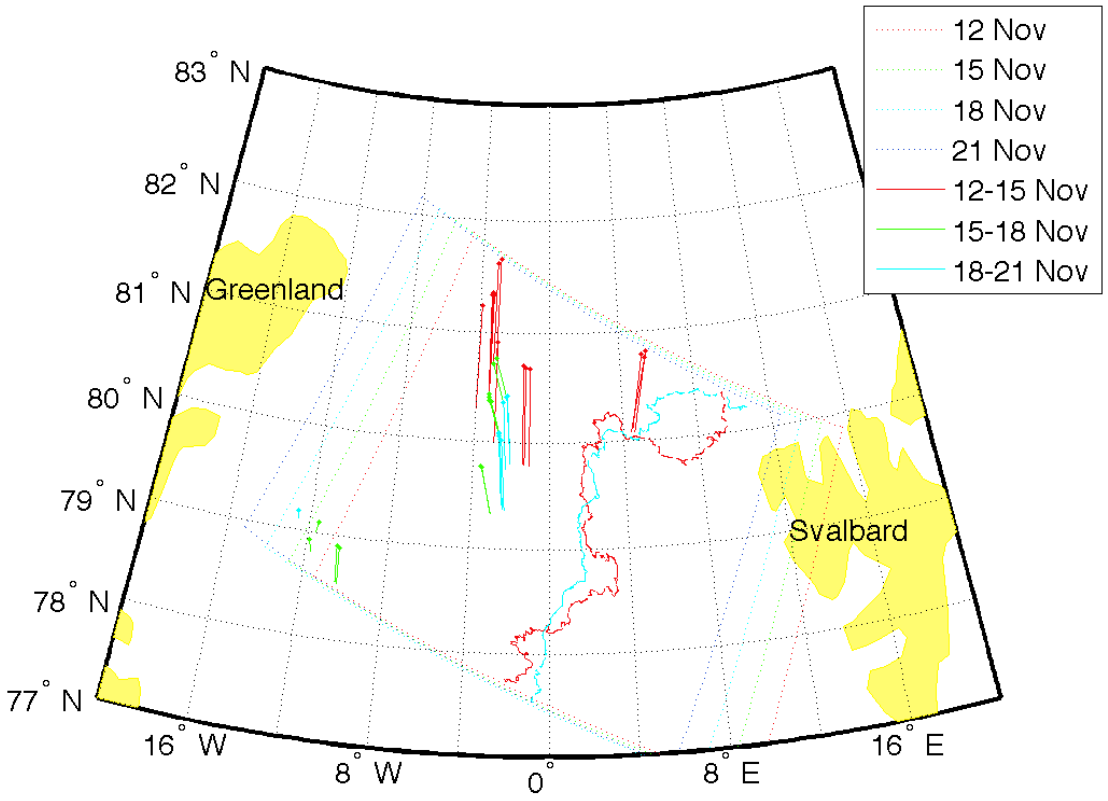

Figure 4.11: Movement of ice objects identified and tracked in November 2008.

objects. In June this was dropped to -22 dB for some images; between July and September it was necessary to go as low as -26 dB. The lower brightness values in the summer months are due to surface melting and the presence of liquid water in the snowpack and melt ponds on the surface.

Fewer tracks have been generated overall than might be expected for two reasons. One is the nature of the ice in the late and early spring, where closed pack containing a large amount of first year ice does not lend itself to the easy identification of individual objects. This is where 'traditional' cross correlation motion tracking techniques are already known to be effective, so pursuing the use of ITSARI in these conditions is not a pressing concern. Where objects have been identified the temporal resolution of three to five days is effective at this time of year when the shape of individual pieces of ice is not changing very rapidly between image acquisitions. In the summer months the pack is more open so individual objects are more easily segmented and selected, however, the ice objects change their shape rapidly at this time of year due to accelerated melt and break up, so tracking between

images between three and five days apart proves tricky. Objects may also move more rapidly in open water (e.g. within the polynya that forms adjacent to the fast ice edge in the summer months) so move out of the study area more quickly at this time of year. It is expected that tracking on a shorter temporal resolution would produce far superior results at this time of year. The greatest success occurs in the early winter months, October - December, where multiyear ice that has survived the summer in the Arctic ocean stands out as bright objects, due to low salinity, and strong edge reflections (due to a combination of ridging and rafting increasing ice freeboard), against a background of newly forming first year ice that appears dark to radar due to high brine content. Held within the pack, these multiyear ice floes are not changing shape rapidly enough to cause a problem, nor moving out of the study area too rapidly to be tracked. Those objects that have been tracked from one image pair to the next in October, November and December are most likely multiyear ice floes that survived the summer in the Arctic, brine free with bright signatures so easy to segment and identify.

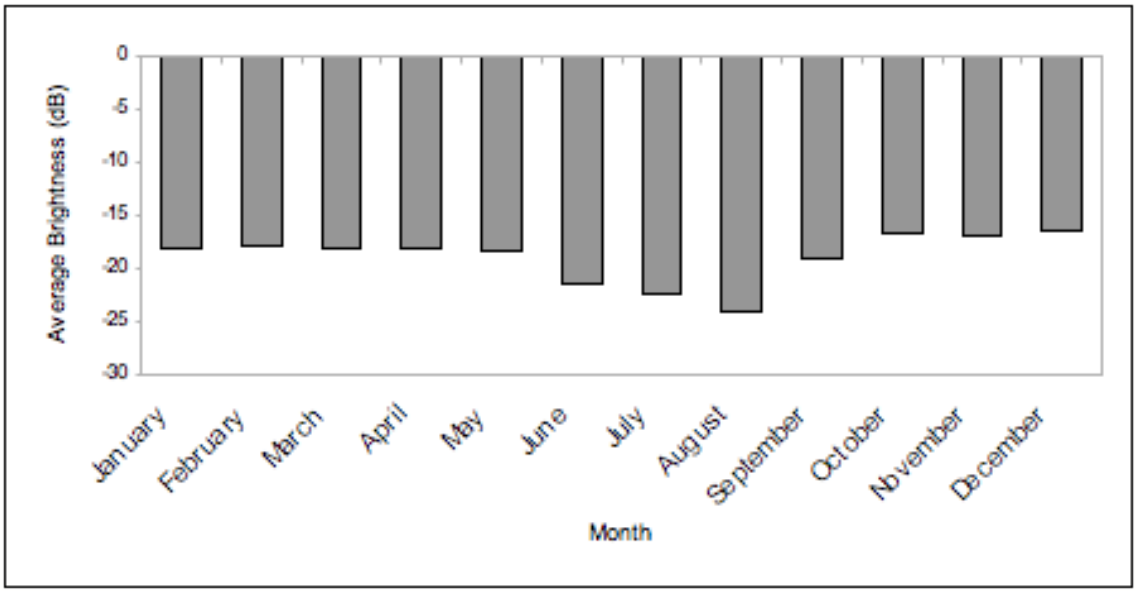

Figure 4.12: Brightness of objects identified by month, 2008.

Velocity throughout the year The quickest travel is in the winter; January February, November and December, while the slowest travel is in late spring, May (Figures 4.13 and 4.15). There is a trend for direction of travel to change from SE to S to SW as the objects move to more southerly latitudes (Figure 4.16). This

is connected to the flow of the East Greenland Current and / or prevalent winds in these zones. There appears to be more south-eastwards travel in spring and summer as opposed to more south-westwards travel in November and December (Figure 4.17). This is connected to the increased importance of winds associated with low pressure systems located over Iceland in the winter months. The speed of movement is higher in the centre of the strait than on the western side (close to the fast ice edge) in the winter months; this is less noticeable in the summer months (Figure 4.14).

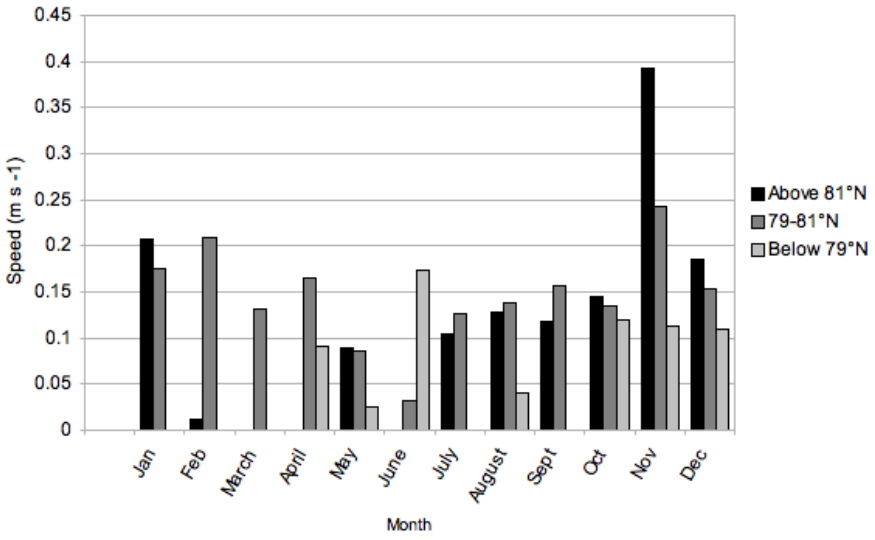

Figure 4.13: Speed of movement of objects in different latitude zones by month.

Average speeds vary between 0.01 and 0.39 m s^{-1}, but this highest average speed is thought to be an artifact generated by only having a couple of particularly high speed objects in that latitude category. For the middle group, 79° – 81° N, where the most individual matches were obtained, speeds varied between 0.01 – 0.25 m s^{-1}. The overall average speed for west of -8° is 0.11 m s^{-1}, between -8° and -4° the overall average speed is 0.18 m s^{-1}, and east of -4° it is 0.22 m s^{-1} (Figure 4.15).

4.3 The Barents Sea

The aim of this case study was to show that the algorithm could be used successfully elsewhere in the Arctic. Thirty-one images were acquired on dates between the 2nd

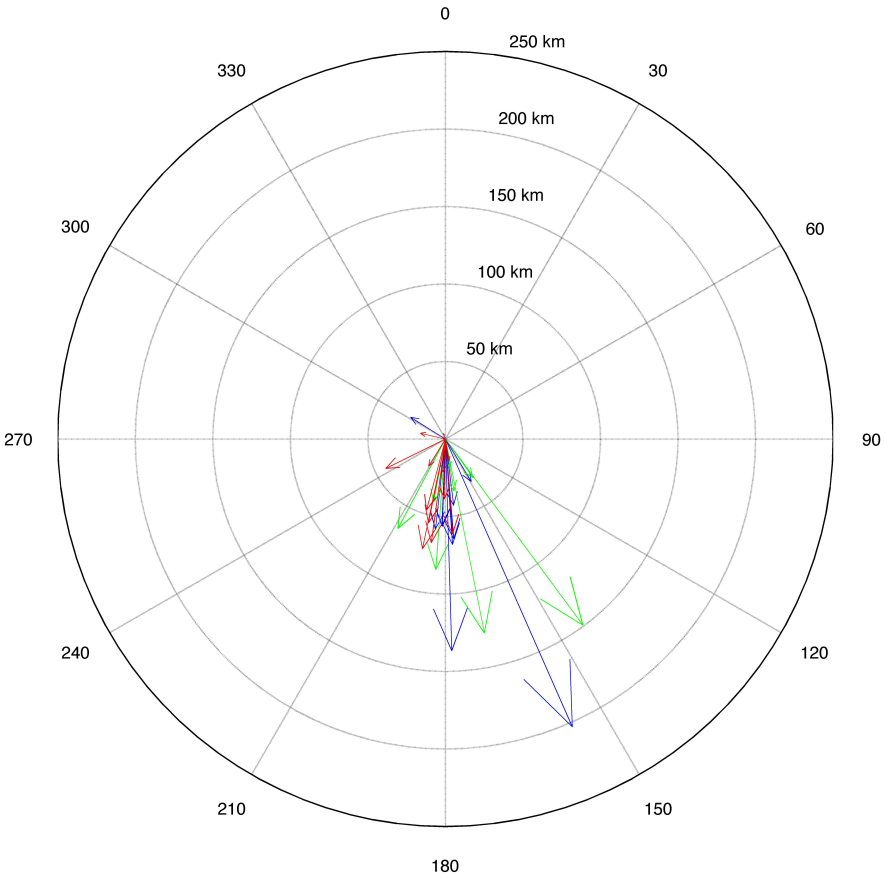

Figure 4.14: Average distance and direction travelled by month for three longitudinal zones: west of -8° (red), between -8° and -4° (blue) and east of -4° (green) of the Fram Strait

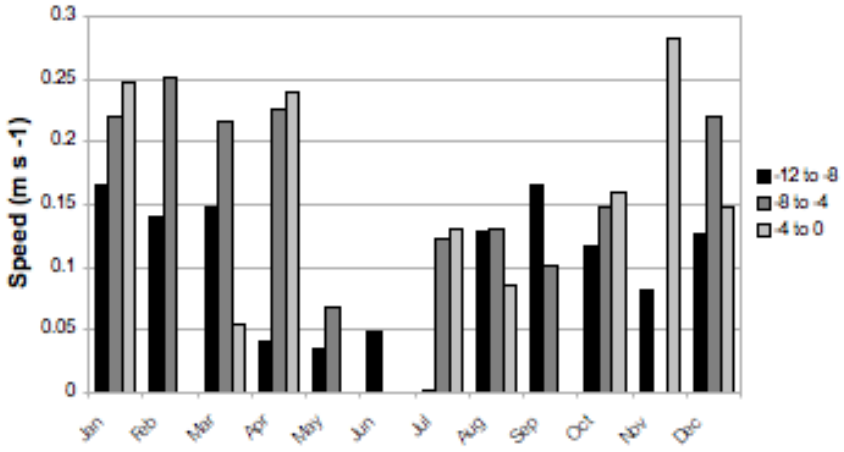

Figure 4.15: Speed of movement by longitudinal zone for each month. The overall average speed for west of -8° is 0.11 m s $^{-1}$, between -8° and -4° the overall average speed is 0.18 m s^{-1}, and east of -4° it is 0.22 m s^{-1}.

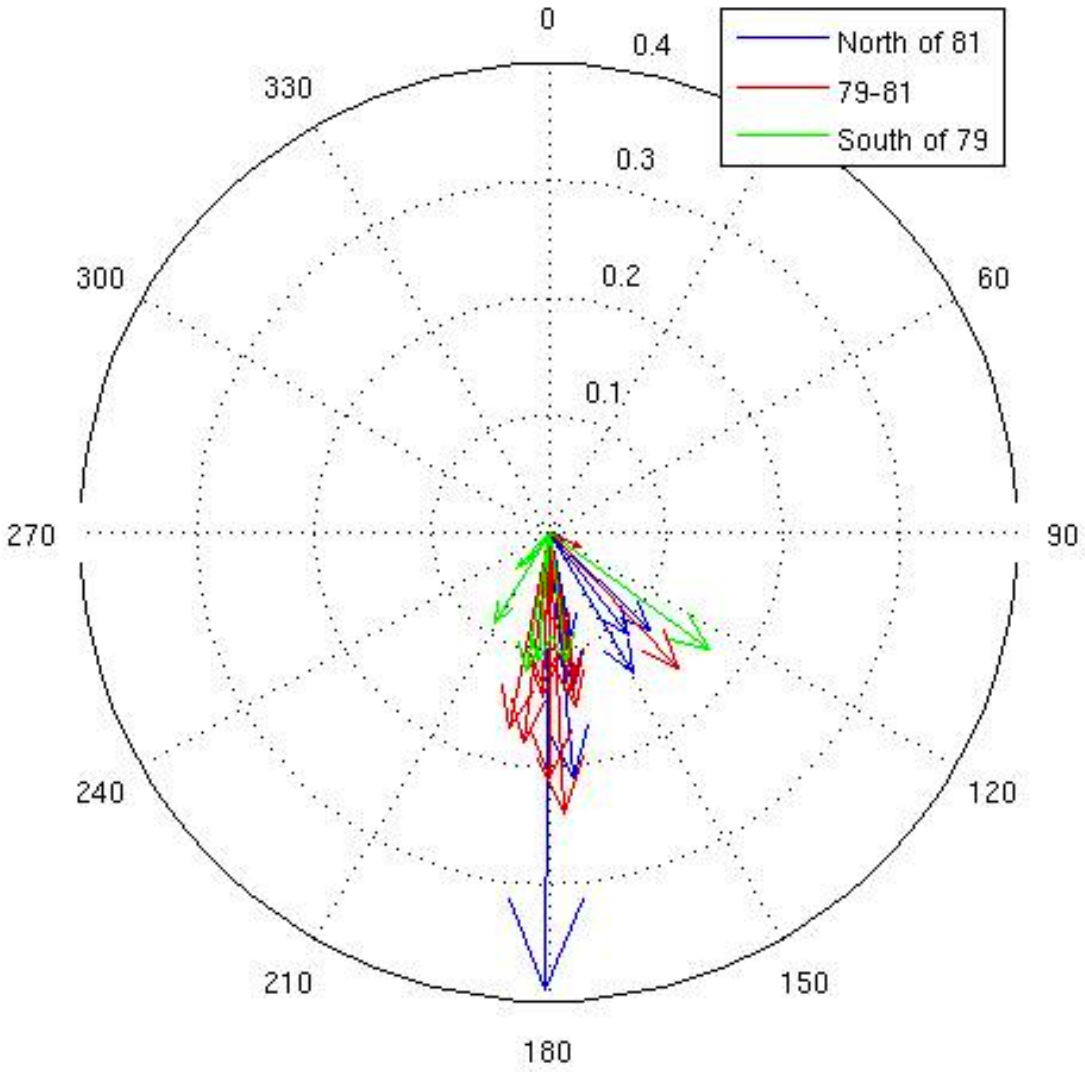

Figure 4.16: Direction and speed (m s^{-1}) of movement in three latitudinal zones.

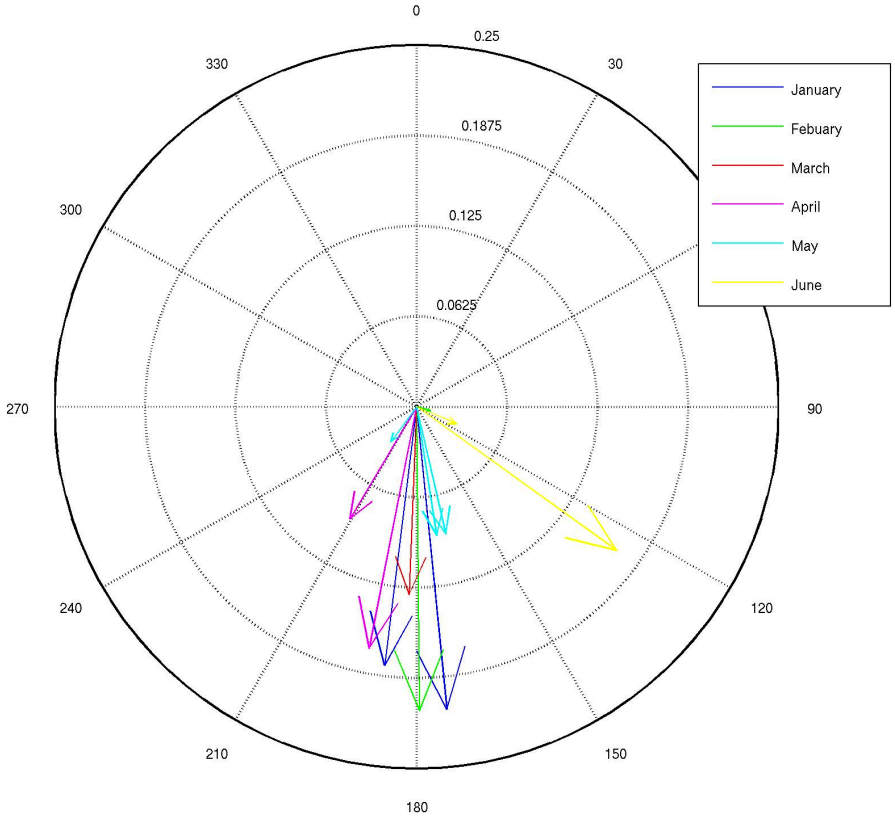

(a) January - July

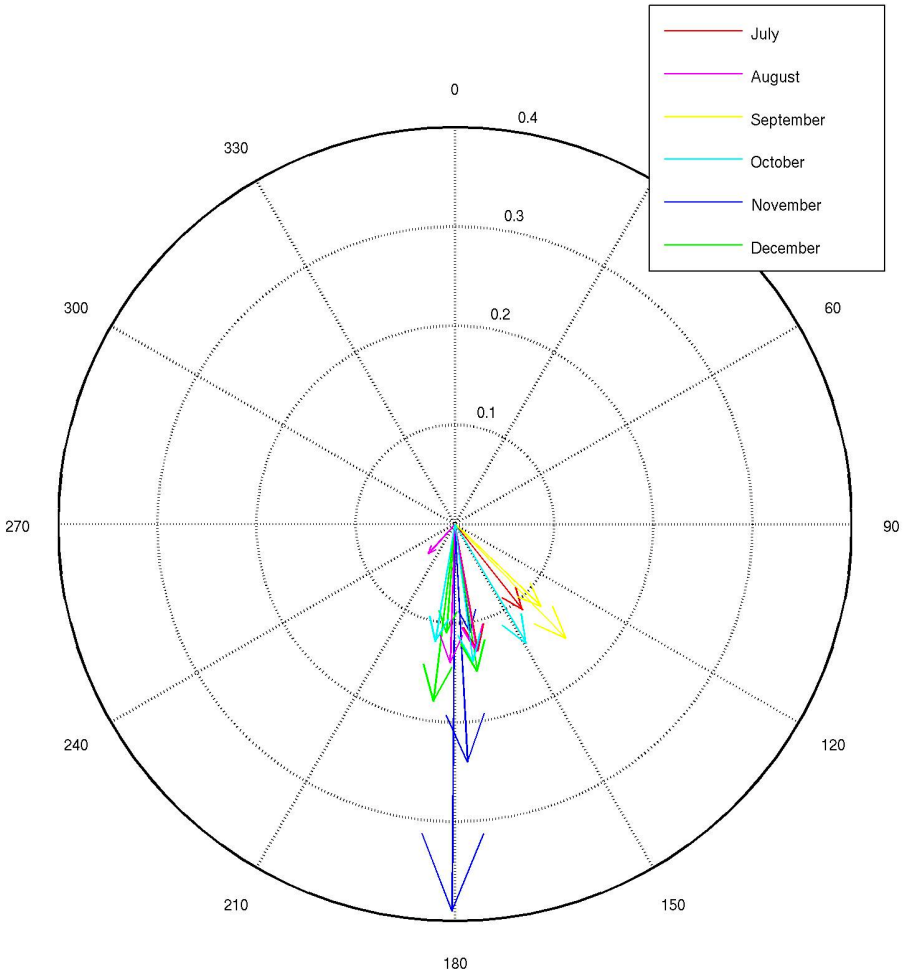

(b) July-December

Figure 4.17: Direction and speed (m s^{-1}) of movement by month.

and 26th February 2009. This also gave the opportunity to look at images in which some the ice floes appeared darker rather than lighter than their surroundings. It was found that far fewer objects were identified in this case study. This is due to a high incidence of first year ice moving as a close pack that does not lend itself to separation into individual objects at the resolution of the images.

Objects that were identified include some ice floes that are darker than their surroundings, and some that are brighter than the surrounding pack (hypothesized to be multiyear ice floes within the mainly first year ice), and some leads. Leads were hardest to track as they change in shape more rapidly than the floes themselves, and can also freeze over, or close up, or new leads appear, in the time between one image and the next.

The interannual variability of sea ice volume in the Barents Sea is mainly determined by variations in sea ice import from the central Arctic. This import is primarily driven by the local wind field (Koenigk et al., 2009). High pressure over Novaya Zemlya and below normal pressure over Svalbard strengthens the winds across the northern border of the Barents Sea and thus the sea ice transport into the Barents Sea. The maximum ice extent in the Barents sea is controlled primarily by anomalies in sea surface temperatures during the late winter (Francis and Hunter, 2007). The negative phase of the North Atlantic Oscillation (see Chapter 6) may also leads to an enhanced sea level pressure gradient between Svalbard and Novaya Zemlya and thus enhance ice transports. Modelling suggests that sea ice variation in the Barents Sea does not significantly modulate the storm track and large scale atmospheric circulation in the area (Koenigk et al., 2009).

4.4 Concluding Remarks

The results presented have shown success using the ITSARI algorithm to identify and track objects from Envisat Wide Swath images in Arctic conditions at all times of the year. The objects tracked are sea ice floes and distinctive features such as

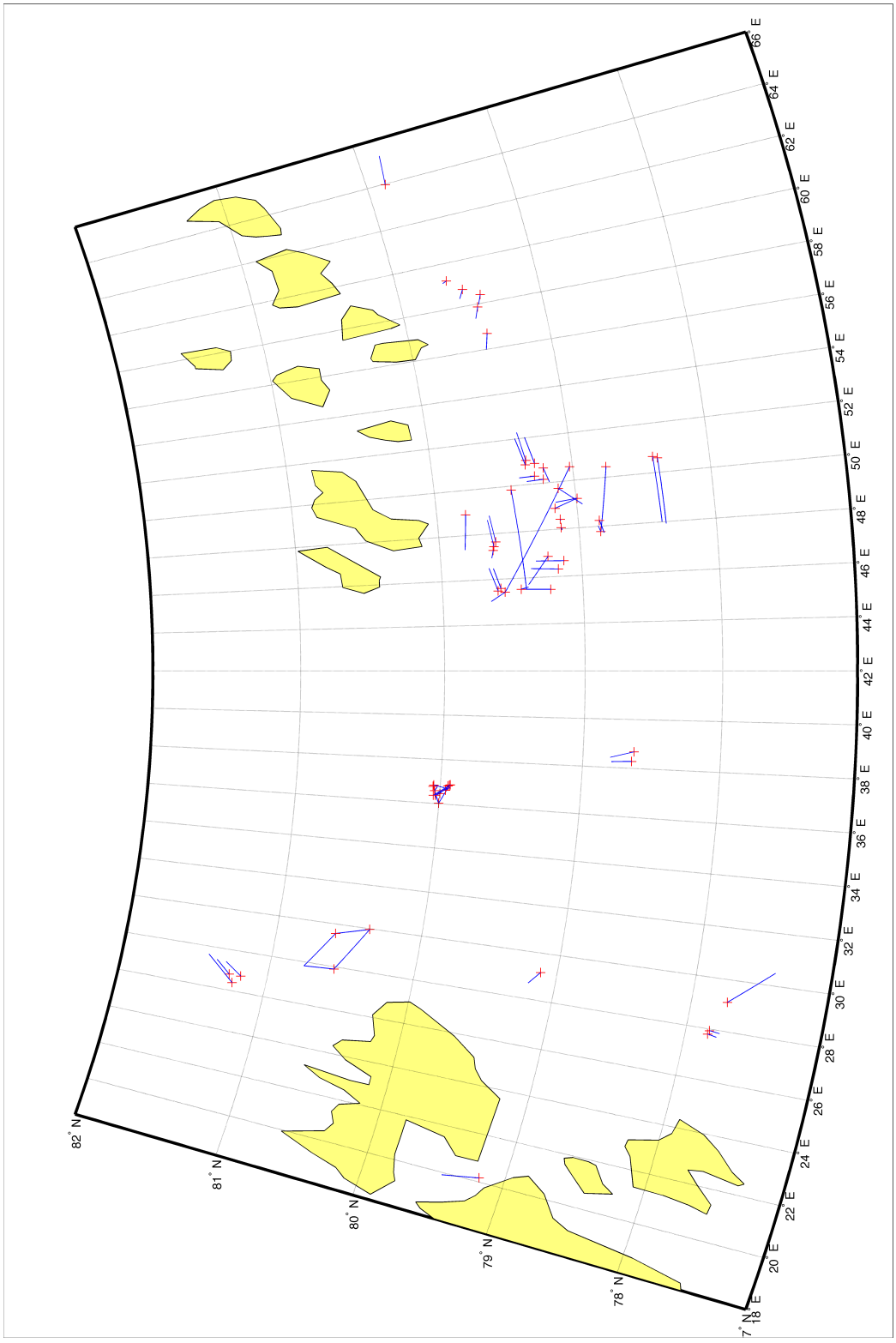

Figure 4.18: Locations of objects tracked in the Barents Sea case study.

ridges. In several instances it was possible to track the same object through a series of image pairings.

The ITSARI algorithm relies on the successful shape matching of objects between one image and the next. For a successful match the objects must not only be present in both images, but also have been selected as one of the 'ice object' segments, therefore the object must retain an average brightness value above the threshold. Because edge effects contribute to total backscatter, an incidence angle change (so the sensor no longer 'sees' the same edges) may result in lost objects. If an object is identified in both images then it should be matched so long as the shape has not changed dramatically. Image pairings with a shorter temporal difference yielded more successful object matches. This is to be expected as the objects will have had less opportunity to change shape or brightness, or to drift out of the region. Some of the objects tracked are discrete ice floes, others are features, e.g. ridges: members of this latter category are most likely to change shape between images. Successful matches at longer temporal ranges all occurred during the months where ice brightness signatures are known to be more stable. To obtain best results in the summer months images would ideally be obtained on a daily or more frequent basis, due to the highly changeable nature of the ice and more rapid movement at this time. The lower brightness thresholds necessary in the summer months are an expected result, due to the presence of liquid water in the snowpack, and of melt ponds on the surface.

In chapter 5 we move on to look at the use of ITSARI with data from different sensors.

Chapter 5

Adapting ITSARI to data from other sensors

This chapter describes case studies that focus on the use of the ITSARI algorithm to process information from different sensors. The first section explains the use of the algorithm to process Radarsat 2 data, including combining information from two polarisations. In the second section the algorithm is used to process information from Cosmo Sky Med X-band. Radarsat is another C band sensor (Canadian Space Agency), while Cosmo Sky Med is a constellation of four satellites (Italian Space Agency) carrying X band SAR.

5.1 Radarsat

Here we will explore the processing of Radarsat data using subsections centred on 79.5454° N 9.5224° W from two Radarsat images from August 2010 (Figure 5.1). The data supplied is dual polarisation: there is data in 'HH' polarisation, meaning the pulse of radiation emitted from the instrument was horizontally polarised and the returns in the same polarisation were recorded; and 'HV' polarisation, meaning the vertically polarised component of the returns from that same beam of horizontally polarised radiation. The image resolution is 25m.

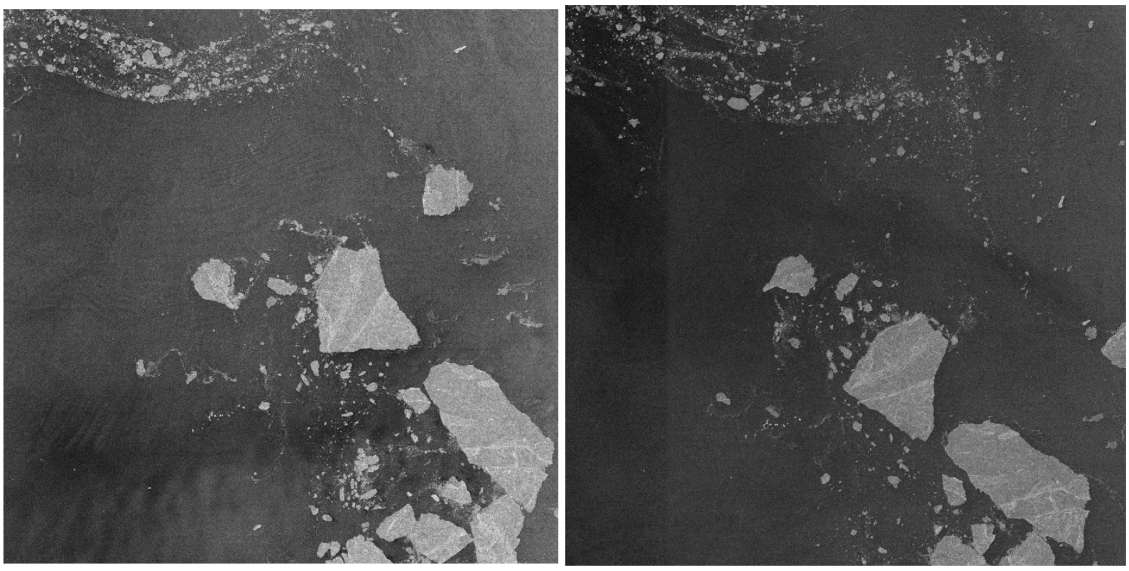

(a) 16 August 2010 (b) 17 August 2010

Figure 5.1: Image subsections centred on 79.5454°N 9.5224°W from two dates in August 2010.

Simple band mathematics were applied to combine these two bands. Four possibilities were tested: a) adding the two bands together, b) multiplying them together, c) dividing one by the other and d) a simple ratio:

$$(HH - HV)/(HH + HV) \tag{5.1}$$

Band mathematics were carried out on the intensity images prior to conversion to dB for processing with ITSARI. Of these four options, adding the two together produced the best results when ITSARI was applied to the resulting image. Because the HV component of the backscatter is very low, adding it to the HH component adds information without moving the backscatter values in dB far from those of the single HH band.

The threshold for the separation of ice objects from the background increases from -18 dB to -14 dB on images that were preprocessed to combine the bands in this way. The HV component adds information about volume scatterers such as snow and cold, old ice and about reflections from dihedral interfaces e.g. rafts, fractures and ridges. Figure 5.2 shows objects identified from the two subset images above using a segmentation threshold of 11 and a brightness threshold of -14 dB.

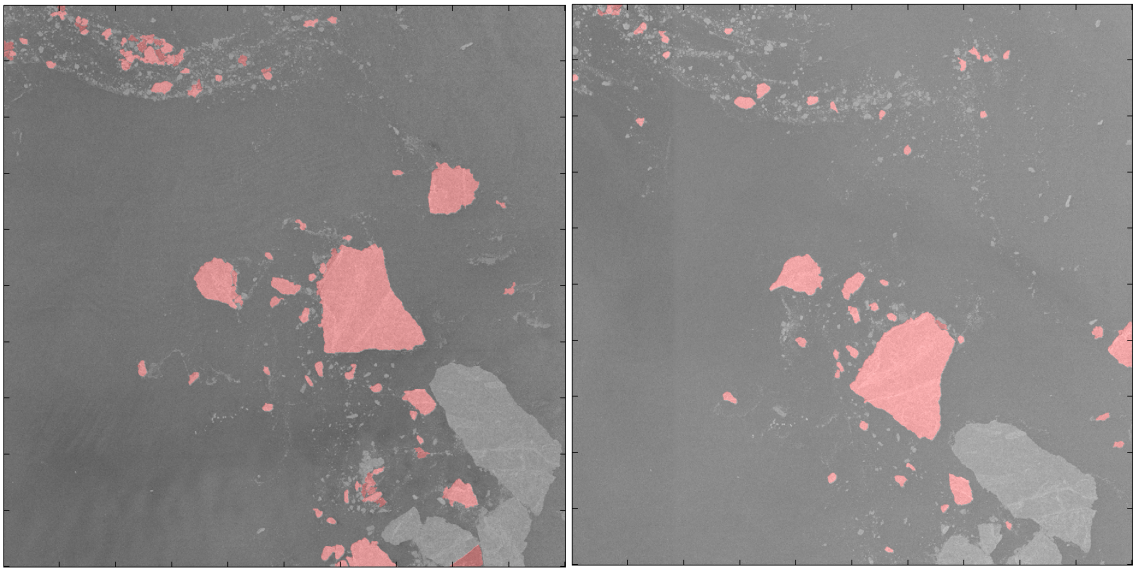

(a) 16 August 2010 (b) 17 August 2010

Figure 5.2: Objects identified using ITSARI are shown in pink on the two images from Figure 5.1

In this short example 10 objects were tracked (Figure 5.3). The objects successfully tracked here have an average brightness value of -8 dB. The average direction of movement is 71°(towards east-north-east) at an average speed of 0.19 m s $^{-1}$. Over this period of time it appears that the floes are being pushed by the wind in the opposite direction to the flow of the East Greenland Current. They are in any case closer to the Greenland coast than the main flow of the current. Further exploration of the movement of ice in the Fram Strait in August 2010 using Radarsat images and its relationship to reanalysis ocean currents and wind vectors can be found in Chapter 8.

5.2 Using the ITSARI Algorithm with Cosmo Sky Med data

5.2.1 Part 1: February 2010

Cosmo Sky Med (CSM) is a constellation of four satellites each carrying an X-band SAR sensor (Italian Space Agency). The data received is at 5m resolution, so with this case study we move from C to X band, and also to much finer resolution than

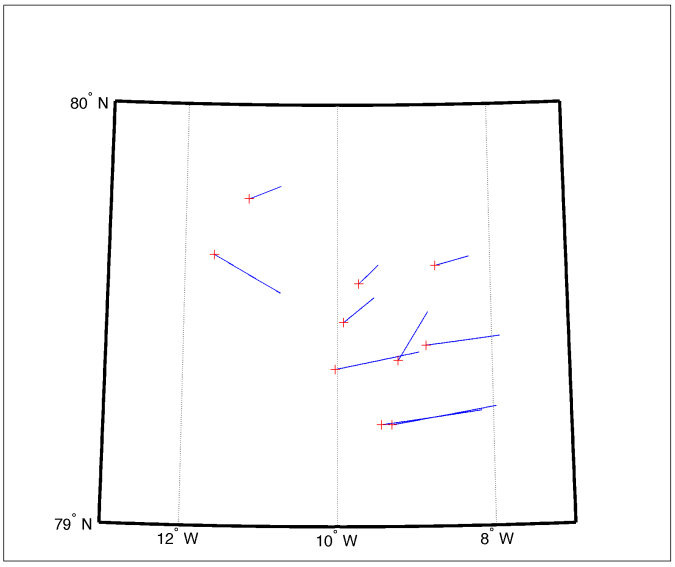

Figure 5.3: Direction of movement of ice objects tracked between between the 16th and 17th August 2010. The start of each track is marked with a cross.

that of the Envisat data used in the previous chapter. This case study focuses on a set of 3 CSM images of an area in the Beaufort Sea, acquired at 4:00 and 12:00 UTC on the 11th February 2010, and 23 hours later at 11:00 UTC on the 12th February 2010 (Figure 5.4).

The Beaufort Sea is located in the western Arctic, north of the Alaskan coast. Ice concentration and ice types are expected to be different again here to that of the Fram Strait and Barents Sea examples of the previous chapter. The ice in the Beaufort Sea is within the Beaufort Gyre, a current that flows west along the northern coast of Alaska, before turning north and mixing with waters inflowing through the Bering Strait from the Pacific to return across the pole as the Transpolar Current (Brown et al., 1989). Sea ice motion in the Beaufort Sea is characterized in winter by anticyclonic circulation associated with a predominant sea level pressure high in the region (Lukovich et al., 2011). The strength and position of the Beaufort Gyre are regulated by the atmospheric circulation in the region (Timmermans et al., 2011). Owing to prevailing anticyclonic (clockwise) winds generated by the Arctic high, the Beaufort Gyre accumulates fresh water from sea ice melt, Pacific Water inflows through Bering Strait, river runoff and atmospheric precipitation in the

upper ocean primarily by Ekman convergence. In the Bering sea the ice edge location appears to be governed almost completely by anomalies in the flow around the Aleutian low; when this semi-permanent feature is strong, the ice edge is influences primarily by zonal wind anomalies (Francis and Hunter, 2007). The Beaufort Sea was the site of a large amount of sea ice melt in the record breaking low sea ice summer of 2007 (Perovich et al., 2008).

The three images were imported from Geotiff using the new version of the ITSARI workflow described in Chapter 3. For this first exercise 'quicklooks', with a resolution of 25 m, were used instead of the full scenes.

The exercise in adapting ITSARI to work with the CSM images was successful: 36 objects were matched between the first and second images and 21 between the second and third images. Figure 5.4 contains a series of images that walks the reader through the tracking of objects from one image to the next. Figure 5.4a shows the first image with the movement vectors of objects tracked between the first two images. Figure 5.4b shows the same movement vectors but overlaid on the second image. Finally, Figure 5.4c shows the third image with the movement vectors of objects tracked from the second image to this image. The ice pack in the area at this time is very uniform without many well defined ice floes. There is a large lead present with brighter areas (corner reflectors) on either side. Other bright, linear objects may be smaller leads and cracks, or ridges. The features targeted by the tracking are mainly leads, or the corner reflectors from the edges of leads within the close pack. The westward motion of the ice is due to the Beaufort Gyre.

Figure 5.5 shows three examples of the type of objects that were identified and tracked in this exercise. Many of the objects were ridges or leads rather than specific floes (see for example Figure 5.5c). This shows the versatility of the algorithm.

From the tracks generated by the ITSARI algorithm it is possible to look at the speed and direction of travel of the objects. Thirty-six objects were tracked between

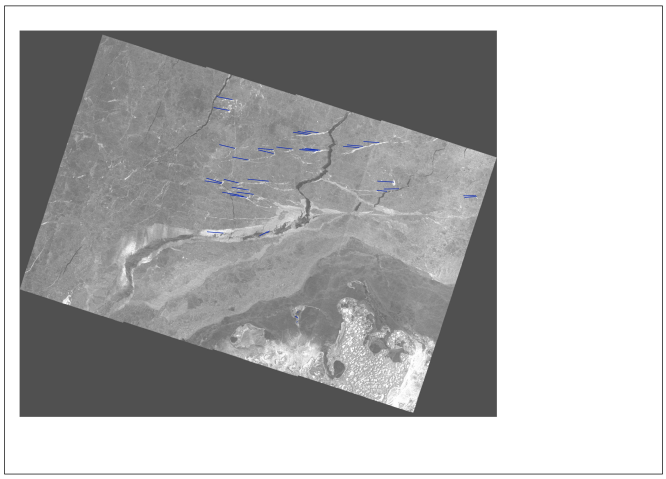

(a) 11 February 2010, 04:02:21

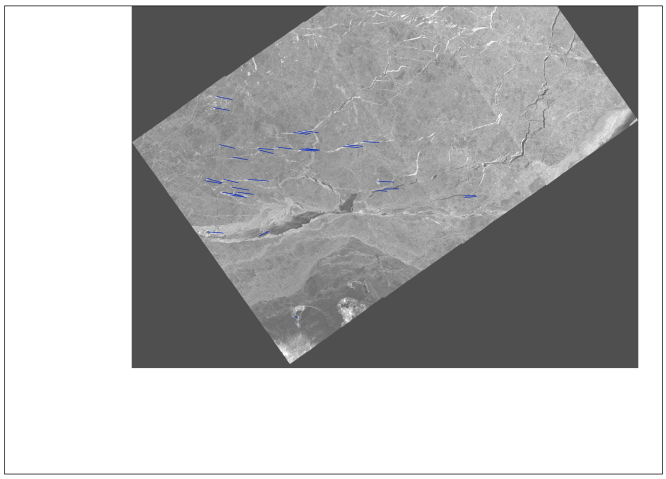

(b) 11 February 2010, 12:47:19

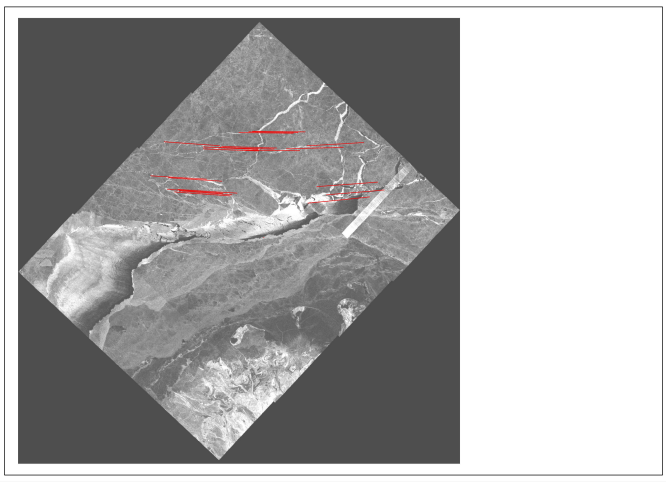

(c) 12 February 2010, 12:59:26

Figure 5.4: a) Image from 11th February 2010, 04:02:21 (top) with movement vectors for objects tracked between 04:02 and 12:47 on 11th February. b) Image from 11th February 2010, 12:47:19 with the same movement vectors. c) Final image from 12th February 2010, 11:59:26 with movement vectors for objects tracked between 12:47 11th February - 11:59 12 th February.

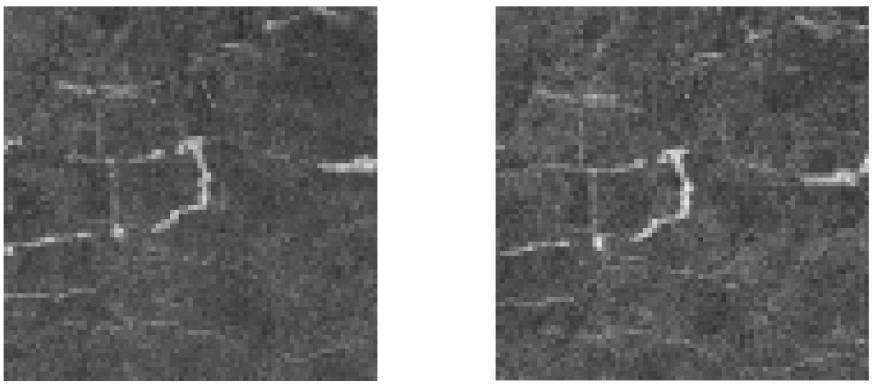

(a) Object 1

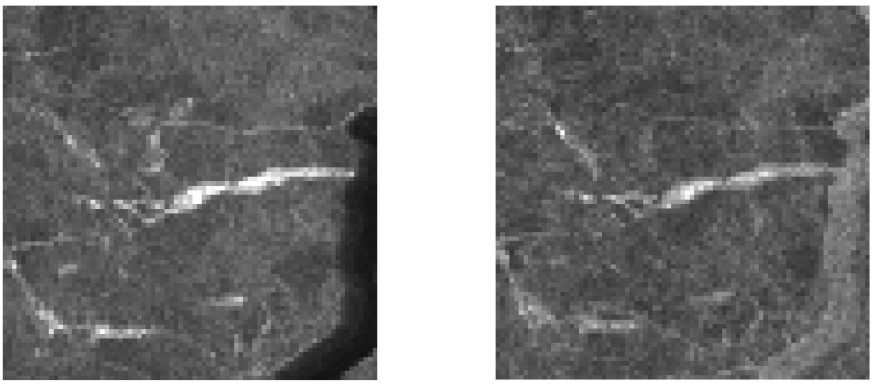

(b) Object 2

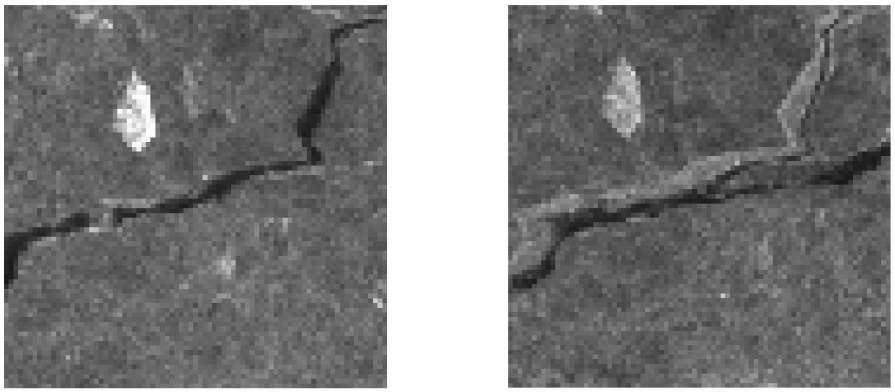

(c) Object 3

Figure 5.5: Three examples of the type of objects that were matched in this exercise, on the left is how the object appears in the first image and on the right how the same object appears in the second image.

the first pair of images, at an average speed of 0.16 ± 0.059 m s $^{-1}$, travelling on average 5.5 ± 1.8 km towards the west (Figure 5.6). During the following 23 hours the objects are still travelling west, at 0.24 ± 0.058 ms^{-1}, giving them an average travel distance of 20 ± 4.8 km (Figure 5.7). Twenty-one objects were tracked in this second pairing, of which 20 were continuations of tracks begun in the first pairing.

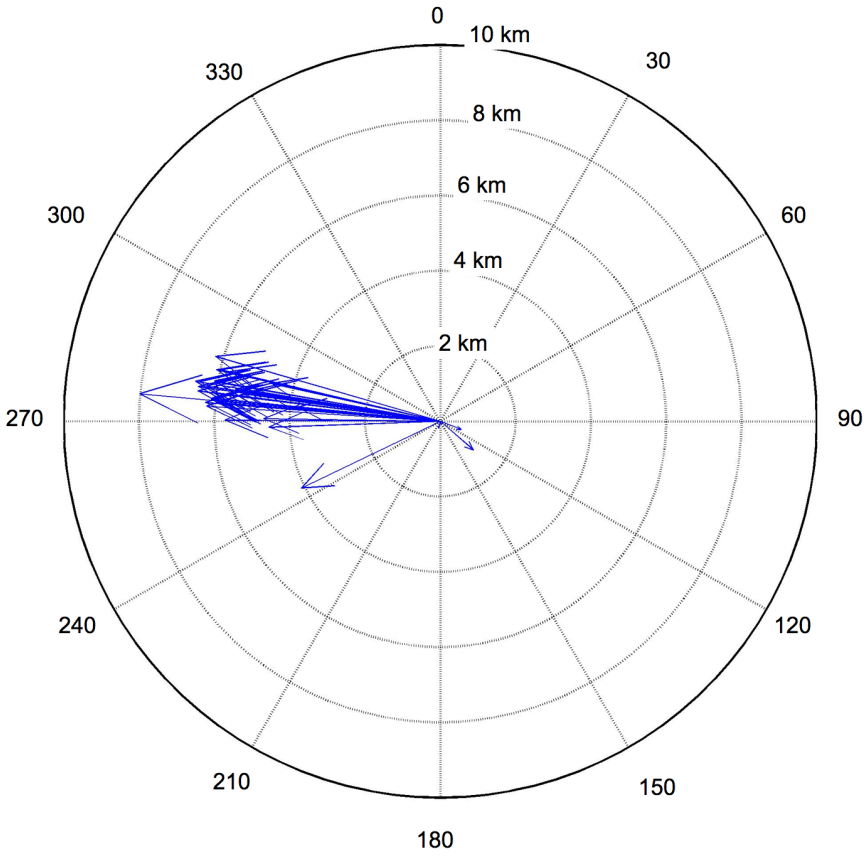

Figure 5.6: Compass rose showing direction and distance travelled by 36 ice objects tracked between between 04:00 and 12:47 UTC on the 11th February 2010.

It is possible to build up the track of an individual object over several consecutive images. Figure 5.8 shows the tracks generated from two matching exercises with the three example images, including a close up in part b. Several of the objects have been matched from the first to the second image and then on to the third. It is noteworthy that the third was at a different incidence angle to the first two but successful object matching / tracking is still possible.

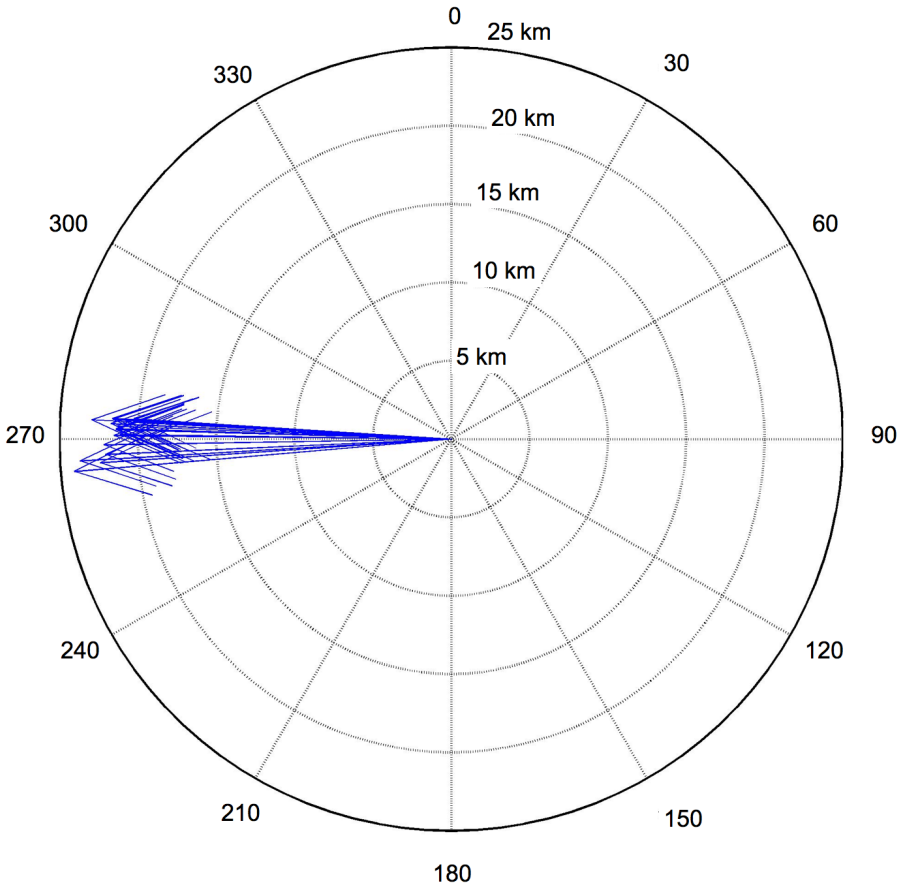

Figure 5.7: Compass rose showing direction and distance travelled by 21 ice objects tracked between between 12:47 UTC on the 11$^{\text{th}}$ February 2010 and 11:59 UTC on the 12$^{\text{th}}$ February 2010.

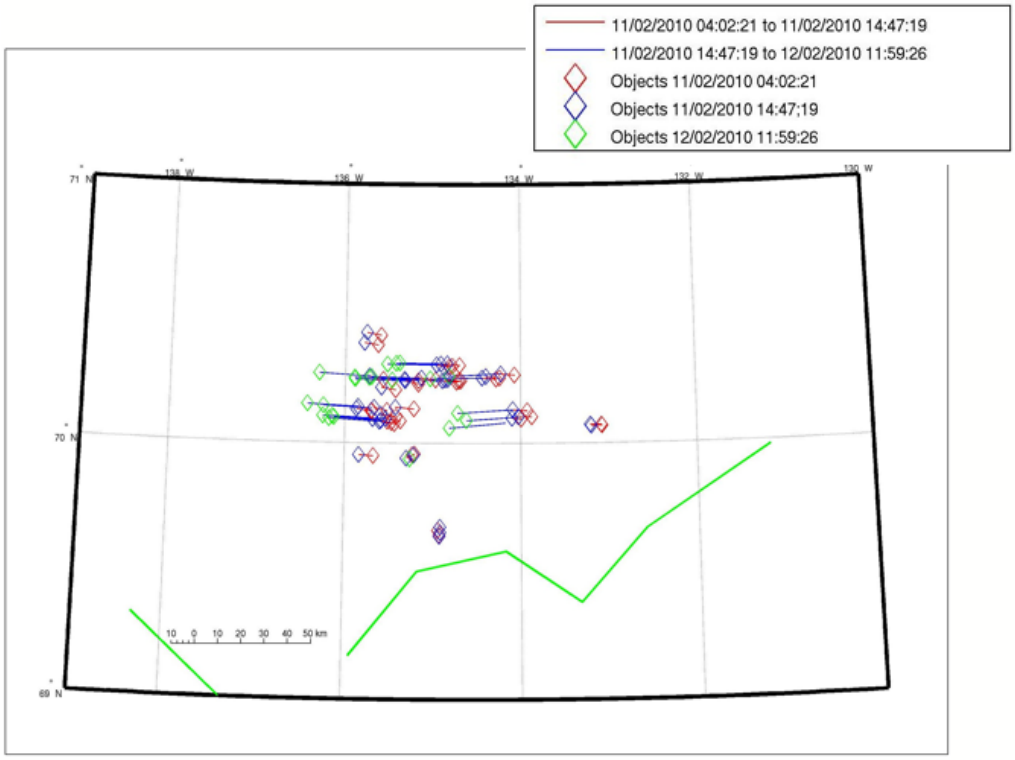

(a) Location of objects tracked in February 2010

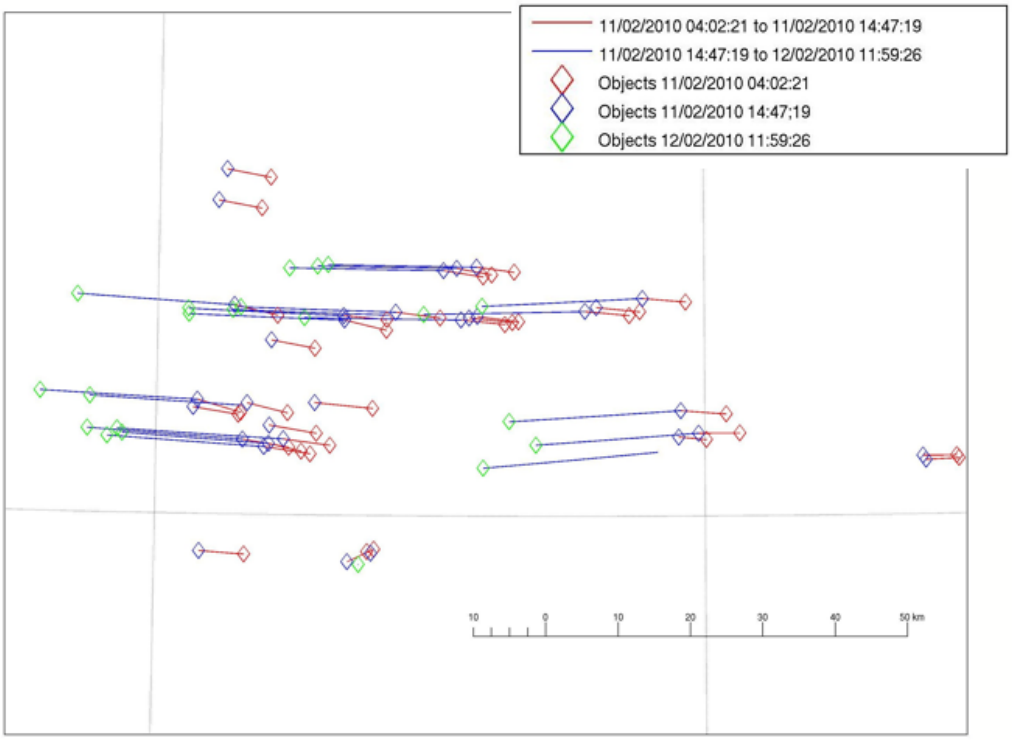

(b) Close up of the centre of the above map

Figure 5.8: Tracking objects between three Cosmo SkyMed images from February 2010. The coast is outlined in green. Movement of ice held in the Beaufort Gyre is towards the west.

5.2.2 April 2010

For the second part of this investigation into the tracking of ice movement from CSM, 34 images of the same Beaufort Sea area as used in the previous section were acquired over 10 days, in April 2010, at intervals of two to thirteen hours (Table 5.1). The pack is slightly different in character in April compared with February as there is a little more open water and fewer bright linear reflectors in the image. Similar to the February example, most of the objects tracked are small brighter areas or parts of leads. Thirty image pairs yielded more than one match, averaging five matches per image pair (Table 5.2). The average direction of travel for all matches over all image pairs is 187 ° with a variation of 80 degrees. This variability is thought to be due to the various influences of tides overlaid on the movement towards the west in the Beaufort Gyre. Movement towards the west driven by the ocean current is visible alongside smaller movements that may be wind driven or produced by the action of the tides. Figure 5.9 plots average direction and speed of travel for each pair.

5.3 Concluding remarks

In this chapter I have demonstrated that it is possible to use the algorithm with data from a different C band sensor (Radarsat), and with X band data (Cosmo Sky Med), with extremely promising results. This concludes the first half of the thesis in which I have been concerned almost exclusively with algorithm testing and development. In the second half of the thesis I explore the use of information gained using ITSARI to study the interaction of ocean currents and wind forcing with the movement of sea ice through the Fram Strait; beginning with a literature review in Chapter 6 that provides an introduction to the main oceanic and climate dynamics of the region.

Table 5.1: Cosmo Sky Med Images acquired for part two of the case study

Acquisition Date	Acquisition Time (UTC)
19-04-2010	03:00:59
19-04-2010	05:43:38
19-04-2010	12:04:43
19-04-2010	14:10:51
20-04-2010	12:52:36
20-04-2010	14:29:00
21-04-2010	03:07:02
21-04-2010	05:13:40
21-04-2010	11:34:49
21-04-2010	14:16:53
22-04-2010	03:25:12
22-04-2010	05:31:38
22-04-2010	11:52:44
22-04-2010	14:35:00
23-04-2010	11:40:47
23-04-2010	14:04:47
24-04-2010	05:37:37
24-04-2010	12:28:36
24-04-2010	14:04:47
25-04-2010	03:31:15
25-04-2010	05:07:38
25-04-2010	12:16:37
25:04:2010	14:22:53
26-04-2010	03:01:56
26-04-2010	05:07:37
26-04-2010	12:34:34
26-04-2010	14:10:48
27-04-2010	03:19:07
27-04-2010	05:25:36
27-04-2010	11:46:43
27-04-2010	14:28:55
28-04-2010	03:37:16
28-04-2010	05:13:36
28-04-2010	12:22:35

Table 5.2: Results of matching exercise with CSM images from April 2010

No	Start date and time	End date and time	No of matches	Average direction (°)	Standard deviation of direction	Average speed (m s $^{-1}$)	Max speed (m s $^{-1}$)	Min speed (m s $^{-1}$)	Average distance (km)	Max distance (km)	Min distance (km)
1	19/04/2010 03:00:59	19/04/2010 05:43:38	8	121.90	91.55	0.02	0.06	0.01	0.23	0.56	0.09
2	19/04/2010 05:43:38	19/04/2010 12:04:43	2	264.25	49.34	0.02	0.03	0.01	0.45	0.7	0.16
3	19/04/2010 05:43:38	19/04/2010 14:10:51	4	197.74	37.35	0.01	0.02	0.00	0.33	0.70	0.10
4	20/04/2010 12:52:36	20/04/2010 14:29:00	2	248.55	3.77	0.10	0.16	0.04	0.58	0.92	0.24
5	19/04/2010 14:10:51	20/04/2010 14:29:00	2	340.94	4.70	0.02	0.02	0.02	1.63	1.76	1.50
6	19/04/2010 12:04:43	20/04/2010 14:29:00	5	57.08	137.16	0.01	0.02	0.00	0.96	1.86	0.03
7	20/04/2010 14:29:00	21/04/2010 03:07:02	9	160.19	96.79	0.01	0.03	0.00	0.50	1.38	0.09
8	21/04/2010 03:07:02	21/04/2010 05:13:40	3	98.56	76.56	0.04	0.05	0.04	0.33	0.41	0.29
9	21/04/2010 05:13:40	21/04/2010 11:34:49	3	251.55	87.54	0.01	0.02	0.00	0.32	0.49	0.03
10	21/04/2010 11:34:49	21/04/2010 14:16:53	10	179.62	80.95	0.04	0.12	0.01	0.37	1.12	0.12
11	22/04/2010 03:25:12	22/04/2010 05:31:38	5	97.40	96.25	0.08	0.19	0.01	0.61	1.48	0.06
12	22/04/2010 05:31:38	22/04/2010 11:52:44	5	159.67	33.50	0.04	0.06	0.02	0.90	1.28	0.56
13	22/04/2010 11:52:44	22/04/2010 14:35:00	9	138.01	81.33	0.06	0.20	0.00	0.54	1.90	0.03
14	22/04/2010 14:35:00	23/04/2010 11:40:47	5	181.92	64.74	0.01	0.02	0.00	0.93	1.57	0.32
15	23/04/2010 11:40:47	23/04/2010 14:04:47	2	241.37	19.80	0.04	0.04	0.03	0.31	0.37	0.05
16	24/04/2010 05:37:37	24/04/2010 12:28:36	2	271.67	91.51	0.01	0.02	0.01	0.34	0.42	0.27
17	24/04/2010 14:04:47	25/04/2010 03:31:15	2	101.21	1.84	0.07	0.08	0.07	3.56	3.80	3.32
18	25/04/2010 03:31:15	25/04/2010 05:07:38	3	54.91	111.57	0.29	0.48	0.11	1.66	2.75	0.64
19	25/04/2010 12:16:37	25:04:2010 14:22:53	7	341.66	135.23	0.02	0.06	0.01	0.17	0.45	0.05
20	25:04:2010 14:22:53	26/04/2010 03:01:56	7	175.33	73.64	0.01	0.02	0.01	0.62	1.07	0.26
21	26/04/2010 03:01:56	26/04/2010 05:07:37	2	139.11	29.56	0.06	0.06	0.05	0.42	0.44	0.40
22	26/04/2010 05:07:37	26/04/2010 12:34:34	3	182.27	46.41	0.02	0.03	0.01	0.58	0.68	0.40
23	26/04/2010 12:34:34	26/04/2010 14:10:48	2	124.27	81.71	0.04	0.06	0.02	0.23	0.33	0.13
24	26/04/2010 14:10:48	27/04/2010 03:19:07	2	80.30	28.31	0.01	0.02	0.00	0.60	1.05	0.15
25	27/04/2010 03:19:07	27/04/2010 05:25:36	5	118.11	114.71	0.01	0.02	0.01	0.11	0.16	0.06
26	27/04/2010 05:25:36	27/04/2010 11:46:43	2	303.36	20.90	0.01	0.01	0.01	0.30	0.33	0.26
27	27/04/2010 11:46:43	27/04/2010 14:28:55	14	254.54	50.49	0.04	0.11	0.01	0.37	1.04	0.08
28	27/04/2010 14:28:55	28/04/2010 03:37:16	11	243.99	75.02	0.04	0.09	0.00	2.07	4.10	0.07
29	28/04/2010 03:37:16	28/04/2010 05:13:36	7	225.09	104.12	0.05	0.15	0.02	0.31	0.89	0.13
30	28/04/2010 12:22:35	29/04/2010 03:06:59	3	261.44	25.78	0.12	0.17	0.09	6.63	8.92	4.89
Average			5	187.2	80	0.04			0.9		

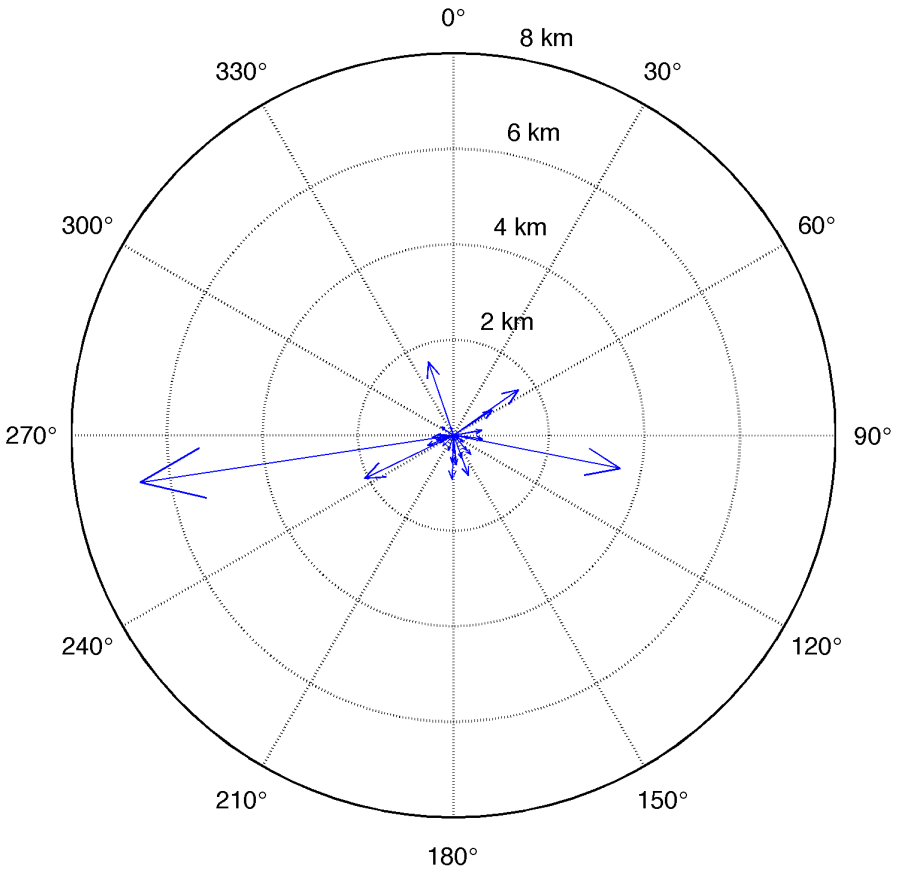

(a) Compass rose showing average direction and distance of travel for each image pair listed in Table 5.2

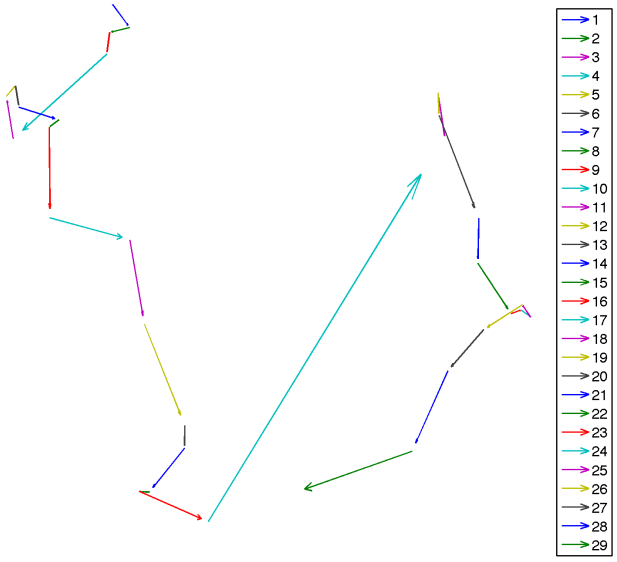

(b) Plot showing average direction and speed of travel for each image pair in chronological order. Number in legend corresponds to number identifying each image pair in Table 5.2

Figure 5.9: Average direction and distance of travel of objects identified using CSM images from April 2010.

Chapter 6

Arctic Atmospheric & Ocean Circulation

6.1 Introduction

The Arctic is a unique region. Most of the area north of 70° N is occupied by ocean (Serreze and Barry, 2005). This is almost entirely surrounded by land. Between 20° E and 2° W, the Fram Strait connects the Arctic ocean to the North Atlantic. This is the widest and deepest passage connecting the Arctic Ocean to the wider ocean circulatory system. Other connections exist through the Bering Strait, along the West Greenland coast, and between the islands of the Canadian Archipelago. The Fram Strait is the only deep water connection (Serreze and Barry, 2005; Bigg, 2003; Dowdeswell et al., 1997). The movement of sea ice in the Arctic is closely linked to both climate and ocean currents (Brown et al., 1989; Bigg, 2003). In this chapter I first introduce the atmospheric and ocean circulation of the wider Arctic area, and its impact on sea ice movement patterns, before moving the focus to my study area for the second half of the thesis, the Fram Strait.

6.2 Atmospheric Circulation

The Arctic climate system is characterised by low thermal energy and intimate couplings between the atmosphere, ocean and land (Serreze and Barry, 2005). The Arctic is a major part of the northern hemisphere heat sink. Poleward energy transport by the ocean and atmosphere is strongest in winter; and closely linked to the location of primary storm tracks, (Serreze and Barry, 2005; Barry and Chorley, 1998). Mean winter circulation (Figure 6.1) at sea level is dominated by three centres of action: the Icelandic low off the east coast of southern Greenland, the Aleutian low (off Alaska) and the Siberian High in central Asia (Brown et al., 1989; Bigg, 2003). This pattern is strongest in the winter months. These lows are weaker in summer; by July the Icelandic low is weak and low pressure extends over the East Canadian Arctic (Brown et al., 1989). The lows are maintained due to their position downstream of major mid-tropospheric stationary troughs, surface heating contrasts, and regional cyclogenesis. Weak low pressure also characterises the central Arctic Ocean in summer. Winter cyclones are most prominent on the Atlantic side of the Arctic, taking a northerly to easterly track. It is also possible for the North Atlantic cyclone track to extend deep into the Arctic. Near surface winds are typically light in the central Arctic, with mean annual speeds averaging 4 - 6 m s^{-1}.

The North Atlantic Oscillation (NAO) is a large scale alternation of atmospheric mass with centres of action near the Icelandic low and the Azores high. The NAO alternates between a 'high-index' pattern characterized by an intense Iceland low with a strong Azores ridge to its south and a 'low index' pattern in which the signs of these anomaly cells are reversed (Dickson et al., 1999). Changes to Arctic climate are is partly the result of multi-decadal variability in the NAO and arises largely outside the Arctic Ocean (Dickson et al., 1999). The pressure difference between these two main cells is the conventional index of NAO activity. The NAO may be the regional manifestation of an annular hemispheric mode of variability characterized by the alternation of atmospheric mass between the polar cap and the middle latitudes in both the Atlantic and Pacific ocean basins. This mode is the Arctic Oscillation. The signature of the AO on local temperature and precipitation is essentially the

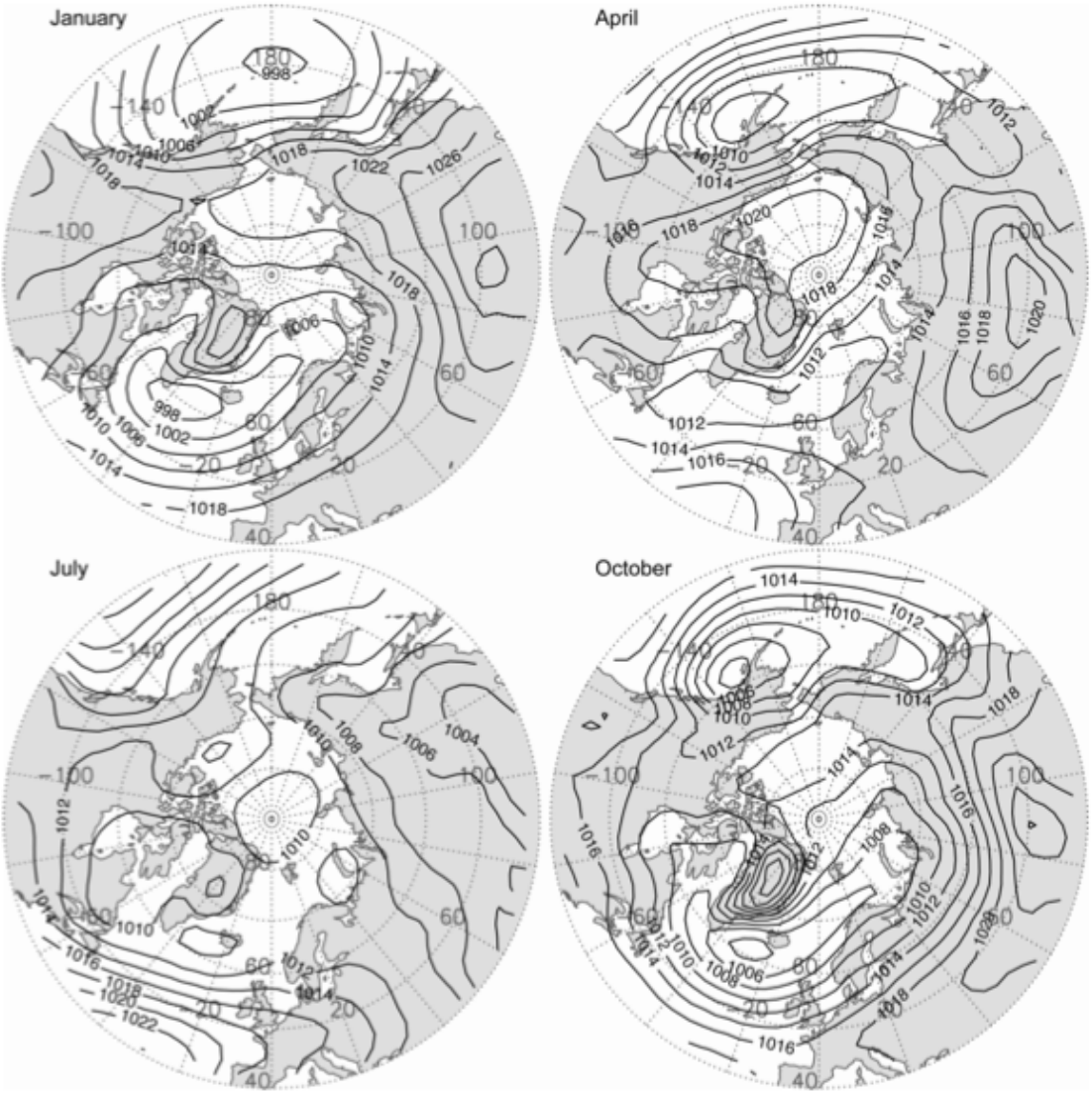

Figure 6.1: Mean Sea Level pressure (hPa) for the four mid-season months over the period 1970-1999, based on NCEP/NCAR data (From Serreze and Barry (2005)) The prominent features of autumn and winter are the mean Icelandic and Aleutian lows in the northern north Pacific and northern north Atlantic, respectively, and the Siberian High over northern Eurasia. In summer this pattern is less prominent. The mean July field shows weak low pressure over the central Arctic Ocean.

same as that of the NAO.

The downwelling long wave radiation flux and cloud cover strongly influence winter surface air temperature variability in the Arctic. The highest winter temperature values are found in the Atlantic sector, due to strong surface heat fluxes from open water, and the transport of sensible and latent heat by extratropical cyclones, steered by stationary planetary waves. Sea ice has a crucial role in the energy balance of the climate system (Jaiser et al., 2011; Fisel et al., 2011; Germe et al., 2011; Koenigk et al., 2006). Sea ice extent influences the large scale atmospheric circulation of the region. The insulating properties of the ice limit the heat and mass exchanges between the ocean and atmosphere while its high albedo controls the amount of solar radiative energy absorbed at the earth surface. Leads and polynyas in the ice locally permit strong sensible and latent heat fluxes into the atmospheric boundary layer; preventing winter surface air temperatures over the Arctic reaching such extreme lows when compared with the Antarctic.

Snow has a high albedo, an insulating effect on underlying sea ice, and a role in storing precipitation. Maximum snow depths on the sea ice may reach 300mm in May; rapid snowmelt in June and July leads to a minimum of between 0 - 30 mm in August (Serreze and Barry, 2005). The largest volume of precipitation in the region, exceeding 1000 mm (mean annual) and locally higher, is found in the Atlantic sector: south east Greenland and Scandinavia. This is a reflection of the northwest extension of the primary North Atlantic cyclone track forcing a convergence of moisture into the region (Serreze and Barry, 2005). Seasonality of precipitation corresponds with the seasonality of the North Atlantic cyclone track, with a cold season maximum, and summer minimum.

In the mid troposphere (2 to 6 km altitude) circulation a well developed cyclonic vortex is present in the Fram Strait region for much of the year (Barry and Chorley, 1998). The winter vortex is strongly asymmetrical. Isobars running roughly parallel to the East coast of Greenland are more closely spaced than those towards the centre of the Strait. This vortex is part of the primary North Atlantic cyclone track; its

circulation weakens and becomes more symmetrical when latitudinal distribution of solar heating becomes more even in spring and summer. Lee side vorticity production occurs off south east Greenland. Rapid deepening of lows referred to as polar mesocyclones or polar lows along the sea ice edge is frequently observed (Rasmussen and Turner, 2003; Klein and Heinemann, 2002). There are relatively few closed lows over the Greenland ice sheet.

Polar lows are intense maritime mesocyclones of typically 100-150 km diameter (Rasmussen and Turner, 2003; Klein and Heinemann, 2002). These intensify rapidly, with surface wind reaching hurricane speeds. The Bering Sea is a common location for the formation of polar lows, maritime systems with near-surface winds exceeding 15 m s $^{-1}$, which commonly develop in oceans subject to cold polar outbreaks, where cold continental air is advected over relatively warm open water. Baroclinic instability associated with upper air cold air advection and cold air masses over relatively warm water is the dominant mechanism for mesocyclones developing over the Norwegian Sea (Klein and Heinemann, 2002). Two mechanisms for the formation of polar lows are conditional instability of the second kind (Cumulonimbus convection) and wind induced surface heat exchange. Katabatic winds may lead to the formation of polar lows via the second method, channelling of flow in large valleys leads to a convergence, and generation of cyclonic vorticity (Klein and Heinemann, 2002). Katabatic winds are well documented further south on the east coast of Greenland (Klein and Heinemann, 2002; Heinemann and Klein, 2002; Heinemann, 1999). It is possible that katabatic flow may also occur from the slopes of the Greenland Ice Sheet in the north east, however, Heinemann and Klein (2002) record that in the north-east no significant synoptic support of the katabatic winds is present and the synoptic pressure gradient is even opposed to the katabatic force in some regions.

In winter strong westerlies in the mid and upper stratosphere (40-50 km altitude) are flowing around a deep, cold polar vortex. In spring this vortex field shifts off-pole to near Eurasia. In the troposphere eddy transports are largely associated with travelling synoptic scale waves associated with migrating cyclones and anticyclones.

In the stratosphere such transports are associated with long planetary waves. One phenomenon that affects circulation in the stratosphere is sudden stratospheric warmings (Rasmussen and Turner, 2003). These are rather complicated processes (vertically propagating waves and 'preconditioning' focus wave action towards the polar vortex). They can cause stratospheric temperatures to rise, and the circumpolar vortex to reverse to easterly flow for a couple of days, with a knock on effect on the surface wind direction.

In winter, strong (3 -10 m s^{-1}) northerly winds prevail in the region adjacent to the east Greenland coast (Schneider and Budeus, 1997), however in summer wind speeds decrease dramatically (0-4 m s^{-1}), oscillating from north to south. Northerly winds on the east side of Greenland are often the result of high pressure systems over Greenland itself. Greenland presents a high, steep and cold topographic barrier to the atmosphere that is capable of diverting and distorting air flow around it (Harden et al., 2011; Petersen et al., 2009). Barrier winds are low level jets formed when air is forced towards a steep topographic barrier. Air is dammed and a pressure gradient perpendicular to the barrier develops, leading to geostrophic flow along the barrier. Evidence from south Greenland suggests barrier flows are not classic geostrophically balanced barrier flows but have a significant ageostrophic component and are precisely controlled by synoptic-scale systems (Petersen et al., 2009). Barrier winds are known to also occur in the north of Greenland; but there is a lack of wind speed data from this region to provide the finer details (Harden et al., 2011).

6.3 Ocean Circulation in the Arctic

The Arctic ocean covers 14 million km^2. The central Arctic Ocean contains two major deep basins; the Amerasian and Eurasian, separated by the Lomonosov Ridge (Serreze and Barry, 2005). The Arctic Ocean is uniquely limited in its connections to other world oceans. The shallow, narrow, Bering Strait connects it to the Pacific while the Greenland and Norwegian Seas connect to the Atlantic. There are also shallow passageways (at their shallowest only 85-140m deep) that provide

connections through the Canadian archipelago to Baffin Bay and the Labrador Sea (Figure 6.2). North of the Greenland-Scotland ridge the whole area can be referred to as the Arctic Mediterranean, which contains the Arctic Ocean and the Nordic seas. Nordic Seas is a collective name for the fairly shallow Barents Sea and three deep ocean regions: the Norwegian Sea, the Iceland Sea and the Greenland Sea which are separated from one another by submarine ridges (Hansen and Osterhus, 2000).

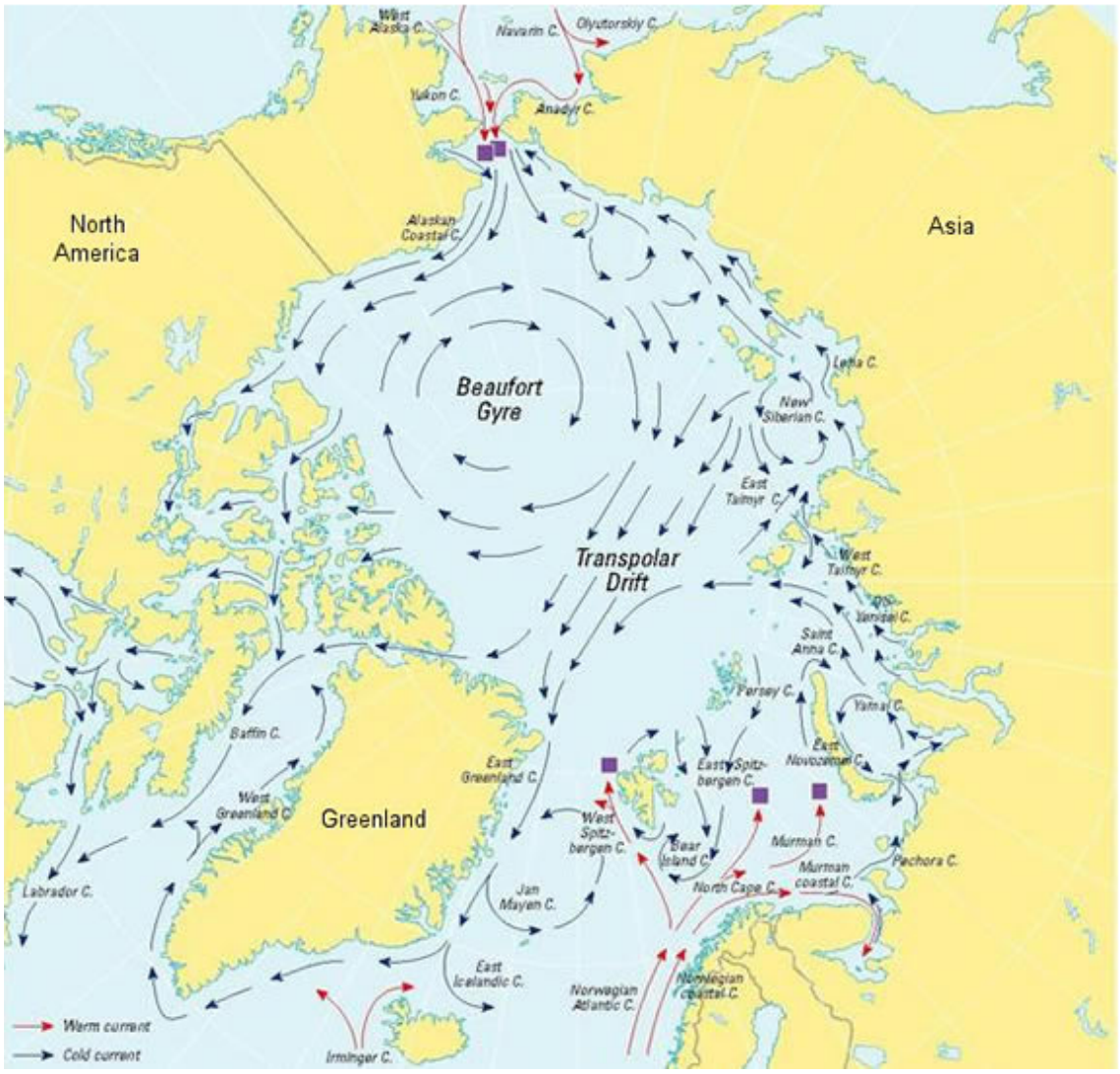

Figure 6.2: Arctic Ocean Circulation. Image courtesy of Arctic Monitoring and Assessment Programme (AMAP) graphics database at: http://www.amap.no/

Ocean current flow in the Arctic Ocean is driven by the wind resulting in sub-polar cyclonic surface gyres. The location of these gyres is modified by the positioning of the surrounding land masses. Ice drift in the Arctic ocean is dominated by two large

scale transport regimes (Brummer et al., 2003): the Beaufort gyre located in the American - Canadian sector of the Arctic and the Transpolar drift stream extending from the Siberian coast to the Fram Strait (Figure 6.2). In the north Pacific, gyre flow consists of the Oyashio and Alaska currents. A clockwise gyre is centred over the Canadian Basin. The land mass of Greenland also disrupts gyral flow in the North Atlantic. The transpolar drift stream carries ice towards the Fram Strait. Both a surface and a deep current exit the Arctic Ocean through the Fram Strait (Serreze and Barry, 2005; Schneider and Budeus, 1997), the surface current carrying with it 10-20 % of the Arctic's ice annually. In the opposite direction,the inflow of Atlantic waters to the Arctic Ocean has two main branches, one West of Svalbard and one through the Barents Sea.

The main surface outflow from the Arctic is the East Greenland Current (EGC), extending to considerable depth below the Arctic surface layer (Serreze and Barry, 2005). This carries ice southwards to the southern tip of Greenland, where it converges with the warm Irminger Current and most of the ice melts. The Arctic Ocean has a key role in the mechanisms responsible for the properties of water fed into the Atlantic limb of the global thermohaline circulation (Karcher et al., 2005). The properties of both intermediate and deep waters exiting the Arctic in the EGC change considerably from the Fram Strait to the Greenland Sea, indicating interactions with recirculating waters (Rudels et al., 2005). Heat loss to the atmosphere occurring in the Arctic Mediterranean cools the upper waters making them denser. They sink, forming intermediate and deep waters that re-cross the Greenland-Scotland ridge and sink into the deep North Atlantic. This promotes a compensating northward flow of warm surface water across the ridge (Rudels et al., 2005).

The Arctic Ocean is characterised by a low salinity layer at the ocean surface. This is maintained by river input; the Arctic receives 11 % of the world's river flow while only accounting for 1 % of the total world ocean area (Serreze and Barry, 2005). There is also an influx of low salinity waters from the Pacific through the Bering Strait. Temperatures in this surface layer are near to the salinity-adjusted freezing

point. The region below this surface layer, to 200 - 300 m depth, is characterised by a rapid increase in salinity and an increase in temperature to maximum values around 300 - 500 m depth (Brown et al., 1989; Bigg, 2003; Serreze and Barry, 2005). This stable stratification inhibits vertical mixing. As sea ice forms the brine rejected increases the density of the surface layer and the depth of vertical mixing. As ice melts in summer the surface becomes fresher and vertical mixing is inhibited (Serreze and Barry, 2005).

Shallow submarine plateaux extend from Greenland to Scotland, preventing deep Atlantic water from entering the Arctic. Northward transport of heat crosses the Greenland-Scotland Ridge. In the Fram Strait region the temperature maximum at 300-500 m depth marks the inflow of warm Atlantic waters. Northward heat transport is highest in winter (Schauer et al., 2004). Dominance of deep overflows over surface outflows in the water budget argues that thermohaline forcing dominates over direct wind stress and esturine forcing in driving the Atlantic Water inflow across this ridge (Hansen and Osterhus, 2000). This means that the north eastern Atlantic is much warmer at the surface than other oceans at similar latitudes (Hansen and Osterhus, 2000).

Curry and Mauritzen (2005) present evidence from reconstructions of ocean properties based on data collected between 1953 and 2002 that the salinities of water masses in the high-latitude North Atlantic Ocean have been decreasing since the early 1970's. This is expected to act to slow northward heat transport, cooling the North Atlantic. Changes in sea surface temperature and salinity within the Arctic Basin are closely linked to atmospheric circulation (Timmermans et al., 2011).

6.4 Sea Ice Motion

The freshwater surface layer described above allows sea ice to form readily in the Arctic Ocean. Sea ice is intimately coupled with the atmosphere, energy budget, atmospheric circulation, surface energy budget and hydrologic budget. Ice growth

and melt are determined by both deformation and thermodynamic forcing. New ice thickens at 3 - 10 cm a day at temperatures between -10 °to -30 °C. Over the course of a yearly cycle the formation of sea ice can affect climate in a variety of ways, for example, sea ice melt draws the heat out of the atmospheric column in summer. In winter the North Atlantic, especially the Greenland Sea, is an area of deep water production, important in driving the ocean's thermohaline circulation; and there are strong temperature gradients and hence enhanced baroclinicity along sea ice margins.

Sea ice is in constant motion due to wind stress, water stress, floe to floe interaction and ocean tilt (Serreze and Barry, 2005). The change in momentum of a parcel of ice can be described by the momentum balance (Serreze and Barry, 2005):

$$\frac{m\partial\vec{U}}{\partial t} = -mf\vec{k} \times \vec{U} + \vec{T_a} + \vec{T_w} + \vec{F} - mg\nabla H \tag{6.1}$$

where the term on the left is the rate of change in momentum where m is ice mass per unit area and U is ice velocity (this assumes no change in mass). The first term on the right is stress due to the Coriolis force, where f is the Coriolis parameter and k is a unit vector normal to the surface. T_a and T_w are the air and water stresses. F is internal ice stress. The final term describes ocean tilt, where H is dynamic height of the sea surface and g is gravitational acceleration (Serreze and Barry, 2005).

The relative magnitude of the terms of the momentum balance may vary seasonally and spatially. Ice motion varies significantly from day to day largely in response to variations in wind field. There are difficulties separating pack ice motion caused by local winds from that due to general current patterns. The dominant terms are air and water stress, Coriolis force and ice interaction. Ice interaction is largest in winter and near the coast.

The mean ice drift pattern (Figure 6.3) roughly resembles the distribution of mean sea level pressure. Apart from fast ice, the annual drift pattern is dominated

by the Beaufort Gyre and the Transpolar Drift Stream. The pattern is maintained by roughly equal wind and ocean current contributions. In the circumpolar and eastern Arctic and the Fram Strait, the annual mean sea ice drift is best explained by the sea level pressure (SLP) difference across the Arctic Ocean along meridians 270°E and 90°E (Vihma et al., 2012). It can take up to 3 years for a parcel of ice to move along the Transpolar Drift. Ice velocities in the Trans-Polar Drift Stream progressively increase towards the Fram Strait, where mean drift speeds are 0.05 - 0.1 m s^{-1}. Still higher ice velocities are observed in the Greenland Sea. Of the total ice area of the Arctic basin, 10-20 % exits annually through the Fram Strait (Serreze and Barry, 2005; Brummer et al., 2003).

The annual mean sea ice drift has been attributed to a variety of different forcings. Away from the coast 70 % of the variance of ice motion at daily to monthly time scales is explained by the local surface geostrophic wind (Brummer et al., 2003). Both drift buoys and ice floes have been shown to follow atmospheric isobars (Ogi et al., 2008; Kwok and Rothrock, 1999). Ekman drift is the rightward drift of ice relative to geostrophic wind. Pack ice is is said to move at 2 - 3.8 % of prevailing wind speed and between 8° and 30° to the right of wind direction in the northern hemisphere (Schneider and Budeus, 1997; Brummer et al., 2003), with turning angle increasing to as much as 51° during a cyclone event (Brummer et al., 2003). This has a strong seasonality between as low as 0.007 % and 5° in winter and as high as 0.011 % and 18° in summer. The stability of the atmosphere plays its part, as increased low level stability in winter acts to reduce surface wind stress and decrease the turning angle between geostrophic wind and wind stress vector.

Because winds are highly variable their forcing tends to cancel out at longer timescales, allowing the steady currents to play a stronger role. Since turning angle is to the right of the geostrophic wind, cyclonic ice motion is associated with divergence within the pack, and anti-cyclonic motion is associated with convergence. Convergence within the pack can cause rafting and breaking up of ice floes. Sea ice extent and concentration anomalies can all be linked to climate interactions and feedbacks including preconditioning and summer atmospheric forcing.

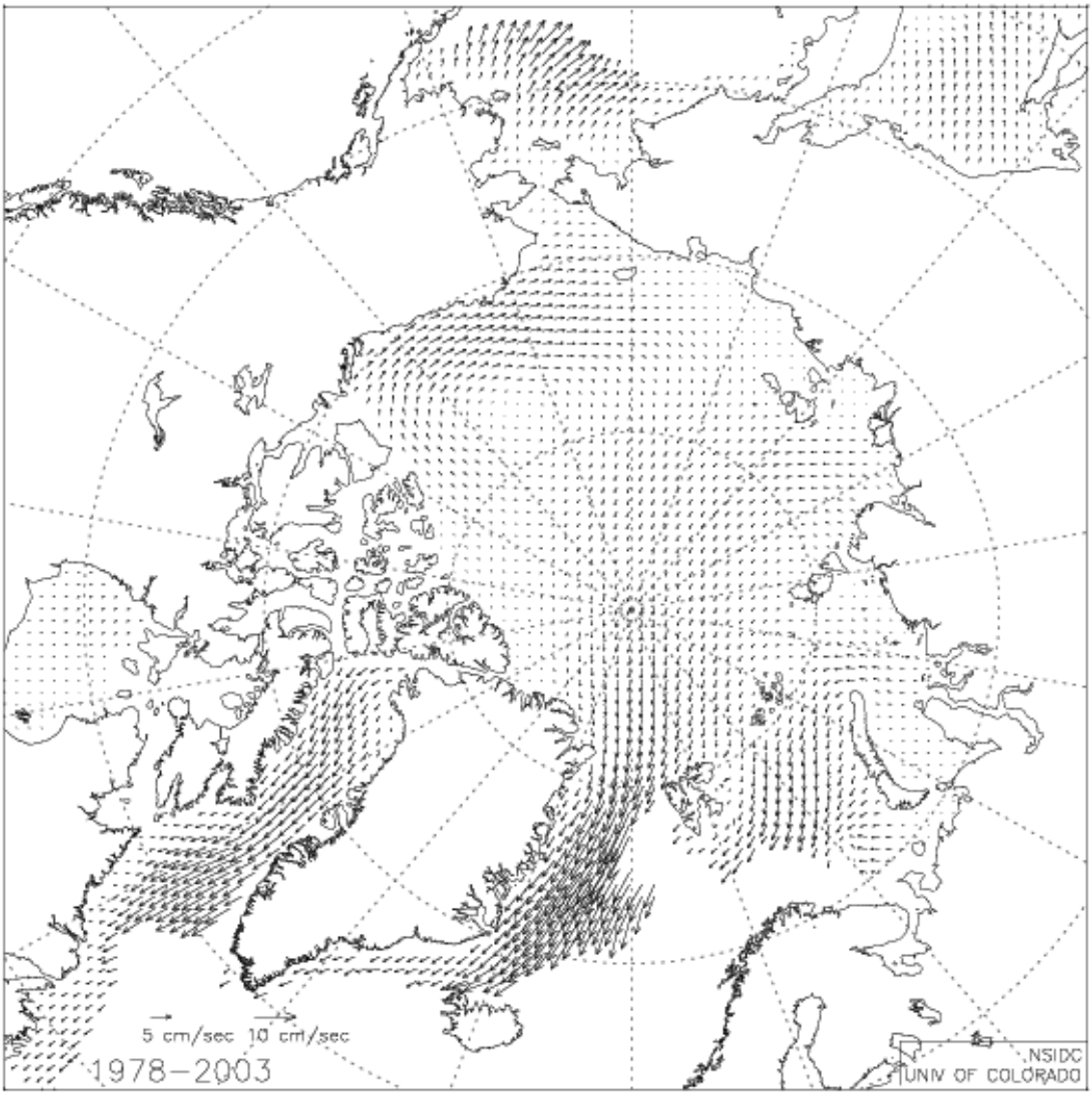

Figure 6.3: Mean Sea Ice motion from 1978 to 2003. Arrows show the direction and velocity of the ice, with longer arrows representing higher velocities. Image courtesy of National Snow and Ice Data Centre, University of Colorado, Boulder, CO, from: http://nsidc.org/cryosphere/seaice/processes/circulation.html

The motion of icebergs is also controlled by ocean currents modified by the Coriolis effect (Phillips and Laxon, 1995). It is commonly held that icebergs drift relative to the ocean current at 2 % of the wind speed (Bigg et al., 1997), this suggests that the ocean current determines the direction of drift but the wind moderates its speed. Bergs with a shallower draft are more strongly affected by the wind.

6.5 Fram Strait Outflow

The sea ice outflow through the Fram Strait is a major component of the mass balance of the Arctic Ocean (Kwok and Rothrock, 1999; Kwok et al., 2004; Fahrbach et al., 2001; Spreen et al., 2006; Komuro and Hasumi, 2007). Ice thickness trends in the Fram Strait are indicative of the thickness trends in the Arctic Ocean (Kwok et al., 2004; Vinje, 2001), while variability of sea ice transport through the Fram Strait impacts on the intensity of the Atlantic deep circulation (Komuro and Hasumi, 2007; Karcher et al., 2005; Spreen et al., 2006).

The Fram Strait east of 0° W is dominated by outflowing Arctic Ocean waters and recirculating Atlantic and deeper water masses (Rudels et al., 2005). Two streams of Atlantic water enter the Arctic Ocean, the Fram Strait branch, and the warmer, more saline, Barents Sea branch (Rudels et al., 2005). Near the shelf break on the western edge of the Fram Strait the East Greenland Current (EGC) transports a significant amount of fresh water southward from the Arctic Ocean (Meredith et al., 2001).

The East Greenland Current (EGC) is the key carrier of freshwater from the Arctic into the northern North Atlantic via Fram Strait (Cox et al., 2010; Karcher et al., 2005). The EGC flows southward out of the Arctic through Fram Strait and along the eastern margin of Greenland via Denmark Strait (Cox et al., 2010). As the EGC flows over the wide East Greenland shelf at Denmark Strait, the current crosses the Kangerdlugssuaq Trough, a large canyon that cuts across the shelf (up to 600 m deep, relative to the 250 m deep shelf). The path of the EGC either enters

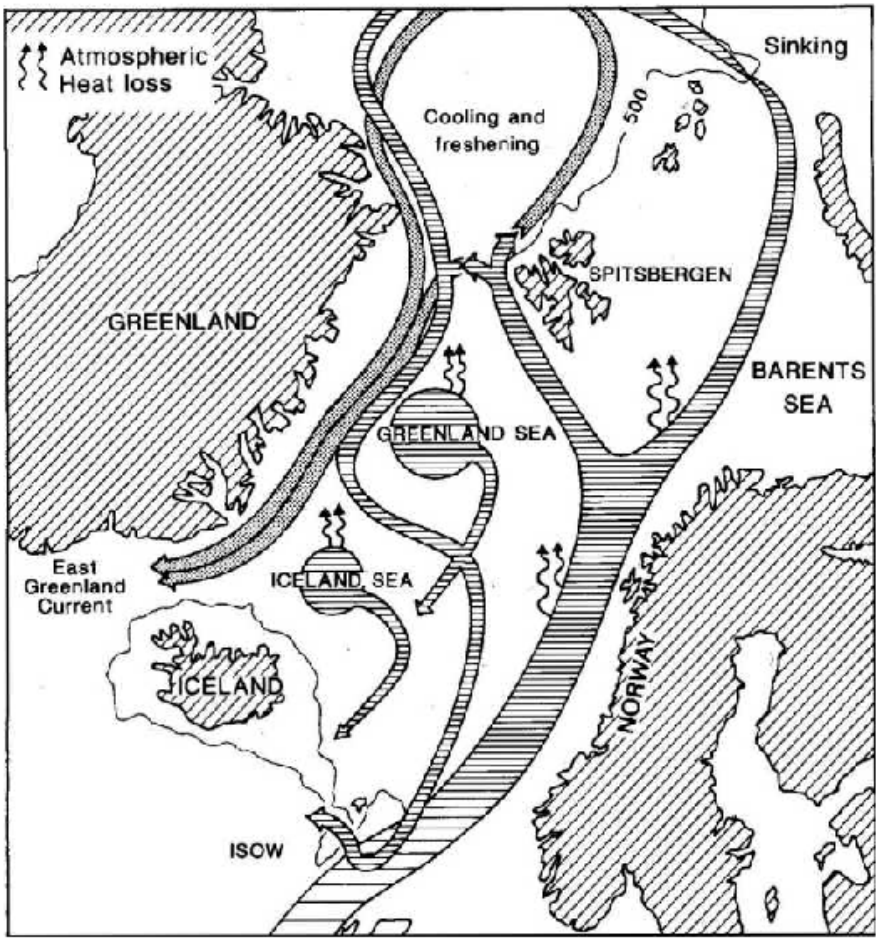

Figure 6.4: Ocean currents of the Fram Strait area (From Bigg (2003), adapted from Mauritzen (1996)). Warm water flows in the Norwegian Coastal Current into the Norwegian Sea, there cooling, freshening, and sinking. Two water masses result, one leaving the Norwegian Sea through the Faeroe Channel at depth and the other constituting the less dense East Greenland Current.

the canyon with no recirculation, or bifurcates so the main current cuts across the canyon causing an anticyclonic eddy at the head of the canyon (Cox et al., 2010). The general circulation of the northeast Greenland shelf is governed by an anticyclonic gyre centred at about 70°N and 12°W (Figure 6.4). Associated with this gyre is a northward flowing coastal current (Schneider and Budeus, 1997).

The northeast water polynya (NEWP), located on the continental shelf northeast of Greenland, is a recurring summer polynya that begins opening around May/June, gradually increases in size, then closes in September (Schneider and Budeus, 1997). To the south the polynya is bounded by shelf ice, the Norske Oer Shelf Ice (NOSI), extending 60-80km offshore at about 79°30'N from the mouth of Nioghalvfjerdsbrae to Belgica Bank. The islands of Henrik Kroyer Hokme may be connected with the coast via a fast ice bridge.

The bathymetry of the northeast Greenland shelf is dominated by a trough system around Belgica Bank consisting of Belgica Trough, Norske Trough and Westwind Trough. These are 300-500m deep, with Norske trough separating Belgica Bank from the coast (Schneider and Budeus, 1997). NOSI is underflown by currents in this trough. Ob Bank is a second shallow area found at the northernmost boundary of the northeast Greenland shelf. Winter shelf ice here may persist into summer. In winter strong northerly wind outbreaks push newly formed sea ice out of the Ob bank region, but since the air sea temperature difference at that time can amount to 30°C, new ice forms rapidly to balance the ice export. In summer this difference does not exist so the north east water polynya remains open. Opening of the polynya is attributed to the combined effect of NOSI and a northward flowing coastal current, the North East Greenland Coastal current (NEGCC), but this does not explain areas of open water south and north of Ob Bank (Schneider and Budeus, 1997). Several groups of icebergs with a freeboard of 10-20m and diameters of up to 300m, are grounded within Ob Bank Shelf Ice (OBSI) (Schneider and Budeus, 1997). Icebergs grounded within OBSI act as anchor points for sea ice (Schneider and Budeus, 1997). There are still icebergs grounded within this region 15 years after Schneider and Budeus (1997) described them in their paper - from personal observation while

on field work in the Fram Strait in September 2010.

Extensive effort has been made to estimate the flux of ice and fresh water through the Fram Strait. The average annual sea ice flux for the period 1991-1998 was 866,000 km^2 per year; with thickness estimates from upward looking sonar this equates to 2218 km^3 yr^{-1} (Kwok et al., 2004). Estimates of the sea ice volume flux between 1970 and 1990 through the Fram Strait range from 1600 to 5000 km^3 yr^{-1} and show high inter-annual variability (Spreen et al., 2006; Vinje, 2001; Kwok et al., 2004); For example, Widell et al. (2003) report monthly fluxes of 200 km^3 calculated using data from upward looking sonar, while Spreen et al. (2006) found fluxes as low as 70 km^3 in two 30 day periods.

Volume flux estimates can be hampered by lack of reliable thickness data. Ice fluxes measured from remotely sensed data are mainly cold season fluxes dues to the problems using cross correlation techniques on images in summer conditions. The largest volume flux occurs in autumn and winter, associated with strong northerly winds in the strait. The flux is smallest in summer when westerlies slacken and are replaced by weak southerlies. Ice volume flux is not evenly distributed across the Strait, but is strongly concentrated towards its western side (Spreen et al., 2006), although near the Greenland coast thick land-fast ice prevails.

The Fram Strait is a data sparse region for atmospheric information, investigations on the impact of pressure systems on ice drift are reliant on drift buoys from the International Arctic Buoy programme, and ships of opportunity (Brummer et al., 2003). Wind forcing is major agent for ice efflux, with anomalies associated with variations in the high-latitude atmospheric circulation (Vinje, 2001; Dickson et al., 1999). Vinje (2001) suggests that 60 % of the annual flow in the Fram Strait was directly wind-driven while 40 % was due to ocean currents.

Except for years with an extreme negative NAO, correlation of winter ice export with the NAO index is high (Kwok et al., 2004; Vinje, 2001; Inoue and Kikuchi, 2007;

Dickson et al., 1999; Tsukernik et al., 2010; Kwok and Rothrock, 1999). Winter NAO index explains 63 % of the variance in the annual efflux of ice since 1976 (Dickson et al., 1999), so that a 1 standard deviation change in winter NAO index is associated with a 200 km^3 change in annual ice flux (Dickson et al., 1999). The sea level pressure gradient over the Fram Strait explains more than 80 % of the variance in ice flux over the period 1978-1996 (Kwok and Rothrock, 1999). Germe et al. (2011) also show that inter-annual variability of winter Arctic sea ice concentration is linked to sea level pressure anomaly in the Nordic Seas Marginal Ice Zone, while Tsukernik et al. (2010) suggest that the sea ice pressure gradient between two poles centred on the Barents and Greenland seas has a larger influence on ice motion through the Fram Strait than does the NAO index. Anticyclonic circulation anomalies over the Greenland Sea can prevent sea ice from drifting southwards (Inoue and Kikuchi, 2007).

In the eastern parts of the European Arctic an extension of sea ice is expected during the negative phase of the NAO and sea ice retraction is expected during its positive phase, due to relationships between local wind conditions and Atlantic inflow (Dickson et al., 1999; Germe et al., 2011). The dominant wind forcing in recent years has been the anomalous airflow associated with the extreme positive phase of the NAO, however, Fram Strait outflow is also associated with negative phases of NAO (Dickson et al., 1999). It is possible that NAO index is not simply correlated with ice flux through the Fram Strait, that conditions conductive to ice flux can occur during both extrema of the NAO, that the closest correspondence between increased ice flux and NAO occurs during NAO positive conditions but that an enhanced efflux can occur during the opposite extreme state of the NAO (Dickson et al., 1999). Because the latter would occur at a time when the ice flux is generally reduced, this 'event' may appear more conspicuous by contrast.

The passage of cyclones over the Fram Strait has been shown using large scale ice motion fields from SSM/I to speed up ice movement (Brummer et al., 2003, 2008). The Fram strait experiences up to twelve cyclones a month. Cyclone impact on sea ice depends on the location of the track within the Fram Strait. The more

easterly the track, the larger the ice export (Brummer et al., 2008). Pre-existing sea ice concentration also plays a part (Brummer et al., 2008). Brummer et al. (2003) found that average ice drift of 0.21 m s $^{-1}$ increased to 0.6 m s $^{-1}$ during cyclone passage. During a cyclone event ice drift amounted to 1.6 % of the geostrophic wind with a turning angle of 51° on average (Brummer et al., 2003). Increasing sensible and latent heat fluxes directly over the reduced ice cover of the Greenland Sea during NAO positive phase ice retraction have contributed to the observed increase in the number of cyclones in that sector (Dickson et al., 1999).

Negative NAO and anomalous westerly winds are also associated with the formation of the 'Odden Sea ice feature' between 73° and 77° N, just to the south of our study area (Rogers and Hung, 2008). A high NAO index will also be associated with stronger and more frequent cyclones through the region, which are likely to trigger more and stronger barrier winds (Harden et al., 2011; Dickson et al., 1999). During the high index phase of the NAO storm activity extends northeastward into the Norwegian-Greenland seas accompanied by an increase in the incidence of deep storms (to 15 per winter).

Ice thinning and stronger winds in the region have led to an increase in sea ice drift speed since the 1950s (Spreen et al., 2011). The West Spitsbergen current has a strong annual cycle with maximum transport in winter (February) and minimum in summer (August), while the variability of the East Greenland Current is less clear, and semi annual fluctuations are more prominent (Fahrbach et al., 2001). For the period 1996-2000 ice velocity was generally in a SSW direction and aligned to the shelf break, with a mean southward component of 0.16 m s^{-1} (Widell et al., 2003). Schneider and Budeus (1997) conclude that between 1990 and 1993 the pack ice velocity in southern NEWP results from the velocity of the NEGCC and 2.5 % of the wind velocity, rotated 25° to the right. Starting in June the influence of the NEGCC starts to exceed the weakening winds. South of Ob Bank no significant or persistent geostrophic currents are observed and wind stress remains a major driving force.

Ice and water exiting from the Fram Strait leads to a major export of freshwater from the Arctic (Aagaard and Carmack, 1989; Karcher et al., 2005; Tsukernik et al., 2010; Dickson et al., 2007). Fram Strait ice export increased between 2004-2008, with a 37 % increase in winter 2007 - 2008 (Smedsrud et al., 2008). The long term mean sea ice flux through the Fram Strait is around half the long term mean fresh water flux (Meredith et al., 2001). Large export of freshwater and sea ice leads to increased salinity of upper ocean and development of mixed layer in the Arctic Ocean, suppressing sea-ice growth in the following winter; meanwhile the North Atlantic becomes less saline (Inoue and Kikuchi, 2007; Bethke et al., 2006; Komuro and Hasumi, 2007). Events of 'sea ice flush out', where there is an increase in transport of sea ice from the Arctic through the Fram Strait, such as experienced in 2005, are predicted to rise in the future (Inoue and Kikuchi, 2007). Salinity anomalies such as that in the Labrador Sea in the beginning of the 1970s may be due to large positive anomalies in the ice export through the Fram Strait (Koenigk et al., 2006; Belkin et al., 1998).

Upper ocean salinity in the region between the North Pole and Fram Strait is observed to be appreciably less there in summer 2010 compared to no significant change in ocean freshwater flux through the Strait between 1998 and 2008 (from a decade long record of mooring measurements) (Timmermans et al., 2011). The most likely cause of the freshening appears to be a redistribution of fresh water within the Arctic Ocean forced by changes in the prevailing wind field that allowed fresh surface water to escape the Beaufort Gyre and penetrate the Eurasian Basin (Timmermans et al., 2011). The extent to which the anomalously fresh surface waters observed along the Greenwich meridian in 2010 and close to the north coast of Greenland in 2009 and 2010 contributed to enhanced freshwater fluxes at Fram Strait is not known (Timmermans et al., 2011). Model results (to 2050) predict that export of freshwater to lower latitudes through the Fram Strait will increase, but the magnitude of these increases varied from model to model (Holland et al., 2007).

6.6 Recent changes in Arctic sea ice extent and their relationship to ice export through the Fram Strait

The Arctic climate system has undergone rapid change in recent years (Serreze and Francis, 2006; Comiso, 2006; Perovich and Richter-Menge, 2009; Serreze et al., 2007; Giles et al., 2008). Sea ice extent reached a record minimum in 2007 (Perovich et al., 2008; Drobot et al., 2008; Comiso et al., 2008; Kwok and Rothrock, 2009). There has been much debate over whether changes in Arctic sea ice extent over the past decade were due to the ice thinning or to ice movement and export.

A multitude of sources corroborate that Arctic sea ice has thinned or decreased in extent in recent decades (Johannessen et al., 1999; Comiso, 2002; Kwok and Rothrock, 2009; Comiso and Nishio, 2008; Giles et al., 2008; Francis and Hunter, 2007; Comiso et al., 2008; Perovich et al., 2008). Kwok and Rothrock (2009) cite a 1.75m decrease in average thickness since 1980, while Giles et al. (2008) present evidence that average winter sea ice thickness following the record low extent in 2007 was 0.26 m thinner than the 2002-03 to 2007-08 average.Estimations of the rate of decline between 1978 and1996 range from 2.2 to 3.4 % per decade (Comiso et al., 2008; Francis and Hunter, 2007; Johannessen et al., 1999; Comiso and Nishio, 2008) to 9% per decade (Comiso, 2002). More recently ice cover in the Arctic Ocean has decreased at a rate of 10.1 -10.7% per decade in the past 10 years (Comiso et al., 2008; Francis and Hunter, 2007). Associated with this loss of extent is a change in the composition of the ice, with (for example) a 14 % reduction in area of multiyear ice in winter since 1978 (Johannessen et al., 1999), that brings with it a decrease in ice thickness. The significant decrease in the extent of Arctic sea ice at the end of summer is coupled with decrease in the amount of perennial sea ice making the ice cover more susceptible to changes in atmospheric and ocean forcing (Perovich and Richter-Menge, 2009).

The thickness of the ice in the Fram Strait has also decreased. There was an overall decrease of 0.45 m in ice thickness in the Fram Strait over the period 1991-1998 with a decrease of 0.23 m over the winter months between December and March (Vinje, 2001). Correspondingly, the mode of the multi-year ice thickness exhibits an overall decrease of 0.55 m and a winter decrease of 0.42 m. This is a lower rate of decrease than that in the Arctic Ocean quoted above.

Atmospheric circulation may be driving sea ice decline (Deser and Teng, 2008). There is large inter-annual variability in ice drift and concentration (Spreen et al., 2006; Kwok and Rothrock, 1999; Lukovich and Barber, 2007). Decadal shifts in variability can be linked to North Atlantic Oscillation (NAO) (Serreze et al., 2007; Koenigk et al., 2006; Deser and Teng, 2008; Bluthgen et al., 2012). A positive NAO results in a more cyclonic motion of ice in the Arctic due to altered surface winds (Serreze et al., 2007; Koenigk et al., 2006; Deser and Teng, 2008). This results in ice compression towards the western Arctic, ice loading into the Transpolar Drift, together with an acceleration of the Transpolar Drift carrying excessive ice out of the Fram Strait (Nghiem et al., 2007; Deser and Teng, 2008). Modelling different scenarios confirms that without the NAO forcing recent changes in ice extent would be smaller than observed (Serreze et al., 2007). Anomalous cyclonic wind circulation associated with the upward trend in winter NAO flushes old thick ice out of the Arctic via the Fram Strait, causing the winter pack ice to thin which in turn pre-conditions the summer ice pack for enhanced melt (Deser and Teng, 2008; Rigor and Wallace, 2004).

When the winter Arctic Oscillation (AO) is in its positive mode, sea level pressure over the Icelandic Low region and extending into the Arctic is anomalously low and the Beaufort Sea High is weak, promoting a cyclonic (anticlockwise) sea ice circulation anomaly in the Beaufort Sea. This is expressed as decreased ice transport from the west to the eastern Arctic, increased ice transport out of the Arctic Ocean through Fram Strait, and increased transport of ice away from the Siberian coast, leaving open water areas that foster new ice formation (Rigor et al., 2002). By promoting more thin ice in spring, the positive AO sets the stage for negative summer

ice extent anomalies. Conversely, during a negative AO phase, sea level pressure is above normal over the Arctic, most prominently in the vicinity of the Icelandic Low. Ice motion tends to have an anticyclonic (clockwise) anomaly therefore the Beaufort Gyre is stronger, leading to enhanced ice transport (Koenigk et al., 2006) from the western to the eastern Arctic where ice thickens by ridging and rafting against the Siberian coast. The stronger Beaufort Gyre also sequesters and thickens ice in the Canada Basin. Collectively, these processes favor survival of sea ice through summer (Rigor et al., 2002; Stroeve et al., 2011; Morison et al., 2012).

In recent years the correlation between summer AO index and sea ice extent observed above has become weaker than it was, for example during summer 2002 and 2003 the summer AO was in a high-index phase, which favors above normal ice concentrations along the Alaskan coast, and yet record minima were observed during both years (Rigor and Wallace, 2004).

Ekman drift during the summer plays an important role in regulating annual minimum Arctic sea ice extent (Comiso and Nishio, 2008). Ogi et al. (2008) link the 2007 low to strong poleward drift over the western Arctic induced by anomalously high sea level pressure over the Beaufort Sea persisting throughout much of the summer, and associated summer winds, in combination with pre-conditioning by events of previous years. Ogi and Wallace (2007) agree that years with low sea ice extent are characterized by anticyclonic circulation anomalies over the Arctic with easterly wind anomalies over the marginal seas where the year-to-year variability of sea ice concentration is largest. Summer circulation anomalies cause changes in sea ice extent primarily by way of Ekman drift in the marginal seas. Ice export is a stronger driver of thinning in the Arctic Ocean than ocean heat fluxes (Smedsrud et al., 2008; Holloway and Sou, 2002).

Reduced cloudiness and enhanced downwelling radiation are also associated with the 2007 record low sea ice extent by Kay et al. (2008), although Schweiger et al. (2008) disagree that sunny skies were the defining factor. Perovich et al. (2008) suggest that ice is thinning due to melt being driven by solar heating of the upper

ocean in the Beaufort Sea. This is a classic ice albedo feedback: melting ice allows more heating of the upper ocean, which melts more ice (Perovich et al., 2008). Winter ice extent is of particular interest as a strong indicator of this ice-albedo feedback.

These recent changes mean that the oldest ice types have effectively disappeared from the Arctic. This much reduced extent of thicker ice, coupled with ice albedo feedbacks, leaves the Arctic vulnerable to further loss of ice extent (Maslanik et al., 2007). Future changes in Arctic sea ice cover and consequent changes in ice-albedo feedback represent one of the largest uncertainties in the prediction of future temperature rise (Laxon et al., 2003; Perovich and Richter-Menge, 2009). In some model scenarios the Arctic is ice free in late summer by the end of the century (Gregory et al., 2002; Smedsrud et al., 2008) or even earlier. Ice export through the Fram Strait has been shown to be an important component of these changes in ice extent.

The following chapter expands the case study introduced in Section 4.2, comparing the ice movement vectors generated using ITSARI with data on surface ocean currents and surface wind strength and direction in the Fram Strait area, to gain an insight into the forces driving Fram Strait ice export. Chapter 8 continues the theme of comparing ice movement with surface ocean and wind for late summer images on a one or two day temporal resolution.

Chapter 7

Ice Movement in the Fram Strait

7.1 Introduction

In this chapter we take a more detailed look at the movement vectors produced from the analysis of a series of images acquired over the course of the year 2008. This study was introduced in Chapter 4. As noted in Chapter 4 the temporal resolution in this study is coarse, and images are acquired from three to ten days apart. The ice movement is compared to oceanographic and atmospheric forcing factors in the hope of gaining an insight into what drives Fram Strait ice export.

For each month of the year a map has been produced showing all the tracks generated from image pairings within that month. On each map the location of each image acquired that month is shown with a dotted line, with the exception of the map for February, where there were more images than any other month so including the image location outlines made things crowded. Where it was possible to identify the sea ice edge and/or the fast ice edge in the image (using the ITSARI algorithm), these are marked with a dashed line in the same colour as the outline of the image on which they were identified (or as identified in the legend for February). For simplicity, date and corresponding colour for both sea ice edge and image location

outline is listed only once in the key. The movement vectors are grouped by image pairing, and denoted as such in each key. To support the analysis of these results other figures compare the movement vectors to surface level ocean currents from the SODA reanalysis data set available at http://soda.tamu.edu/data.htm (Carton and Giese, 2008); and to wind speed and direction from NCEP/NCAR reanalysis data provided by the NOAA/ESRL Physical Sciences Division, Boulder Colorado, from their web site at http://www.esrl.noaa.gov/psd/data/composites/day/ (Kalney, 1996). Surface air pressure charts from the UK Met Office achieved at www.wetterzentrale.de/topkarten/fsfaxbra.html are also used to support analysis of the meteorological conditions. There are three months (April, June and November) where drift buoy data from the International Arctic Buoy Programme (available at http://iabp.apl.washington.edu/) exists for the Fram Strait. In these cases the drift buoy tracks have been included with the surface ocean data from SODA reanalysis.

SODA stands for 'Simple Ocean Data Assimilation' reanalysis of ocean climate variability. The observation set is as complete as possible and includes the historical archive of hydrographic profiles supplemented by ship intake measurements, moored hydrographic observations, and remotely sensed SST and sea level (Carton and Giese, 2008). The forecast model utilizes Parallel Ocean Program physics with an average 0.25°x0.4°x40-level resolution. A sequential assimilation algorithm is used with a 10-day updating cycle (Carton and Giese, 2008). The reanalysis and associated experiments are available online in monthly-averaged form, mapped onto a uniform 0.5°x0.5°x40-level grid. The surface ocean currents used here are the 5m vertical level from the SODA reanalysis product

7.2 January

In January, five image pairings yield movement vectors (Figure 7.1). The fast ice edge is located around 10 °W and ice extent around 4 °E. Movement of the objects identified is consistently towards the south, with speeds greater towards the centre of

the strait than adjacent to the fast ice edge in the west. On the 11th January there is a zone of high pressure extending from the east coast of Greenland into the western Fram Strait. By the 14th January this begins to give way to low pressure, which remains for the rest of the month. (Figure 7.2). The wind vectors from reanalysis data show constant northerlies of varying strengths (Figure 7.3). In January the ice movement vectors for all time steps appear to be mainly wind driven, ice movement is either aligned with surface wind or deviating to the right of surface wind due to Coriolis force. Speeds are greater towards the centre of the strait than adjacent to the fast ice edge. Figure 7.4 shows the SODA surface ocean. The East Greenland current is clearly apparent in the centre of the strait between -6° and -2°longitude, with less strong flow closer to the Greenland coast. The direction of movement of the ice objects is consistent with the southward movement of the East Greenland Current, modified by the winds. The main thrust of the East Greenland current is further east than the area where most ice movement vectors were generated. It is possible that this is due to ice moving too rapidly in the main current to be easily tracked at this temporal resolution.

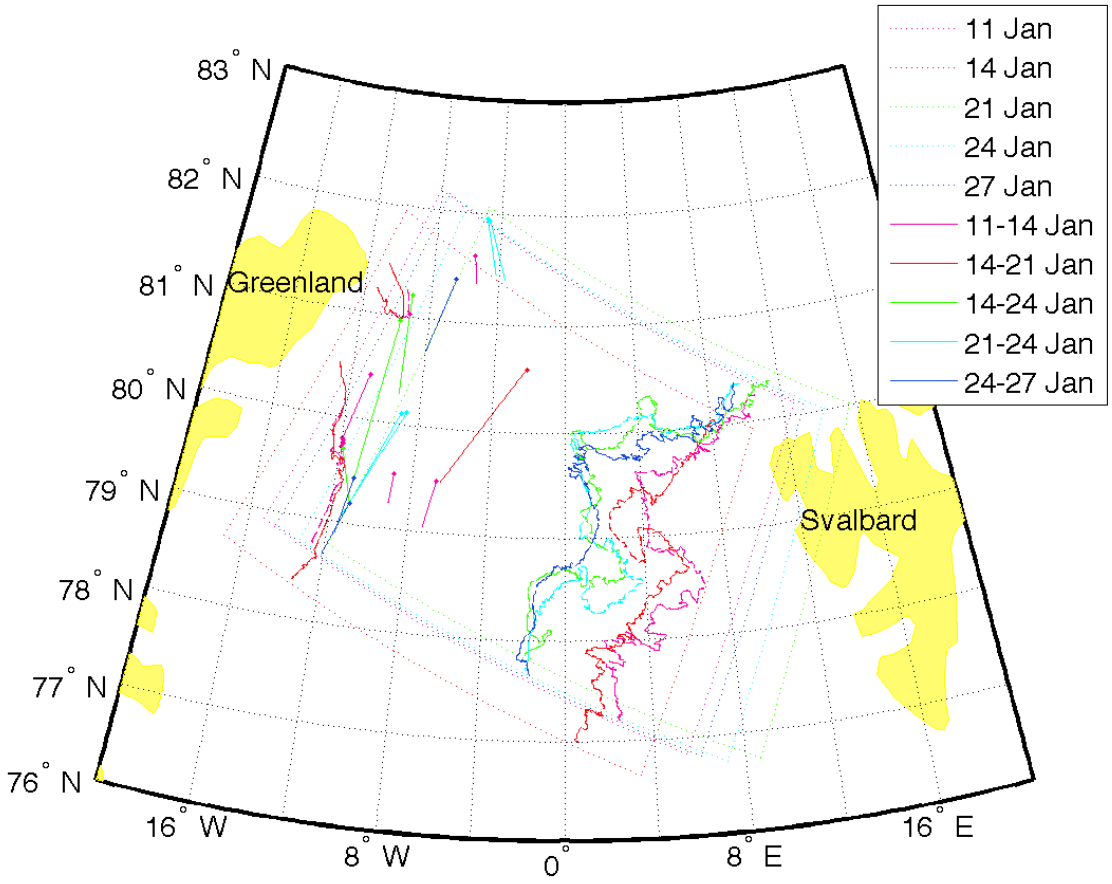

Figure 7.1: Movement of ice objects identified and tracked in images from January 2008. Note fast ice edge around 10 °W and ice extent around 4 °E. Movement is consistent towards the south, with speeds greater towards the centre of the strait than adjacent to the fast ice edge.

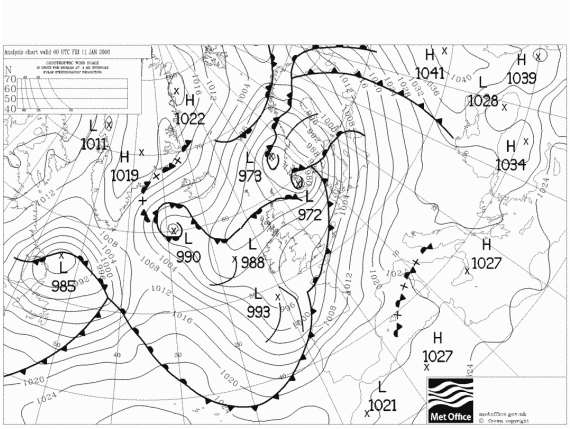

(a) 11January

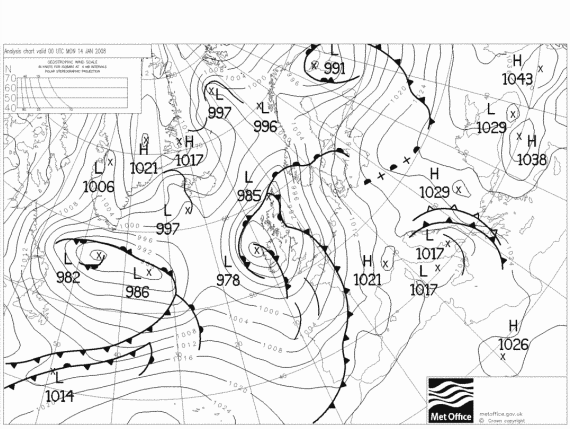

(b) 14 January

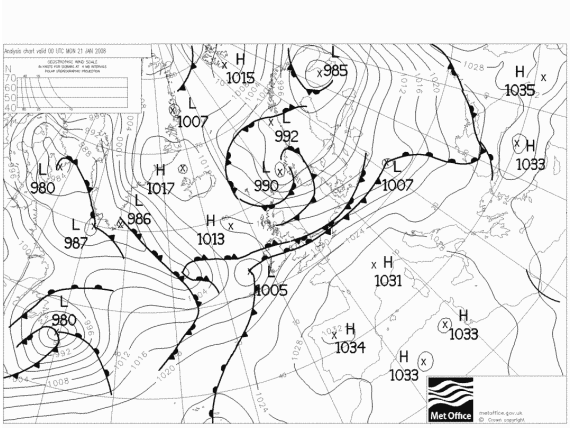

(c) 21 January

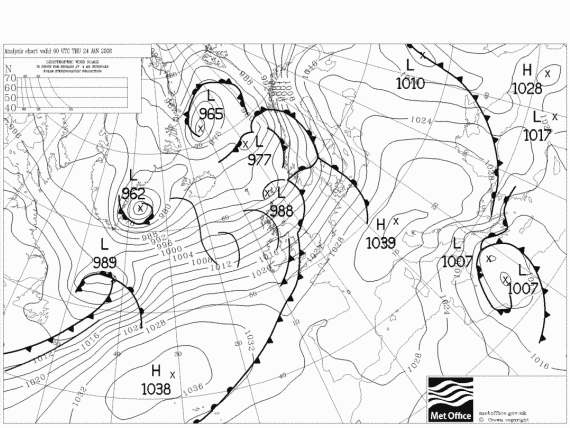

(d) 24 January

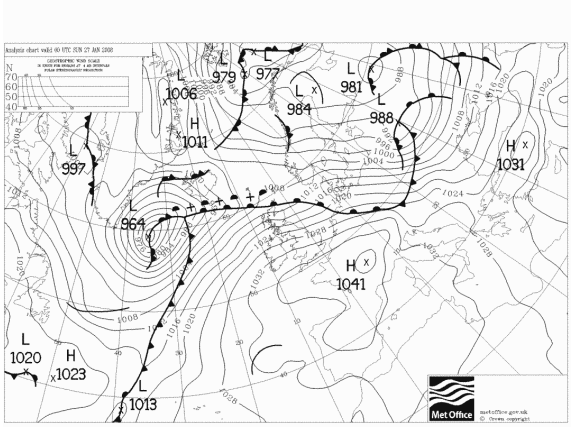

(e) 27 January

Figure 7.2: Surface air pressure in January 2008. On the 11$^{\text{th}}$ January (a) there is a zone of high pressure extending from the east coast of Greenland into the western Fram Strait. by the 14$^{\text{th}}$ January (b) this is giving way to low pressure, which remains for the rest of the month. From UK Met Office data available at www.wetterzentrale.com.

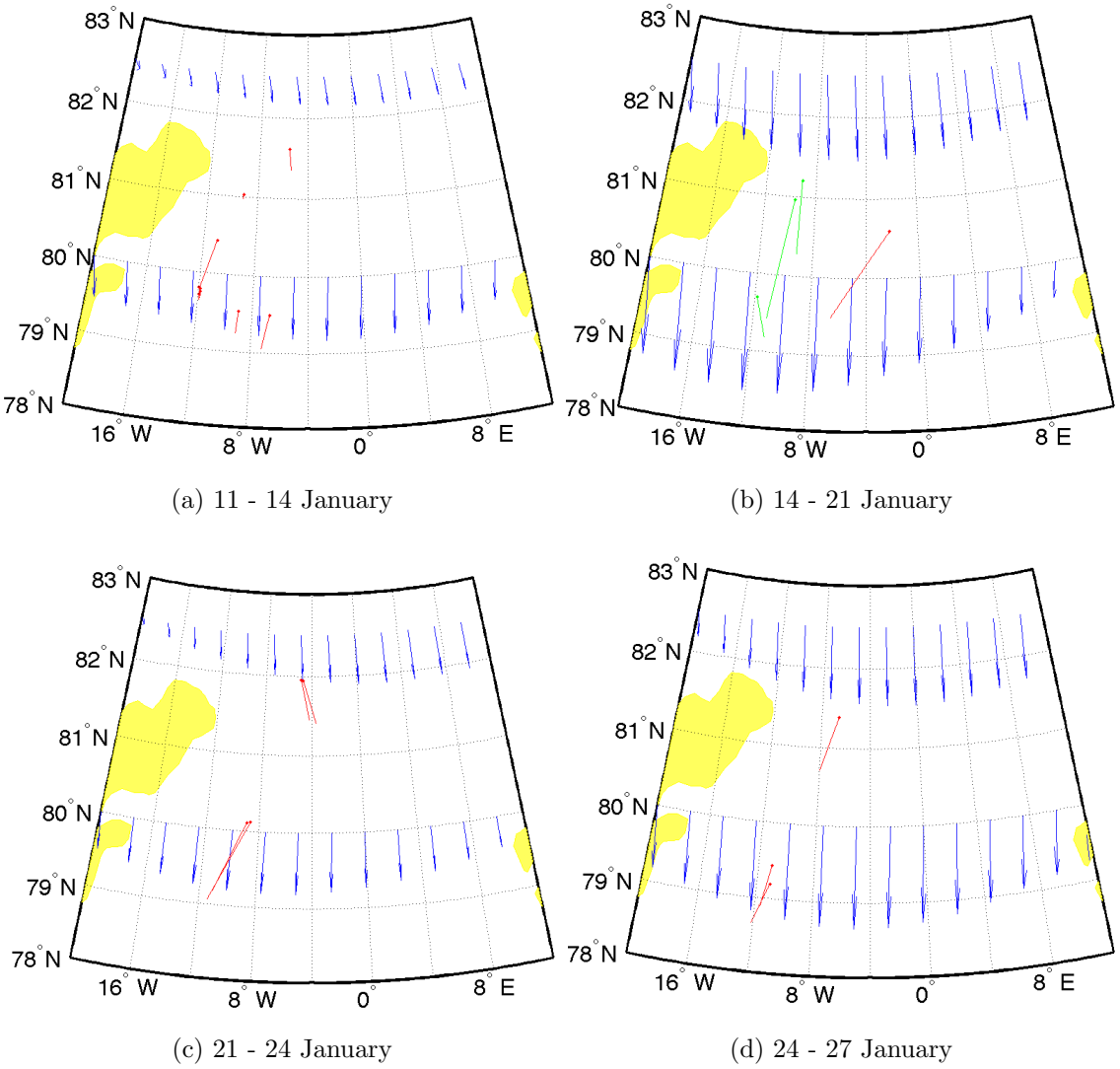

(a) 11 - 14 January

(b) 14 - 21 January

(c) 21 - 24 January

(d) 24 - 27 January

Figure 7.3: Comparison of movement vectors generated using ITSARI with surface wind vectors from reanalysis, January 2008. The wind was the main driving force this month, with movement vectors in line with surface wind or deviating to the right of surface wind due to Coriolis force.

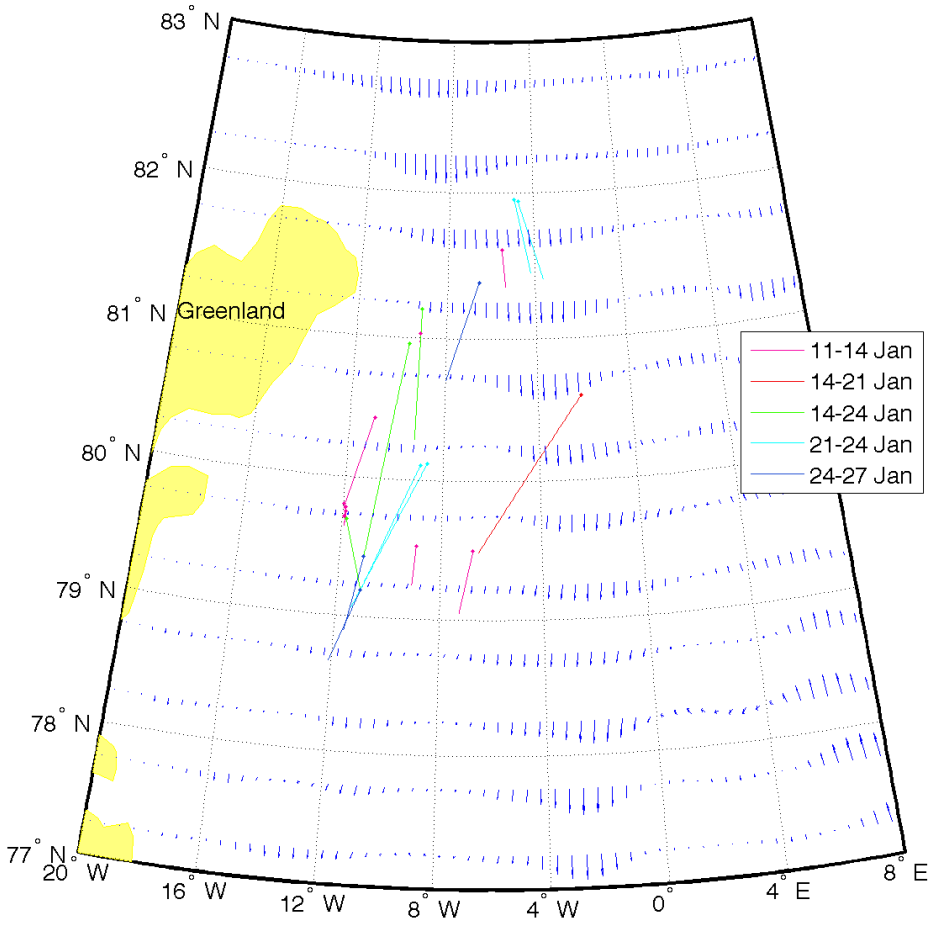

Figure 7.4: Ice movement vectors for the month of January compared to ocean reanalysis surface movement vectors from SODA reanalysis data. The East Greenland current is clearly apparent in the centre of the strait between -6 and -2 longitude, with less strong flow closer to the Greenland coast. Speeds are greater towards the centre of the strait than adjacent to the fast ice edge.

7.3 February

In February a larger number of images than any other month, on a shorter temporal resolution, have been processed because this month was used for the first case study (see Section 4.1) (Figure 7.5, see also the figures in section 4.1). Seventeen image pairings yield movement vectors. At the beginning of the month high pressure over Greenland and low pressure over the Norwegian side of the Fram Strait (Figure 7.6) result in the isobars being aligned north - south in the Strait, promoting northerly winds (Figure 7.9). Between the 2nd and 8th February high pressure moves out into the Strait; the resulting southerly winds can be seen in Figures 7.9. By the 11th February low pressure is again well established in the Strait and the strength of the wind suggests that a storm event is taking place. This has blown itself out by 13th February; more gentle northerlies persist until the next storm event between the 16th and 18th February. Another cyclone follows between the 20th and 26th February (Figure 7.8), its passage across the strait can be clearly seen in the wind vectors in Figures 7.10 and 7.11.

It is evident that when the wind is from the north the ice movement is more clearly towards the south than when the wind is in the opposite direction (Figures 7.9, 7.10 and 7.11), and that the passage of cyclones across the strait acts to speed up ice movement.

Differences in the ocean currents between January and February are very subtle (Figure 7.12), indeed over the course of the year the ocean currents do not change a great deal from month to month. Many of the ice movement vectors are well aligned with the ocean surface currents, perhaps because this has been a month characterised by strong winds driving both ice movement and ocean surface current. Movement is again quicker further out towards the centre of the Strait than close to the Greenland coast.

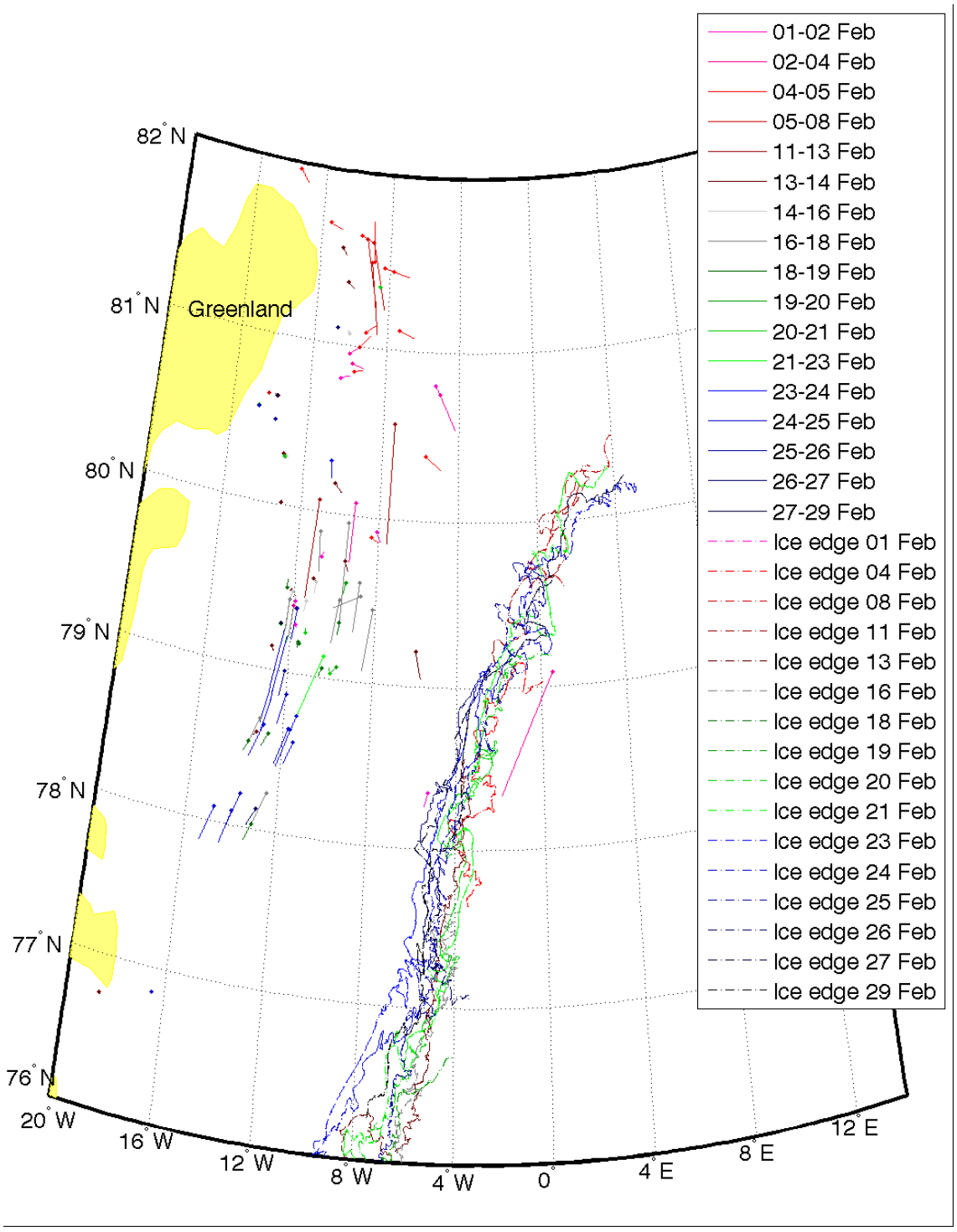

Figure 7.5: Ice movement in February 2008. The movement is quickest in the centre of the Strait. Ice adjacent to the fast ice edge is moving slowly.

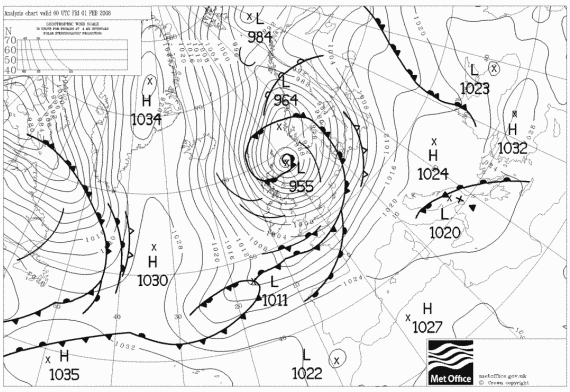

(a) 01 February

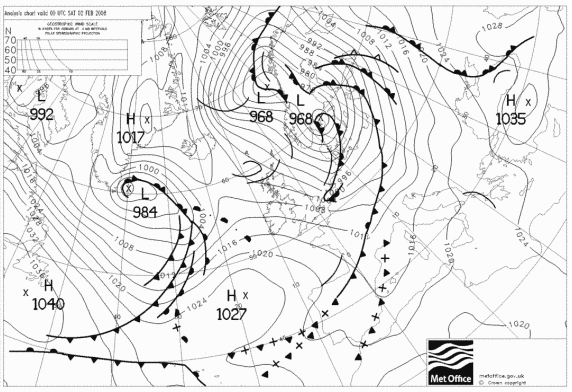

(b) 02 February

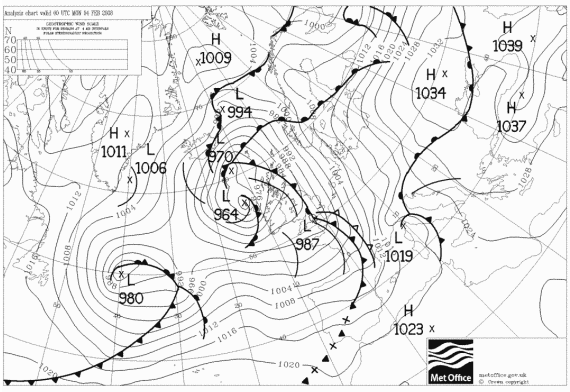

(c) 04 February

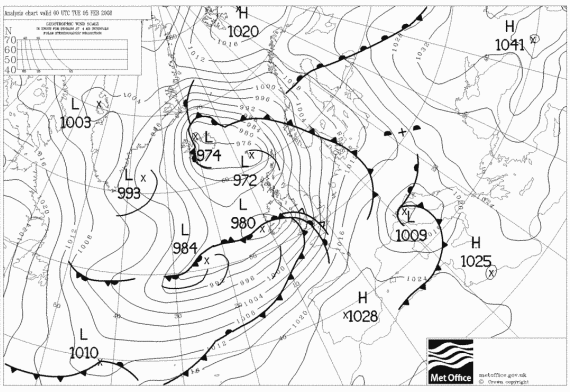

(d) 05 February

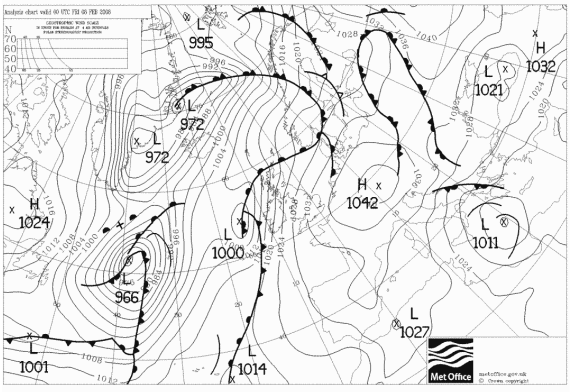

(e) 08 February

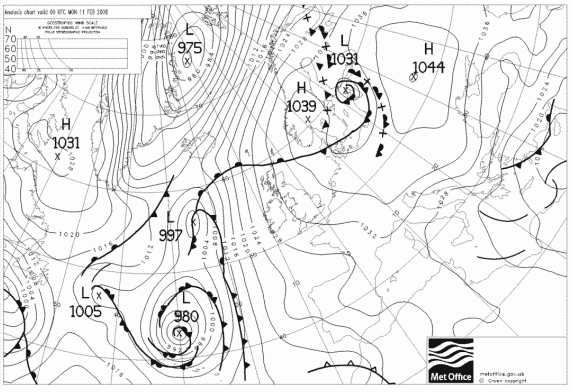

(f) 11 February

Figure 7.6: Surface air pressure between the 01st and 11th February 2008. From UK Met Office data available at www.wetterzentrale.com.

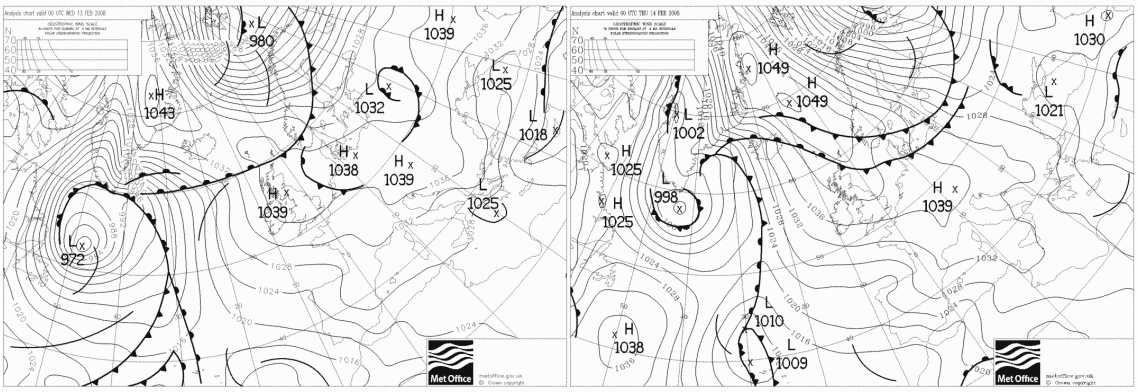

(a) 13 February (b) 14 February

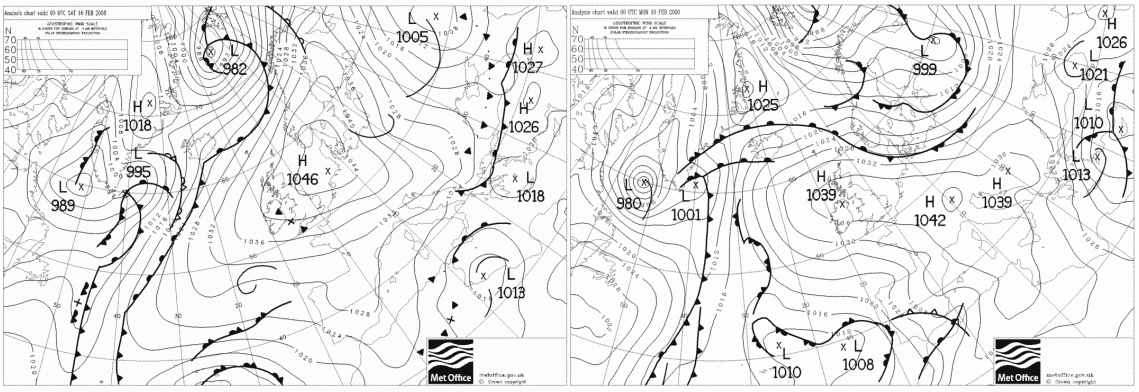

(c) 16 February (d) 18 February

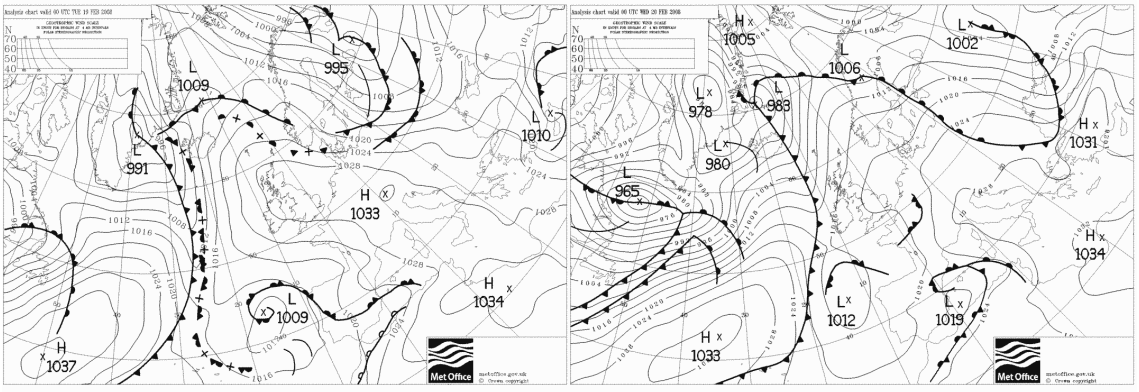

(e) 19 February (f) 20 February

Figure 7.7: Surface air pressure between the 13$^{\text{th}}$ and 20$^{\text{th}}$ February 2008. From UK Met Office data available at www.wetterzentrale.com.

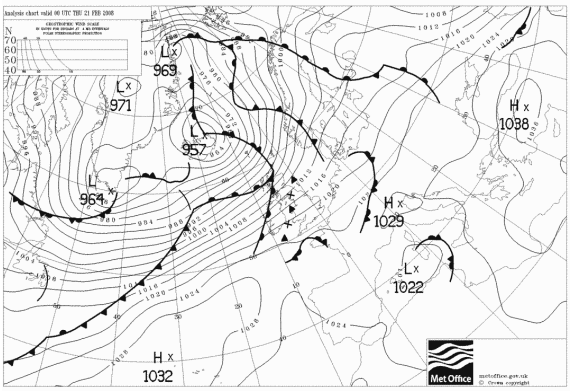

(a) 21 February

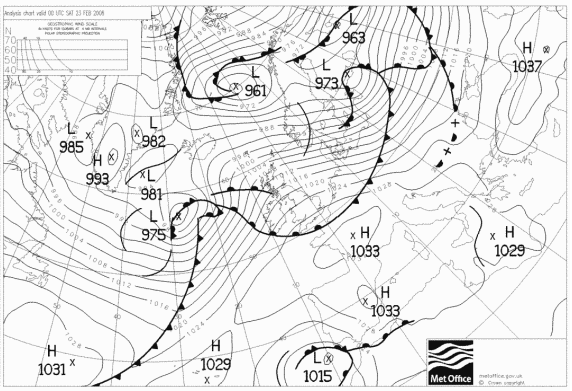

(b) 23 February

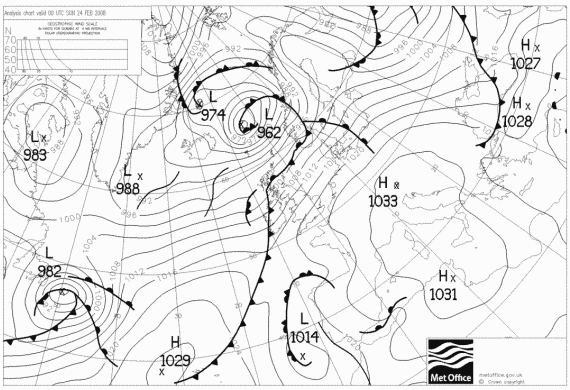

(c) 24 February

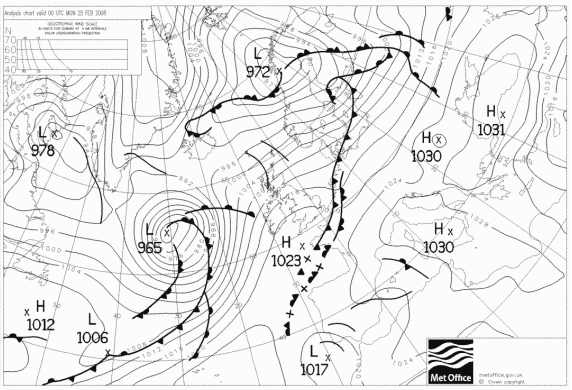

(d) 25 February

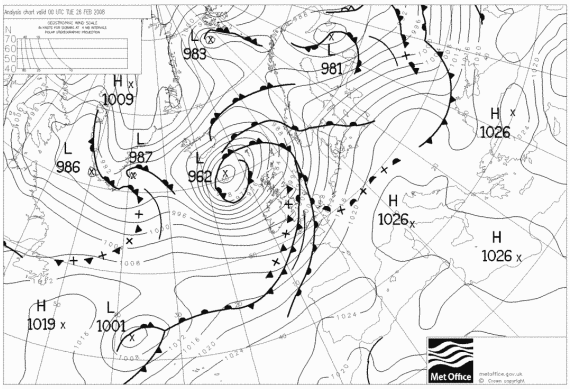

(e) 26 February

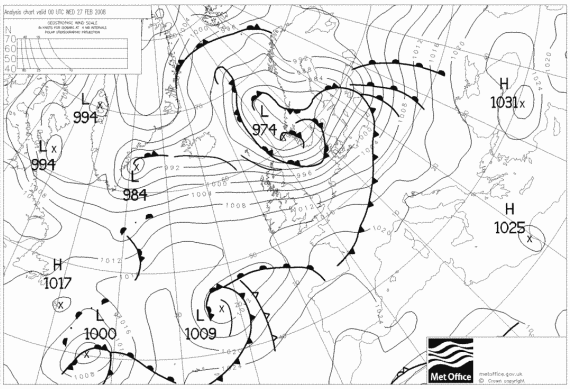

(f) 27 February

Figure 7.8: Surface air pressure between the 21st and 27th February 2008. From UK Met Office data available at www.wetterzentrale.com.

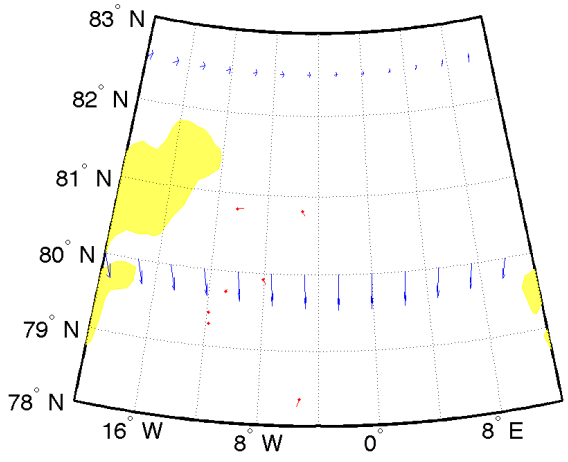

(a) 1 - 2 February

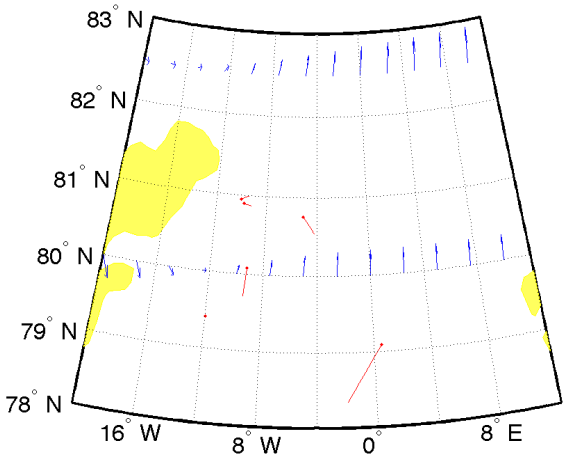

(b) 2 - 4 February

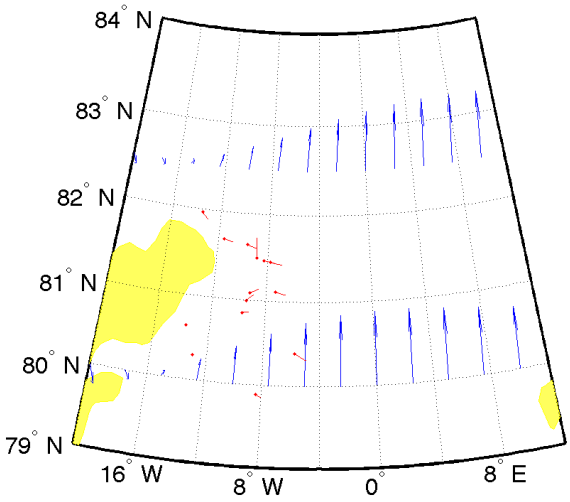

(c) 4 - 5 February

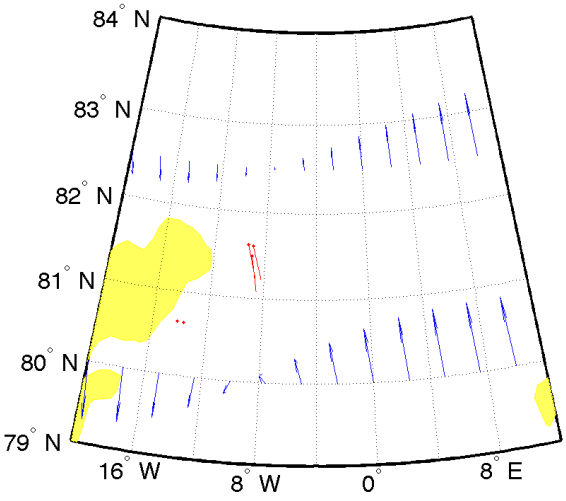

(d) 5 - 8 February

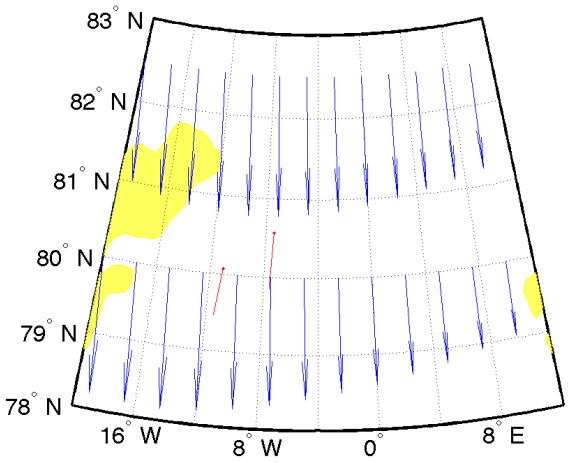

(e) 11 - 13 February

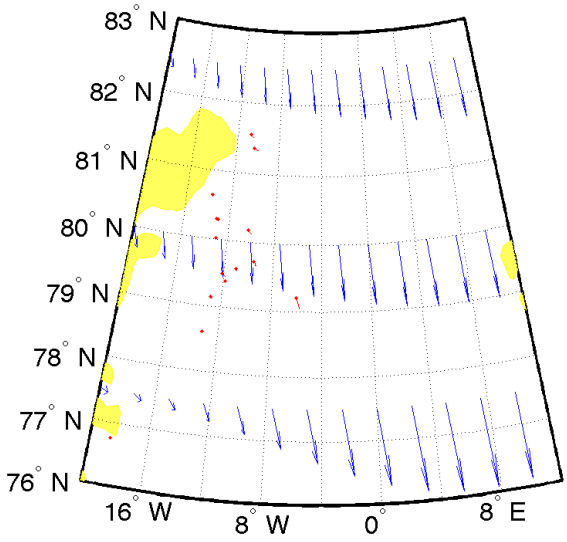

(f) 13 - 14 February

Figure 7.9: Comparison of movement vectors generated using ITSARI with surface wind vectors from reanalysis., 1st - 13th February 2008.

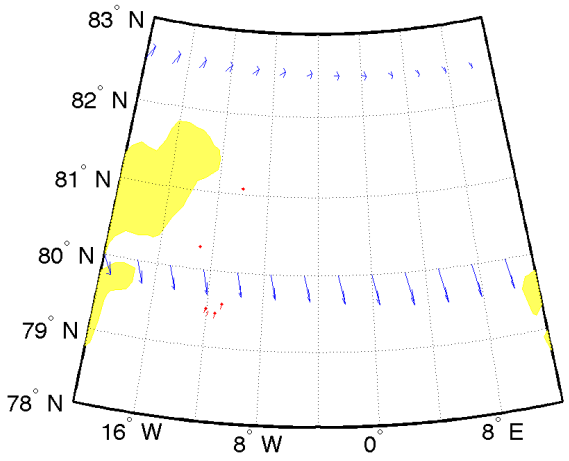

(a) 14 - 16 February

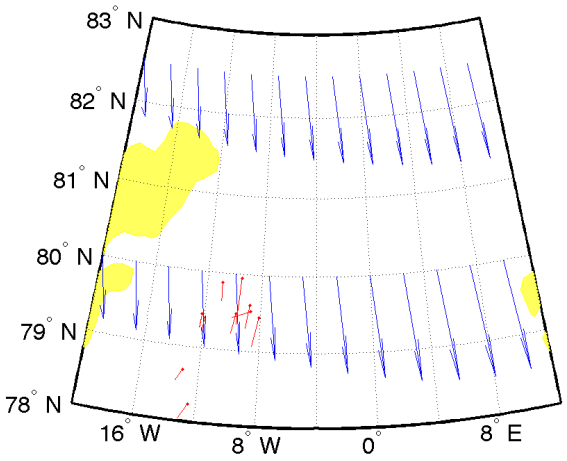

(b) 16 - 18 February

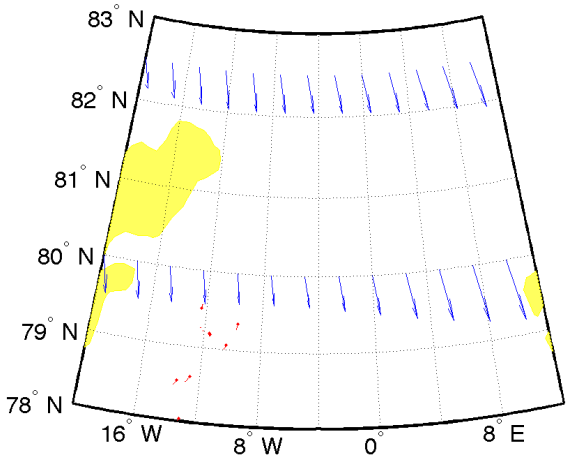

(c) 18 - 19 February

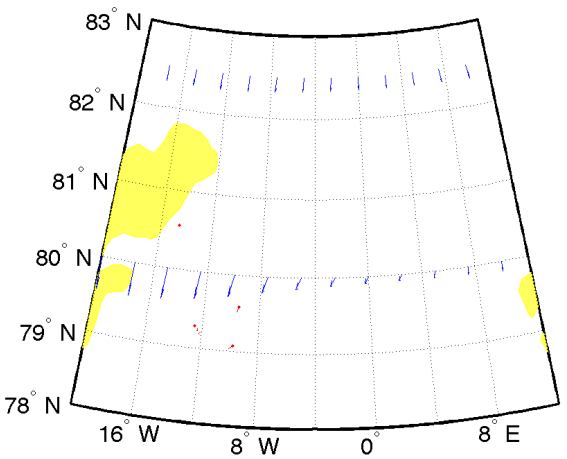

(d) 19 - 20 February

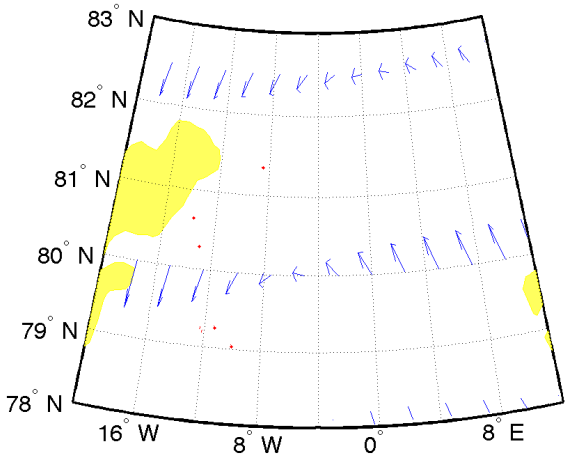

(e) 20 - 21 February

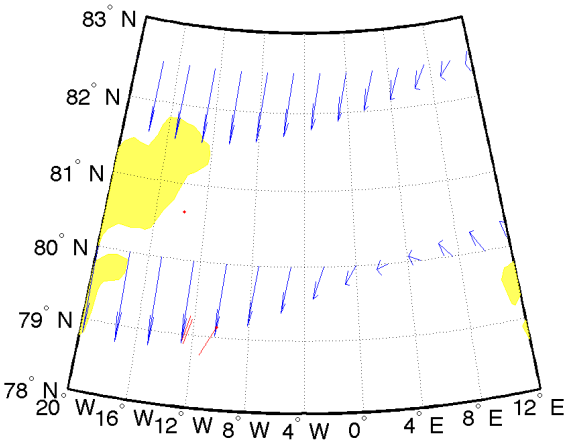

(f) 21 - 23 February

Figure 7.10: Comparison of movement vectors generated using ITSARI with surface wind vectors from reanalysis, 14th - 23rd February 2008.

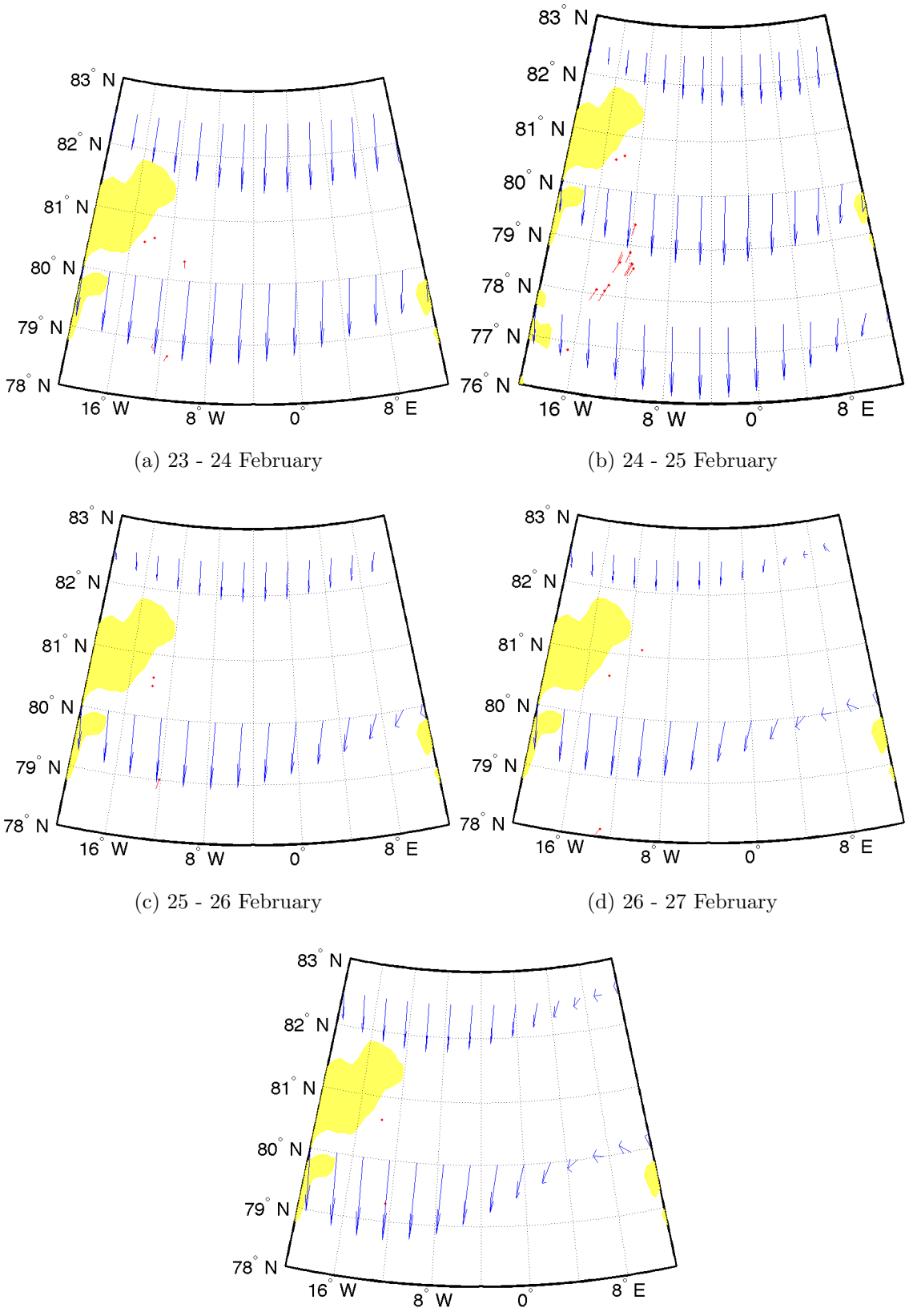

(a) 23 - 24 February

(b) 24 - 25 February

(c) 25 - 26 February

(d) 26 - 27 February

(e) 27 - 19 February

Figure 7.11: Comparison of movement vectors generated using ITSARI with surface wind vectors from reanalysis, 23rd - 29th February 2008.

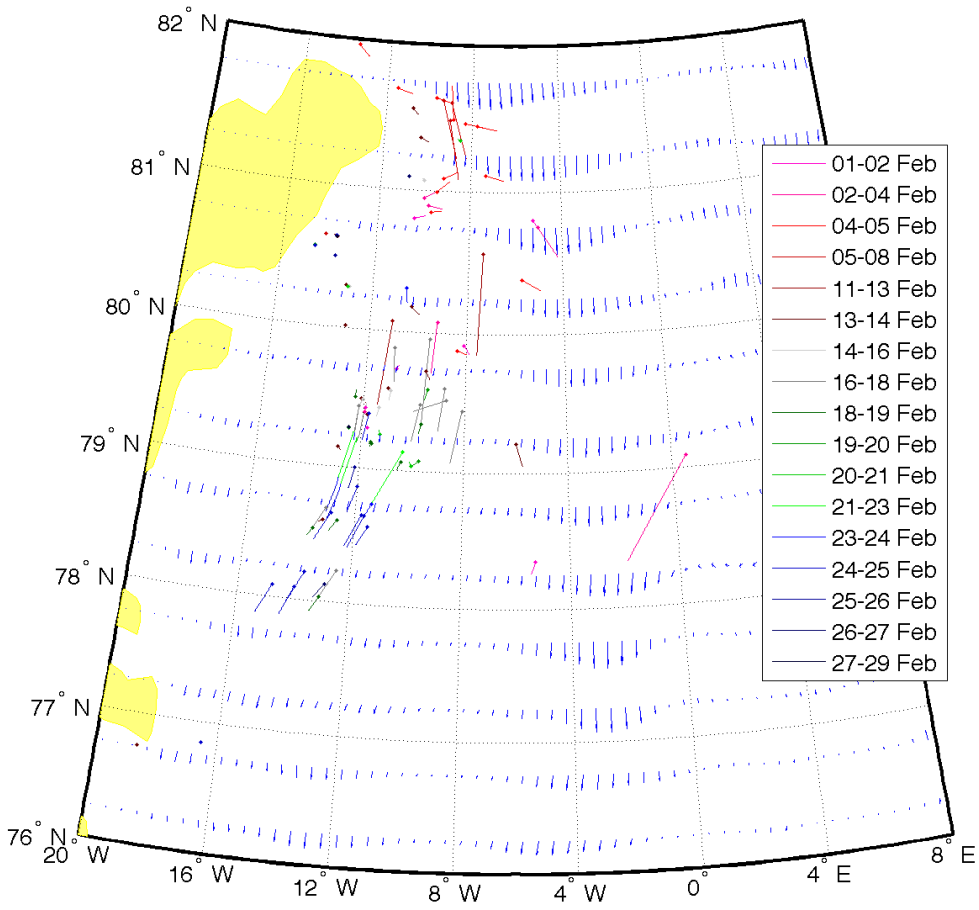

Figure 7.12: Ice movement vectors from the month of February compared to surface current data from SODA ocean reanalysis.

7.4 March

In March the vectors identified are sparse due to the nature of the ice (close pack with few easily identifiable objects) and coarse temporal resolution. Three image pairs yield ice movement vectors (Figure 7.13). At the beginning of the month low pressure is present in the Fram Strait with high pressure over the east coast of Greenland. (Figure 7.14). This high pressure moves out into the Strait on the 8th March, then moves away towards the south as low pressure re-establishes itself. The expected northerlies and north easterlies drive floe movement towards the south (Figure 7.15). In March the wind appears to be a stronger influence than the ocean. Those objects where ocean currents are weak appear to be solely wind driven, while objects in the stronger part of the EGC have all been wind deflected Figures 7.16

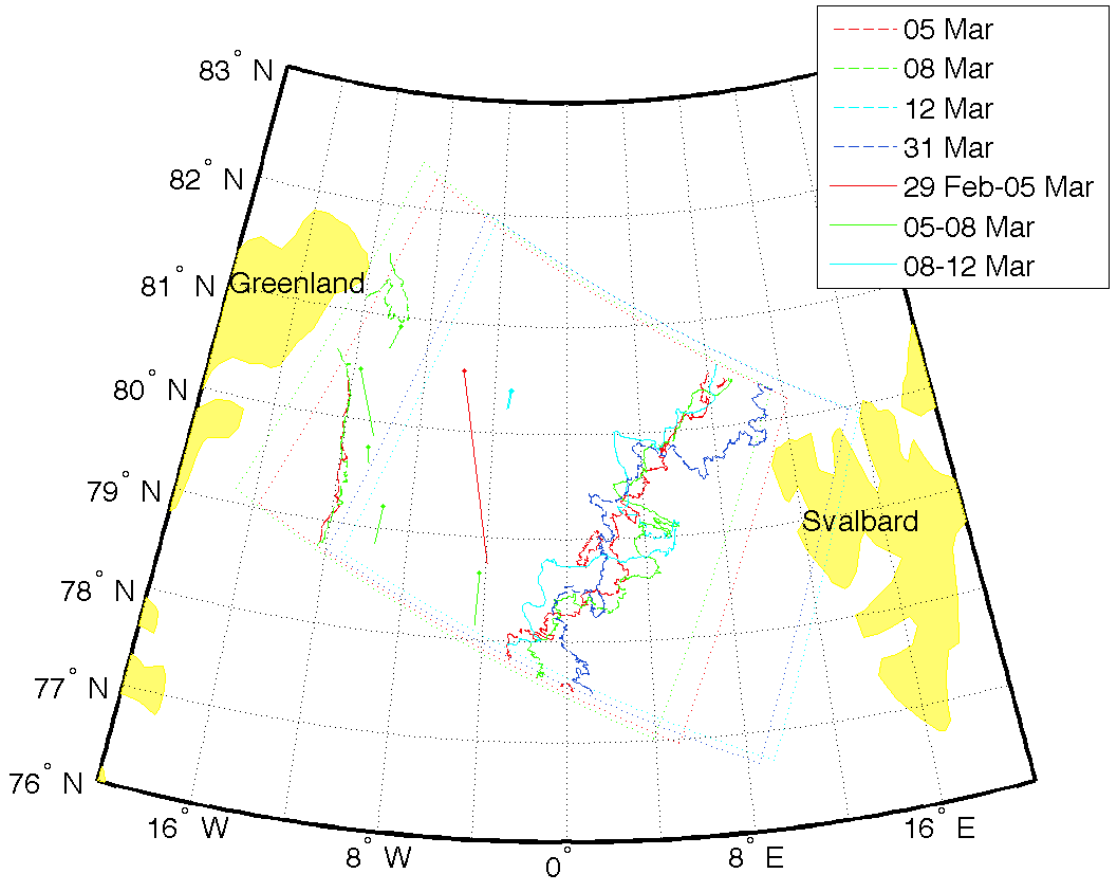

Figure 7.13: Movement of ice objects identified and tracked in images from March 2008. Objects identified and tracked are sparse due to the nature of the ice and the coarse temporal resolution of the images

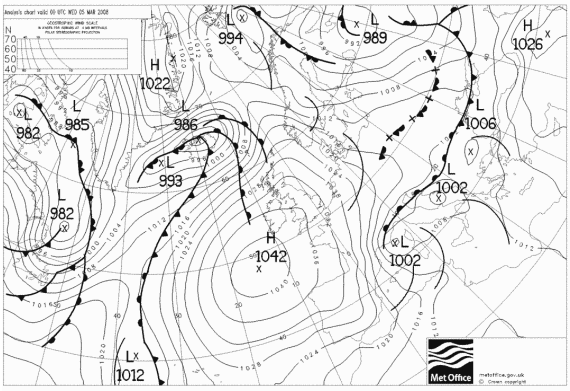

(a) 05 March

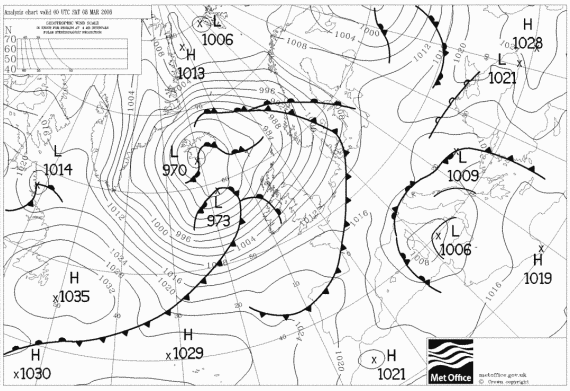

(b) 08 March

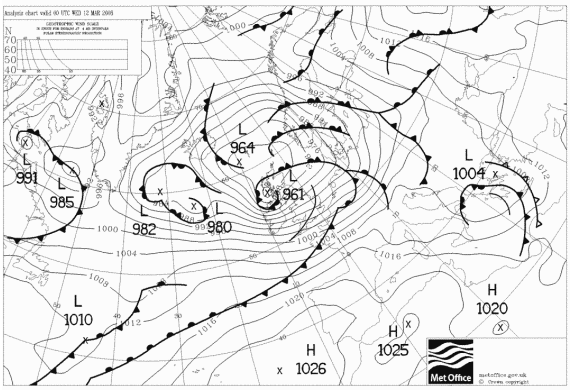

(c) 12 March

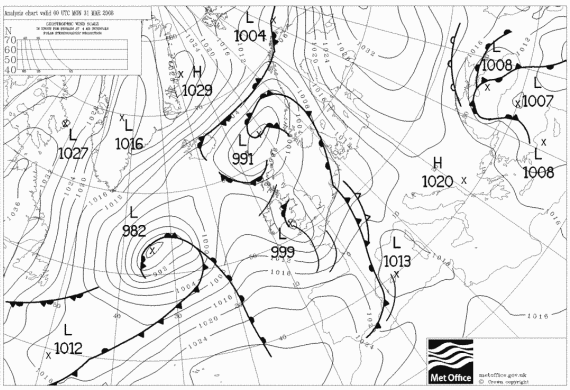

(d) 31 March

Figure 7.14: Surface air pressure in March 2008. At the beginning of the month low pressure is present in the Fram Strait with high pressure over the east coast of Greenland. This high pressure moves out into the Strait on 8th March, then moves away towards the south as low pressure re-establishes itself.From UK Met Office data available at www.wetterzentrale.com.

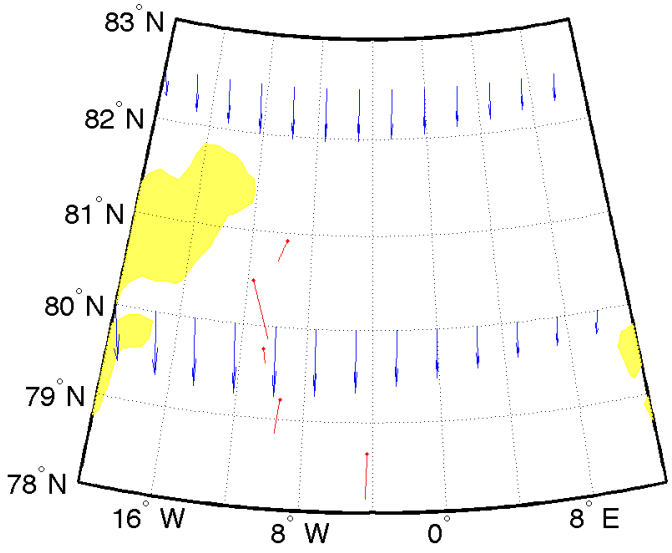

(a) 05 - 08 March

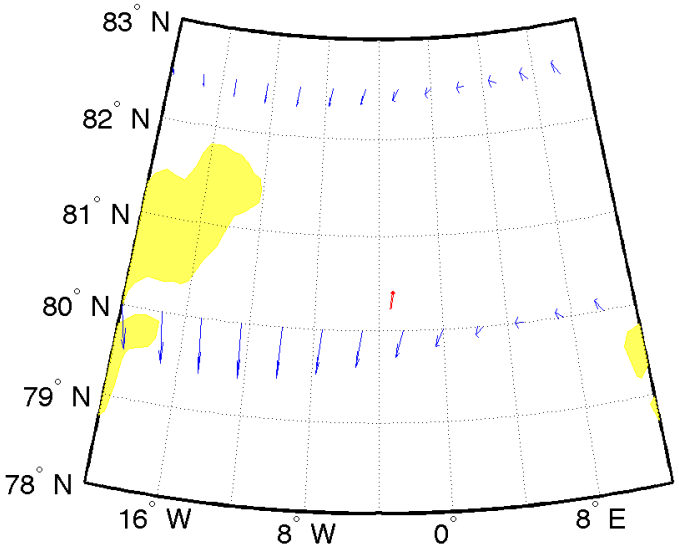

(b) 08 - 12 March

Figure 7.15: Comparison of movement vectors generated using ITSARI with surface wind vectors from reanalysis; March 2008. Those objects closer to the west where ocean currents are weak appear to be solely wind driven, while objects in the stronger part of the EGC (in the second time slot) have all been deflected by the north-easterly winds flowing around the low pressure zone is it moves away to the south east.

7.5 April

In April four image pairs generate ice movement vectors. Ice movement is again more rapid in the centre of the Fram Strait, that is towards the limit of ice extent, rather than adjacent to the fast-ice edge (Figure 7.17). This month is characterised

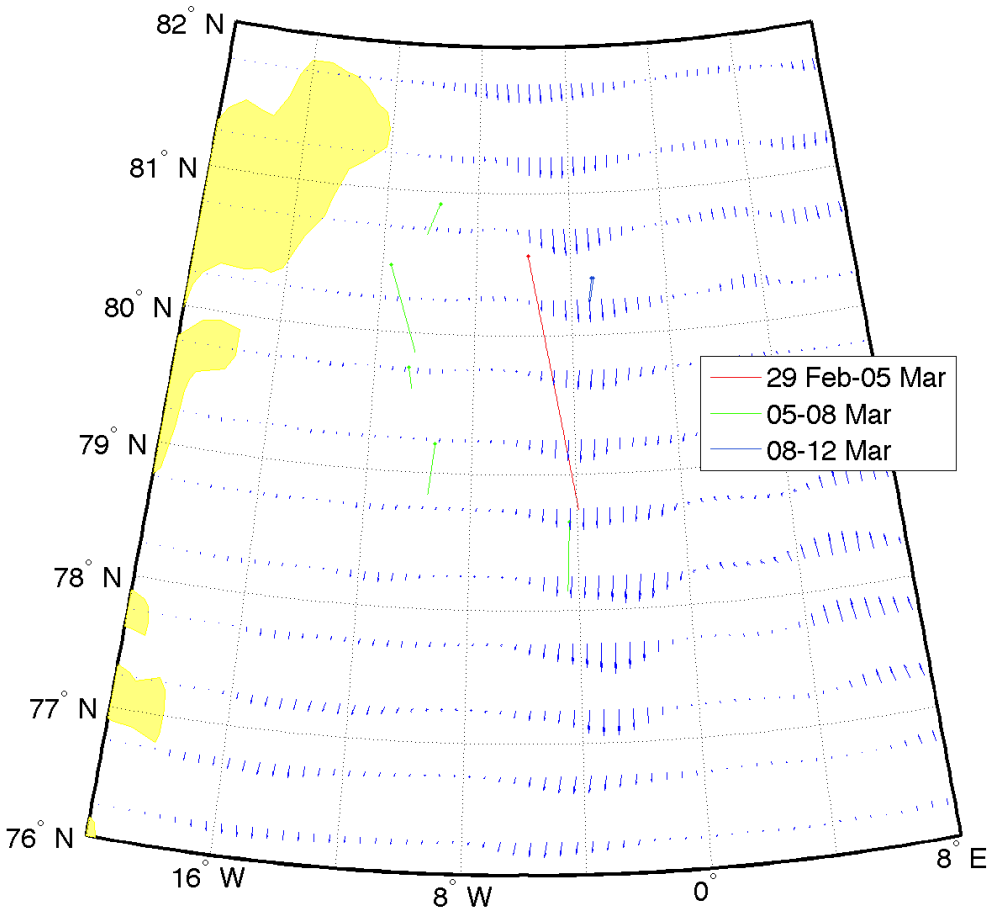

Figure 7.16: Ice movement vectors from the month of March compared to surface current data from the SODA reanalysis project. Those objects where ocean currents are weak appear to be solely wind driven, while objects in the stronger part of the EGC have all been deflected by the winds.

by unusually high pressure in the Strait, in particular between the 19th and 22nd April (Figure 7.18). Between the 9th and 19th April vectors are moving towards the north west which is consistent with southerly winds generated by high pressure to the east of the vectors location. These southerlies do not show up in the reanalysis surface wind data (Figure 7.19) but are suggested by the pressure charts. This set of vectors that are moving contrary to the wind are also moving contrary to the ocean currents, which in this area are weak (Figure 7.20). For all other vectors this month the wind appears to be the main driving factor, with deflection of vectors due to the Coriolis force rather than ocean currents. One drift buoy track is available in the appropriate area this month (Figure 7.20); the movement of the buoy is in general agreement with movement of the ice objects that have been tracked.

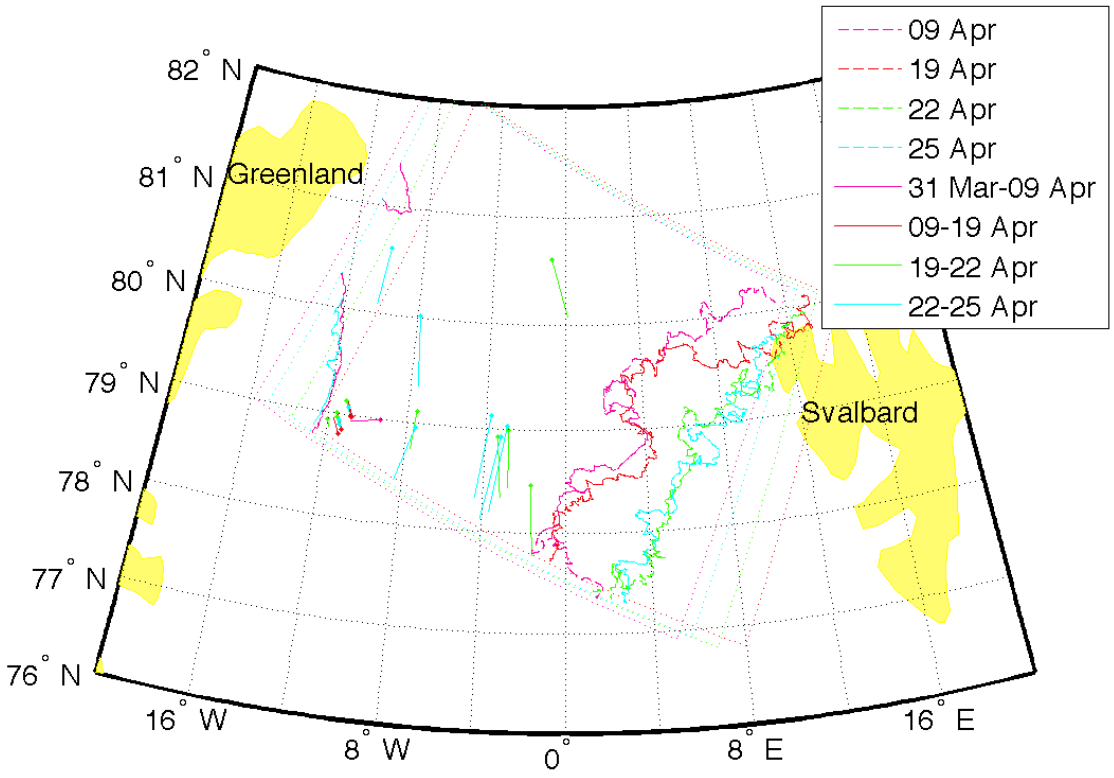

Figure 7.17: Movement of ice objects identified and tracked in images from April 2008.

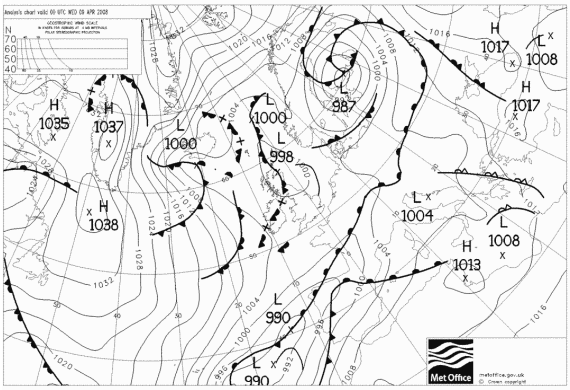

(a) 09 April

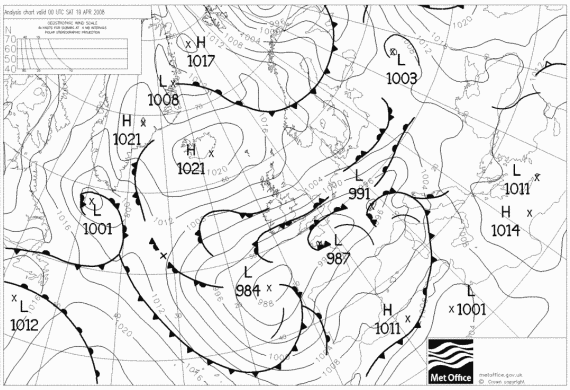

(b) 19 April

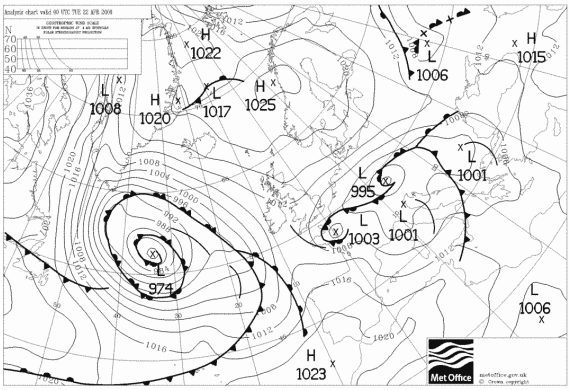

(c) 22 April

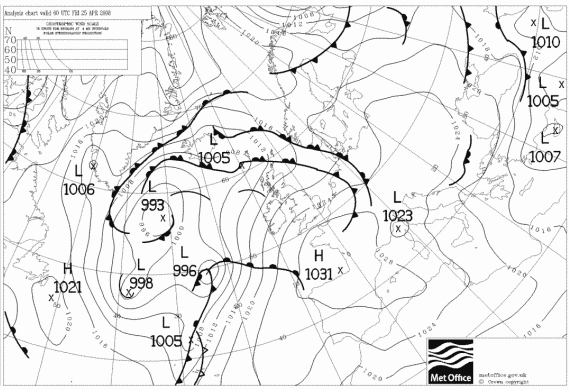

(d) 25 April

Figure 7.18: Surface air pressure in April 2008. From UK Met Office data available at www.wetterzentrale.com

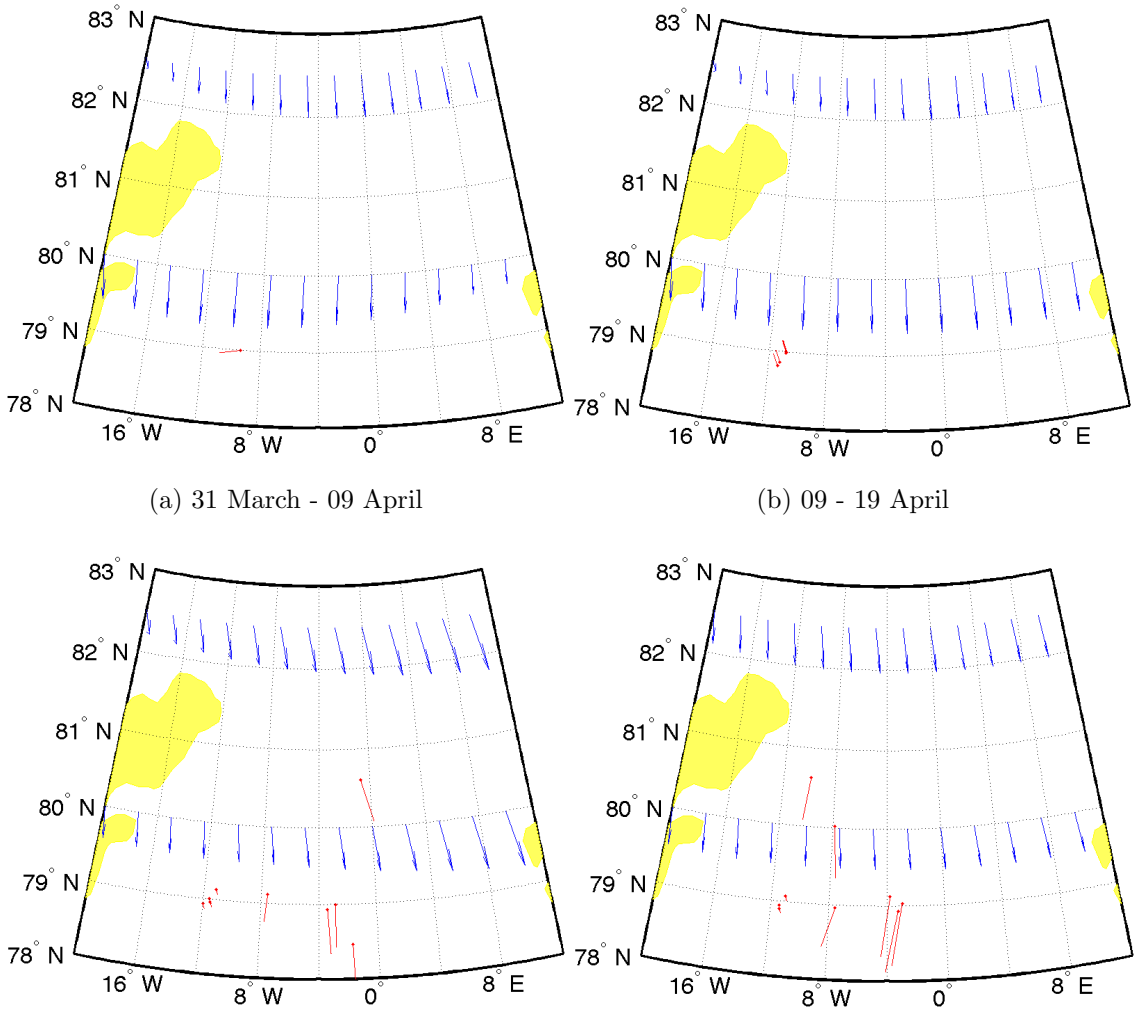

(a) 31 March - 09 April

(b) 09 - 19 April

(c) 19 - 22 April

(d) 22 - 25 April

Figure 7.19: Comparison of movement vectors generated using ITSARI with surface wind vectors from reanalysis, April 2008. Between the 9^{th}-19^{th} April ice movement is contrary to the driving force of the wind. This is most likely an artifact of the longer time period, wind direction and ice movement is expected to have varied within this time.

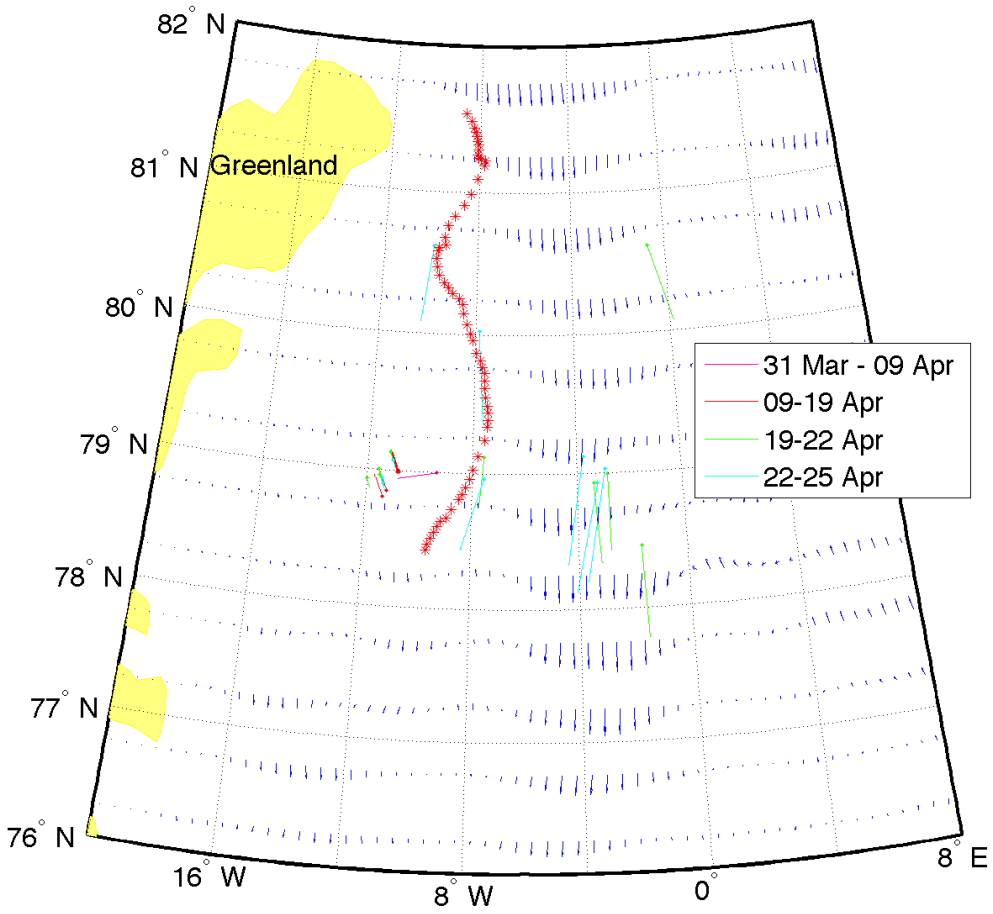

Figure 7.20: Comparison of vectors generated using ITSARI with surface ocean currents from SODA reanalysis data, April 2008. Three different regions can be identified, close to the fast ice edge ice movement is minimal, between -10 and -8°ice movement reaches higher speeds, currents are weak and appear to have little effect on ice movement, between -8 and 0°ice movement is obviously within the EGC but affected also by the wind and/ or Coriolis force. The red dots mark the track of a buoy from the Arctic buoy project.

7.6 May

In May again, few objects have been identified due to the temporal resolution and to the nature of the ice, three image pairs generate movement vectors (Figure 7.21). High pressure develops in the Fram Strait around the 17th May, then gives way to the low pressure more typical of the region for the remainder of the month (Figure 7.22). Northerly winds weaken towards the end of the month, but there is no appreciable slowing of the ice movement associated with this (Figure 7.23). All but one of the vectors is in the region where the EGC is not strong, so surface ocean current appears to have a minimal impact (Figure 7.24). Some objects in the area adjacent to the Greenland coast where the ocean currents are less strong are moving in opposition to the wind. These may be caught in a surface eddy that is not visible in the reanalysis data.

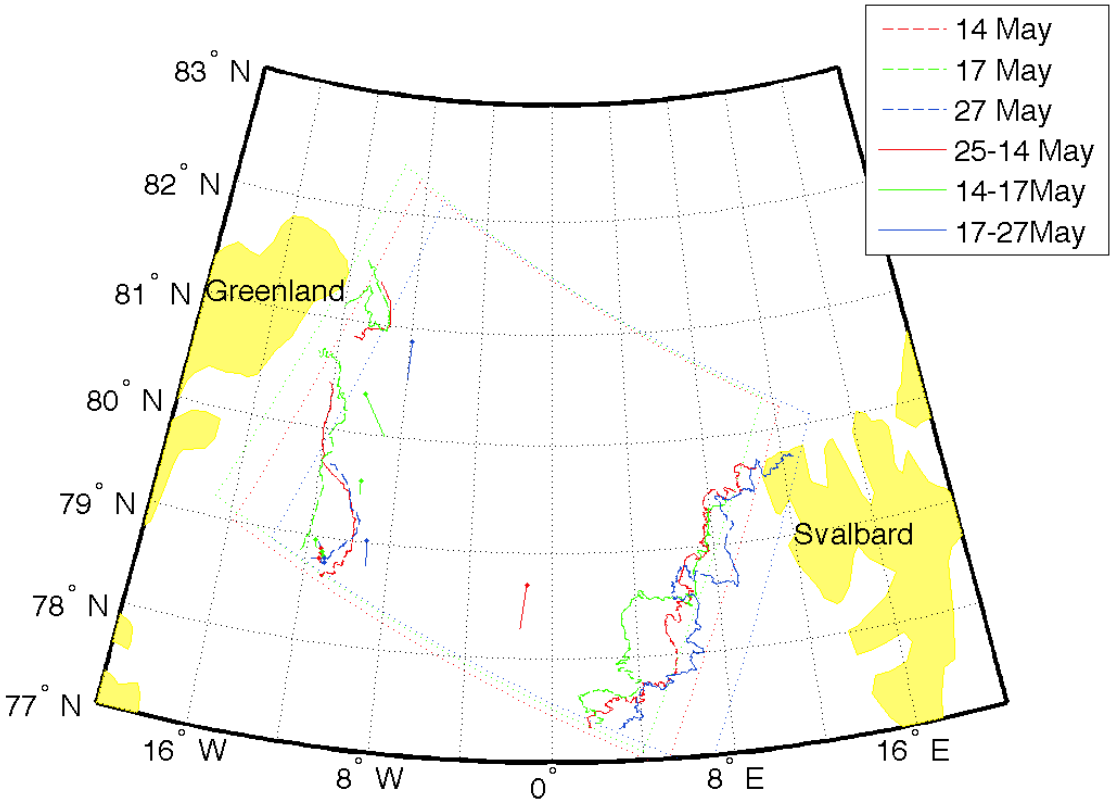

Figure 7.21: Movement of ice objects identified and tracked in images from May 2008. Again few objects have been identified due to the temporal resolution and to the nature of the ice.

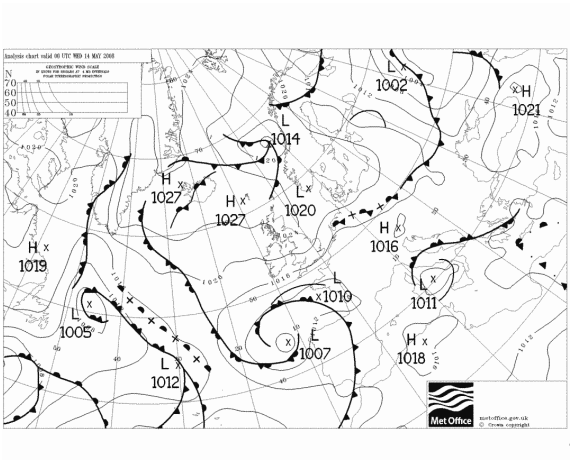

(a) 14 May

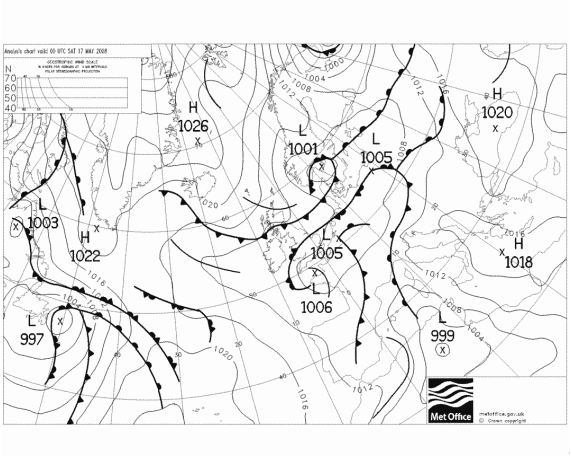

(b) 17 May

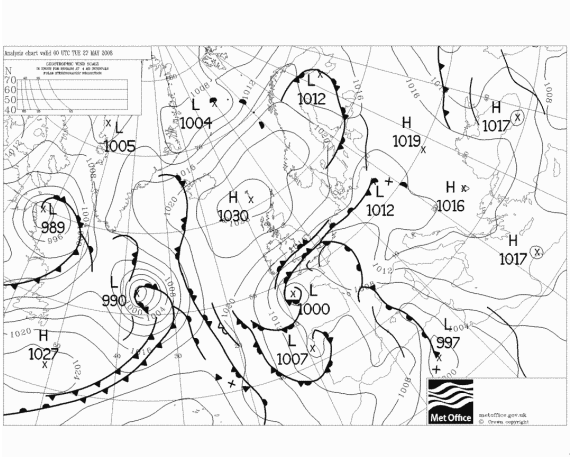

(c) 27 May

Figure 7.22: Surface air pressure in May 2008. From UK Met Office data available at www.wetterzentrale.com.

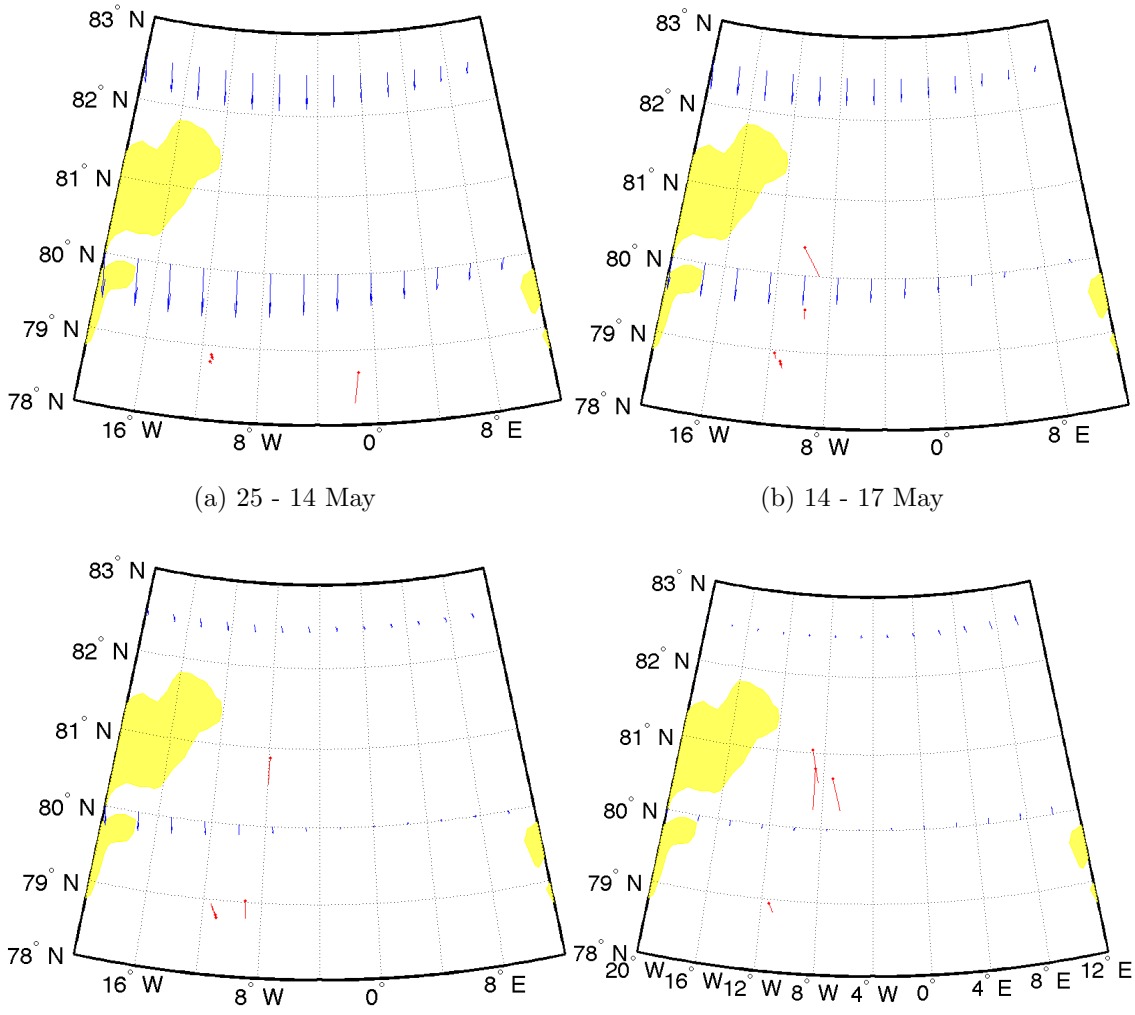

(a) 25 - 14 May

(b) 14 - 17 May

(c) 17 - 27 May

(d) 27 May - 02 June

Figure 7.23: Comparison of movement vectors generated using ITSARI with surface wind vectors from reanalysis, May 2008.

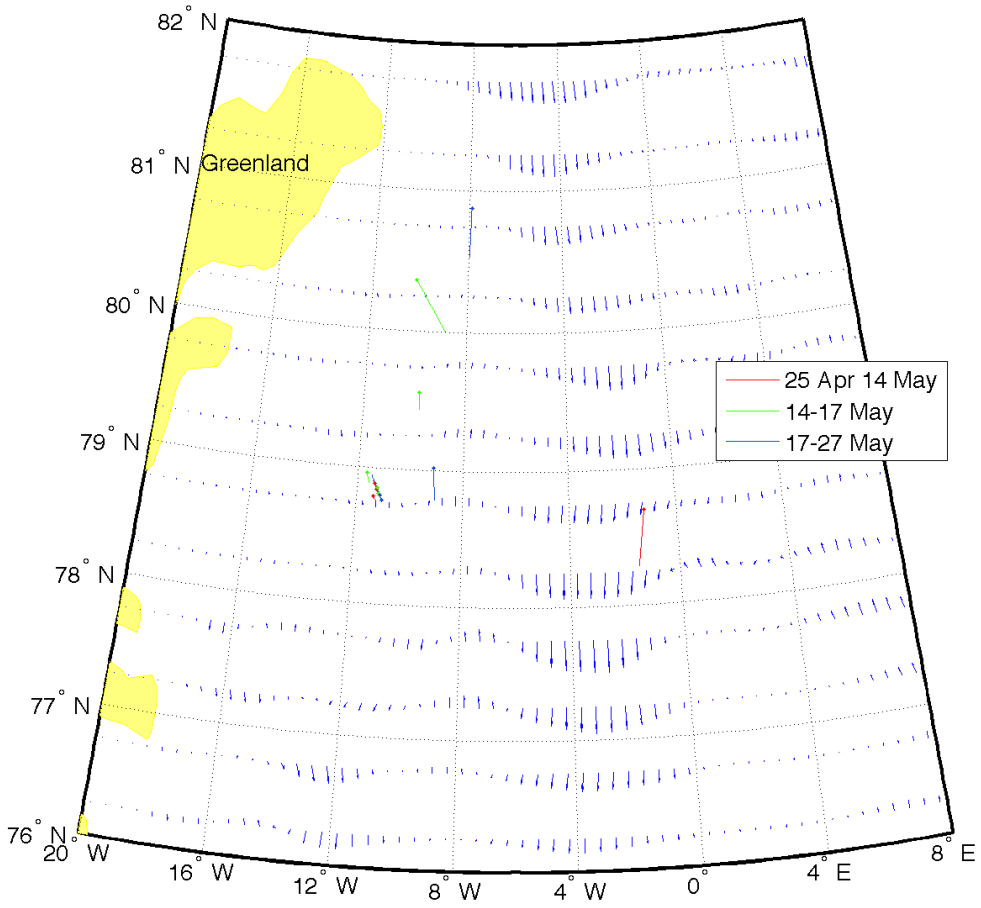

Figure 7.24: Vectors generated using ITSARI compared to surface ocean current vectors from SODA reanalysis. All but one of the vectors is in the region where the EGC is not strong, so surface ocean current appears to have a minimal impact.

7.7 June

In June again identified vectors are sparse (Figure 7.25). Early in the month low pressure prevails in the Fram Strait. By the 15th June high pressure is pushing out from the Greenland coast. Northerly winds would be expected between the isobars of the 18 June, changing to southerlies by the 21st (figure 7.26). It can be seen that between 18th and 21st June the vectors do not align to the reanalysis winds or to each other perhaps showing the influence of this change in wind direction. There is evidence of southerly winds associated with the movement of high pressure into the Strait on the 15th June, followed by the return of strong northerlies (Figure 7.27). There are several buoy tracks available this month (Figure 7.28), unfortunately these are further east than the vectors generated by ITSARI, so do not provide much of a comparison. There is some evidence that the buoy tracks vary in speed of southward movement, perhaps due to variation in wind forcing.

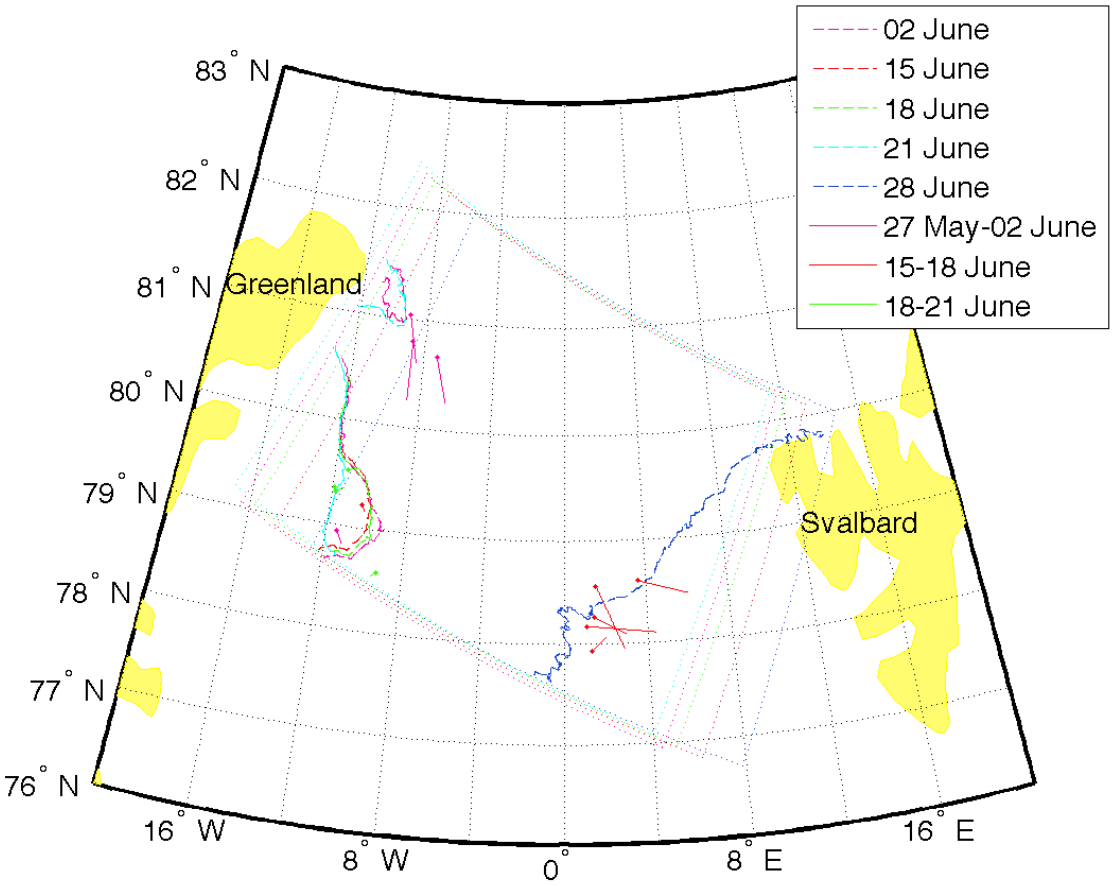

Figure 7.25: Movement of ice objects identified and tracked in images from June 2008.

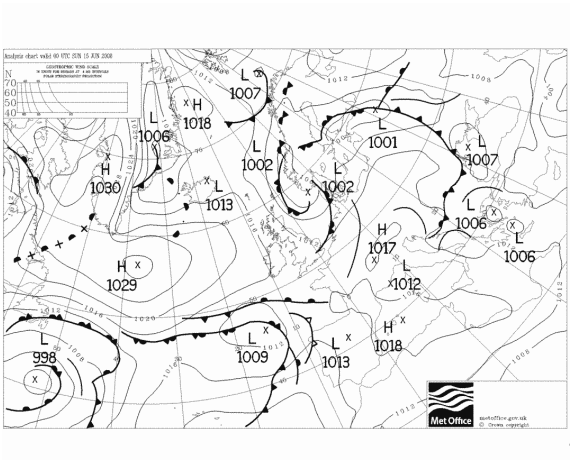

(a) 15 June

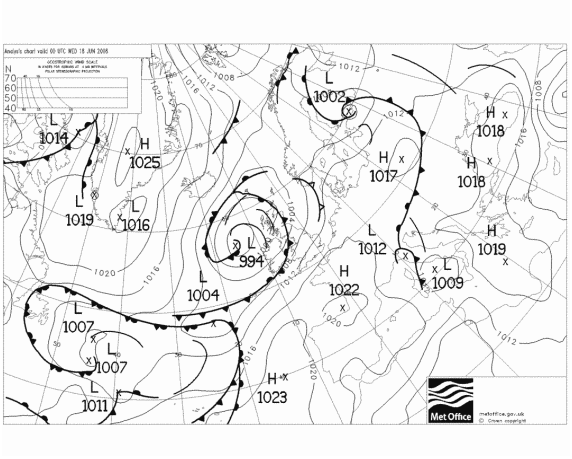

(b) 18 June

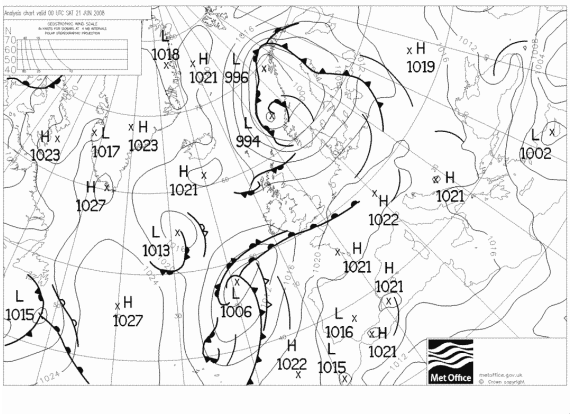

(c) 21 June

Figure 7.26: Surface air pressure in June 2008. Early in the month low pressure prevails in the Fram Strait. By the 15$^{\text{th}}$ June high pressure is pushing out from the Greenland coast. Northerly winds would be expected between the isobars of the 18$^{\text{th}}$ June, changing to southerlies by the 21$^{\text{st}}$. From UK Met Office data available at www.wetterzentrale.com.

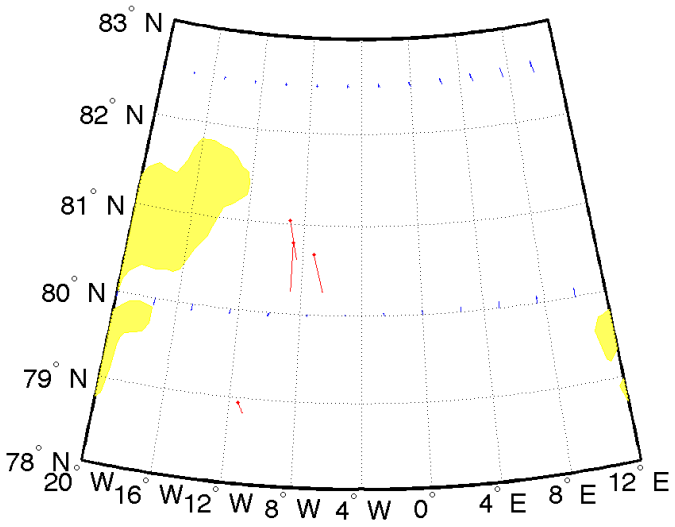

(a) 15 - 18 June

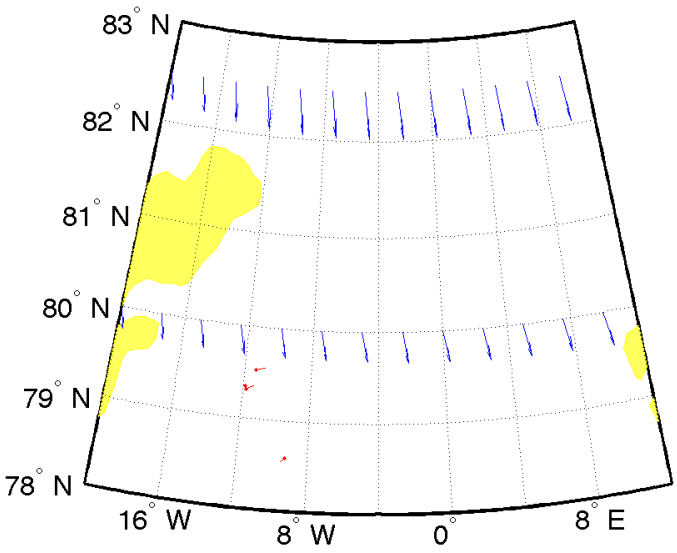

(b) 18 - 21 June

Figure 7.27: Comparison of movement vectors generated using ITSARI with surface wind vectors from reanalysis. June 2008. There is evidence of southerlies associated with the moment of high pressure into the Strait on the 15th June, followed by the return of strong northerlies.

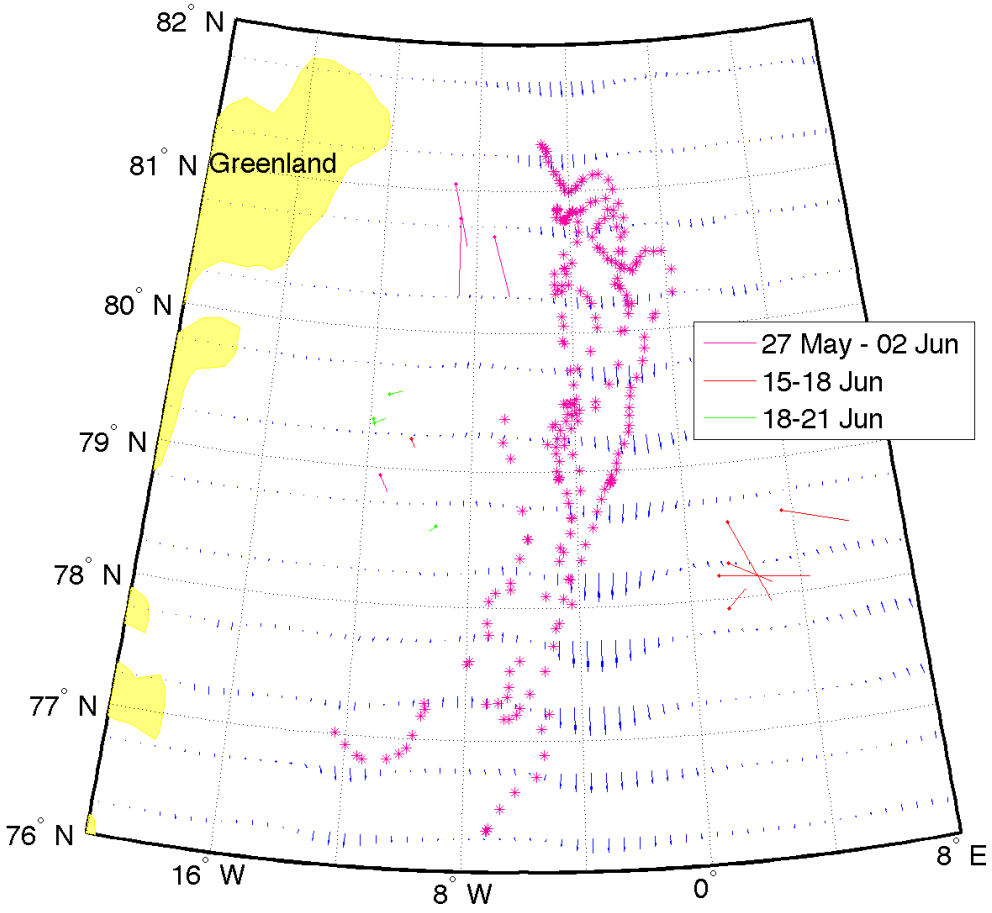

Figure 7.28: Movement vectors generated by ITSARI for the month of June compared to ocean surface current data from the SODA reanalysis project. The red dots represent buoy tracks from the Arctic buoy project.

7.8 July

In July only one image pair produced vectors (Figure 7.29) (see chapter 4 for a discussion of the difficulties associated with tracking from images acquired during the summer months). Individual pieces of ice are moving and breaking independently making the temporal resolution too coarse to successfully match many pieces. Weak northerlies are associated with the weak low pressure that is prevalent in the Strait throughout the month (Figure 7.30). Between the 7th and 23rd July those to the north appear to be driven by the wind (Figure 7.31). Those further south where winds are weaker show evidence of deflection to the west. Between the 30th July and 2nd August one can see the effect of southerly winds deflecting movement from the flow of the East Greenland current, the wind forcing and the EGC are in direct opposition at this time, producing movement towards the east (movement is toward the east rather than west due to Coriolis force playing its part). In this instance the winds are not strong enough to move the ice in the opposite direction to the flow of the EGC, however, vectors are shorter where winds and currents are in opposition than where they are in agreement. The comparison with surface ocean currents is shown in Figure 7.32.

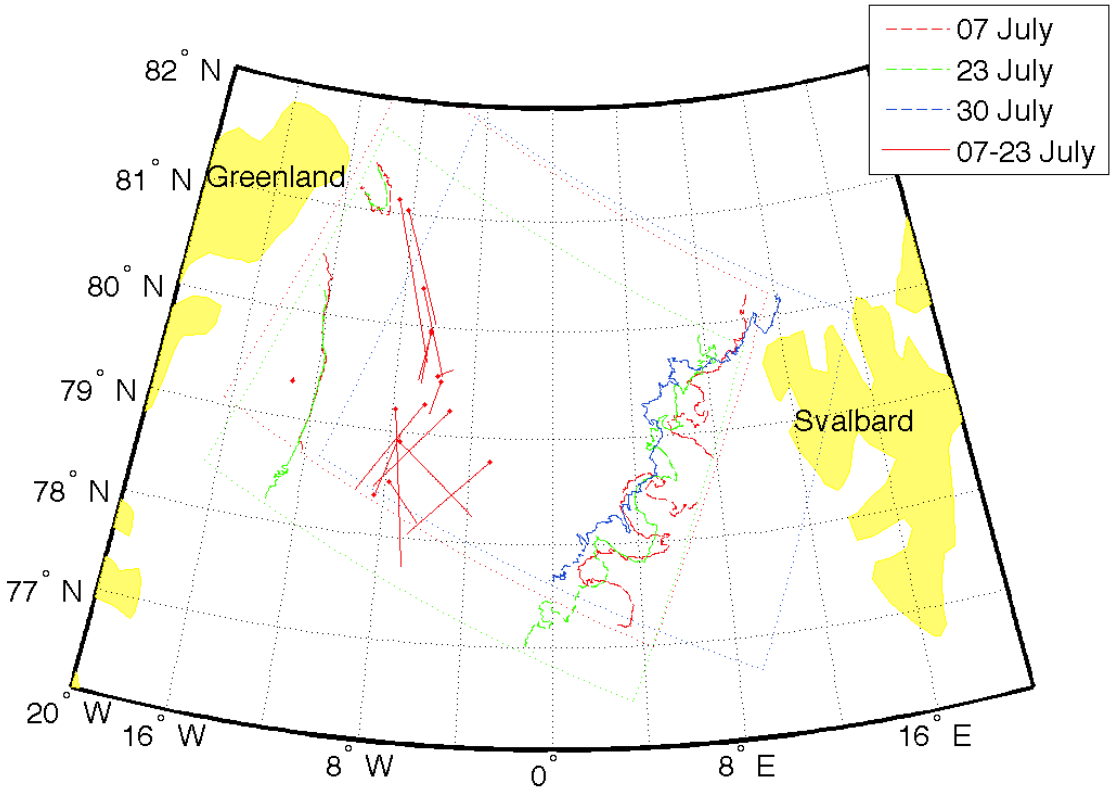

Figure 7.29: Movement of ice objects identified and tracked in images from July 2008.

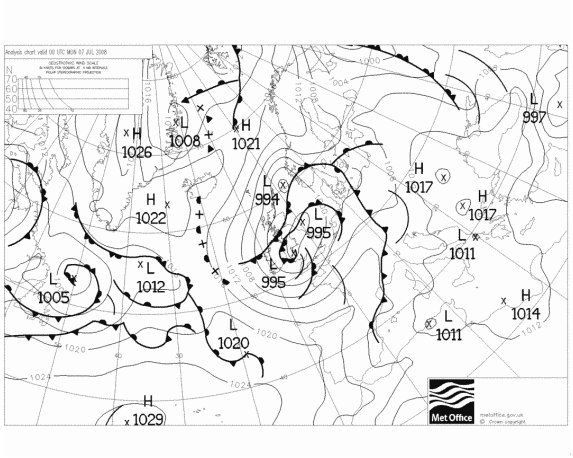

(a) 07 July

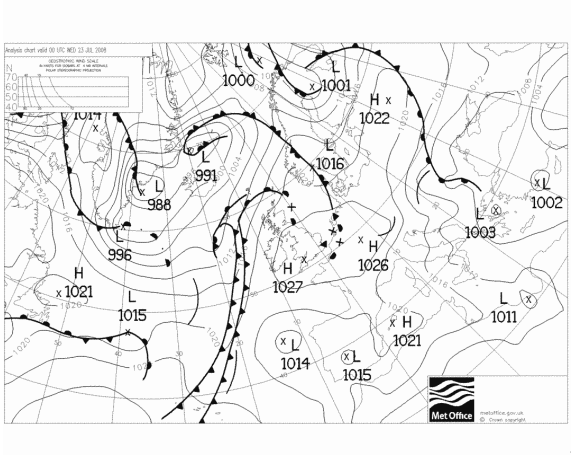

(b) 23 July

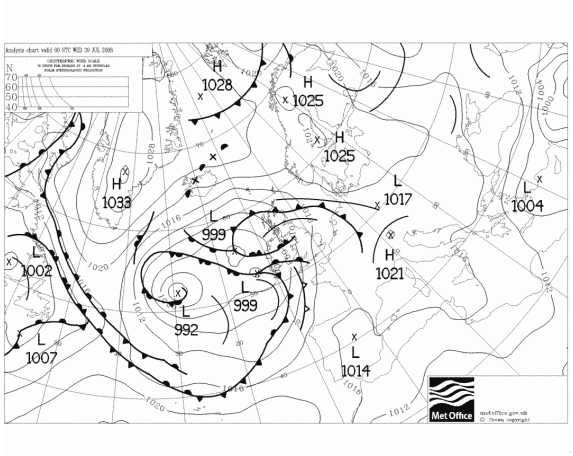

(c) 30 July

Figure 7.30: Surface air pressure in July 2008. From UK Met Office data available at www.wetterzentrale.com.

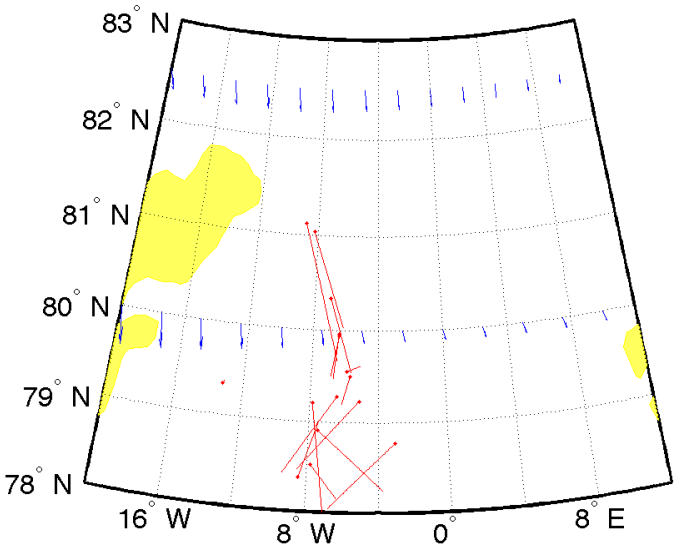

(a) 07 - 23 July

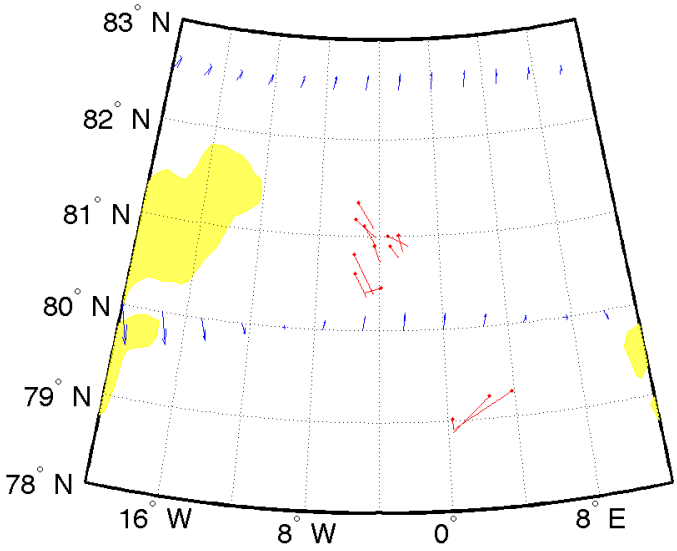

(b) 30 July - 02 August

Figure 7.31: Comparison of movement vectors generated using ITSARI with surface vectors from reanalysis, July 2008.

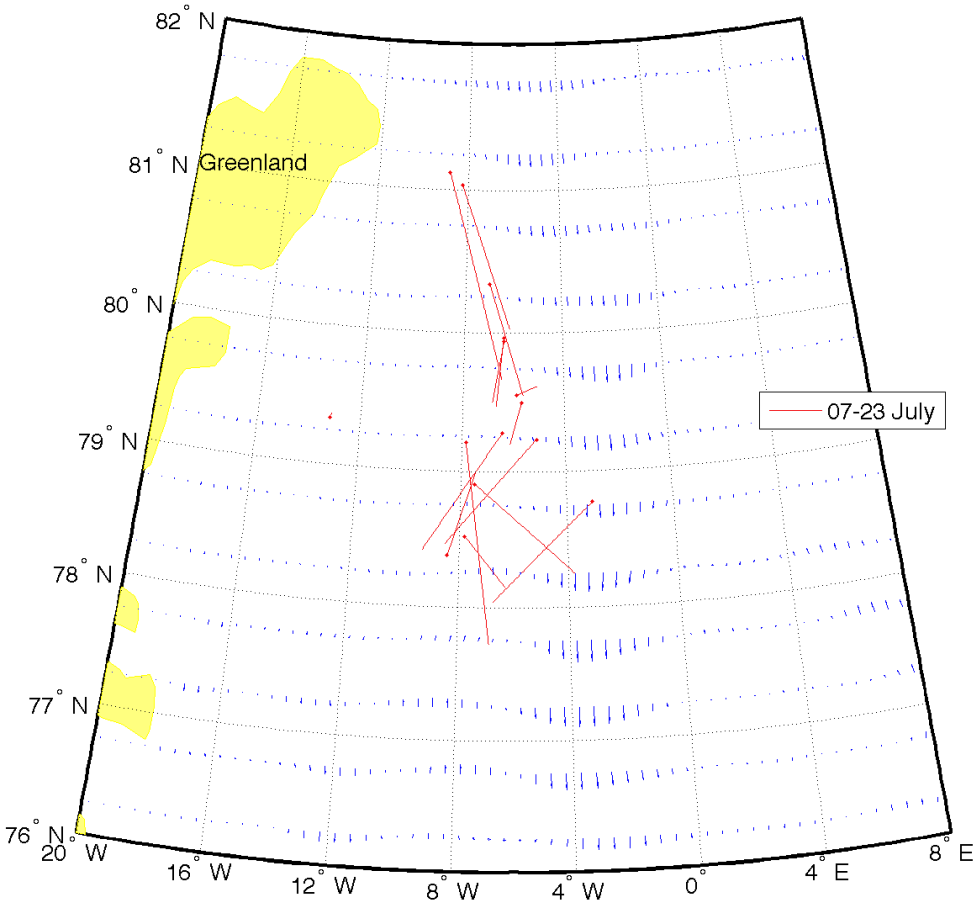

Figure 7.32: Ice movement vectors compared to surface oceans currents from SODA reanalysis, July 2008.

7.9 August

In August ice movement vectors were generated from 7 different movement pairs (Figure 7.33). High pressure is present for much of the month (Figure 7.34). The first set of movement vectors is compared to wind direction in Figure 7.31b above. Between the 2nd and 5th August wind appears to be affecting some vectors more strongly than others (Figure 7.35). The northerly wind strengthens as high pressure develops between the 5th and 8th August, then weakens and reverses direction between the 18th and 24th, as the high moves to the east.. From the 30th August wind is strengthening again from the north and ice movement speeds up. It is hard to relate the movement vectors to the surface ocean currents (Figure 7.36). One thing that is apparent is that there does not appear to be any correlation between the length of a movement vector and the strength of the ocean currents in the area implying that the wind is the dominant factor.

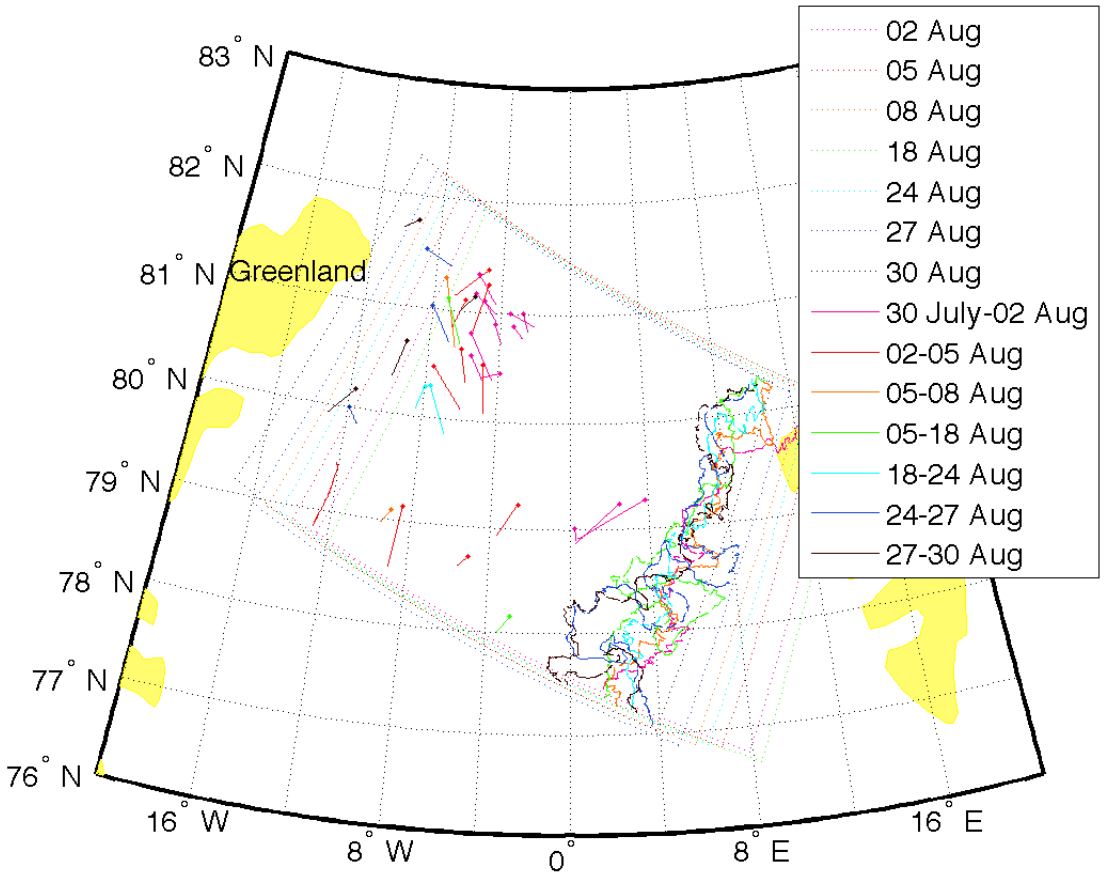

Figure 7.33: Movement of ice objects identified and tracked in seven image pairs from August 2008.

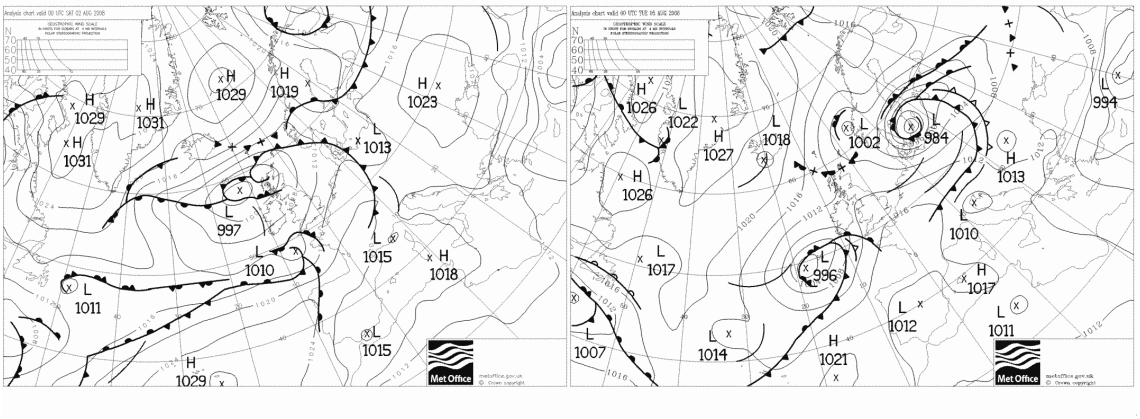

(a) 02 August (b) 05 August

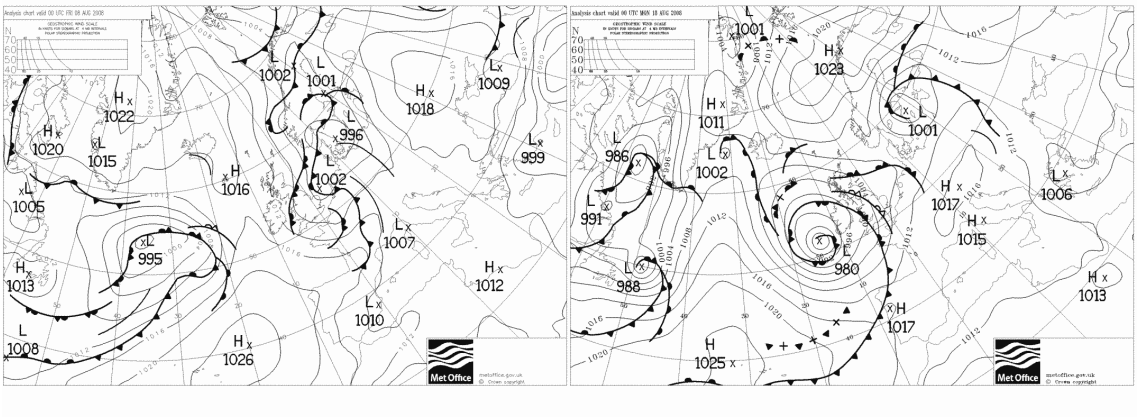

(c) 08 August (d) 18 August

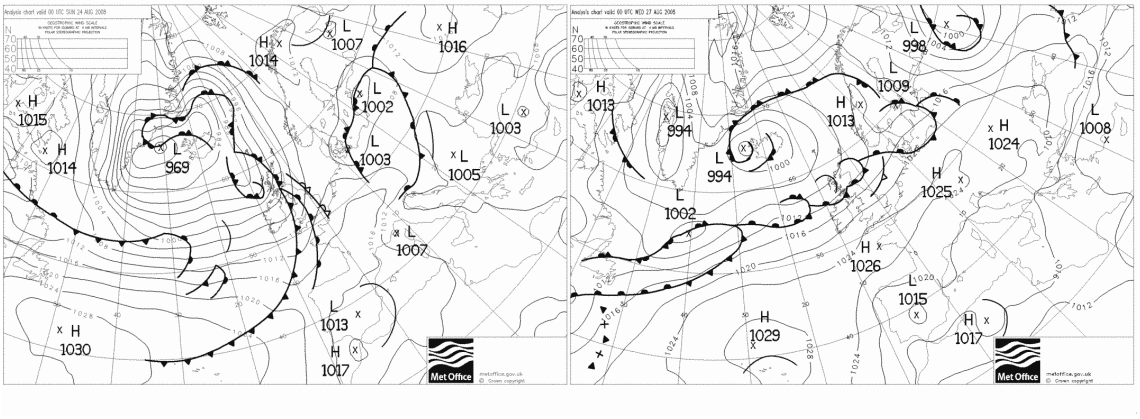

(e) 24 August (f) 27 August

Figure 7.34: Surface air pressure in August 2008. Unusually high pressure is present for much of the month. From UK Met Office data available at www.wetterzentrale.com.

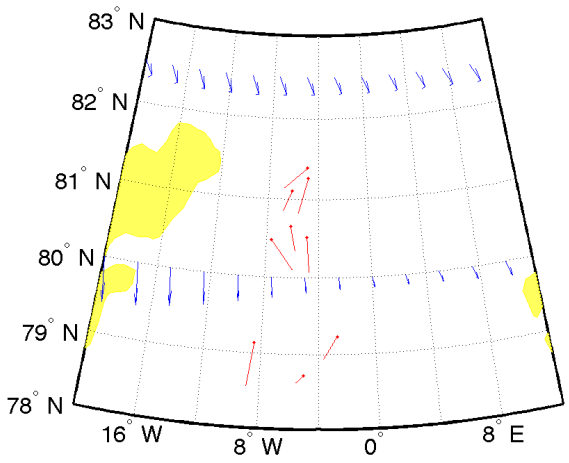

(a) 02 - 05 August

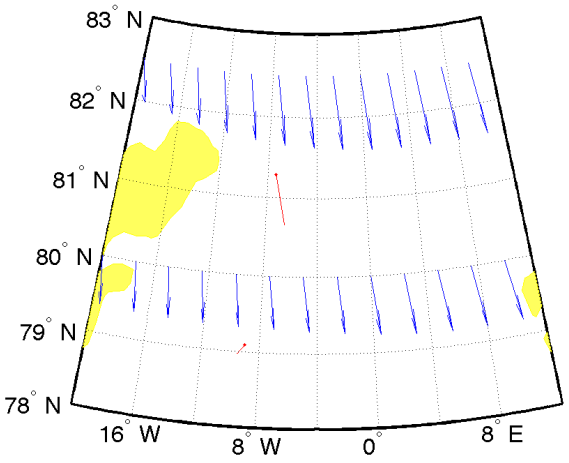

(b) 05 - 08 August

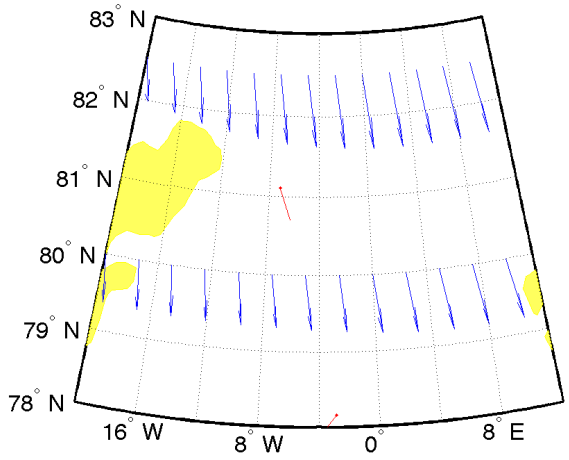

(c) 05 - 18 August

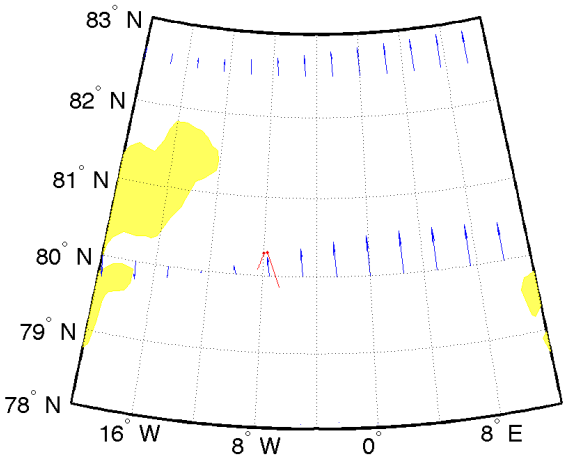

(d) 18 - 24 August

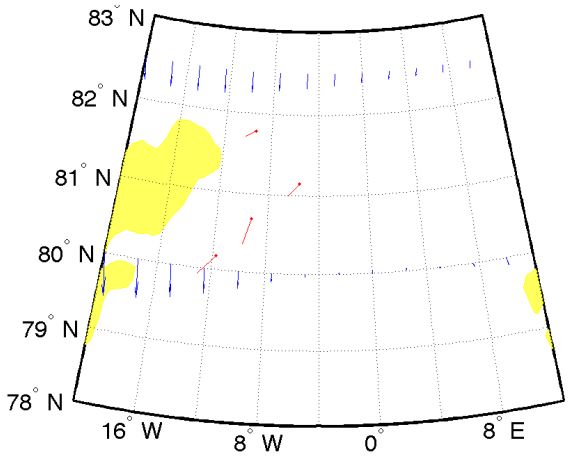

(e) 27 - 30 August

Figure 7.35: Comparison of movement vectors generated using ITSARI with surface vectors from reanalysis. August 2008.

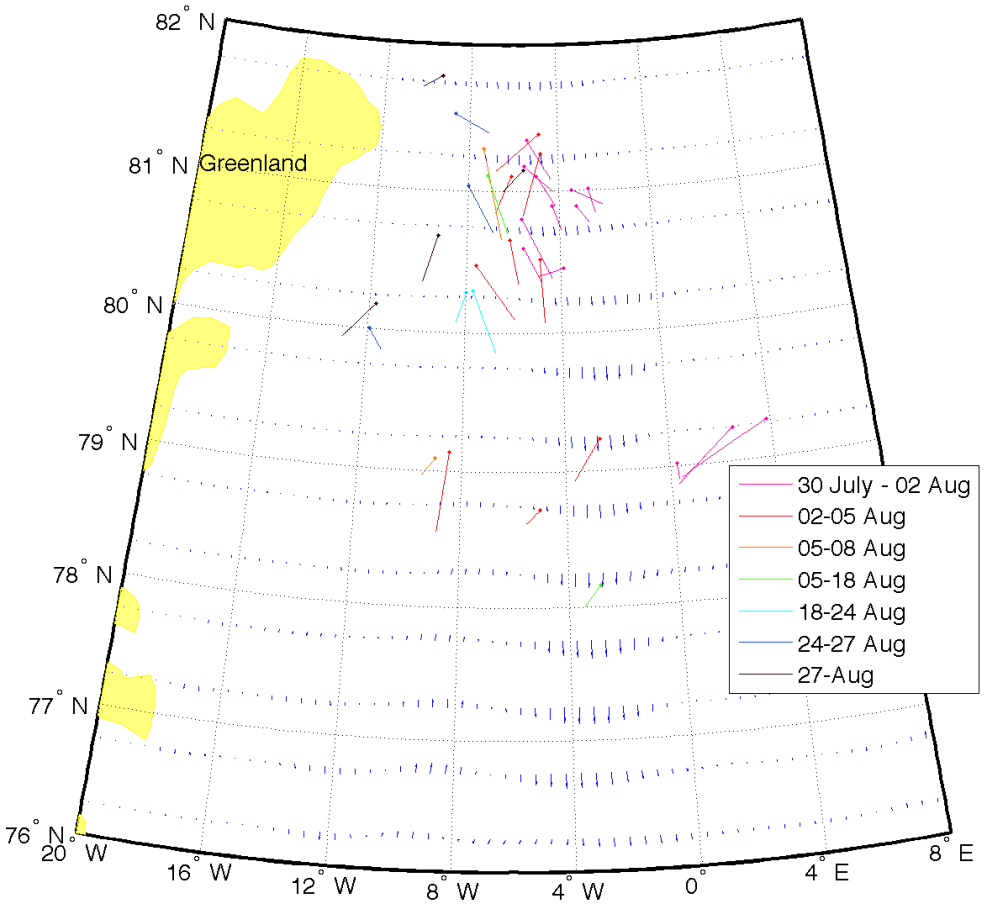

Figure 7.36: Movement of ice in August compared to surface ocean currents from SODA. It is apparent is that there does not appear to be any correlation between the length of a movement vector and the strength of the ocean currents in that area.

7.10 September

In September the ice is moving as a closed pack again as winter begins. In September three image pairs produce ice movement vectors (Figure 7.37). High pressure persists to the south east of the Strait throughout the month, with associated southerly winds (Figure 7.38. Between the 9th and 12th September, and 12th and 15th September; Figure 7.39 shows a very straightforward case of strong southerly winds versus the East Greenland current resulting in movement deflected towards the east. Surface ocean currents from SODA for the month are shown in Figure 7.40.

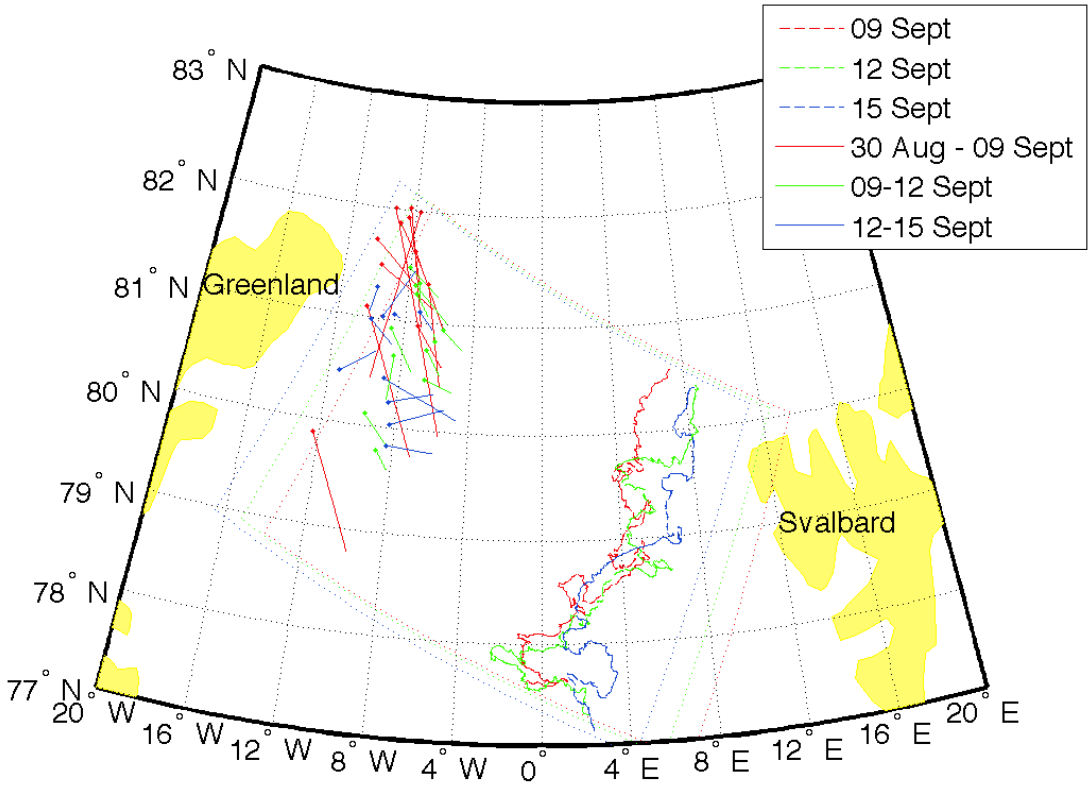

Figure 7.37: Movement of ice objects identified and tracked in images from September 2008.

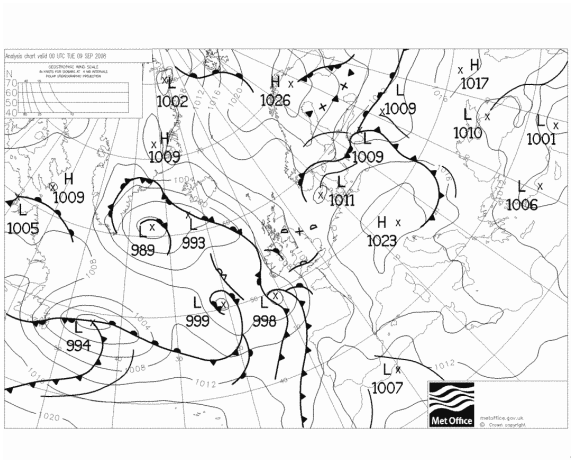

(a) 09 September

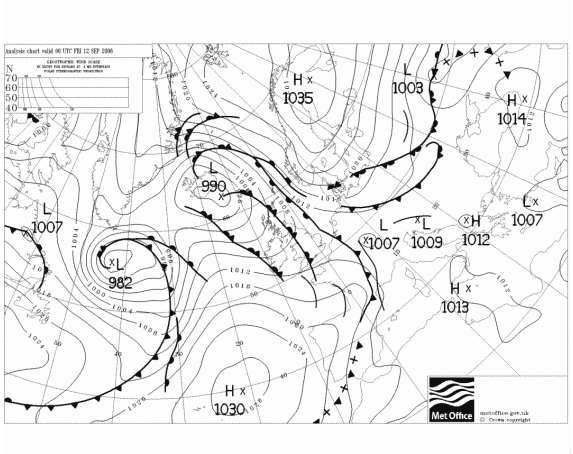

(b) 12 September

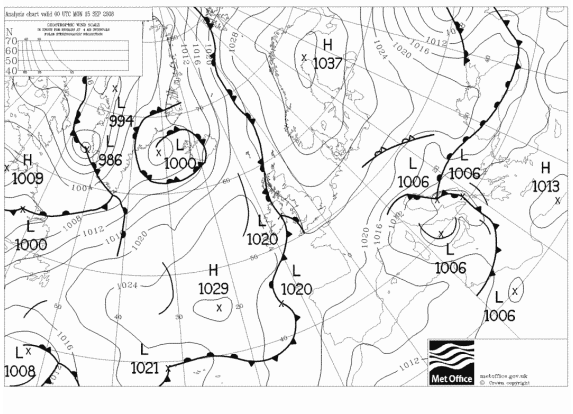

(c) 15 September

Figure 7.38: Surface air pressure in September 2008. High pressure persists to the south east of the Fram Strait throughout the month, indicating that southerly winds would be expected. From UK Met Office data available at www.wetterzentrale.com.

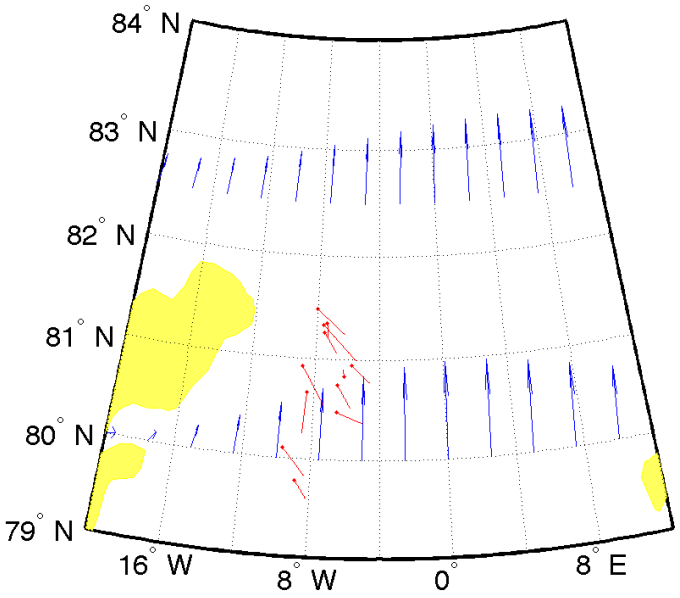

(a) 09 - 12 September

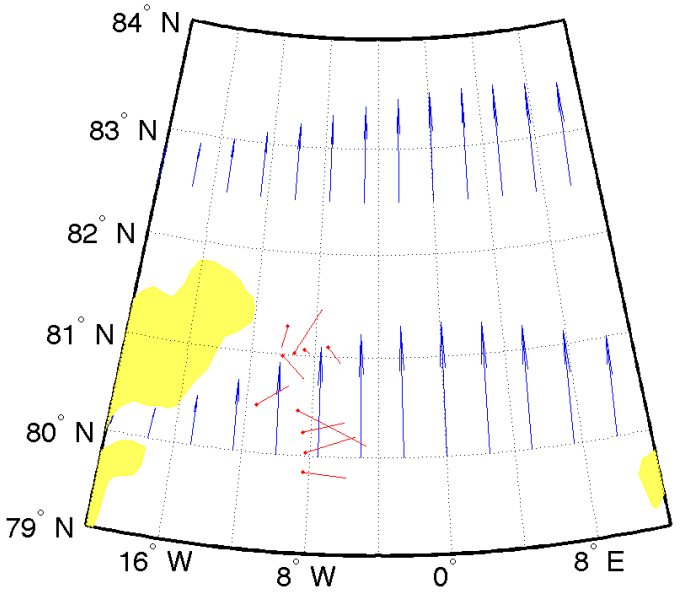

(b) 12 - 15 September

Figure 7.39: Comparison of movement vectors generated using ITSARI with surface vectors from reanalysis, September 2008. Strong southerly winds are in conflict with the East Greenland Current moving South, generating ice movement towards the east (as deflected by Coriolis force).

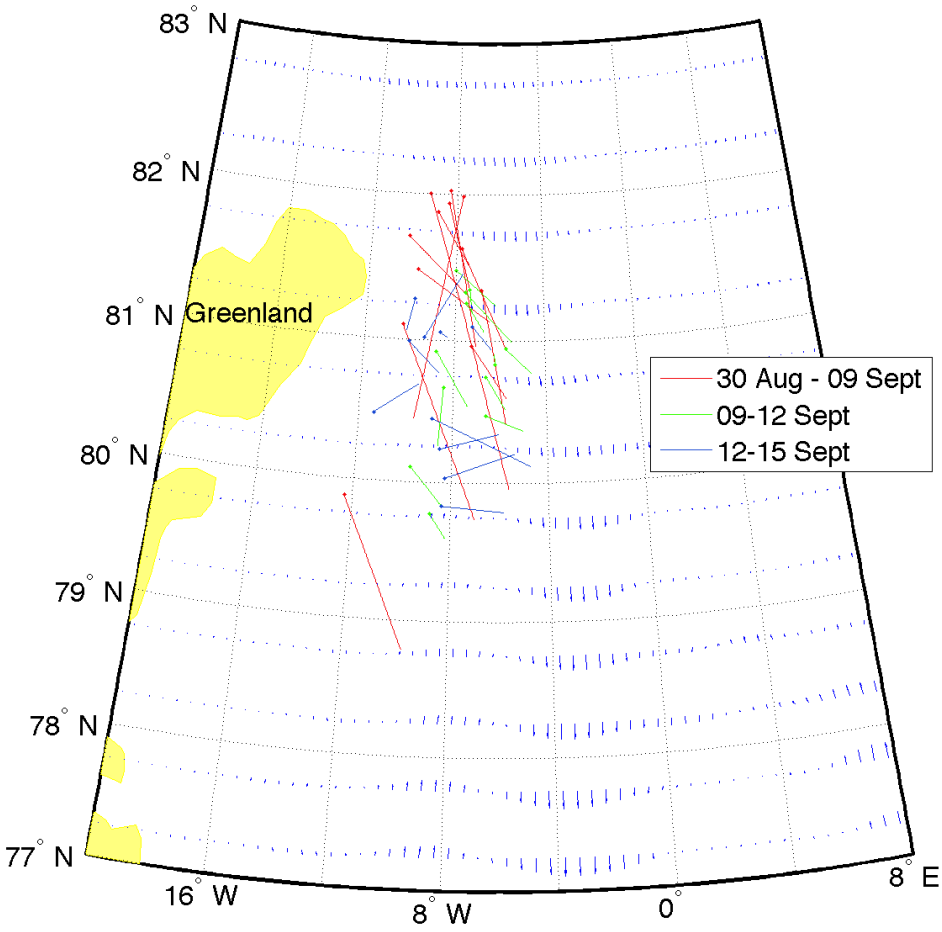

Figure 7.40: Surface ocean currents from SODA with ice movement vectors for the month of September 2008

7.11 October

Throughout October three sets of movement vectors are generated (Figure 7.41). In several cases the same ice object has been tracked in each of the three image pairings, so one can see them arrive in the Strait from the west, then turn to travel southwest at around 81° N. This change of direction could be due to either the East Greenland Current establishing itself from two branches coming in from the east and west, or a result of the prevailing winds. The atmospheric circulation has returned to the prevalent winter pattern of a high over Greenland and a low over the ocean in the Fram Strait (Figure 7.42). Winds from the north-east between the 4th and 11th October strengthen to strong northerlies for the remainder of the month (Figure 7.43). Wind driven movement is in alignment with the East Greenland current, lengthening the movement vectors.

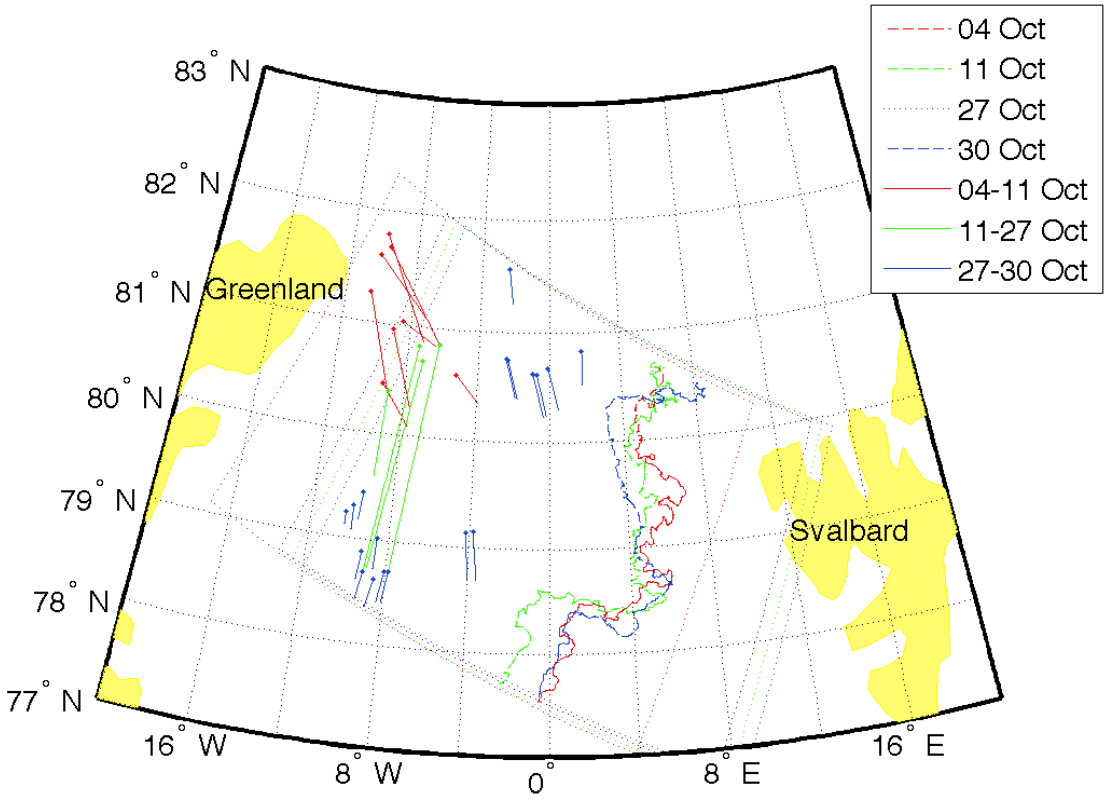

Figure 7.41: Movement of ice objects identified and tracked in images from October 2008.

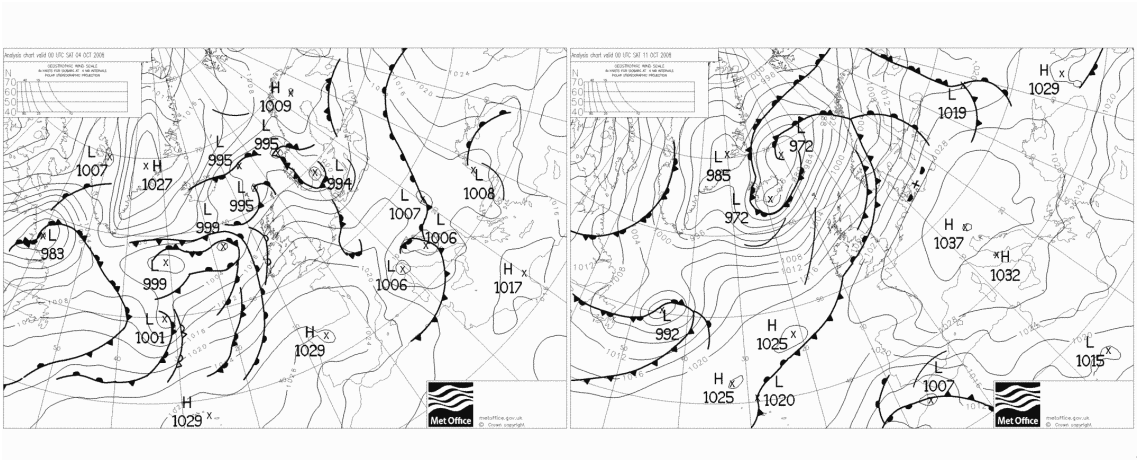

(a) 04 October (b) 11 October

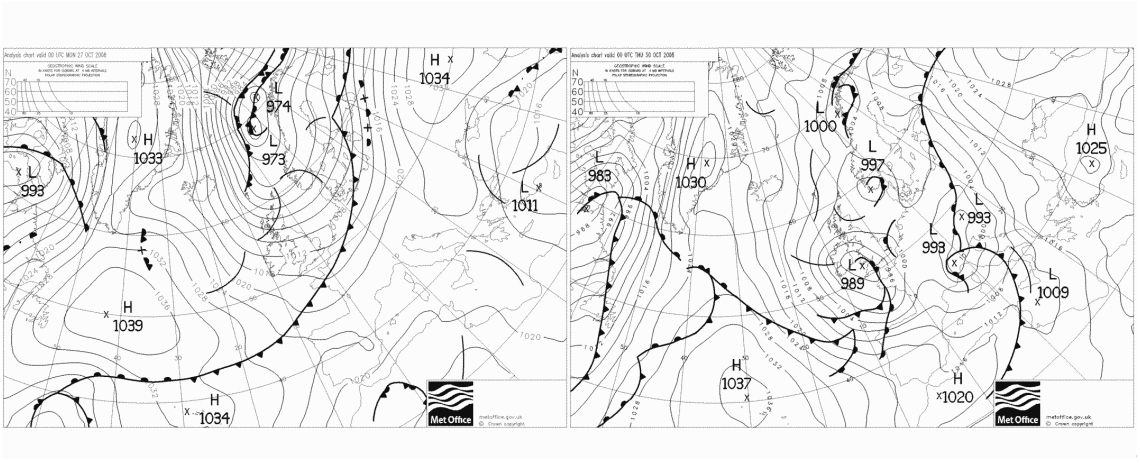

(c) 27 October (d) 30 October

Figure 7.42: Surface air pressure in October 2008. From UK Met Office data available at www.wetterzentrale.com.

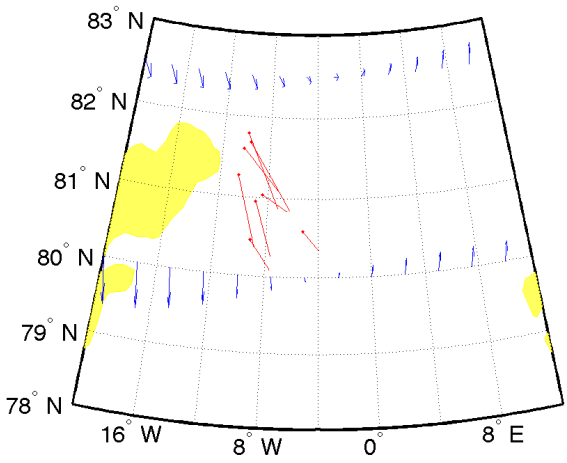

(a) 04 - 11 October

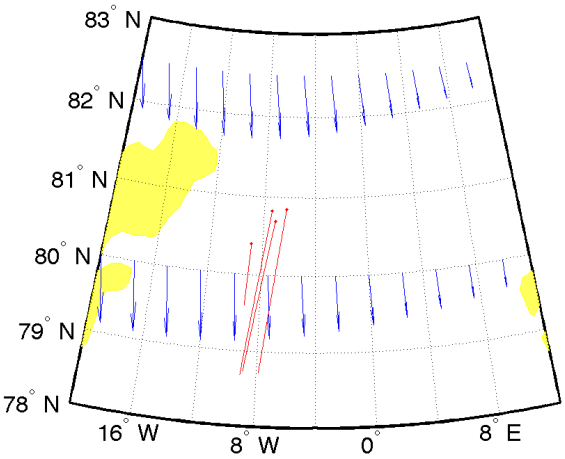

(b) 11 - 27 October

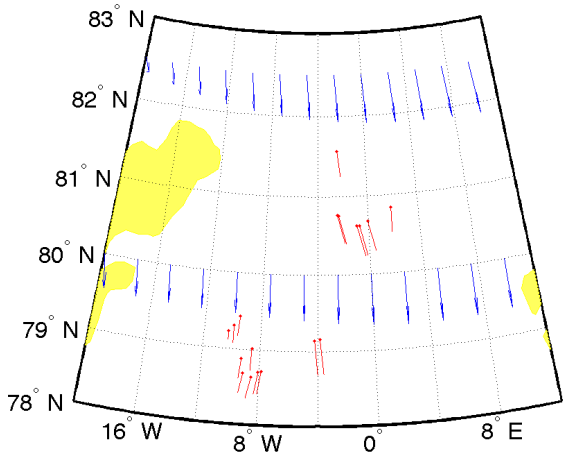

(c) 27 - 30 October

Figure 7.43: Comparison of movement vectors generated using ITSARI with surface vectors from reanalysis, October 2008. The effect of the wind turning, strengthening and then weakening slightly can be seen in the reaction of the movement vectors.

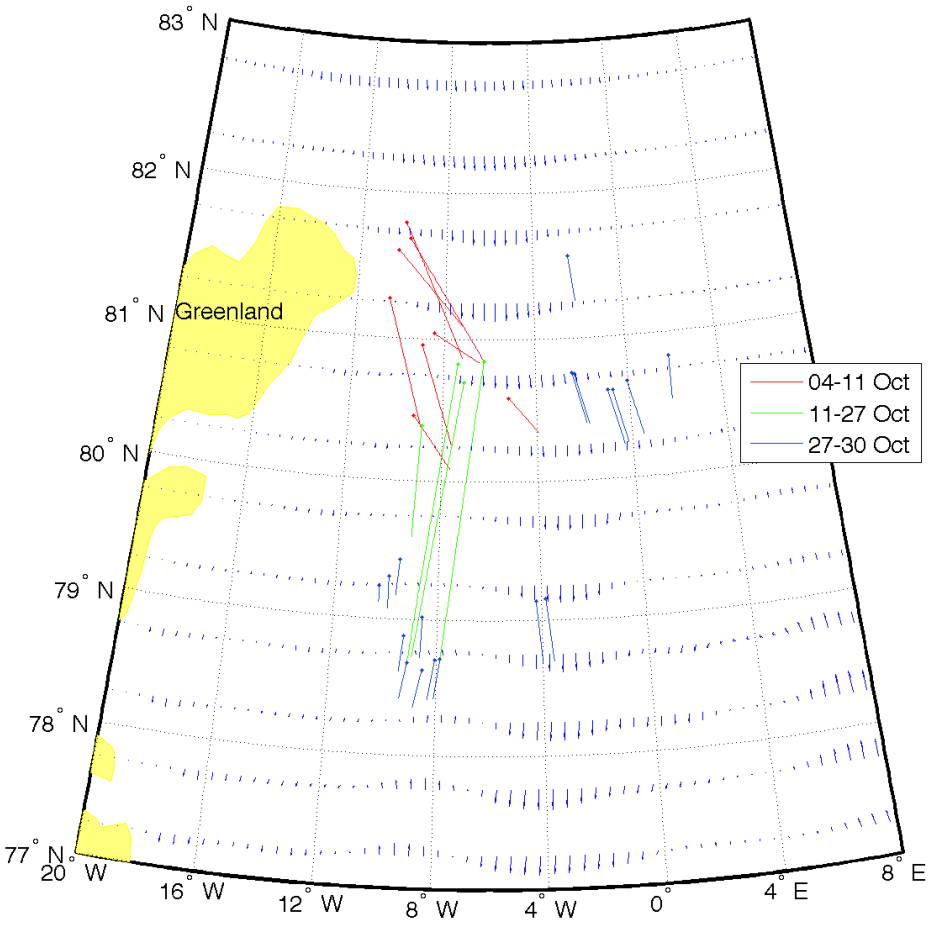

Figure 7.44: Ice movement in the month of October with surface oceans currents from SODA reanalysis. The longer movement vectors are in areas where the current is less strong, suggesting that the wind is the dominant factor here.

7.12 November

Again in November several objects have been tracked from one image pair to the next (Figure 7.45). This time the objects originate towards the centre of the Strait and movement continues in a southward direction throughout the month. This month is again dominated by a low in the Fram Strait and a high over Greenland (Figure 7.46). The expected winds associated with this pattern are northerlies, veering north east or northwest depending on the relative positions of the high and low pressure. The ice movement this month is primarily driven by the wind. The change in direction from movement to the south, to south east and back to south is clearly due to subtle changes in wind direction (Figure 7.47). The majority of this month's objects are in the main thrust of the EGC (Figure7.48). The tracks of ocean buoys available this month are also plotted in Figure 7.48 but are located away from our ice movement tracks.

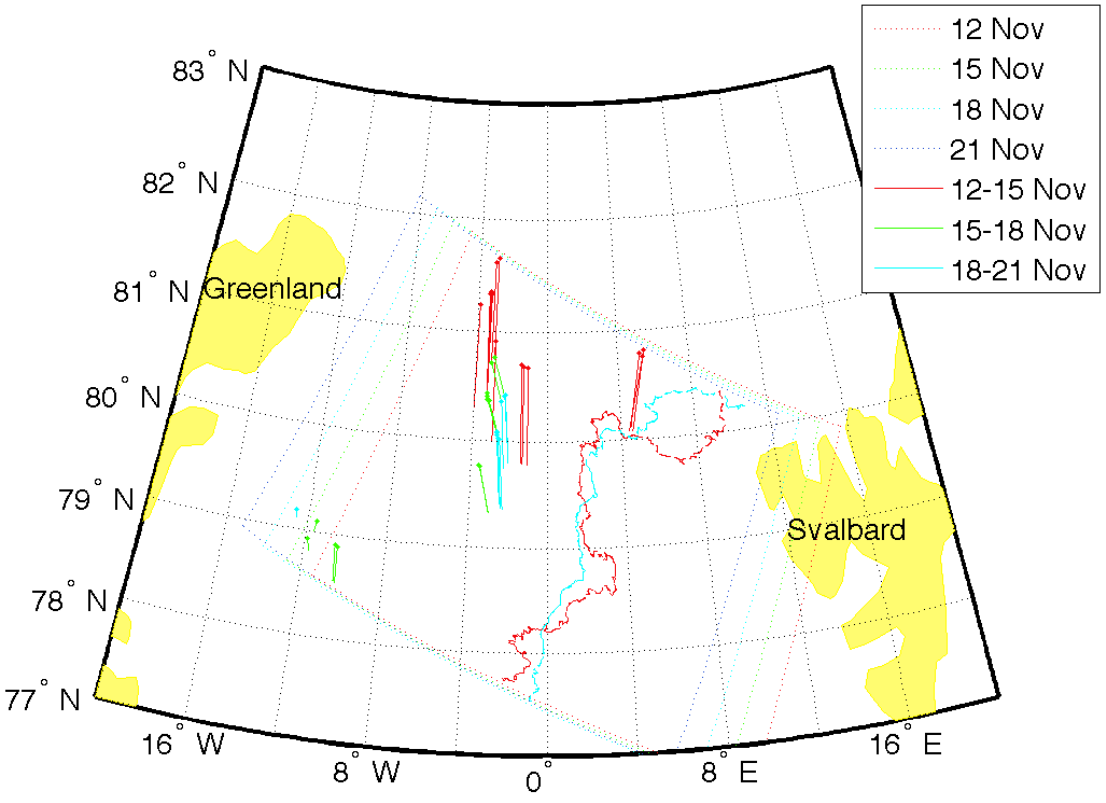

Figure 7.45: Movement of ice objects identified and tracked in images from November 2008.

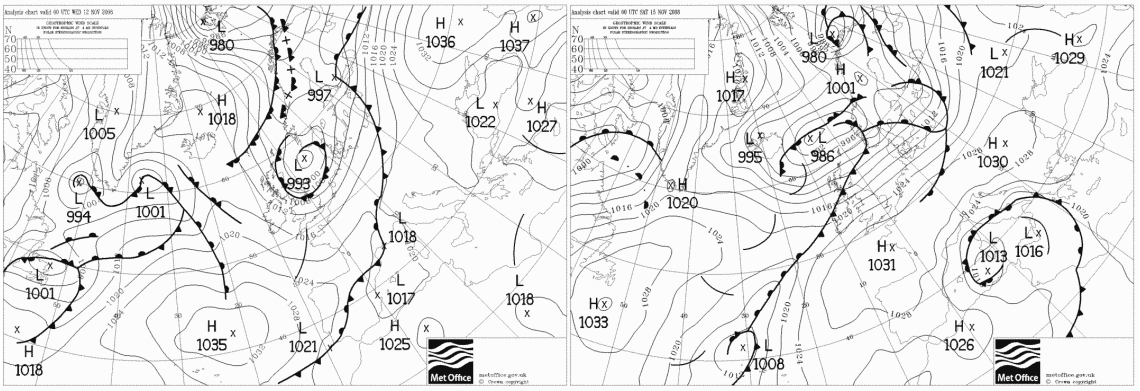

(a) 11 November

(b) 14 November

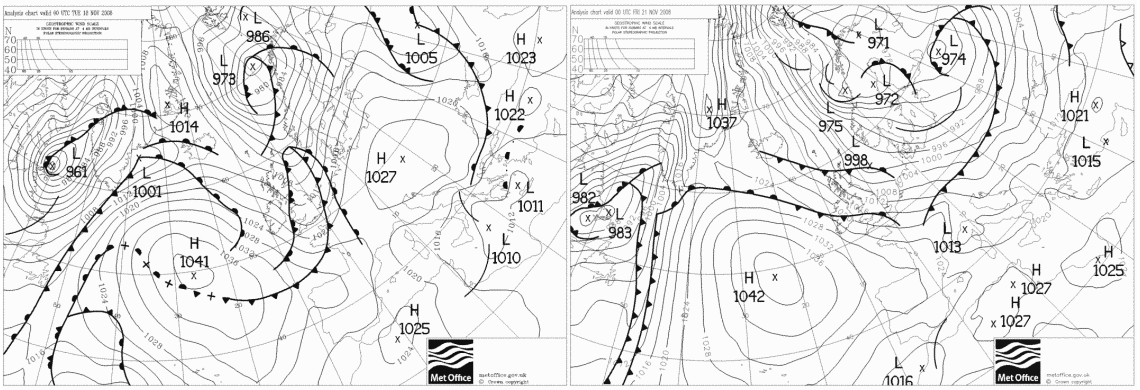

(c) 21 November

(d) 24 November

Figure 7.46: Surface air pressure in November 2008. From UK Met Office data available at www.wetterzentrale.com.

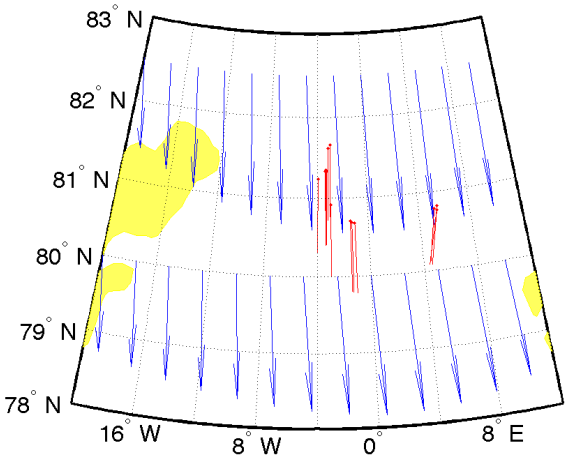

(a) 12 - 15 November

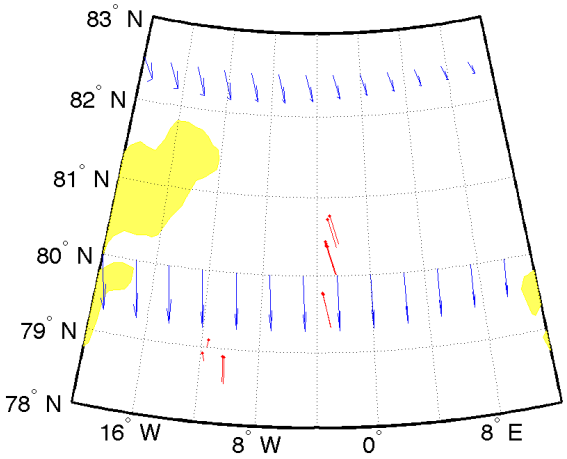

(b) 15 - 18 November

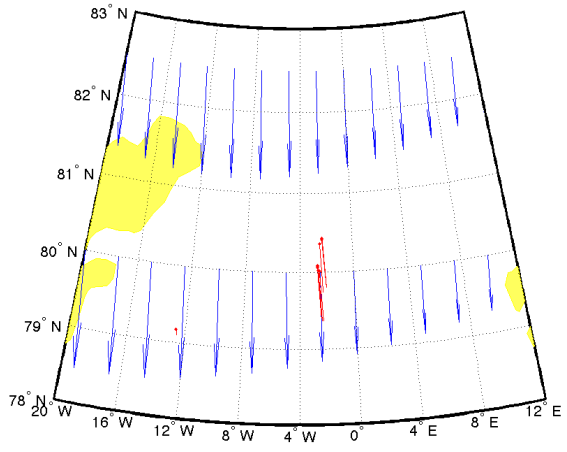

(c) 18 - 21 November

Figure 7.47: Comparison of movement vectors generated using ITSARI with surface vectors from reanalysis, November 2008. Wind forcing is clearly influencing both speed and direction of sea ice movement.

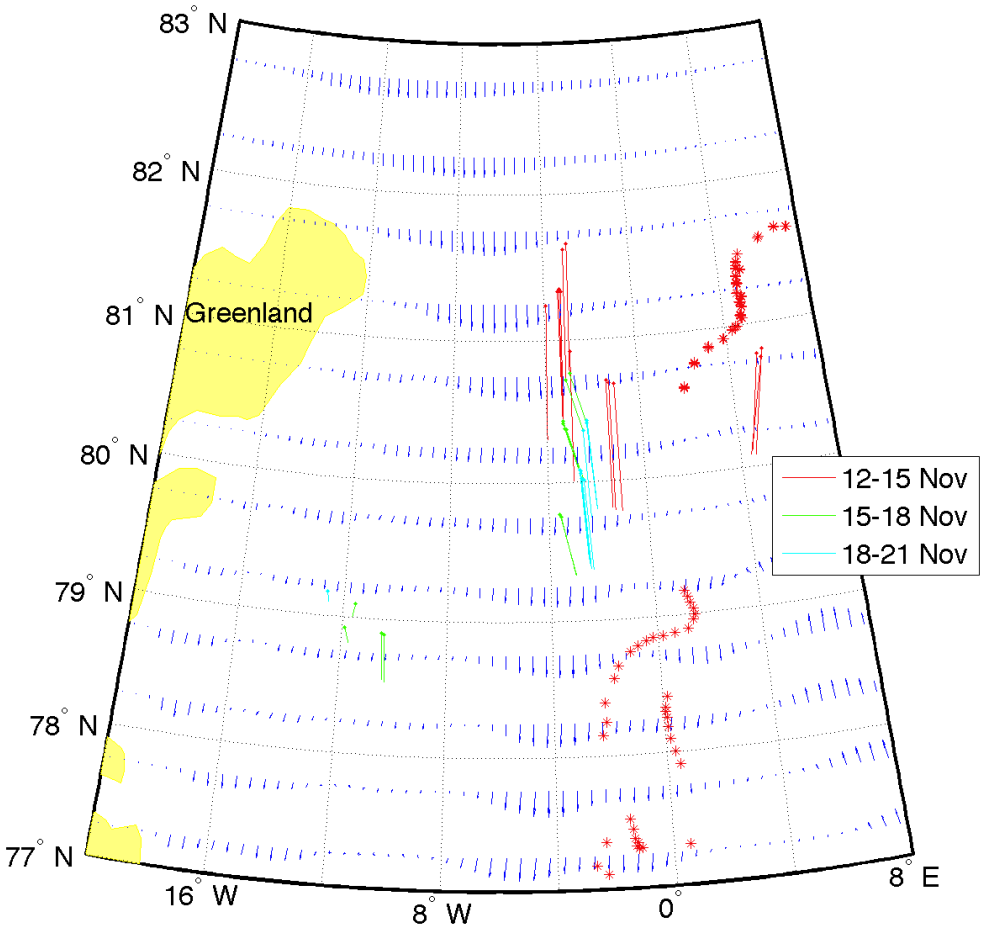

Figure 7.48: Surface ocean currents from SODA with ice movement vectors from the month of November. The majority of this month's objects are in the main thrust of the EGC. There is no indication that the change in direction from movement to the south, to south east and back to south is due to the current. The longer vectors are in the area of stronger surface ocean currents, but it is evident from the direction of ice movement that wind forcing is also at play here. Buoy tracks from the Arctic buoy project are plotted in red.

7.13 December

In December (Figure 7.49) again several tracks continue from one image pair to the next. Again, wind appears to be the dominant influence on both direction and speed of ice movement in these image pairs (Figure 7.51). Several objects appear to enter the Strait from the north west and continue on the same track down the centre of the Strait throughout the month. A bulge in the sea ice edge between 78 - 79° N also appears to be the result of the same wind from the north west. Closer to the fast ice edge and Greenland coast there is more of a step by step change to the object tracks, with several moving first south, then southeast, then south again. Northerly winds dominate throughout the month, with southerlies on the eastern side of the Fram Strait between the 10th and 13th December (c) and 23rd and 26th (e) associated with the movement of low pressure towards the south east (Figure 7.50). Figure 7.52 contains the comparison with surface ocean currents from SODA reanalysis. Again, the longer movement vectors are in the area where surface currents are strongest, but the direction indicates that surface wind direction is also having an effect.

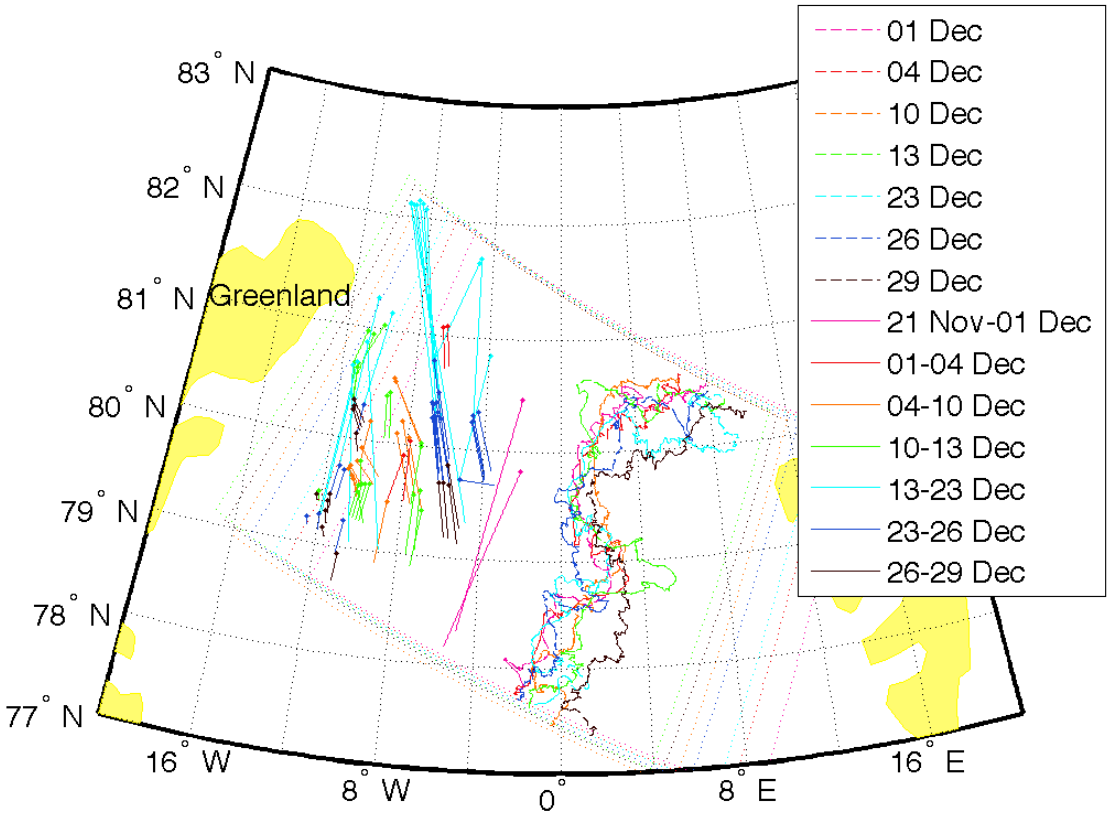

Figure 7.49: Movement of ice objects identified and tracked in images from December 2008.

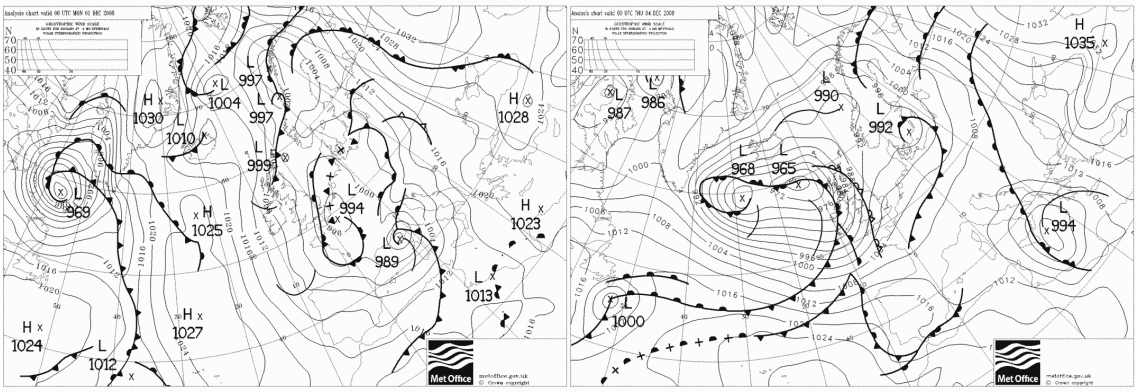

(a) 01 December (b) 04 December

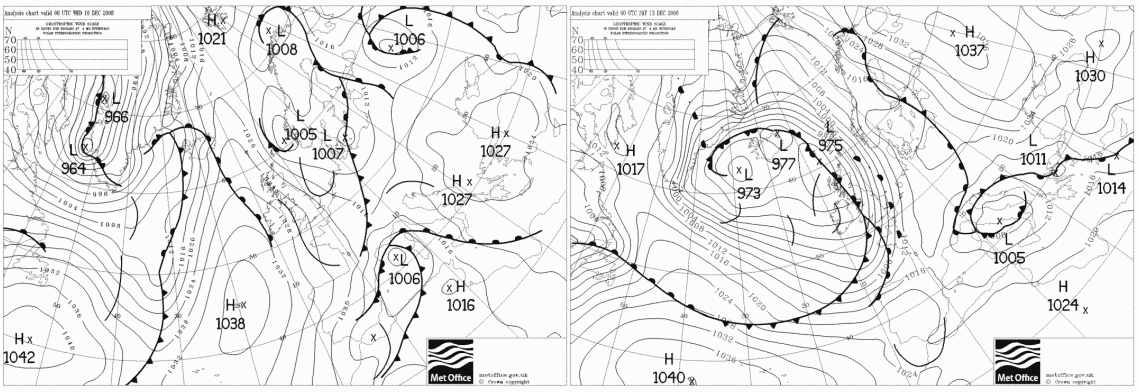

(c) 10 December (d) 13 December

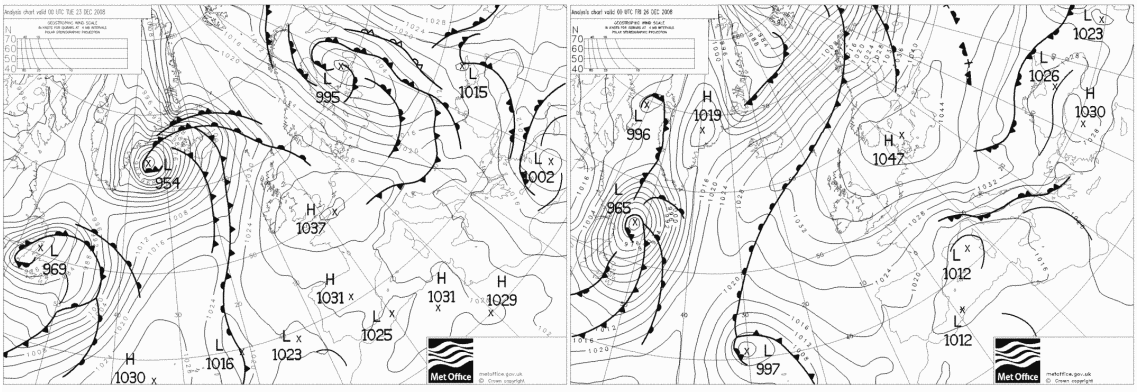

(e) 23 December (f) 26 December

Figure 7.50: Surface air pressure in December 2008. From UK Met Office data available at www.wetterzentrale.com.

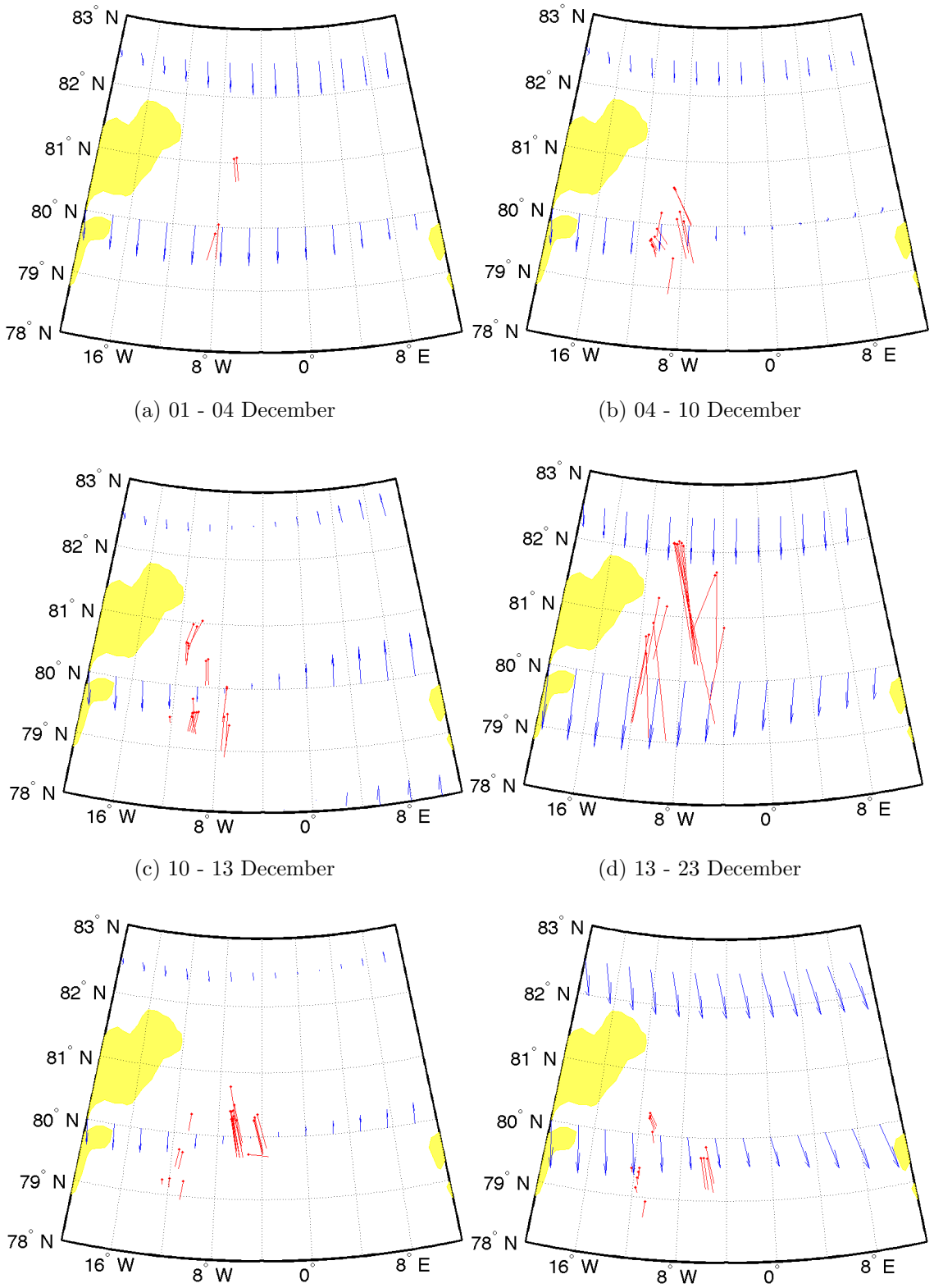

(a) 01 - 04 December

(b) 04 - 10 December

(c) 10 - 13 December

(d) 13 - 23 December

(e) 23 - 26 December

(f) 26 - 29 December

Figure 7.51: Comparison of movement vectors generated using ITSARI with surface vectors from reanalysis, December 2008. Northerly winds dominate throughout the month, with southerlies on the eastern side of the Fram Strait between the 10th and13th December (c) and 23rd and 26th December (e) associated with the movement of low pressure towards the south east. Again, wind appears to be the dominant influence on both direction and speed of ice movement in these image pairs.

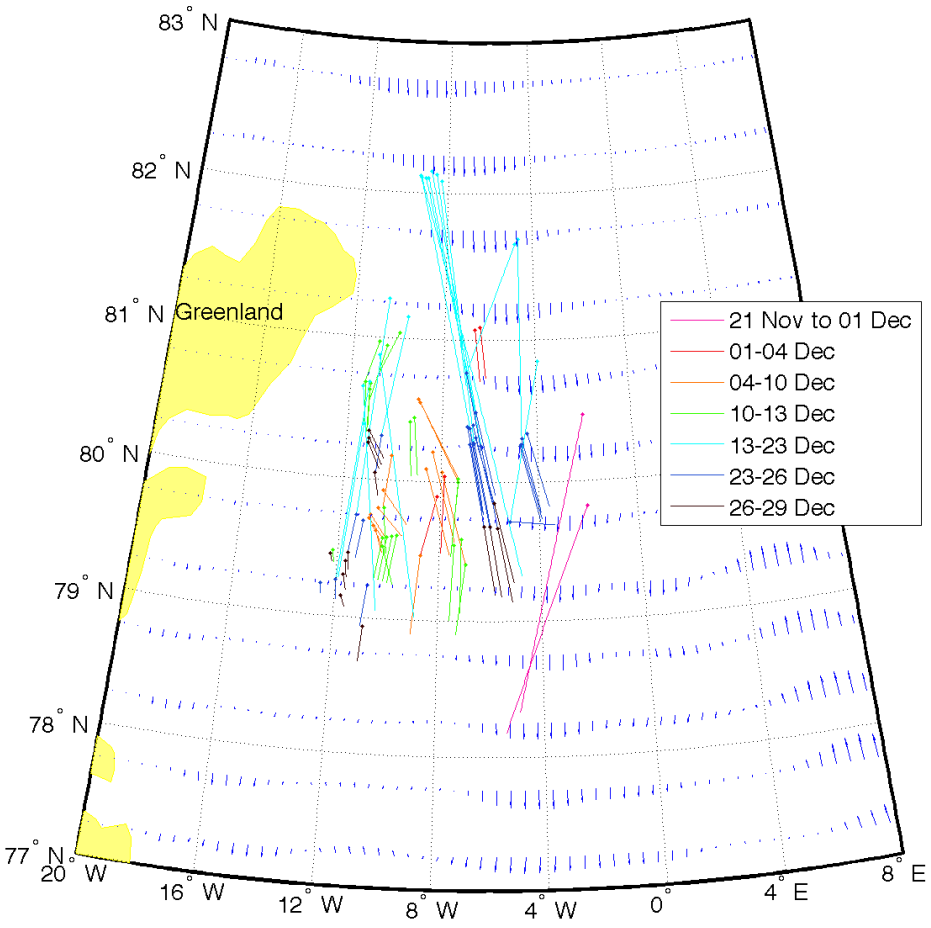

Figure 7.52: Ice movement vectors from the month of December with surface ocean currents from SODA reanalysis. Again, the longer movement vectors are in the area where surface currents are strongest, but the direction indicates that other factors are also having an effect.

7.14 Velocity throughout the year

The greatest speed of travel is in the winter: January February, November and December, while the slowest travel is in late spring: May. This is associated with strong northerly and north westerly winds in the winter months, generated by a quasi-stable pressure system comprising high pressure over north Greenland and low pressure over the Fram Strait. Movement in the summer months (June-August) is less linear than in the rest of the year, as the pack disperses and floes are no longer constrained to move together as a pack. Here we see an increased influence of other meteorological factors such as wind direction (as affected by pressure gradient). There appears to be more south-eastwards travel in spring and summer as opposed to more south-westwards travel in November and December. This is most likely to be due to the effects of the wind forcing as the East Greenland Current does not change direction at this time.

Speeds are higher in the centre of the strait towards the edge of the ice pack than close to the fast ice edge. This is influenced by the location of the strongest flow in the East Greenland Current. There may also be drag against the fast ice edge slowing down water and therefore ice movement in the area immediately adjacent. Interestingly this pattern is less evident during the summer months, possibly due to a greater speed being enabled by the opening of the summer polynya adjacent to the fast ice edge.

There are several factors that can be inferred to influence ice movement over the course of the year. Wind velocity appears to be the dominant influence on ice movement direction over each two to three day interval, while the relentless flow of the East Greenland Current is the dominant influence on ten day to monthly (and presumably longer) timescales. The highest speeds occur when the wind forcing and the East Greenland Current are acting in the same direction. For example, between the 16^{th} and 18^{th} February (Figure 7.10), winds are from the north and the ice is moving at 0.15 m s^{-1} (Table 4.2), whereas between the 20^{th} and 21^{th} February when winds are weak and veering east to south east the ice is moving more slowly at 0.06

m s^{-1}. Or to take another example, ice moves further between the 12th and 15th November than between the 15th and 18th November when the wind is less strong (Figure 7.47).

The wind velocity does not always perfectly explain the speed and direction of ice movement. This may be because sea ice drift depends not only on surface wind but also on the surface aerodynamic roughness and the near-surface stratification (Vihma et al., 2012). Vihma et al. (2012) suggest that the local air-ice momentum flux does better than the surface wind speed alone wind speed in explaining sea ice drift in the Fram Strait. This may explain why some of the surface wind vectors do not explain the direction of ice movement at times when the ocean surface currents do not explain this either.

Sea level pressure charts were chosen because sea ice sits at sea level; but it is possible that the mean sea level pressure charts do not accurately represent airflow over Greenland. Future work using this data should consider the 500hPa and 700 hPa geopotential height charts for additional information.

Ogi et al. (2008) suggest that both drift buoys and ice floes tend to follow atmospheric isobars. There is plenty of evidence in this chapter to support the hypothesis that ice movement follows isobars, including on occasions where winds are not represented in the reanalysis data set.

The passage of cyclones over the Fram Strait has been shown to speed up ice movement (Brummer et al., 2003, 2008). Brummer et al. (2003)found that average ice drift of 0.21 m s^{-1} increased to 0.6 m s^{-1} during cyclone passage. The ice drift pattern is cyclonically curved around the centre of the cyclone loop, ice drift diverges in the loop centre, and converges in adjacent zones. On the east side of the northward moving cyclone, the ice edge was pushed northward because of strong winds, on the rear side the ice edge advanced towards open water, but by a smaller distance because of weaker winds there. Cyclone impact on sea ice depends on

the location of the track within the Fram Strait. The more easterly the track, the larger the ice export (Brummer et al., 2008). There is evidence of this happening in October, between the 4th and 11th October surface winds are from the north west in the west of the Strait and south east in the east of the Strait. Ice is pushed to the south east by the winds in the northern sector. By the 27th October the cyclone has moved away to the south east, bringing stronger winds in its wake, increasing ice movement (Figure 7.43). Another example, from December, does not show the same effects. Between the 23rd and 26th December a cyclonic wind pattern is present, with northerlies on the western side and southerlies on the eastern side. Between the 26th and 29th December the winds strengthen as above as the cyclone moves across the strait, but this does not appear to speed up the ice movement (Figure 7.51).

Barrier winds (winds that occur when cold and stably stratified air is forced by synoptic scale flow towards a topographic barrier) may be generated when air flow towards the Greenland coast is deflected, increasing the windspeed (Petersen et al., 2009). This may be a contributing factor to some of the stronger northerly winds seen in the region, and partly explains why the most rapid ice movement is not always in the area of strongest reanalysis winds or strongest surface current.

Anticyclonic circulation anomalies over the Greenland Sea can prevent sea ice from drifting southwards (Inoue and Kikuchi, 2007). This is clearly shown in September (Figure 7.39) where ice is deflected towards the east.

Mesoscale eddies (fluctuation with time scales of several days which are not correlated between adjacent moorings) occur on daily timescale, so would likely not show in monthly average calculations of surface ocean, such as those used here. Such eddies may be a contributing factor where ice movement does not agree with ocean surface current.

Where the fast ice edge has been mapped there is not much change in its location throughout the year. Nor is there much change in ice extent, but ice area changes

within this extent, as in the summer months a large polynya opens adjacent to the fast ice edge.

Further discussion of the forcing factors acting on the ice to influence its movement will be continued in Chapter 7, with emphasis on the ice behavior in the late summer months (August and September 2010) at a shorter time step.

Chapter 8

Ice movement in late summer

8.1 Introduction

This chapter describes a more detailed case study into the movement of individual ice objects in the Fram Strait in late summer conditions. A mixture of Radarsat and Envisat WS images were acquired throughout August and September 2010 (Table 8.1). In all cases where the sensor was Radarsat the HH & HV bands were combined using basic band maths (matrix addition) into one grey scale image prior to processing with ITSARI as described in Chapter 5. It is interesting to look at ice movement in late summer because this time of year is often avoided by cross correlation tracking algorithms due to problems maintaining a grid of correlation points at a time when the ice is free to move in different directions and change rapidly in character. Ice movement through the Fram Strait at this time of year may be a key component for understanding ice loss from the Arctic Ocean and its impact on changes to ice extent year on year.

As in Chapter 7, the ice motion is described and then the motion vectors generated by ITSARI are compared to ocean currents from SODA reanalysis data available at: http://soda.tamu.edu/data.htm (Carton and Giese, 2008); wind speed & direction from NCEP/NCAR reanalysis data provided by the NOAA/ESRL Physical Sciences Division, Boulder Colorado, from their web site at

Table 8.1: Images acquired during August & September 2010

Acquisition Date	Acquisition Time	Sensor
16-08-2010	08:07	Radarsat
17-08-2010	07:37	Radarsat
19-08-2010	08:19	Radarsat
20-08-2010	07:50	Radarsat
23-08-2010	08:02	Radarsat
24-08-2010	07:33	Radarsat
26-08-2010	08:15	Radarsat
30-08-2010	07:58	Radarsat
30-08-2010	07:59	Radarsat
31-08-2010	07:29	Radarsat
01-09-2010	12:00	Envisat
01-09-2010	20:17	Envisat
02-09-2010	08:11	Radarsat
02-09-2010	21:26	Envisat
03-09-2010	07:41	Radarsat
03-09-2010	20:54	Envisat
04-09-2010	12:06	Envisat
04-09-2010	20:23	Envisat
05-09-2010	21:31	Envisat
06-09-2010	07:54	Radarsat
06-09-2010	21:00	Envisat
07-07-2010	07:25	Radarsat
07-09-2010	12:11	Envisat
08-09-2010	21:37	Envisat
09-09-2010	21:06	Envisat
10-09-2010	12:17	Envisat
11-09-2010	11:45	Envisat
13-09-2010	12:23	Envisat
14-09-2010	11:51	Envisat
15-09-2010	21:17	Envisat
16-09-2010	12:28	Envisat
20-09-2010	12:03	Envisat
22-09-2010	20:57	Envisat
27-09-2010	11:43	Envisat
30-09-2010	11:48	Envisat

http://www.esrl.noaa.gov/psd/data/composites/day/ (Kalney, 1996). Surface air pressure charts from the UK Met Office achieved at: www.wetterzentrale.de/topkarten/fsfaxbra.html are also used to support analysis of the meteorological conditions. A variety of different factors appear to be at play including katabatic winds moving ice offshore, the development of eddies adjacent to the fast ice edge, and the effect of local wind patterns associated with the movement of pressure systems. The effects of localized meteorological conditions can be seen within the bigger picture of southward flow in the East Greenland Current, and Ekman flow at 45° to wind direction. A series of plots showing the speed and direction of movement for each image pair can be found in Appendix A.

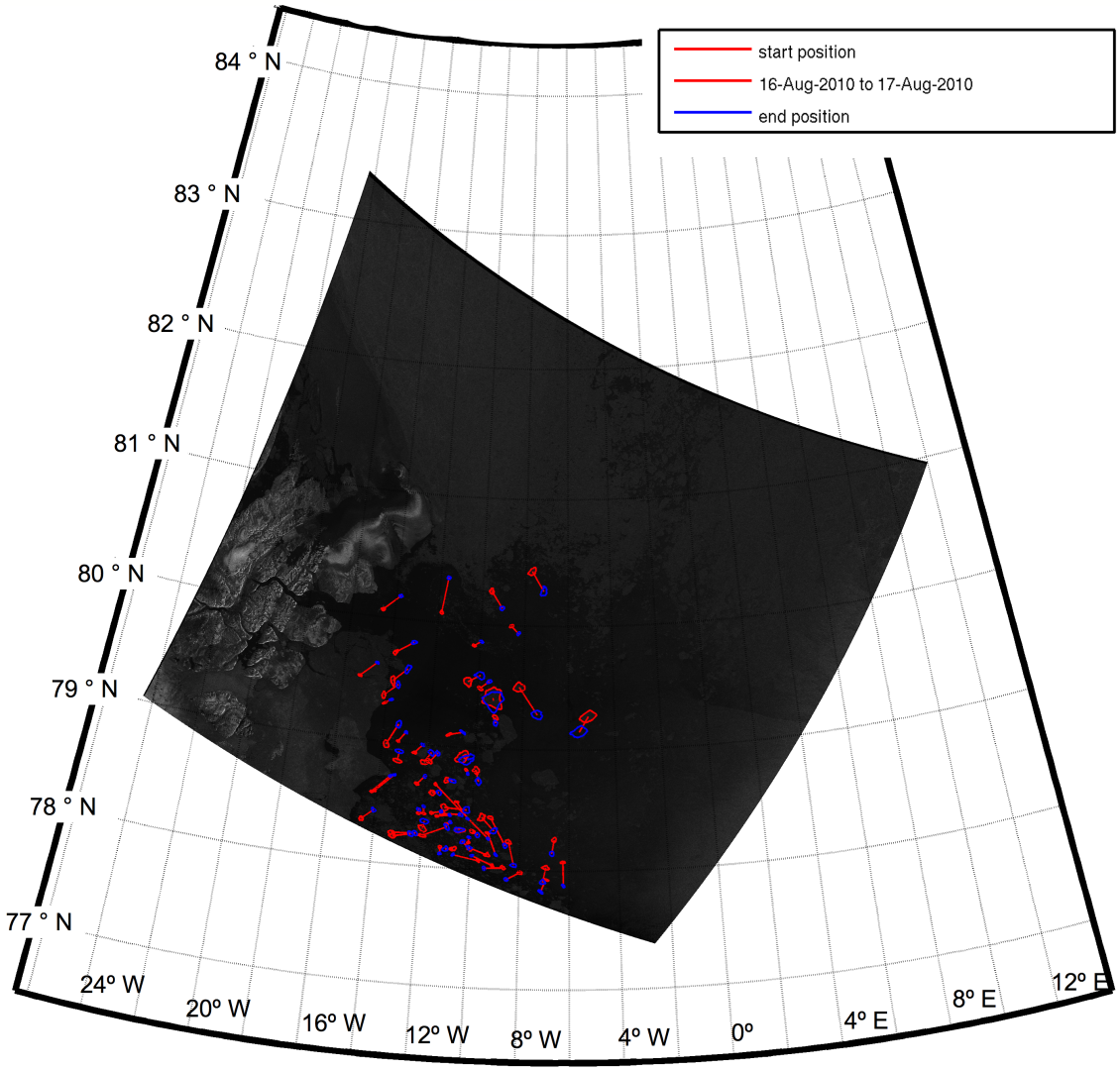

Figure 8.1: Ice object movement, between 16 August (08:07)- 17 August (07:37). The underlying image is from the 16 August. Start point objects in red, finish point objects in blue.

8.2 Results

Figure 8.1 shows how the type of objects that can be identified and tracked appear on the first Radarsat image from 16 August 2010. The East Greenland coast can be seen in the west of the image, with fast ice extending from the coast into the Strait from 14° -8° W. A polynya (area of open water) can be seen adjacent to the Greenland coast at 80° -81° N, extending into the Strait to around 6° W and south alongside the fast ice edge. Many of the objects tracked in this study are floes moving across this polynya.

Table 8.2 details the number of objects tracked from each image pair, with average speed, distance and direction of travel. Over the course of the month the average direction of movement is 158° towards the south west. This reflected the direction of movement of the East Greenland Current, and also the forcing of the prevailing winds, which this month are from the north east. The ongoing southward movement is punctuated by episodes on the shorter temporal resolution of 1 - 2 days where ice moves in other directions defined by variations in wind direction on the same time scale.

Movement vectors from six image pairs between 16 - 26 August are mapped in Figure 8.2. The beginning of the study period (16 - 24 August) is characterised by high pressure over the Greenland coast (Figure 8.3), with a brief interlude of low pressure in the area on the 19 August. Clockwise flow between the isobars of this high pressure zone creates northerly winds in the Fram Strait (Figure 8.3). By 23 August the high pressure zone is moving offshore into the Strait. This is likely to generate southerlies that would move the ice towards the north east (NB: these do not appear in the reanalysis data, Figure 8.4, possibly due to scale).

In the first match (16-17 August) the average flow direction is towards the west at an average speed of 0.17 $\pm$ 0.12 m s $^{-1}$. Between the 16-17 August the prevailing wind is having an effect on ice movement but other factors also appear to play a part. These may include local wind on scale too small to be picked up in the

Table 8.2: Number of objects tracked from each image pair, with average speed, distance and direction of travel

Start Date and time	End Date and time	No of Matches	Average speed (m s^{-1})		Average distance (km)		Average direction (°)	
16-08-10 08:07	17-08-10 07:37	65	0.17	± 0.12	14.5	± 10	104	± 92
17-08-10 07:37	19-08-10 08:19	22	0.14	± 0.05	25.27	± 10	210	± 44
19-08-10 08:19	20-08-10 07:50	15	0.21	± 0.21	18.01	± 18	111	± 101
20-08-10 07:50	23-08-10 08:02	18	0.06	± 0.05	16.39	± 13	318	± 95
23-08-10 08:02	24-08-10 07:33	24	0.29	± 0.04	24.90	± 3	28	± 66
24-08-10 07:33	26-08-10 08:15	20	0.18	± 0.04	30.86	± 7	227	± 30
26-08-10 08:15	30-08-10 07:58	22	0.10	± 0.05	34.32	± 18	107	± 45
26-08-10 08:15	30-08-10 07:59	15	0.14	± 0.07	48.92	± 25	131	± 52
30-08-10 07:58	31-08-10 07:29	37	0.38	± 0.07	32.30	± 6	29	± 9
31-08-10 07:29	02-09-10 08:11	40	0.16	± 0.05	27.75	± 8	197	± 19
02-09-10 08:11	03-09-10 07:41	50	0.13	± 0.06	11.10	± 5	57	± 87
01-09-10 12:00	01-09-10 20:17	14	0.43	±0.2	12.72	± 6	27	±126
01-09-10 12:00	02-09-10 21:26	26	0.25	± 0.19	30.63	±23	76	± 35
02-09-10 21:26	03-09-10 20:54	15	0.26	± 0.11	22.03	±9	223	± 36
03-09-10 20:54	04-09-10 20:23	8	0.22	± 0.17	18.77	± 14	324	± 110
04-09-10 12:06	05-09-10 21:31	9	0.14	± 0.08	16.62	± 10	81	± 26
04-09-10 20:23	05-09-10 21:31	3	0.28	± 0.21	24.95	± 19	44	± 153
05-09-10 21:31	06-09-10 21:00	28	0.28	± 0.09	23.51	± 8	237	± 42
06-09-10 21:00	07-09-10 12:11	22	0.28	± 0.16	15.43	± 9	183	± 76
06-09-10 21:00	08-09-10 21:37	6	0.12	± 0.05	26.19	± 11	66	± 45
08-09-10 21:37	09-09-10 21:06	18	0.31	± 0.09	13.83	± 4	347	± 83
09-09-10 21:06	10-09-10 12:17	12	0.31	± 0.15	18.25	± 8	157	± 39
10-09-10 12:17	11-09-10 11:45	14	0.28	± 0.20	23.57	± 17	31	± 131
11-09-10 11:45	13-09-10 12:23	11	0.09	± 0.03	15.69	± 6	188	± 23
13-09-10 12:23	14-09-10 11:51	6	0.27	± 0.14	22.56	± 12	320	± 6
14-09-10 11:51	15-09-10 21:17	2	0.25	± 0.04	30.25	±5	249	± 16
15-09-10 21:17	16-09-10 12:28	19	0.39	± 0.20	21.53	±11	194	± 19
Averages		20.03	0.23		23.00		158	

reanalysis data set; or ocean currents. One possibility is that an eddy is forming adjacent to the fast ice edge between 78° and 79° N (Figure 8.4a). Mesoscale eddies can fluctuate on daily timescales, so would not be present in surface ocean data (were it available for this month) or be visible in ice movement data over a longer period.

Between 17 August (07:37) - 19 August (08:19) 22 objects are tracked. The average direction of movement is now 210 ± 44 ° (towards south west), while the average speed is 0.14 ± 0.05 m s $^{-1}$. This appears to be a straightforward case of Ekman flow at 45° to the right of the wind direction (Figure 8.4b). In the next image pair; 19 - 20 August there are 15 objects tracked; the average direction of movement changes again, towards the south, with the exception of a couple of objects near the ice edge going in the opposite direction. Those off shore are better aligned with the wind vectors than near shore. It is possible that local near shore winds may be misaligned with larger wind pattern on a spatial scale that is not visible in the reanalysis data set. The winds are weak, so it is also possible that ocean currents may be the dominant forcing at this time.

Movement between 20 - 23 August is not dissimilar to the previous set of matches. Between the 20-23 winds are again weak. Ekman flow may be present in some vectors. There is some evidence to suggest that an eddy may still be present adjacent to the fast ice edge. Flow away from the fast ice edge on the 23 August may be due to katabatic winds flowing off the Greenland Ice Sheet. Between 23 - 24 August travel turns towards the north east, then returns southwest between the 24 - 26 August (several of the same objects have been tracked here as in the previous match, continuous tracks are visible in Figure 8.2). Between the 23 - 24 August the wind direction does not correspond at all well to ice movement vectors, whereas between the 24 - 26 August Ekman flow is again apparent.

Movement vectors generated from six matches between the 26 August - 3 September are shown in Figure 8.5. The high pressure system described in the previous section moves eastwards into the Strait (Figure 8.6) during the early part of this

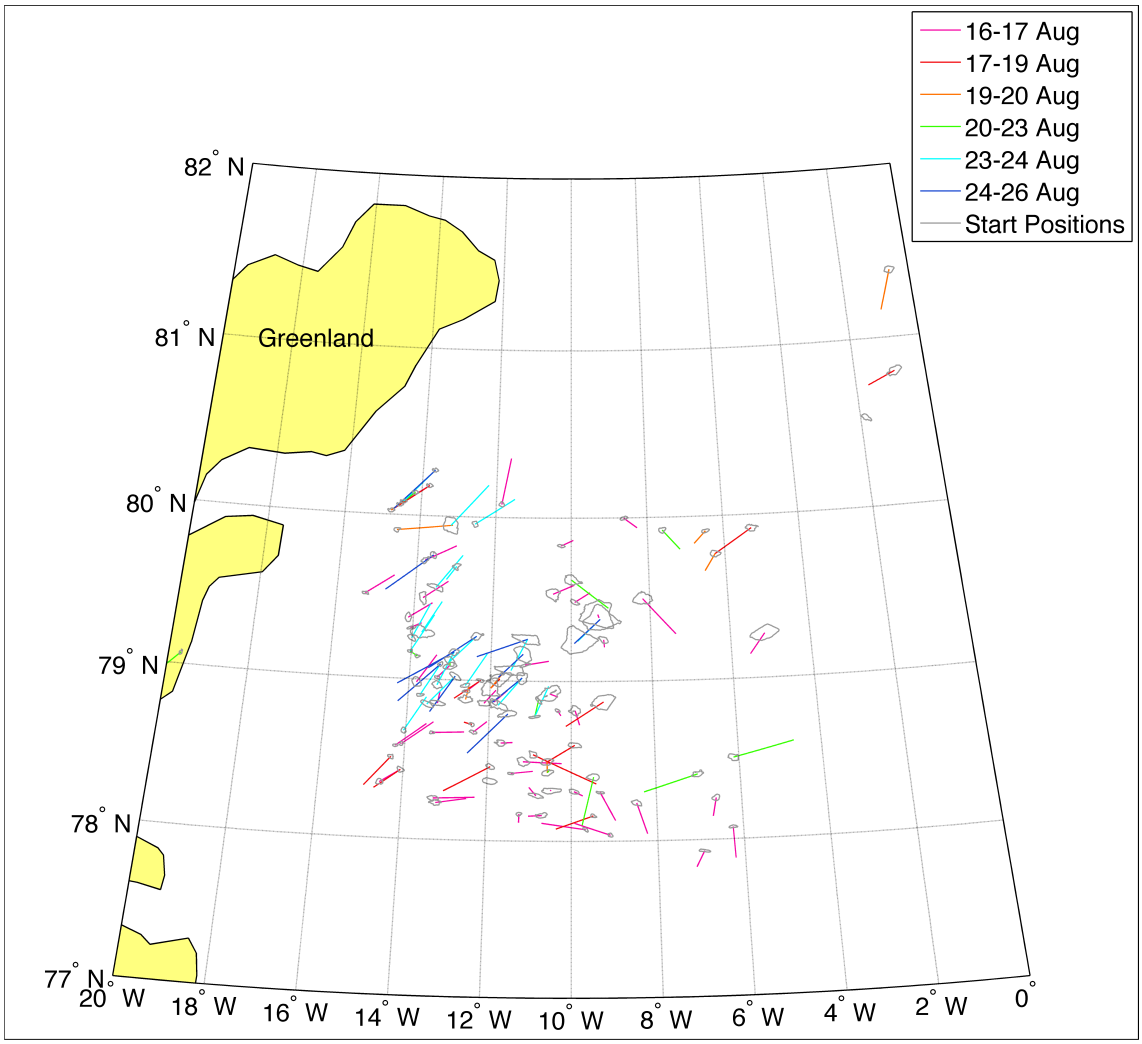

Figure 8.2: Ice movement between 16-26 August.

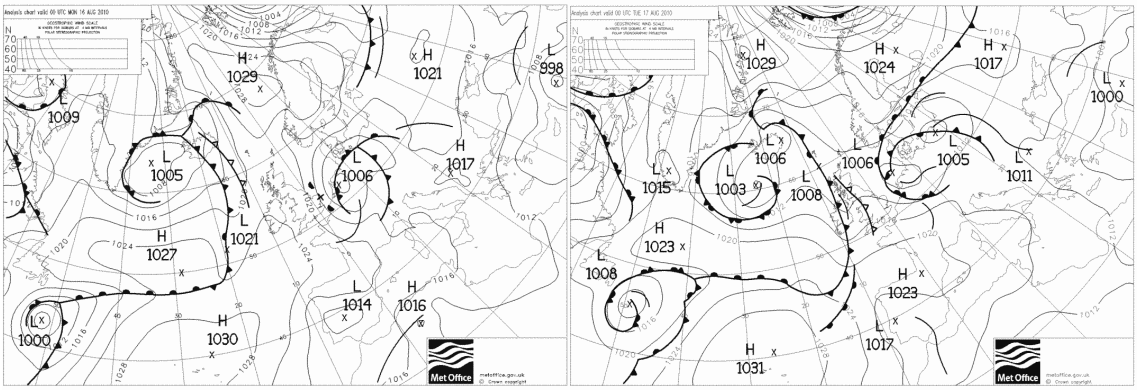

(a) 16-08-2010 (b) 17-08-2010

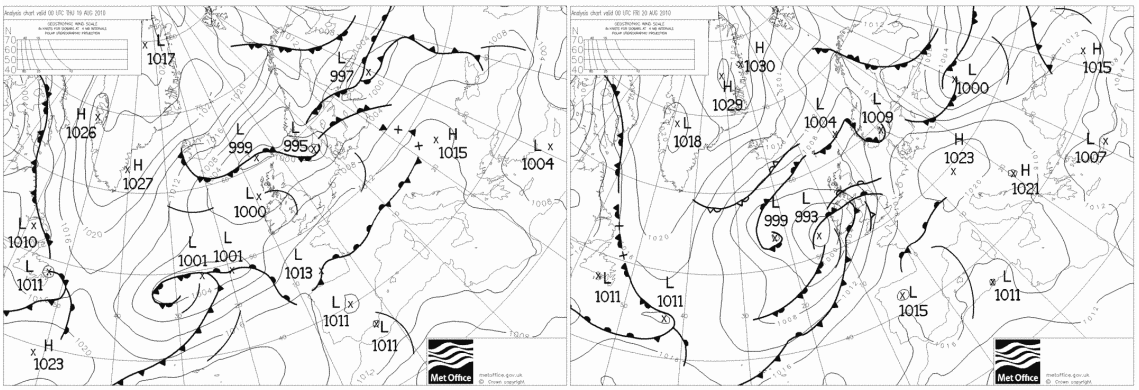

(c) 19-08-2010 (d) 20-08-2010

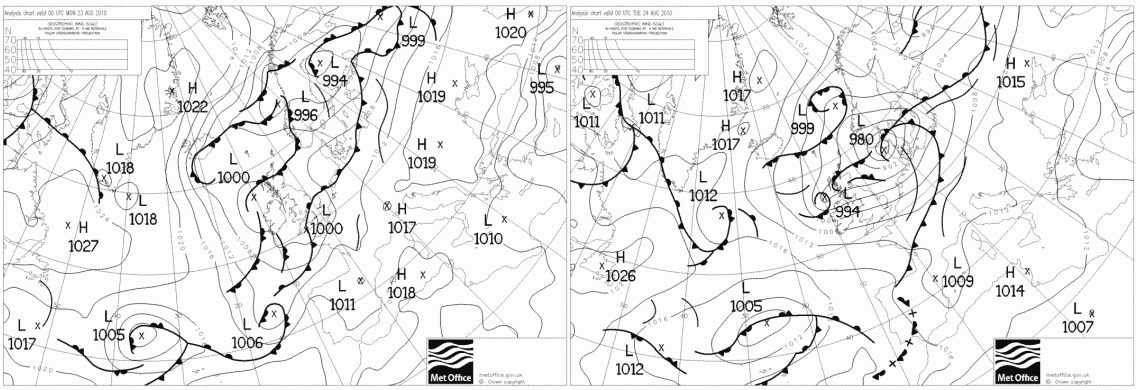

(e) 23-08-2010 (f) 24-08-2010

Figure 8.3: Change in surface air pressure between 16 - 24 August 2010. From UK Met Office data available at www.wetterzentrale.com.

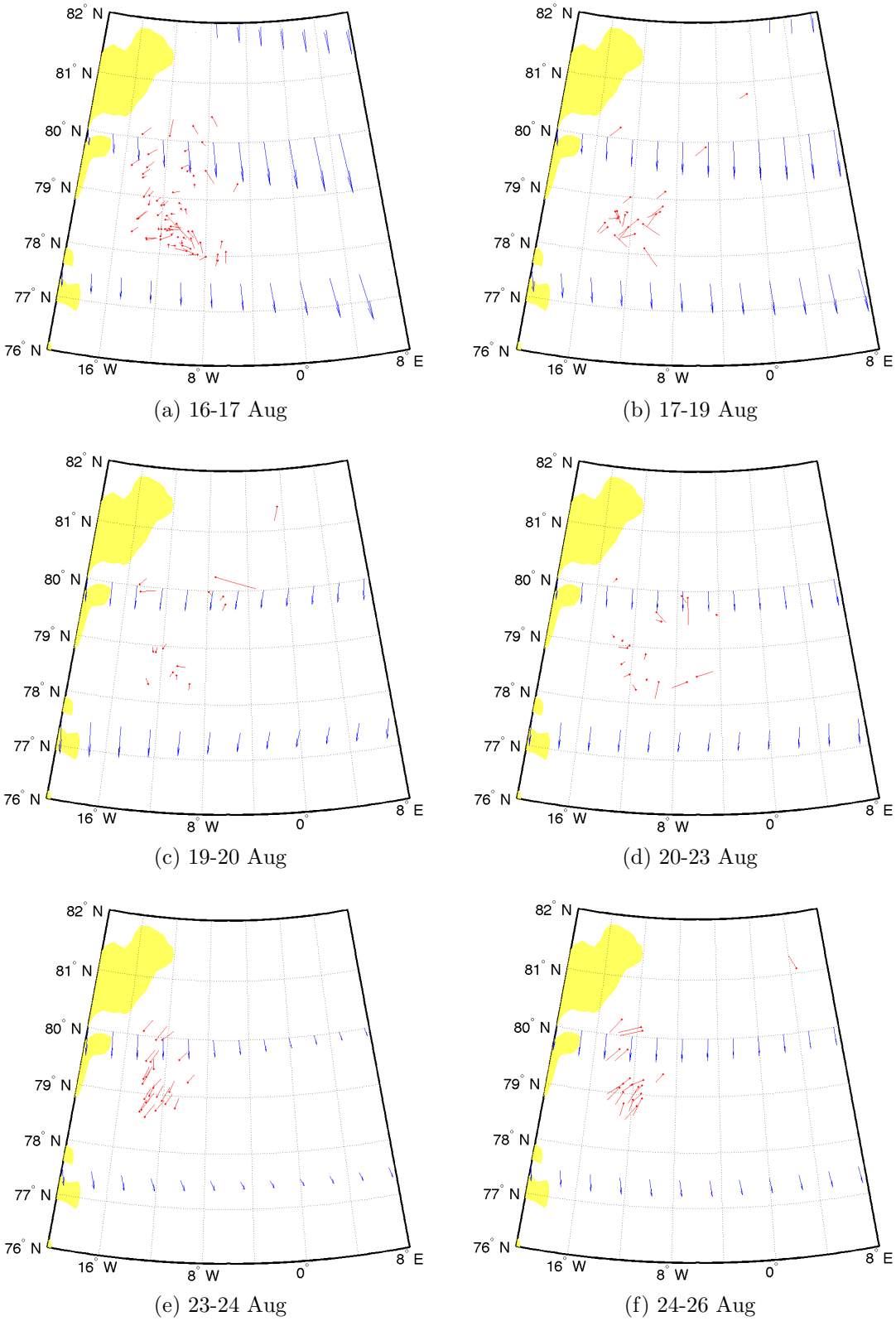

(a) 16-17 Aug

(b) 17-19 Aug

(c) 19-20 Aug

(d) 20-23 Aug

(e) 23-24 Aug

(f) 24-26 Aug

Figure 8.4: Direction of travel compared to wind vectors for first 6 matches (16-26 August).

period, characterised by light winds (Figure 8.7). Between 31 August - 3 September southerly winds are generated over the Fram Strait by the presence of high pressure to the south east and low pressure to the west.

There are two images from the 30 August, each image contained some of the objects from the image on the 26th. Between the 26 August and the first image on the 30 August (07:58) 21 objects were tracked. The average speed is 0.09 ± 0.05 m s $^{-1}$, towards the east and southeast, with vectors further north having a more easterly trajectory. It is important to be aware that this is over 4 days so the ice may have gone back and forth in that time. This illustrates the overarching effect of the East Greenland Current on longer temporal scales. Between the 26 August and the second image on the 30 August (07:59) 15 objects were tracked, some also moving to the south east but some others moving south west. Between the 26 - 30 August the direction of movement is also broadly in agreement with the wind direction from reanalysis (Figures 8.7a and 8.7b).

Thirty - six objects were tracked between 30 - 31 August at an average speed of 0.38 ± 0.07 m s $^{-1}$, towards the north east (29 °). Between 31 August - 2 September 39 objects were tracked, moving south west at an average speed of 0.15 ± 0.05 m s $^{-1}$. In the final matching exercise in this set, between the images from 2 September - 3 September, 50 objects were tracked, again flow has reversed and the objects are heading back to the north east. Between 31 August - 02 September ice movement is contrary to the surface winds from reanalysis, whereas by the 02 - 03 September they are in agreement, suggesting that there may be a lag time between the change in wind direction from weak north easterlies between 30 - 31 August to strengthening south westerlies between 31 August - 3 September.

Matches between 3 - 9 September are mapped in Figure 8.9, while matches between 9-16 September are mapped in Figure 8.12. During this period the average speeds vary between 0.06 - 0.44 ms^{-1}, and the distances travelled by the tracked objects vary between 6 - 30 km. High pressure continues to dominate the south east of the region, with low pressure weakly established to the west until the 9 September,

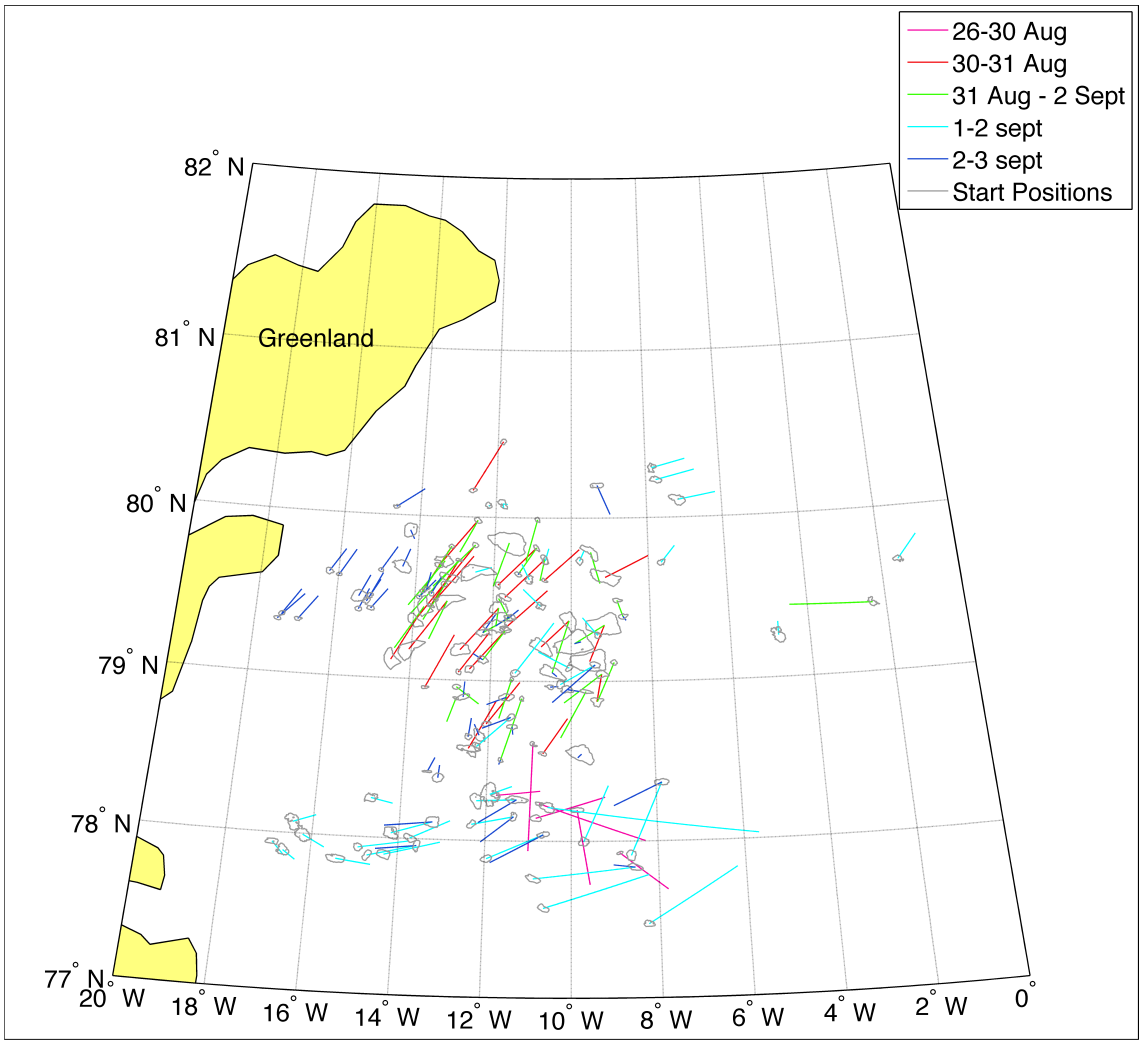

Figure 8.5: Ice movement between 26 August - 3 September.

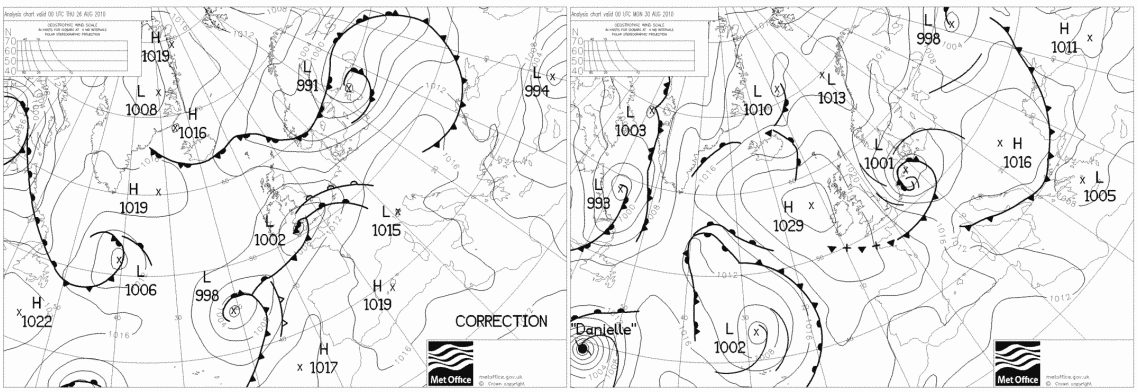

(a) 26-08-2010 (b) 30-08-2010

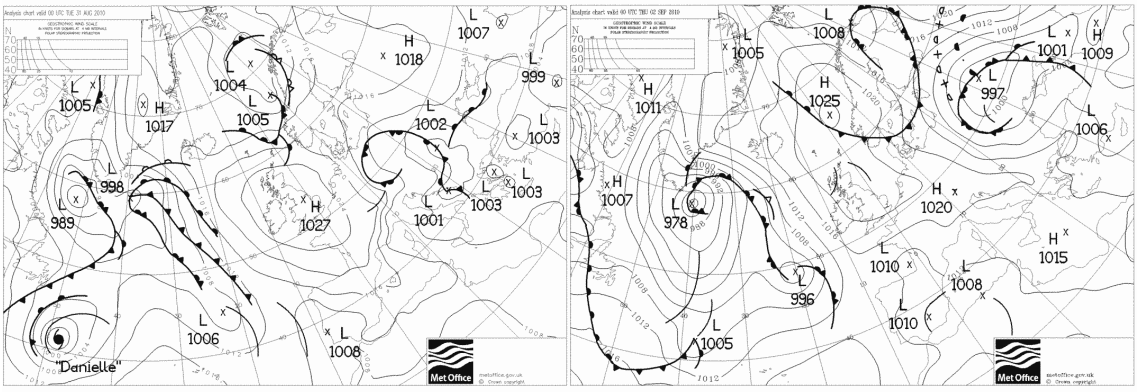

(c) 31-08-2010 (d) 02-09-2010

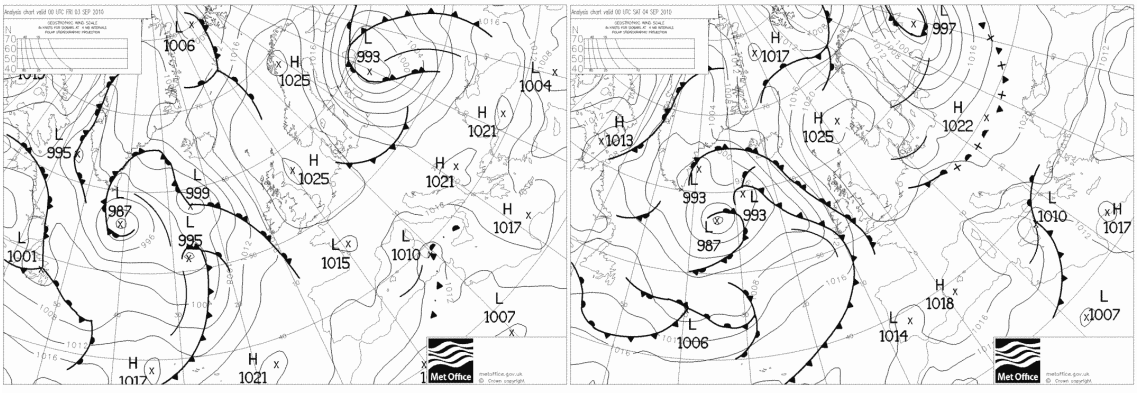

(e) 03-09-2010 (f) 04-09-2010

Figure 8.6: Change in surface air pressure between 26 August - 4 September 2010. From UK Met Office data available at www.wetterzentrale.com.

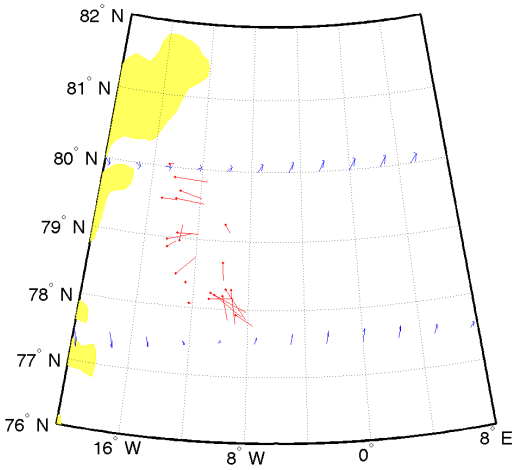

(a) 26-30a Aug

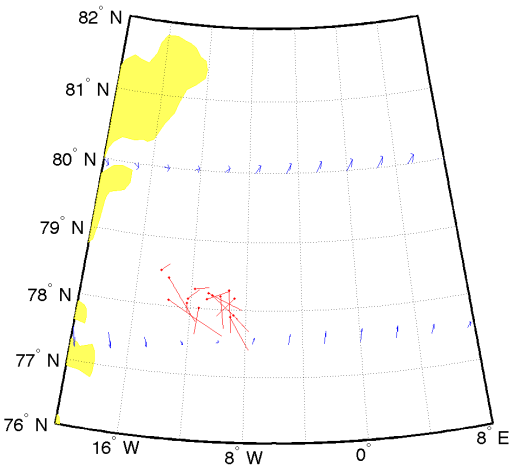

(b) 26-30b Aug

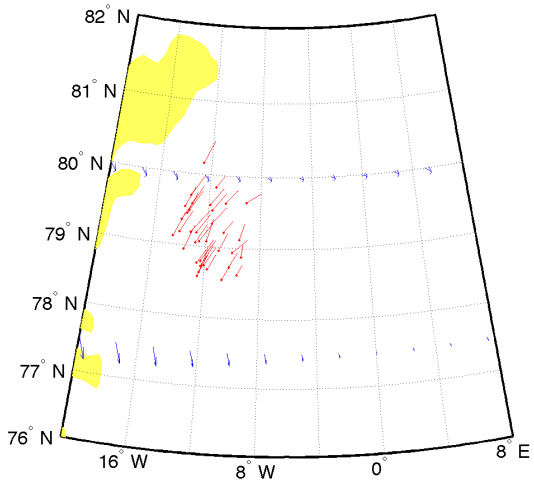

(c) 30-31 Aug

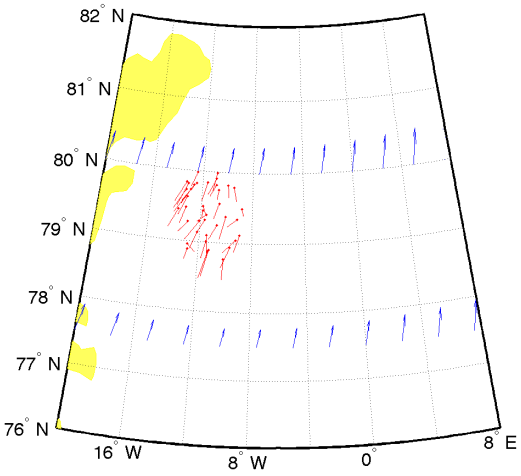

(d) 31 Aug -02 Sept

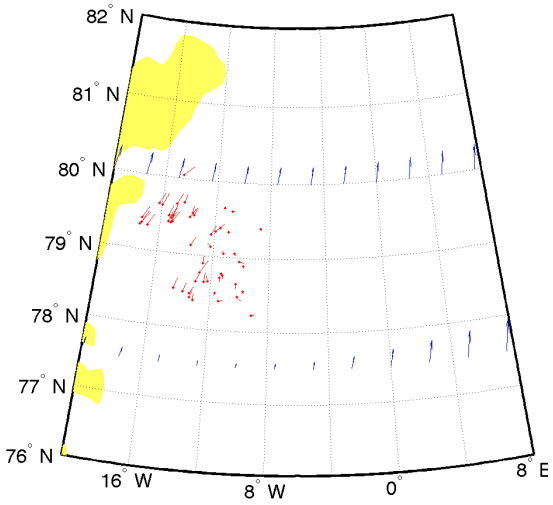

(e) 02 - 03 Sept

Figure 8.7: Direction of travel compared to wind vectors for (26 August - 3 September.

when a low pressure system begins to establish itself in the Strait (Figure 8.10). This situation promotes northerly winds (Figure 8.11). From the 11 -16 September the Fram Strait area is dominated by a deepening low pressure system (Figure 8.13). The movement of this system can be seen in the fluctuating winds between 9 - 14 September, then as the low deepens to the south east of the study area the winds strengthen into strong northerlies (Figure 8.14).

Between 12:00 and 20:17 on 1 September there is an even spread of movement vectors from north west to north east. This is only an 8 hour period and falls at the right time of day for katabatic winds to be influencing ice movement. Over a slightly longer time; 12:00 1 September - 21:26 2 September, movement veers towards the north east (Figure A.4). Between the 3-5 September the ice appears to be being pushed off shore (towards the east), at a location where the wind is weak. Again I hypothesize that this may be influenced by katabatic winds from the Greenland Ice Sheet. Between the 5 -6 September movement is towards the south west at around 79° N, swinging towards the west at around 79° N. This is not in agreement with the wind direction shown by the reanalysis data.

Between the 6-7 movement is in agreement with the wind forcing; towards the south east, while between the 6 - 8 the influence of local off shore winds again appears to play a part and movement is towards the west. Between the 8-9 there are many vectors moving west but also some going east.

Between 9-10 September there is a clear trend towards the south east, this reverses towards the north 10-11 then again south between 11-13 (NB: this last pair may cover a long enough time period that the EGC is the dominant force). These changes of direction are coincident with, or slightly lag, changes in the wind direction (Figure 8.14). Between 13-14 movement towards the north west appears to be a product of the southeasterly winds shown in the wind vectors of the 11 -13 September. As winds revert to northerlies from the 14 September; ice movement shifts back towards the south for the remainder of the month.

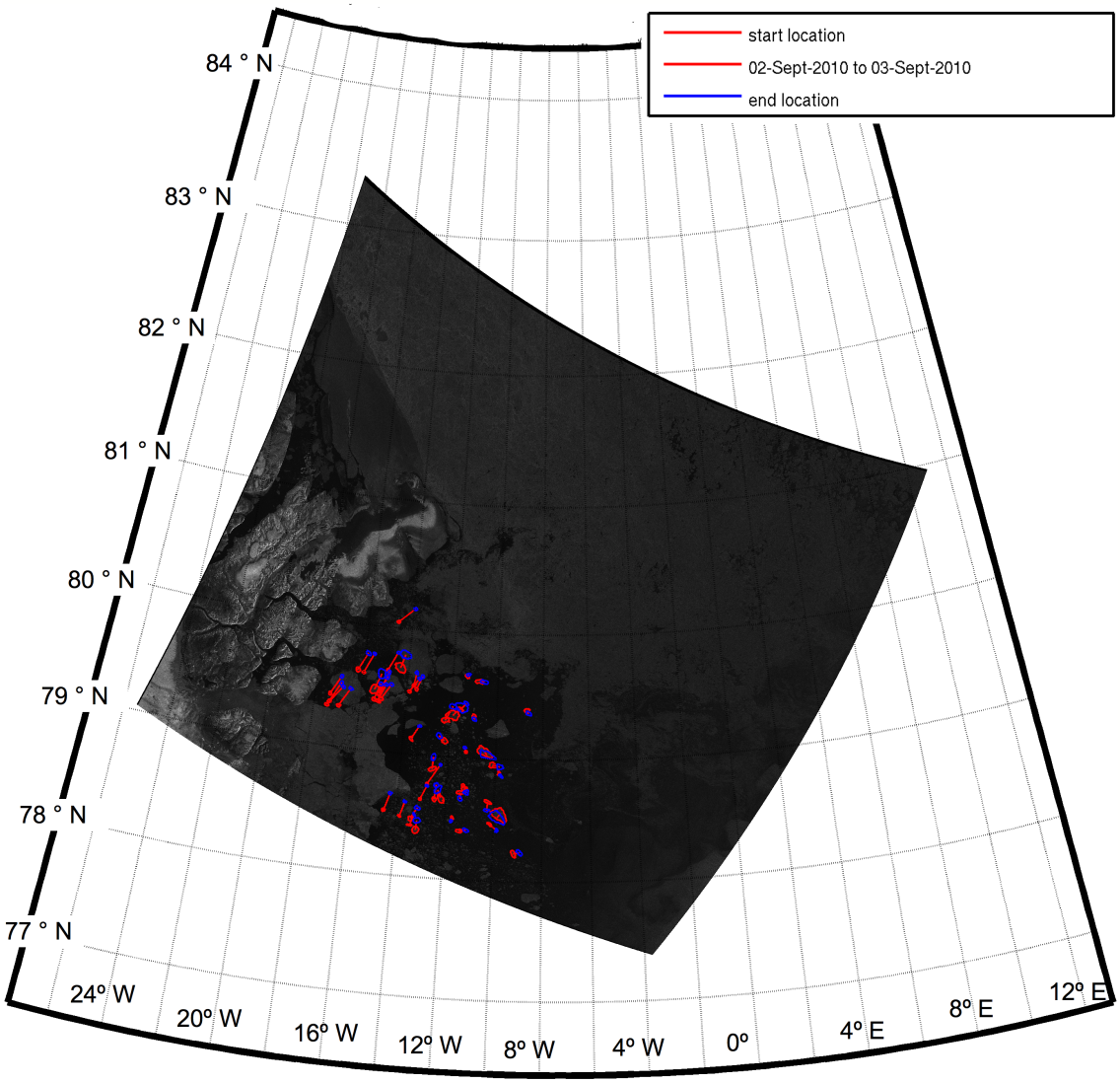

Figure 8.8: Example from 2 - 3 September. 50 ice objects have been tracked. The start location is shown in red, and the end location in blue. This image also shows that there is still an area of open water adjacent to the fast ice edge.

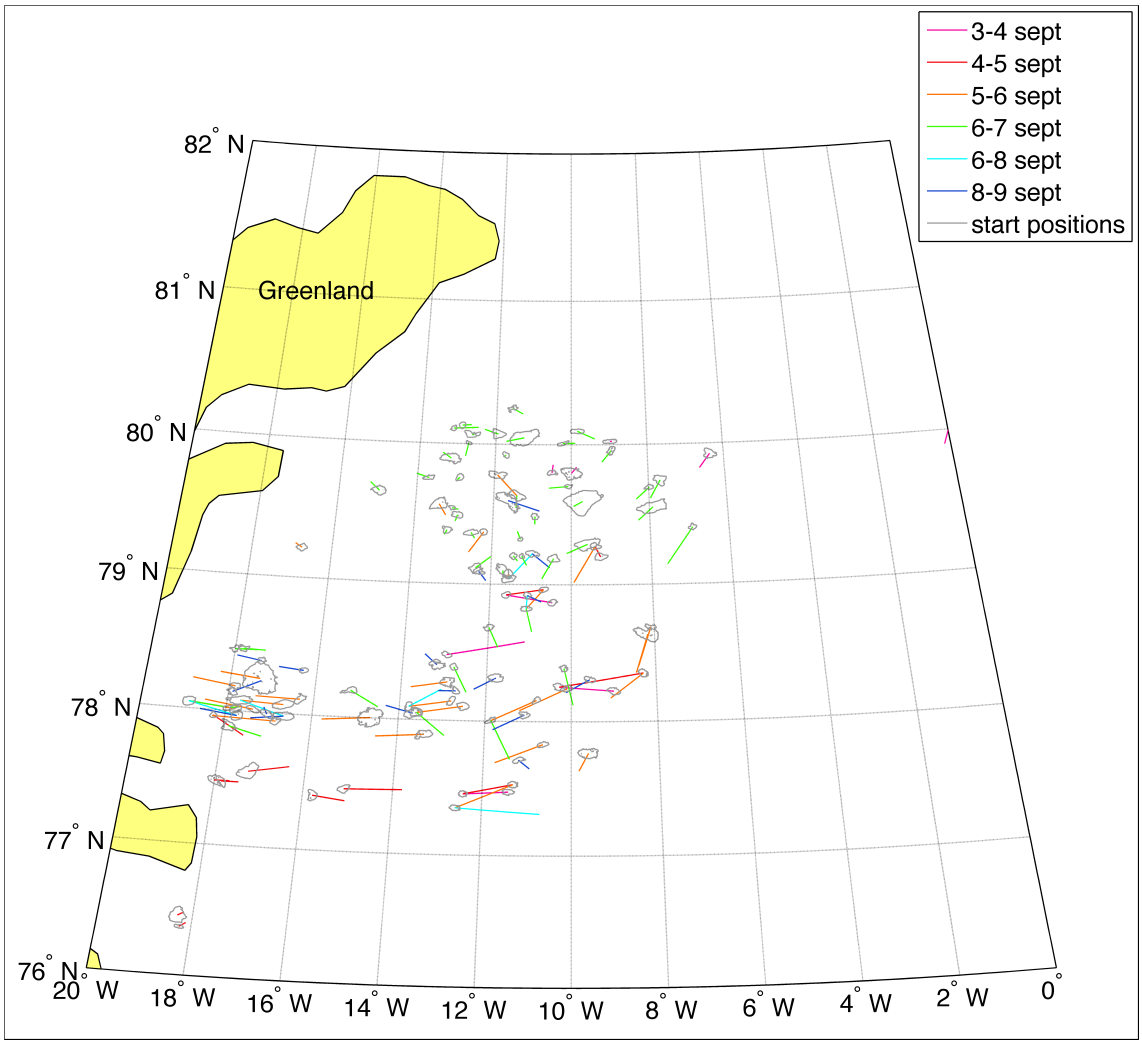

Figure 8.9: Ice movement between 3-9 September.

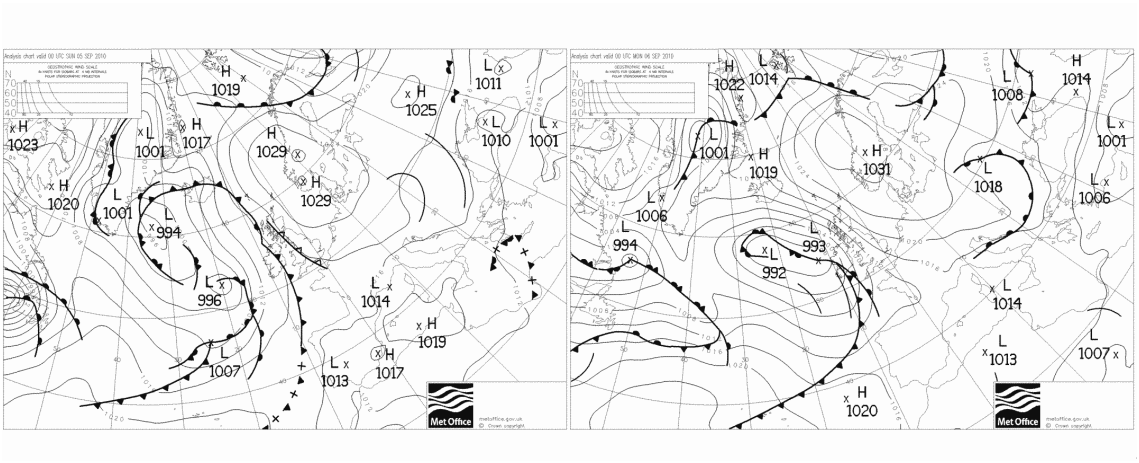

(a) 05-09-2010 (b) 06-09-2010

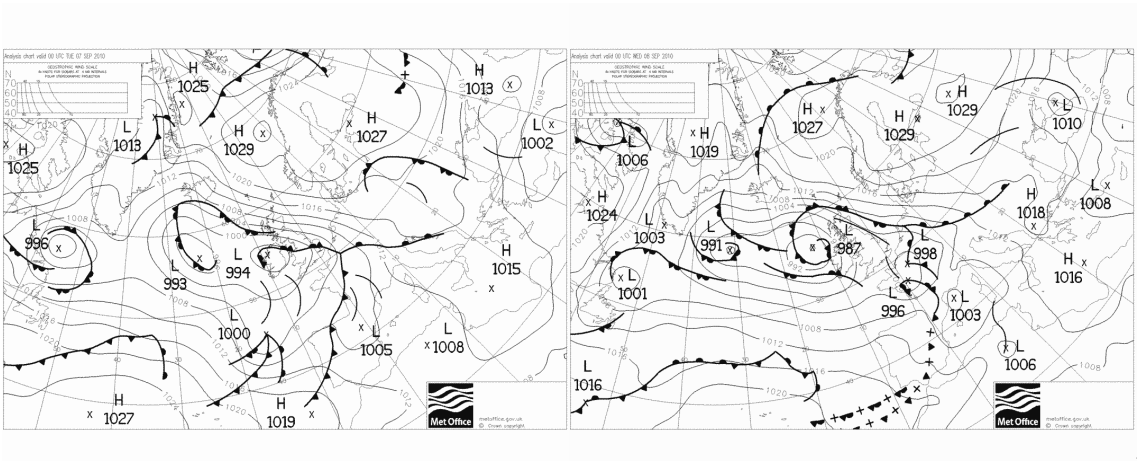

(c) 07-09-2010 (d) 08-09-2010

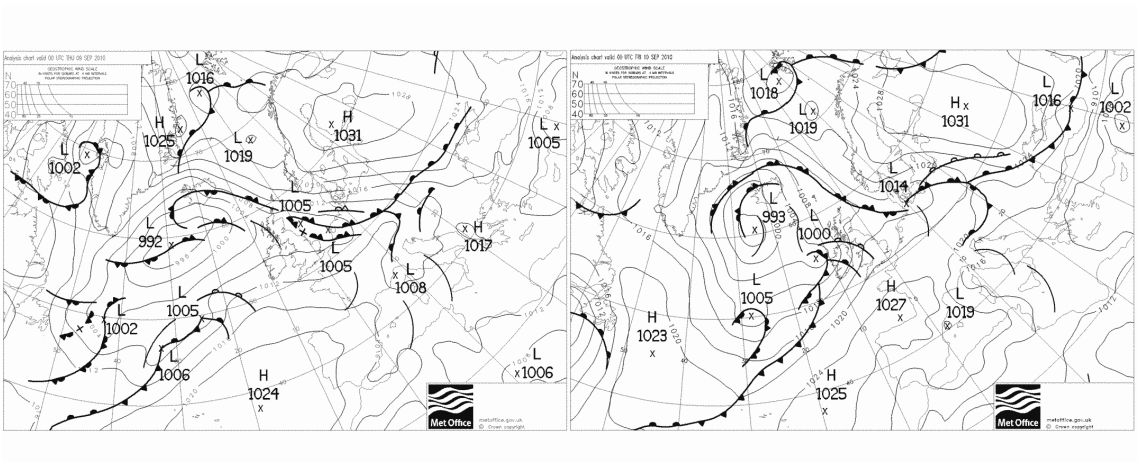

(e) 09-09-2010 (f) 10-09-2010

Figure 8.10: Change in surface air pressure between 5 - 10 September 2010. From UK Met Office data available at www.wetterzentrale.com.

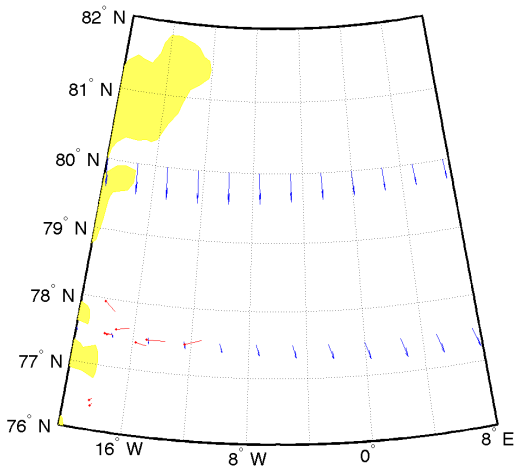

(a) 03 - 04 Sept

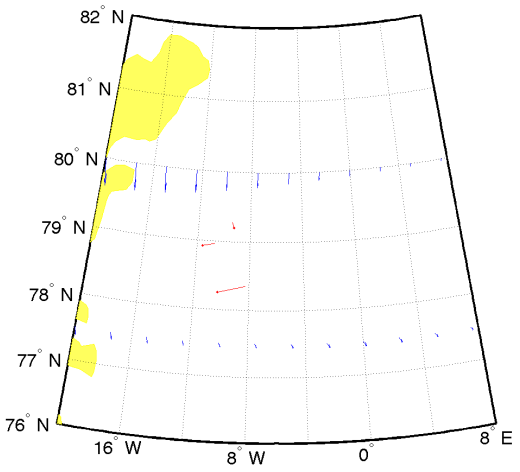

(b) 04 - 05 Sept

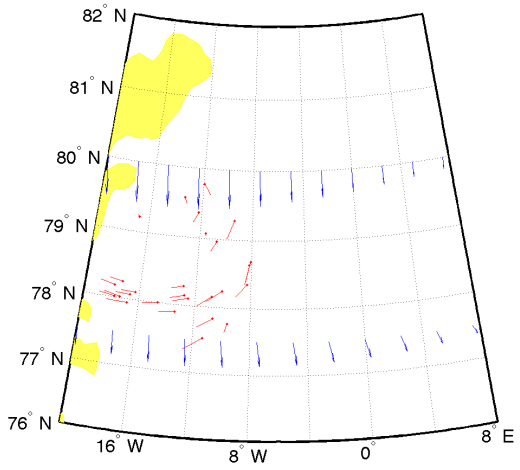

(c) 05 - 06 Sept

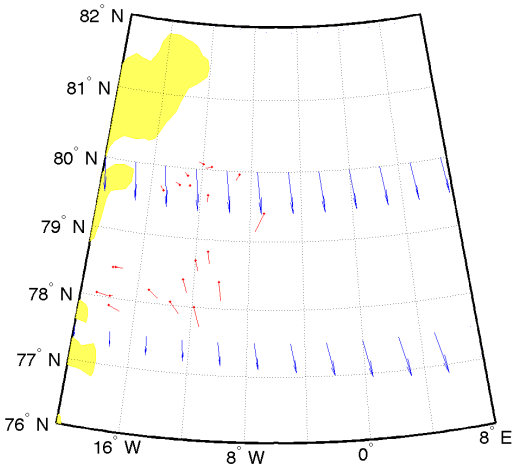

(d) 06 - 07 Sept

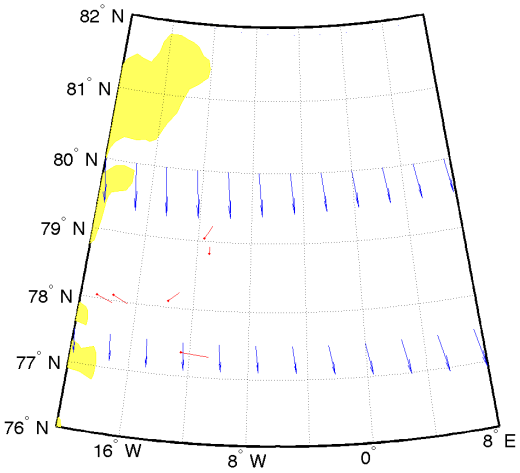

(e) 06 - 08 Sept

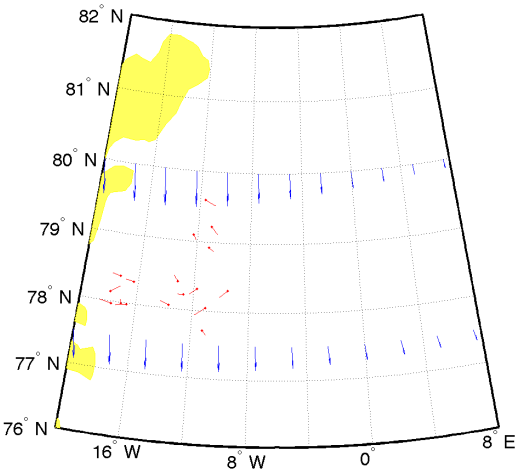

(f) 08 - 09 Sept

Figure 8.11: Direction of travel compared to wind vectors for 03 - 09 September.

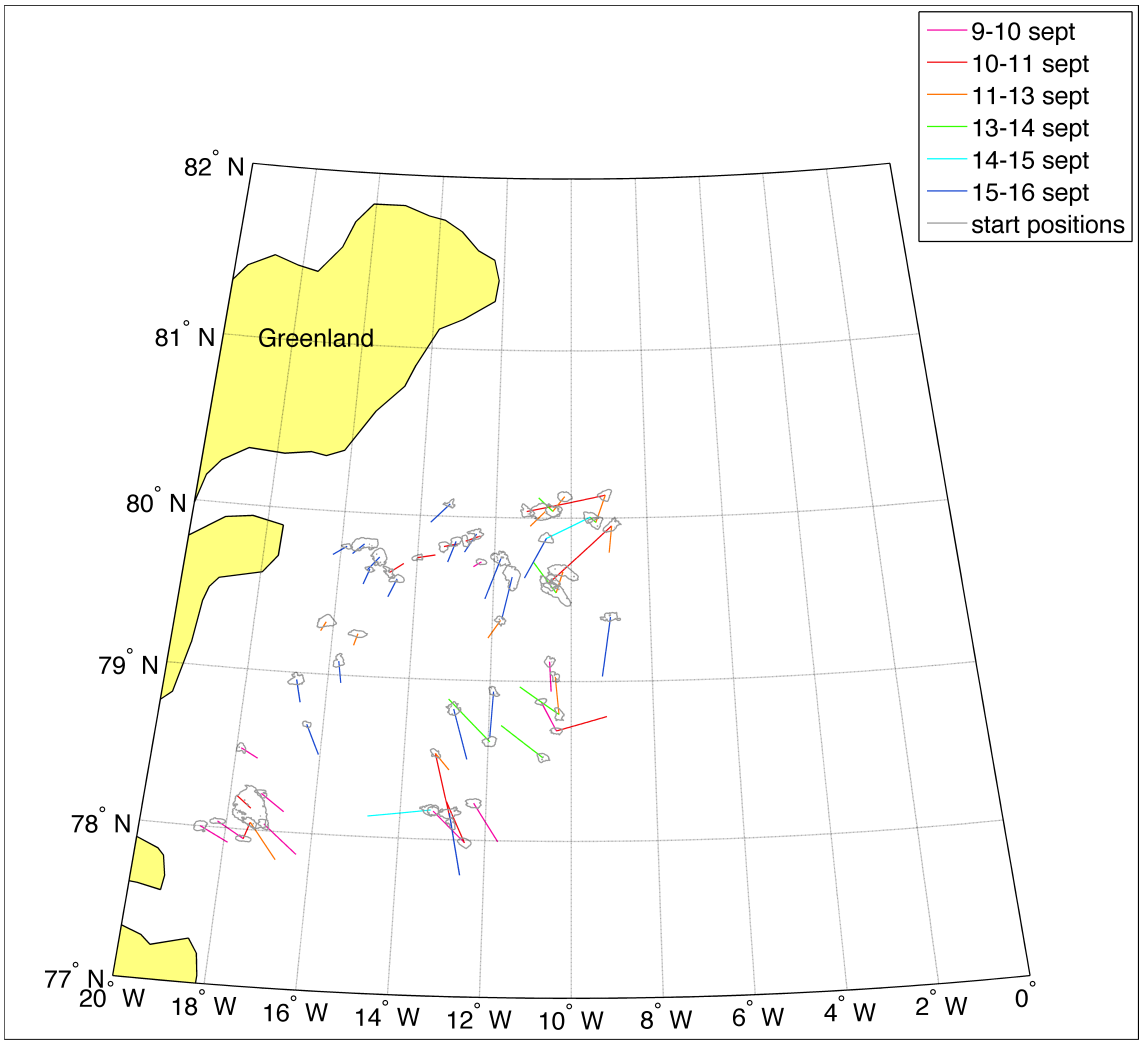

Figure 8.12: Movement vectors between 9-16 September.

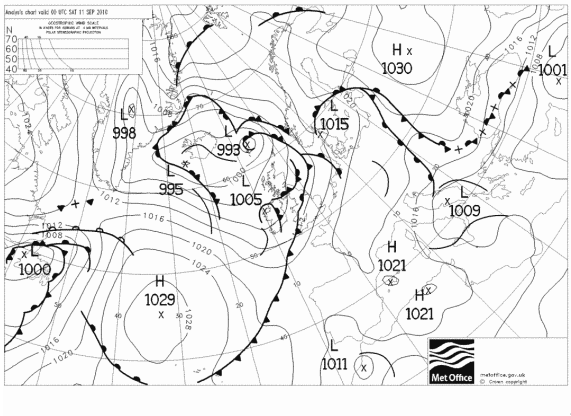

(a) 11-09-2010

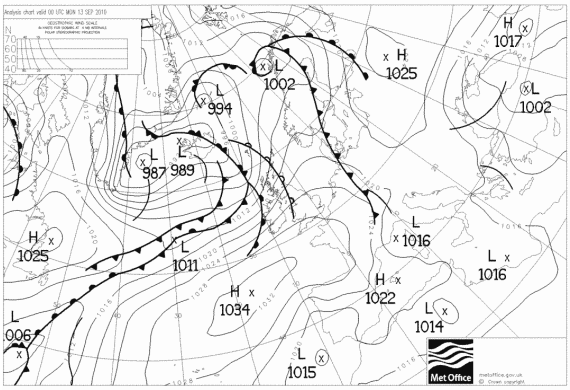

(b) 13-09-2010

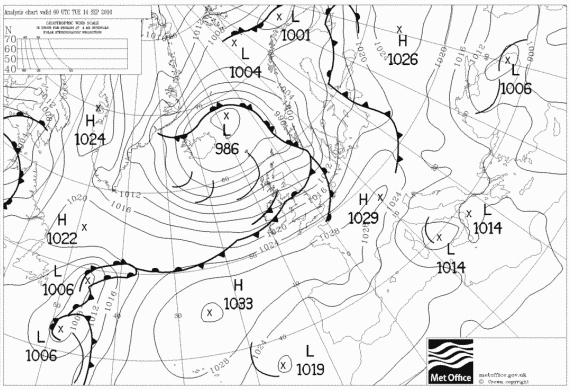

(c) 14-09-2010

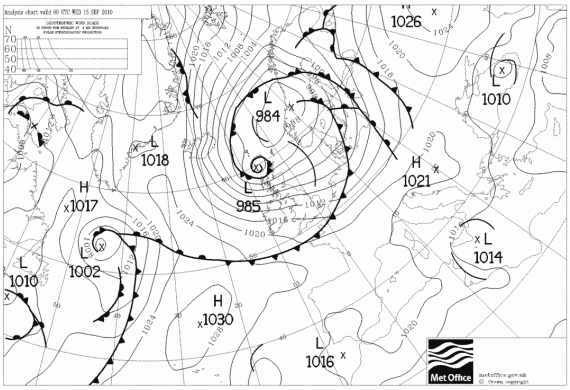

(d) 15-09-2010

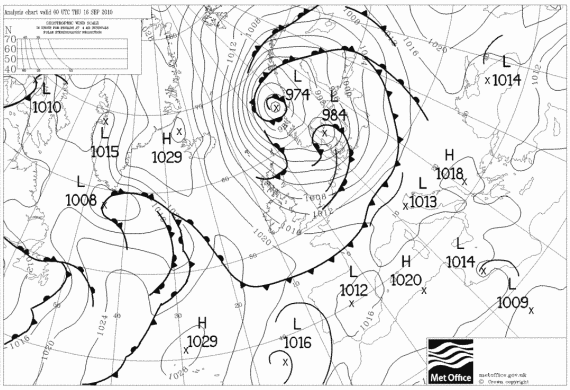

(e) 16-09-2010

Figure 8.13: Change in surface air pressure between 11 - 16 September 2010. From UK Met Office data available at on www.wetterzentrale.com.

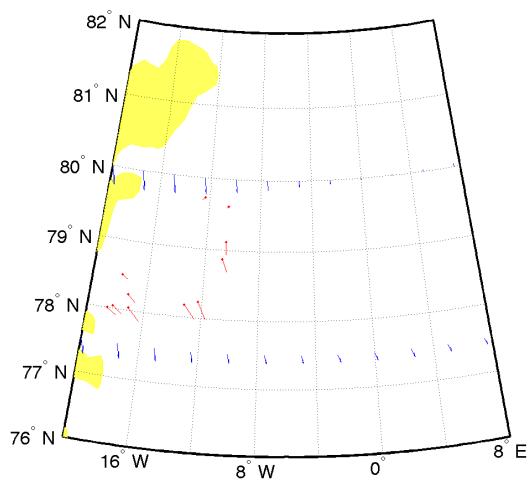

(a) 09 -10 Sept

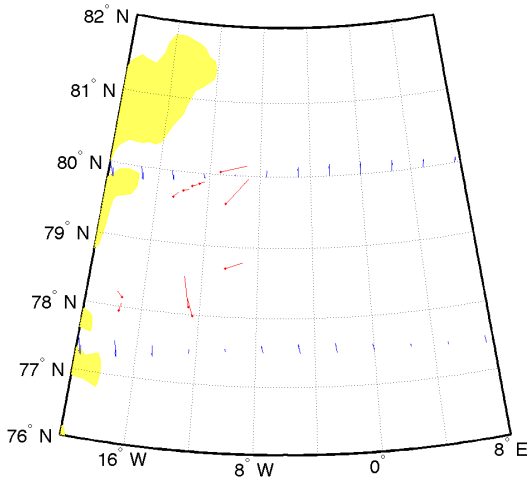

(b) 10 - 11 Sept

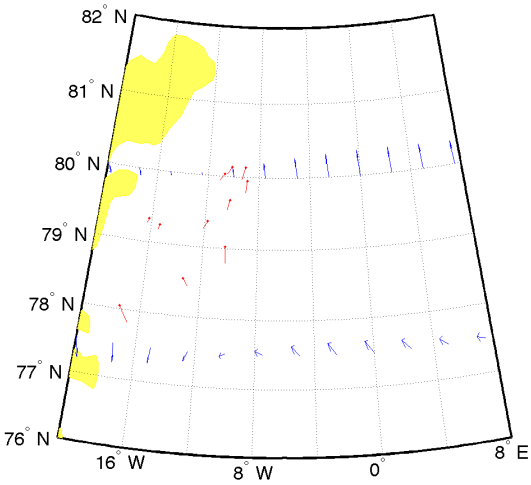

(c) 11 - 13 Sept

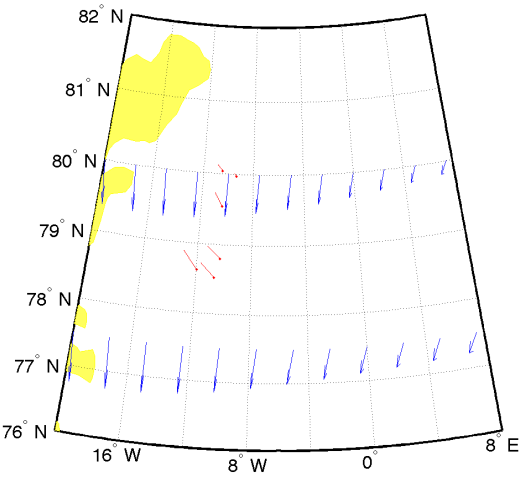

(d) 13 - 14 Sept

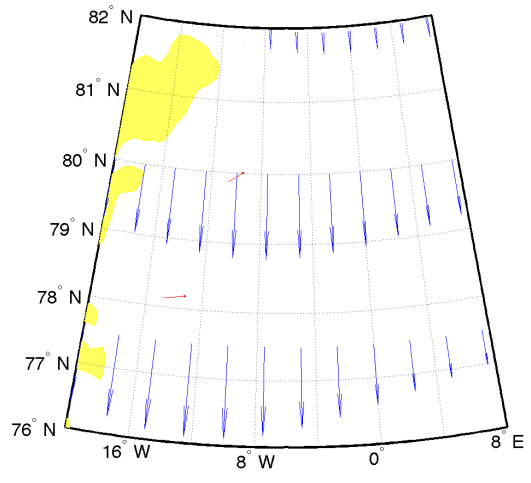

(e) 14 - 15 Sept

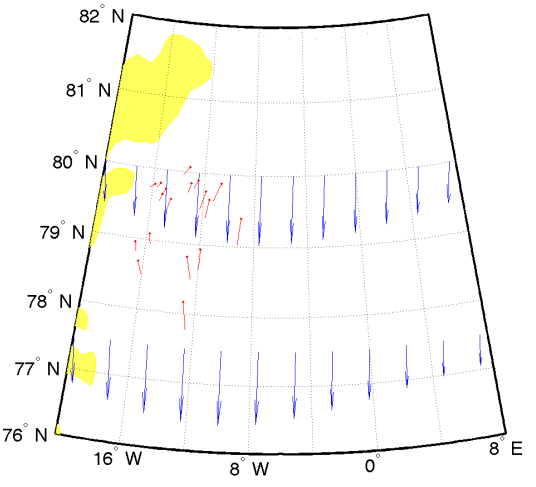

(f) 15 - 16 Sept

Figure 8.14: Direction of travel compared to wind vectors for 03 - 09 September.

8.3 The influence of atmosphere and ocean forcing

The direction of ice movement is varied due to the interplay between ocean currents and wind forcing in the local area. On short temporal scales the wind strength and direction appears to be the dominant forcing on ice movement in this month, in agreement with Brummer et al. (2003). Both Brummer et al. (2003) and Germe et al. (2011) show that sea ice movement and extent is strongly affected by changes in sea level pressure and the winds associated with pressure systems in the surface atmosphere. The effects of the changing pressure systems in the area can clearly be seen in these results, for example the change in direction of movement between the 16th and 23rd August (Figure A.7) as the low pressure system moves away from the area and a high pressure system extends into the Fram Strait then decays again as the next low pressure system strengthens.

There are instances where the movement of the ice is not aligned with the surface winds in the reanalysis data, but the pressure charts for that day indicate that ice movement may be aligned with isobars, i.e. in line with winds that have not been represented in the reanalysis data. An example of this is the northward movement of ice between the 23rd and 24th August, which is against northerly winds on the reanalysis data, but the position of the high pressure over the Strait on the 24th August implies that southerly winds would be generated against the Greenland coast by airflow clockwise around the centre of the high.

Katabatic winds are well documented further south in east Greenland (Heinemann and Klein, 2002; Klein and Heinemann, 2002; Heinemann, 1999) and may also occur within the study area (although it is worth noting that Heinemann and Klein (2002) record that in the north-east no significant synoptic support of the katabatic winds is present and the synoptic pressure gradient is even opposed to the katabatic force in some regions). Katabatic winds are offshore winds that strengthen throughout the day. Where movement is towards the east but there is no evidence of wind flow

in that direction in the reanalysis data it may be that katabatic winds are present, for example on the 1st September and between the 3rd and 5th September.

Barrier winds (winds that occur when cold and stably stratified air is forced by synoptic scale flow towards a topographic barrier) may be generated when air flow towards the Greenland coast is deflected. A pressure gradient develops perpendicular to the barrier, resulting in an approximately geostrophic flow along the barrier and a higher windspeed (Petersen et al., 2009). This may be a contributing factor to rapid ice movement (0.39 m s^{-1}) adjacent to the Greenland coast as the cyclone develops between the 15th and16th September. Barrier flows have a significant ageostrophic component if there is a synoptic cyclone in close proximity (Petersen et al., 2009). Frequency of barrier winds correlates with the monthly North Atlantic oscillation index (Harden et al., 2011). Cyclone impact on sea ice depends on the location of the track within the Fram Strait. The more easterly the track, the larger the ice export (Brummer et al., 2008). My results support this finding, as the most rapid ice movement occurs when low pressure and cyclone patterns are present in the Fram Strait.

Where ice movement is not explained by surface wind it is thought the dominating factor is ocean surface currents. Schneider and Budeus (1997) describe a northward flowing current over the shelf north east of Greenland, connecting this current coupled with weak winds to the formation of a summer polynya adjacent to the fast ice edge. It is possible that the effect of this current can be seen in some of the vectors, for example between the 19th and 20th August when a couple of the ice movement vectors closer to the coast are moving towards the north instead of being pushed south by northerly winds.

There is some correlation between higher speeds and times when the wind forcing aligns with the East Greenland Current; for example between the 5th and 7th September and the 14th and 16th September. Not all of the highest speeds fit this pattern; for example that between the 30 th and 31st August does not. This indicates

that it is possible for strong winds to generate rapid movement against the flow of the East Greenland Current.

Further work that could be added to this analysis could include analysis of the 500hPa and 700 hPa geopotential height charts for additional information about the wind velocity as it is possible that the mean sea level pressure charts do not accurately represent airflow over Greenland. It would also be interesting to calculate the Ekman divergence as a proportion of the wind speed, to ascertain whether our data are in agreement with those presented in the literature (as discussed in Chapter 6). Most interestingly, it may be possible to use this data to derive information about the surface ocean currents in the area

I have demonstrated here that the variation in direction and speed of travel is greater on a shorter time scale. It is apparent that changes in wind direction drive changes in ice movement direction on daily and sub-daily time scales. I do not have enough data on the surface winds of the area to be certain of the provenance of some of the apparent wind forcing on our ice movement vectors, but it appears likely that barrier flows and katabatic winds complicate the picture suggested by surface pressure. Where the temporal resolution is longer than one or two days the influence of the East Greenland Current becomes more dominant, and overall movement is towards the south, for example between the 26th and 30th August (Figures 8.7a and 8.7b).

The results presented in this chapter, and the previous chapter, suggest that the prevailing wind speed and direction have a key impact on the rate of ice export through the Fram Strait. A period in which the wind forcing is in agreement with the East Greenland Current will see greater ice export than a period in which the two are acting in opposite directions.

Chapter 9

Conclusions

9.1 Introduction

The aims of this thesis were twofold: to demonstrate that the ITSARI algorithm could be used to track the movement of sea ice using imagery from a variety of different sensors, at different bands and resolutions; and to gain insight into how the ice export through the Fram Strait is influenced by local atmospheric and oceanographic forcings.

9.2 Using ITSARI to track the movement of individual Sea Ice floes

I demonstrate the use of ITSARI to track individual sea ice floes in three different areas, the Fram Strait, the Barents Sea and the Beaufort Sea. ITSARI is most effective where ice floes maintain their shape over the time period, and remain brighter (in dB) than their background, be it ice floes against water or multi-year ice surrounded by first year ice. There are two scenarios in the various case studies where ITSARI has been shown to be particularly effective:

- First year and multi-year ice against a background of open water
- 'Bright' multi-year ice against a background of first year ice

With regard to the first scenario ITSARI is shown to fill a niche in the world of sea ice remote sensing in that it works well in summer conditions, where traditional cross correlation methods fail. This is demonstrated by the late summer case study in Chapter 8. In particular ITSARI works well where adjacent floes are floating in a more open configuration, as they are thus easily distinguishable from each other against a background of open water, thus easy to segment. The second scenario is demonstrated in the autumn/ winter images from the 2008 case study, when there are multiyear ice floes against a background of first year ice. This could be useful if one was interested in looking specifically at the behaviour of multiyear ice, or if one were interested in movement dynamics of, or interactions between, different types of ice.

The Barents Sea case study serves mainly to illustrate the conditions under which ITSARI works the least well, namely very uniform ice cover (first year ice) with little distinguishing any one floe from those adjacent to it. It is possible that the prevalence of first year ice in the Arctic in recent years will limit the potential use of ITSARI in some areas in the future.

9.3 Using ITSARI with imagery from different sensors

In chapter 5 I demonstrate the adaptation of ITSARI to use with a different C band sensor, Radarsat, and with data from an X band sensor, Cosmo Sky Med. The technique is adaptable to the different sensors with very few problems. The brightness thresholds (dB) for the identification of ice objects are higher at X band than at C band. The size of the objects than can be tracked depends on how many pixels an object occupies, i.e. the object must occupy enough pixels to have a recognizable shape, so at higher resolution smaller objects can be successfully identified and tracked.

9.4 Using ITSARI to identify linear features

The use of this method to identify linear features such as the sea ice or fast ice edge or leads within the pack is also illustrated in several of the case studies: for example ice edges in the Fram Strait and leads in the Beaufort Sea.

9.5 Future algorithm development

ITSARI would benefit from further development in several ways. Firstly advantage should be taken of advances in computing power since the algorithm was first written to investigate the potential for improving the shape matching algorithm by, for example, calculating the shape vector using every degree instead of every 5 degrees, or using the fast Fourier transform to calculate the shape vectors. To aid the segmentation process, the ROA filter in the segmentation could be applied at a greater range of window sizes (again, taking advantage of advances in computing power). The module for identifying long linear features such as the sea ice edge should also be fully developed and integrated into the main workflow of the code. In an ideal world any image pre-processing necessary would be separate from the ITSARI workflow, like wise the georeferencing, leaving ITSARI concerned solely with object identification and tracking. Finally; although the image-processing machine is configured with two 64-bit Intel Xeon E5450 CPUs running at 3 GHz, giving a total of 8 processing cores, and 4GB of RAM. I strongly suspect that the processing did not make full use of this machine as the code was not developed with multithreading in mind, and I was limited to a single Matlab licence. Further development for routine operations should take advantage of parallel processing opportunities.

9.6 Identifying and tracking sea ice floes over the course of a year

The successful identification and tracking of sea ice floes over the course of a year (presented in section 4.2 and chapter 7) represents a significant achievement due to the accommodation that has to be made for changing backscatter characteristics, of the ice itself and its background, that occur in different seasons. The greatest success occurs in the early winter months, October - December, where multiyear ice that has survived the summer in the Arctic ocean stands out as bright objects against a background of newly forming first year ice that appears dark to radar due to high brine content. Where objects have been identified the temporal resolution of three to five days is effective at this time of year when the shape of individual pieces of ice is not changing very rapidly between image acquisitions. Slightly fewer tracks are generated in the late winter and early spring, where closed pack containing a large amount of first year ice does not lend itself to the easy identification of individual objects, but use of the algorithm to build up a general picture of ice movement is still successful. In the summer months the pack is more open so individual objects are more easily identified, however, the ice objects change their shape rapidly at this time of year due to accelerated melt and break up, so tracking between images three to five days apart proves tricky. Tracking on a shorter temporal resolution produces far superior results at this time of year (as demonstrated in chapter 8).

9.7 Ice movement in the Fram Strait

The East Greenland Current, coupled with the prevailing wind, is the main driver for ice export through the Fram Strait. On shorter temporal resolution ice movement is seen to be governed by the winds, with changes to ice movement direction sometimes lagging changes to wind direction. Where the temporal resolution is longer than one or two days the influence of the East Greenland Current becomes more dominant and overall movement is towards the south. Over the course of a year the prevailing northerly winds winds are seen to be pushing the ice in the same direction as the

East Greenland current. My results suggest that the prevailing wind speed and direction have a key impact on the rate of ice export through the Fram Strait. A period in which the wind forcing is in agreement with the East Greenland Current will see greater ice export than a period in which the two are acting in opposite directions.

9.8 Further Research

There are several projects that follow naturally from this work. Further investigation should be made into the ice movement through the Fram Strait over a series of consecutive summers, with a view to discovering how much ice is transiting the area in summer (bearing in mind that traditional cross correlation techniques are typically not applied to the summer months), and whether there is a pattern to the way the fast ice adjacent to the Greenland coast is lost and built up again over the following winter. Of particular interest is the development of polynyas adjacent to the Greenland coast and the movement of ice in this vicinity.

If one has reliable data on the surface wind velocity in an area, then ITSARI could be used to provide information about the surface ocean currents of an area, the ocean current may be derived from the part of the ice velocity that cannot be explained by the wind velocity. This could prove useful in areas where the knowledge of surface ocean currents is subject to uncertainty.

Given the obvious connection between wind velocity and ice movement it would be interesting to look specifically at the relationship between storminess, or individual storm events, and ice movement dynamics. It may also be possible to use the algorithm to provide information about the incidence of barrier winds, or the frequency and extent of katabatic winds off the ice shelf from NE Greenland.

If imagery of a significantly smaller resolution could be acquired it would also be interesting to make an assessment of the contribution of various glaciers on the

Greenland coast to icebergs in this region, and to map out typical paths those icebergs travel before they melt.

There is potential for the algorithm to be put to use monitoring shipping and installation hazards in polar waters.

Bibliography

Aagaard, K., Carmack, E. C., 1989. The role of sea ice and other fresh water in the Arctic circulation. Journal of Geophysical Research 94 (C10), 14485–14498.

Alexandrov, V. Y., Sandven, S., Kloster, K., Bobylev, L. P., Zaitsev, L. V., 2004. Comparison of sea ice signatures in OKEAN and RADARSAT radar images for the northeastern Barents sea. Canadian Journal of Remote Sensing 30 (6), 882–892.

Barry, R. G., Chorley, R. J., 1998. Atmosphere, Weather and Climate, seventh Edition. Routeledge, London.

Belkin, I. M., Levitus, S., Antonov, J., Malmberg, S. A., 1998. Great salinity anomalies in the North Atlantic. Progress in Oceanography 41, 1–68.

Bethke, I., Furevik, T., Drange, H., 2006. Towards a more saline North Atlantic and a fresher Arctic under global warming. Geophysical Research Letters 33 (L21712), doi:10.1029/2006GLO27264.

Bigg, G. R., 2003. The Oceans and Climate, 2nd Edition. Cambridge University Press.

Bigg, G. R., Wadley, M. R., Stevens, D. P., Johnson, J. A., 1997. Modelling the dynamics and thermodynamics of icebergs. Cold regions science and technology 26, 113–135.

Bluthgen, J., Gerdes, R., Werner, M., 2012. Atmospheric response to the extreme Arctic sea ice conditions in 2007. Geophysical Research Letters 39 (L02707, doi:10.1029/2011GL050486).

Bochert, A., 1999. Airborne line scanner measurements for ERS-1 SAR interpretation of sea ice. International Journal of Remote Sensing 20 (2), 329–348.

Brown, E., Colling, A., Park, D., Phillips, J., Rothery, D., Wright, J., 1989. Ocean Circulation. Pergamon in association with the Open University, Oxford.

Brummer, B., Schroder, D., Muller, G., Spreen, G., Jahnke-Bornemann, A., Lauiainen, J., 2008. Impact of the Fram Strait cyclone on ice edge, drift, divergence and concentration: Possibilities and limits of an observational anaylsis. Journal of Geophysical Research - Oceans 113 (C12003).

Brummer, B., Uller, G., Hoeber, H., 2003. A Fram Strait cyclone: Properties and impact on ice drift as measured by aircraft and buoys. Journal of Geophysical Research - Oceans 108 (D7, 4217).

Carlstrom, A., Ulander, L. M. H., 1993. C-band backscatter signatures of old sea ice in the central arctic during freeze up. IEEE transactions on geoscience and remote sensing 31 (4), 819–829.

Carlstrom, A., Ulander, L. M. H., 1995. Validation of backscatter models for level and deformed sea ice in ERS-1 SAR images. International Journal of Remote Sensing 16 (17), 3245–3266.

Carton, J. A., Giese, B. S., 2008. A reanalysis of ocean climate using simple ocean data assimilation (soda). Monthly Weather Review 136 (8), 2999–3017.

Comiso, J. C., 2002. A rapidly declining perennial sea ice cover in the Arctic. Geophysical Research Letters 29 (20), 10.1029/2002GL015650.

Comiso, J. C., 2006. Arctic warming signals from satellite observations. Weather 61 (3), 70–76.

Comiso, J. C., Nishio, F., 2008. Trends in the sea ice cover using enhanced and compatible AMSAR-E, SSM/I and SMMR data. Journal of Geophysical Research (C02S07 doi:10.1029/2007/JC004257).

Comiso, J. C., Parkinson, C. L., Gersten, R., Stock, L., 2008. Accelerated decline in the Arctic sea ice cover. Geophysical Research Letters 35 (L01703).

Cox, K. A., Stanford, J. D., McVicar, A. J., Rohling, E. J., Heywood, K. J., Bacon, S., Bolshaw, M., Dodd, P. A., la Rosa nad D. Wilkinson, S. D., 2010. Interannual variability of Arctic sea ice export into the East Greenland Current. Journal of Geophysical Research 115 (C12063, doi: 10.1029/2010JC006227).

Curry, R., Mauritzen, C., 2005. Dilution of the Northern North Atlantic Ocean in recent decades. Science 308, 1772–1774.

Deser, C., Teng, H., 2008. Evolution of Arctic sea ice concentration trends and the role of atmospheric circulation forcing, 1979–2007. Geophysical Research Letters 35 (L02504).

Dickson, R., Rudels, B., Dye, S., Karcher, M., Meincke, J., Yashayaev, I., 2007. Current estimates of freshwater flux through Arctic and subarctic seas. Progress in oceanography 73, 210–230.

Dickson, R. R., Osborn, T. J., Hurrel, J. W., Meincke, J., Blindheim, J., Adlandsvik, B., Vinje, T., Alekseev, G., Maslowski, W., 1999. The Arctic ocean response to the North Atlantic Oscillation. Journal of Climate 13, 2671–2696.

Dierking, W., Busche, T., 2006. Sea ice monitoring by L-Band SAR: An assessment

based on literature and comparisons of JERS-1 and ERS-1 imagery. IEEE Transactions on Geoscience and remote sensing 44 (2), 957–970.

Dierking, W., Carlstrom, A., Ulander, L. M. H., 1997. The effect of inhomogeneous roughness on radar backscattering from slightly deformed sea ice. IEEE transactions on geoscience and remote sensing 35 (1), 147–159.

Dierking, W., Dall, J., 2007. Sea-ice deformation state from synthetic aperture radar imagery - part 1: comparison of C- and L- band and different polarization. IEEE Transactions on geoscience and remote sensing 45 (11), 3610–3622.

Dierking, W., Dall, J., 2008. Sea-ice deformation state from synthetic aperture radar imagery - part 2: Effects of spatial resolution and noise level. IEEE Transactions on geoscience and remote sensing 46 (8), 2197–2207.

Dowdeswell, J. A., Hagen, J. O., Bjornsson, H., Glazovsky, A. F., Harrison, W. D., Holmlund, P., Jania, J., Koerner, R. M., Lefauconnier, B., Ommanney, C. S. L., Thomas, R. H., 1997. The mass balance of circum-arctic glaciers and recent climate change. Quaternary Research 48, 1–14.

Drobot, S., Stroeve, J., Maslanik, J., Emery, W., Fowler, C., 2008. Evolution of the 2007-2008 Arctic sea ice cover and prospects for a new record in 2008. Geophysical Research Letters 35 (L19501).

Druckenmiller, M. L., Eicken, H., Johnson, M. A., Pringle, D. J., Williams, C. C., 2009. Toward an integrated coastal sea-ice observatory: System components and a case study at Barrow, Alaska. Cold regions science and technology 56, 61–72.

Drucker, R., Martin, S., Moritz, R., 2003. Observations of ice thickness and frazil ice in the St Lawrence Island polynya from satellite imagery, upward looking sonar, and salinity/temperature moorings. Journal of Geophysical Research 108 (C5), 3149.

Fahrbach, E., Meincke, J., Osterhus, S., Rohardt, G., Schauer, U., Tverberg, V., Vercuin, J., 2001. Direct measurments of volume transports through Fram Strait. Polar Research 20 (2), 217–224.

Fetterer, F., Gineris, D., Kwok, R., 1994. Sea ice type maps from Alaska Synthetic Aperature Radar Facility: An assesment. Journal of Geophysical Research 99 (C11), 22,443 –22,458.

Fisel, B. J., Gutowski, W. J., .Hobbs, J. M., Cassano, J. J., 2011. Multiregime states of Arctic atmospheric circulation. Journal of Geophysical Research - Oceans 116 (D20122, doi:10.1029/2011JD015790).

Fjortoft, R., 1999. Segmentation of SAR images by edge detection: Strategy, Optimisation and Implimentation. In: Proceedings of Norwegian Signal Processing Symposium (NORSIG'99). Asker, Norway, pp. 70–75.

Francis, J. A., Hunter, E., 2007. Drivers of declining sea ice in the Arctic winter: A tale of two seas. Geophysical Research Letters 34 (L17503).

Germe, A., Houssais, M.-N., Herbaut, C., Cassou, C., 2011. Greenland Sea sea ice variability over 1979-2007 and its link to the surface atmosphere. Journal of Geophysical Research - Oceans 116 (C10034).

Giles, K. A., Laxon, S., Ridout, A. L., 2008. Circumpolar thinning of Arctic sea ice following the 2007 record ice extent minimum. Geophysical Research Letters 35 (L22502).

Gill, R. S., 2001. Operational detection of sea ice edges and icebergs using SAR. Canadian Journal of Remote Sensing 27 (5), 411–432.

Gill, R. S., Valeur, H. H., 1999. Ice cover discrimination in the Greenland waters using first order texture parameters of ERS SAR images. International Journal of Remote Sensing 20 (2), 373–385.

Gladstone, R., Bigg, G. R., 2002. Satellite tracking of icebergs in the Weddell Sea. Antarctic Science 17 (3), 278–287.

Gregory, J. M., Stott, P. A., Cresswell, D. J., Rayner, N. A., Gordon, C., Sexton, D. M. H., 2002. Recent and future changes in Arctic sea ice simulated by the HadCM3 AOGCM. Geophysical Research Letters 29 (24), 10.1029/2001GL014575.

Haarpainter, J., 2006. Arctic-wide operational sea ice drift from enhanced-resolution QuikScat/Seawinds scatterometry and its validation. IEEE transactions on geoscience and remote sensing 44 (1), 102–107.

Haarpainter, J., Solbo, S., June 2007. Automatic ice-ocean discrimination in SAR imagery. Norut it-rapport, Norut IT, insert URL and date here Jen!

Haas, C., Liu, Q., Martin, T., 1999. Retrieval of Antarctic sea-ice pressure ridge frequencies from ERS SAR imagery by means of in situ laser profiling and usage of a neural network. International Journal of Remote Sensing 20 (15 &16), 3111–3123.

Hall, J. A., Bigg, G. R., Hall, R., 2012. Identification and tracking of individual sea ice floes from envisat wide swath sar images: a case study from fram strait. Remote Sensing Letters 3 (4), 295–304.

Hall, R. J., Hughes, N., Wadhams, P., 2002. A systematic method of obtaining ice concentration measurements from ship-based observations. Cold regions science and technology 34, 97–102.

Hansen, B., Osterhus, S., 2000. North Atlantic-Nordic Seas exchanges. Progress in Oceanography 45, 109–208.

Harden, B. E., I.A.Renfrew, Petersen, G., 2011. A Climatology of Wintertime Barrier Winds off Southeast Greenland. Journal of Climate 24, 4701–4717.

Haykin, S., O.Lewis, E., Raney, R. K., Rossiter, J. R., 1994. Remote Sensing of Sea Ice and Icebergs. John Wiley & Sons, Chichester.

Heinemann, G., 1999. The katabatic wind experiment: an aircraft-based study of katabatic wind dynamis over the Greenland ice sheet. Boundary Layer Meteorology 93, 75–116.

Heinemann, G., Klein, T., 2002. Modelling and observations of the katabatic flow dynamics over Greenland. Tellus 54A, 542–554.

Herbert, W., 1969. Across the top of the world. Prentice Hall Press.

Holland, M. M., Finnis, J., Barrett, A. P., Serreze, M. C., 2007. Projected changes in Arctic Ocean freshwater budgets. Journal of Geophysical Research 112 (G04S55), doi: 10.1029/2006JG000354.

Holloway, G., Sou, T., 2002. Has Arctic sea ice rapidly thinned? Journal of Climate 15, 1691–1701.

Howell, C., Youden, J., Lane, K., Power, D., Randell, C., Flett, D., 2004. Iceberg and ship discrimination with ENVISAT multi polarization ASAR. In: Geoscience and Remote Sensing Symposium Proceedings. pp. 113–116.

Inoue, J., Kikuchi, T., 2007. Outflow of summertime Arctic sea ice observed by ice drifting buoys and its linkage with ice reduction and atmospheric circulation patterns. Journal of the Meteorological Society of Japan 85 (6), 881–887.

Jacka, T. H., Giles, A. B., 2007. Antarctic iceberg distribution and dissolution from ship based observations. Journal of Glaciology 53 (182), 341–356.

Jaiser, R., Dethloff, K., Handorf, D., Rinke, A., J.Cohen, 2011. Impact of sea ice cover changes on the Northern Hemisphere atmospheric winter circulation. Tellus A, Dynamic Meteorology and Oceanography 64 (11595).

Johannessen, O. M., Shalina, E. V., Miles, M. W., 1999. Satellite evidence for an Arctic sea ice cover in transformation. Science 286, 1937–1939.

Kalney, E., 1996. The ncep/ncar reanalysis 40 year project. Bulletin of the American Meteorology Society 77, 437–471.

Karcher, M., Gerdes, R., Kauker, F., Kiberle, C., Yashayaev, I., 2005. Arctic Ocean change heralds North Atlanic freshening. Geophysical Research Letters 32, L21606.

Karvonen, J., Simila, M., Lehtiranta, J., 2007. SAR-based estimation of the baltic sea ice motion. In: Geoscience and Remote Sensing Symposium Proceedings. pp. 2605–2608.

Kay, J. E., L'Ecuyer, T., Gettelman, A., Stephens, G., O'Dell, C., 2008. The contributions of cloud and radiation anomalies to the 2007 arctic sea ice extent minimum. Geophysical Research Letters 35 (L08503).

Klein, T., Heinemann, G., 2002. Interaction of katabatic winds and mesocyclones near the eastern coast of Greenland. Meteorological applications 9, 407–422.

Koenigk, T., Mikolajewicz, U., Haak, H., Jungclaus, J., 2006. Varibility of Fram Strait sea ice export: causes, impacts and feedbacks in a coupled climate model. Climate Dynamics 26, 17–34.

Koenigk, T., Mikolajewicz, U., Jungclaus, J., Kroll, A., 2009. Sea ice in the Barents Sea: seasonal to interannual variability and climate feedbacks in a global coupled model. Climate Dynamics 32, 1119–1138.

Komuro, Y., Hasumi, H., 2007. Effects of variability of sea ice transport through the Fram Strait on the intensity of the Atlantic deep circulation. Climate Dynamics 29, 455–467.

Kwok, R., Cunningham, G. F., Pang, S. S., 2004. Fram Strait sea ice outflow. Journal of Geophysical Research 109 (C01009).

Kwok, R., Curlander, J. C., McConnell, R., Pang, S. S., 1990. An ice motion tracking system at the alaska SAR facility. IEEE Journal of oceanic engineering 15 (1), 44–54.

Kwok, R., Rignot, E., Holt, B., 1992. Identification of Sea Ice Types in Spaceborne Synthetic Aperture Radar Data. Journal of Geophysical Research 97 (C2), 2391 – 2402.

Kwok, R., Rothrock, D. A., 1999. Varibility of Fram Strait ice flux and North Atlantic Oscillation. Journal of Geophysical Research - Oceans 104 (C3), 5177–5189.

Kwok, R., Rothrock, D. A., 2009. Decline in Arctic sea ice thickness from submarine and ICEsat records: 1958-2008. Geophysical Research Letters 36 (L15501).

Land, K., Power, D., Chakraborty, I., Youden, J., Randell, C., McClintock, J., Flett, D., 2002. RADARSAT-1 synthetic aperture radar iceberg detection performance ADRO-2 A223. In: Geoscience and Remote Sensing Symposium Proceedings. pp. 2273–2275.

Lane, K., Power, D., Youden, J., Randell, C., Flett, D., 2004. Validation of synthetic aperture radar for iceberg detection in sea ice. In: Geoscience and Remote Sensing Symposium Proceedings. pp. 125–128.

Langlois, A., Barber, D. G., 2007. Passive microwave remote sensing of seasonal snow-covered sea ice. Progress in Physical Geography 31 (6), 539–573.

Laxon, S., Peacock, N., Smith, D., 2003. High interannual variability of sea ice thickness in the Arctic region. Nature 425, 947–950.

Leung, H., Dubash, N., Xie, N., 2002. Detection of small objects in clutter using a GA-RBF neural network. IEEE Transactions on aerospace and electronic systems 38 (1), 98–117.

Liu, A. K., Martin, S., Kwok, R., 1997. Tracking of Ice Edges and Ice Floes by Wavelet Analysis of SAR Images. Journal of Atmospheric and Oceanic Technology 14, 1187–1198.

Livingstone, C. E., Singh, K. P., Gray, A. L., 1987. Seasonal and regional variations of active/passive microwave signatures of sea ice. IEEE Transactions on Geoscience and Remote Sensing GE-25 (2), 159–173.

Lukovich, J. V., Babb, D. G., Barber, D. G., 2011. On the scaling laws derived from ice beacon trajectories in the southern Beaufort Sea during the Internationl Polar Year - Circumpolar Flaw Lead study, 2007 – 2008. Journal of Geophysical Research - Oceans 116 (C00G07).

Lukovich, J. V., Barber, D. G., 2007. On the spatiotemporal behavior of sea ice concentration anomalies in the Northern Hemisphere. Journal of Geophysical Research 112 (D13117).

Mahoney, A. R., Barry, R. G., Smolyanitsky, V., Fetterer, F., 2008. Observed sea ice extent in the Russian Arctic, 1933-2006. Journal of Geophysical Research 113 (C11005).

Maillard, P., Clausi, D. A., Deng, H., 2005. Operational map-guided classification of SAR sea ice imagery. IEEE Transactions on geoscience and remote sensing 43 (12), 2940–2951.

Marko, J. R., Fissel, D. B., Borg, K., June 2003. Ice-type characterization in a marginal ice zone using RADARSAT and ice profiling sonar: Tools for structural design and navigation planning in ice infested waters, presented at POAC03 June 16–19 Trondheim, norway.

Maslanik, J. A., Fowler, C., Stroeve, J., Drobot, S., Zwally, J., Yi, D., Emery, W., 2007. A younger, thinner Arctic ice cover: Increased potential for rapid, extensive sea-ice loss. Geophysical Research Letters 34 (L24501).

McClintock, J., McKenna, R., May 2007. Grand banks iceberg management. PERD CHC report 20–84, AMEC Earth Environmental and R. F. Mckenna Associates and PETRA International Limited, insert URL and date here Jen!

Melling, H., 1998. Detection of features in first year pack ice by synthetic aperture radar. international journal of remote sensing 19 (6), 1223–1249.

Meredith, M., Heywood, K., Dennis, P., Goldson, L., White, R., Fahrbach, E.,

Schauer, U., Osterhus, S., 2001. Freshwater fluxs through the western Fram Strait. Geophysical Research Letters 28 (8), 1615–1618.

Morison, J., Kwok, R., Peralta-Ferriz, C., Alkire, M., Rigor, I. G., Andersen, R., Steele, M., 2012. Changing Arctic Ocean freshwater pathways. Nature 481, 66–70.

Nghiem, S. V., Bertoia, C., 2001. Study of multi-polarisation C-band backscatter signatures for Arctic sea ice mapping with future satellite SAR. Canadian Journal of Remote Sensing 27 (5), 387–402.

Nghiem, S. V., Rigor, I. G., Perovich, D. K., abd J. W. Weatherly, P. C.-C., Neumann, G., 2007. Rapid reduction of Arctic perennial sea ice. Geophysical Research Letters 34 (L19504).

Nystuen, J. A., Garcia, F. W., 1992. Sea ice classification using SAR backscatter statistics. IEEE transactions on geoscience and remote sensing 30 (3), 502–509.

Ogi, M., Rigor, I. G., McPhee, M. G., Wallace, J. M., 2008. Summer retreat of Arctic sea ice: Role of summer winds. Geophysical Research Letters 35 (L24701).

Ogi, M., Wallace, J. M., 2007. Summer minimum Arctic sea ice extent and the associated summer atmospheric circulation. Geophysical Research Letters 34 (L12705).

Onstott, R. G., Shuchman, R. A., 2004. Synthetic Aperture Radar Marine Users Manual. NOAA/NESDIS Office of Reasearch and Applications, http://www.sarusersmanual.com/, Ch. 3, pp. 81–115.

Panagopoulos, S., Soraghan, J. J., 2004. Small target detection in sea clutter. IEEE Transactions on Geoscience and Remote Sensing 42 (7), 1355–1364.

Perovich, D. K., Richter-Menge, J. A., 2009. Loss of sea ice in the Arctic. Annual Review of Marine Science 1, 417–441.

Perovich, D. K., Richter-Menge, J. A., Jones, K. F., 2008. Sunlight, water and ice: Extreme Arctic sea ice melt during the summer of 2007. Geophysical Research Letters 35 (L11501).

Petersen, G., I.A.Renfrew, G.W.K.Moore, 2009. An overview of barrier winds off southeastern Greenland during the Greenland Flow Distortion experiment. Quarterly Journal of the Royal Meteorological Society 135, 1950–1967.

Phillips, H. A., Laxon, W., 1995. Tracking of Antarctic tabular icebergs using passive microwave radiometry. International Journal of Remote Sensing 16 (2), 399–405.

Power, D., Youden, J., Randell, C., Flett, D., 2001. Iceberg detection capabilities of RADARSAT synthetic aperture radar. Canadian Journal of Remote Sensing 27 (5), 476–486.

Rasmussen, E. A., Turner, J. (Eds.), 2003. Polar Lows Mesoscale Weather Systems in the Polar Regions. Cambridge University Press.

Rees, W. G., 2001. Physical Principles of Remote Sensing. Cambridge University Press, Cambridge.

Rignot, E., Drinkwater, M. R., 1994. Winter sea-ice mapping from multiparameter synthetic-aperture radar data. Journal of Glaciology 40 (134), 31–45.

Rigor, I. G., Wallace, J. M., 2004. Variations in the age of Arctic sea-ice and summer sea-ice extent. Geophysical Research Letters 31 (L09401), doi:10.1029/2004GL019492.

Rigor, I. G., Wallace, J. M., Colony, R. L., 2002. On the response of sea ice to the Arctic Oscillation. Journal of Climate 15 (18), 2648–2663.

Rogers, J. C., Hung, M.-P., 2008. The Odden ice feature of the Greenland Sea and its association with atmospheric pressure, wind and surface flux variability from reanalyses. Geophysical Research Letters 35 (L08504).

Rudels, B., Bjork, G., Nilsson, J., Winsor, P., Lake, I., Nohr, C., 2005. The interaction between waters from the Arctic Ocean and the Nordic Seas north of Fram Strait and along the East Greenland current: results from the Arctic Ocean-02 Oden Expedition. Journal of Marine Systems 55, 1–30.

Schauer, U., Fahrbach, E., Osterhus, S., Rohardt, G., 2004. Arctic warming through the Fram Strait: Oceanic heat transport from 3 years of measurements. Journal of Geophysical Research 109, C06026.

Schneider, W., Budeus, G., 1997. Summary of the Northeast Water Polynya formation and development (greenland sea). Journal of Marine Systems 10, 107–122.

Schweiger, A. J., Zhang, J., Lindsay, R. W., Steele, M., 2008. Did unusually sunny skies help drive the record sea ice minimum of 2007. Geophysical Research Letters 35 (L10503).

Sephton, A. J., Brown, L. M. J., Macklin, J. T., Partington, K. C., Veck, N. J., Rees, W. G., 1994. Segmentation of synthetic aperture radar imagery of sea ice. International Journal of Remote Sensing 15 (4), 803–825.

Serreze, M. C., Barry, R. G., 2005. The Arctic Climate System. Cambridge Atmosphere and Space Science Series. Cambridge University Press.

Serreze, M. C., Francis, J. A., 2006. The Arctic on the fast track of change. Weather 61 (3), 65–69.

Serreze, M. C., Holland, M. M., Stroeve, J., 2007. Perspectives on the Arctics shrinking Sea-Ice cover. Science 315, 1533–1536.

Silva, T. A. M., 2006. Quantifying Antarctic icebergs and their melting in the ocean. Ph.D. thesis, Department of Geography, University of Sheffield, Winter Street, Sheffield, S10 2TN.

Silva, T. A. M., Bigg, G., 2005. Computer-based identification and tracking of Antarctic icebergs in SAR images. Remote Sensing of Environment 94, 287–297.

Smedsrud, L. H., Sorteberg, A., Kloster, K., 2008. Recent and future changes of the Arctic sea-ice cover. Geophysical Research Letters 32, L20503.

Spreen, G., Kern, S., Stammer, D., Forsberg, R., Haarpainter, J., 2006. Satellite-based estimates of sea-ice volume flux through Fram Strait. Annals of Glaciology 44, 321–328.

Spreen, G., Kwok, R., Menemenlis, D., 2011. Trends in arctic sea ice drift and the role of wind forcing: 1992-2009. Geophysical Research Letters 38 (L19501).

Stroeve, J., Maslanik, J., Serreze, M. C., Rigor, I. G., Meier, W., Fowler, C., 2011. Sea ice response to an extreme negative phase of the Arctic Oscillation during winter 2009/2010. Geophysical Research Letters 38 (L02502).

Sun, Y., 1996. Automatic ice motion retrieval from ERS-1 SAR images using the optical flow method. International Journal of Remote Sensing 17 (11), 2059–2087.

Timmermans, M.-L., Proshutinsky, A., Krishfield, R. A., Perovich, D. K., Richter-Menge, J. A., Stanton, T., .Toole., J. M., 2011. Surface freshening in the Arctic Ocean's Eurasian Basin: An apparent consequence of recent change in the wind-driven circulation. Journal of Geophysical Research - Oceans 116 (C00D03).

Touzi, R., Lopes, A., Bousquet, P., 1988. A statistical and geometrical edge detection for SAR images. IEEE Transactions on Geoscience and Remote Sensing 26 (6), 764–773.

Tschudi, M. A., Maslanik, J., Perovich, D. K., 2008. Derivation of melt pond coverage on Arctic sea ice using MODIS observations. Remote Sensing of Environment 112, 2605–2614.

Tsukernik, M., Deser, C., Alexander, M., Tomas, R., 2010. Atmosphereic forcing of Fram Strait sea ice export: a closer look. Climate Dynamics 35, 1349–1360.

Ulander, L. M. H., Carlstrom, A., Askne, J., 1995. Effect of frost flowers , rough saline snow and slush on the ERS-1 SAR backscatter of thin arctic sea-ice. International Journal of Remote Sensing 16 (17), 3287–3305.

Vihma, T., Tisler, P., Uotila, P., 2012. Atmosphereic forcing on the drift of arctic sea ice in 1989 - 2009. Geophysical Research Letters 39 (L02501).

Vinje, T., 2001. Fram Strait ice fluxes and atmospheric circulation: 1950 - 2000. Journal of Climate 14, 3508–3517.

Vogel, P., Canela, M., Duesmann, B., 2010. ENVISAT mission extension beyond 2010. In: ESA Living Planet Symposium, Bergan, Norway.

Wakabayashi, H., Matsuoka, T., Nakamura, K., Nishio, F., 2004. Polarimetric characteristics of sea ice in the sea of Okhotsk observed by airborne L-band SAR. IEEE transactions on geoscience and remote sensing 42 (11), 2412–2425.

Walker, N. P., Partington, K. C., Woert, M. L. V., Street, T. L. T., 2006. Arctic sea ice type and concentration mapping using passive and active microwave sensors. IEEE Transactions on Geoscience and Remote Sensing 44 (12), 3574–3584.

Weissling, B., Ackley, S. F., Wgner, P., Xie, H., 2009. EISCAM - Digital image acquisition and processing for sea ice parameters from ships. Cold regions science and technology 57, 49–60.

Widell, K., Osterhus, S., Gammelsrod, T., 2003. Sea ice velocity in the Fram Strait monitored by moored instruments. Geophysical Research Letters 30 (19), 1–4.

Williams, R. N., Rees, W. G., Young, N. W., 1999. A technique for the identification and analysis of icebergs in synthetic aperture radar images of Antarctica. International Journal of Remote Sensing 20 (15 & 16), 3183–3199.

Willis, C. J., Macklin, J. T., Partington, K. C., Teleki, K. A., Rees, W. G., Williams, R. G., 1996. Iceberg detection using ERS-1 synthetic aperture radar. International Journal of Remote Sensing 17 (9), 1777–1795.

Woodhouse, I. H., 2006. Introduction to Microwave Remote Sensing. Taylor and Francis.

Yackel, J. J., Barber, D. G., 2000. Melt ponds on sea ice in the Canadian Archipelago 2. on the use of RADARSAT-1 synthetic aperture radar for geophysical inversion. Journal of geophysical research 105 (C9), 22061–22070.

Yackel, J. J., Barber, D. G., 2007. Observations of snow water equivalent change on landfast first-year sea ice in winter using synthetic aperture radar data. IEEE Transactions of Geoscience and Remote Sensing 45 (4), 1005–1015.

Yackel, J. J., Barber, D. G., Hanesiak, J. M., 2001. Melt ponds on sea ice in the Canadian Archipelago 1. variability in morphological and radiative properties. Journal of Geophysical Research 105 (C9), 22049–22060.

Appendix A

Additional Data for Chapter 8

The following pages contain graphs showing speed and direction for each of the images pairs from which movement vectors were generated in August and September 2010. These accompany the case study presented in Chapter 8.

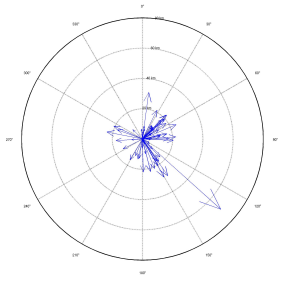

(a) Distance & direction travelled 16-17 August

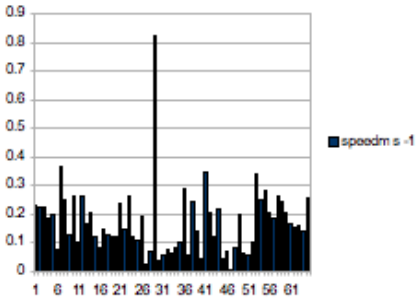

(b) Speed 16-17 August

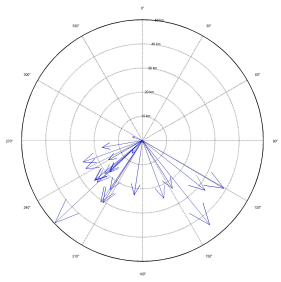

(c) Distance & direction travelled 17-19 August

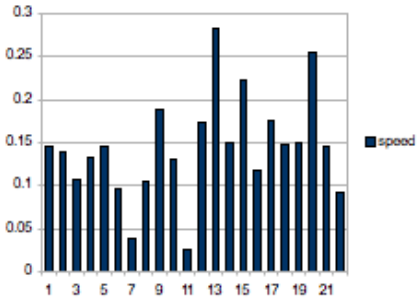

(d) Speed 17 - 19 August

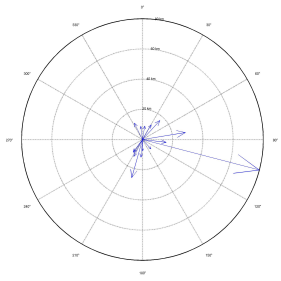

(e) Distance & direction travelled 19 - 20 August

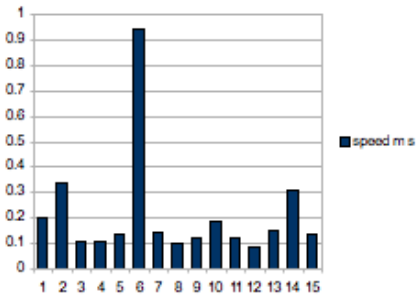

(f) Speed 19 - 20 August

Figure A.1: Speed, distance & direction of travel between: a) & b) 16 - 17 August, c) & d)17-19 August, e) & f) 19-20 August. Between 16 - 17 August the direction of travel is very variable, or could be described as having two distinct components, movement towards the south west and movement in the opposite direction towards the north east. Between 17 - 19 August the direction is less variable, between south east - south west. Between 19-20 some of the objects tracked are again moving back towards the north east. With a few exceptions speeds are consistent between 0.01-0.03 m s $^{-1}$ in all three.

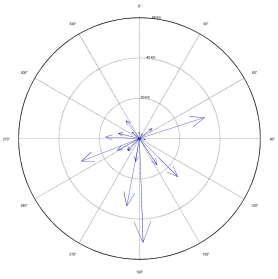

(a) Distance & direction travelled 20 - 23 August

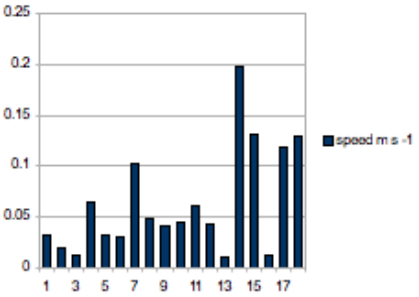

(b) Speed 20 - 23 August

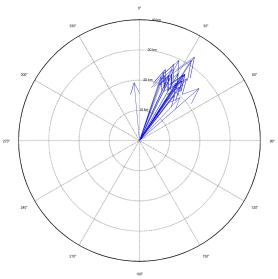

(c) Distance & direction travelled 23 - 24 August

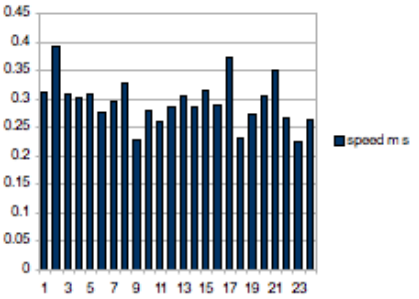

(d) Speed 23- 24 August

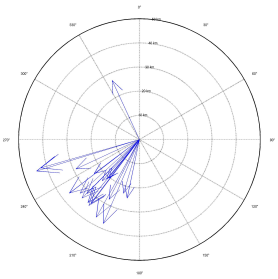

(e) Distance & direction travelled 24 - 26 August

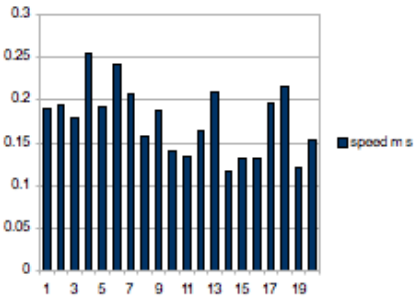

(f) Speed 24 - 26 August

Figure A.2: Speed, distance & direction of travel between a) & b) 20 - 23 August, c) & d) 23-24 August, e) & f) 24-26 August. Between 20 - 23 August the direction of movement is very inconsistent and speeds are slower than previously (all below 0.2 m s $^{-1}$ and most below 0.05 m s $^{-1}$). Speed then picks up again (between 0.2 - 0.3 m s $^{-1}$) and movement is consistently towards the North East. In the following pair, 24 - 26 August, all but one tracked objects are moving towards the South West, at slightly slower speeds.

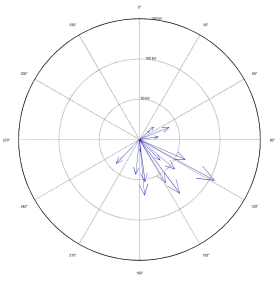

(a) Distance & direction travelled 26 - 30 August

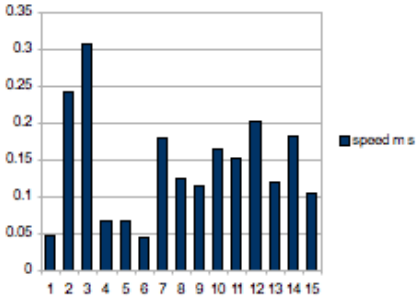

(b) Speed 26 - 30 August

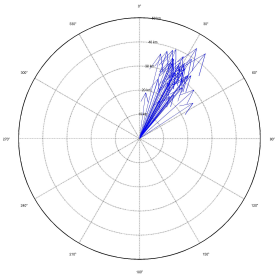

(c) Distance & direction travelled 30 - 31 August

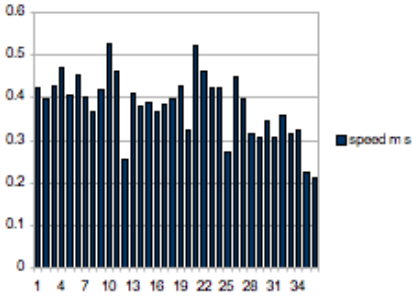

(d) Speed 30 - 31 August

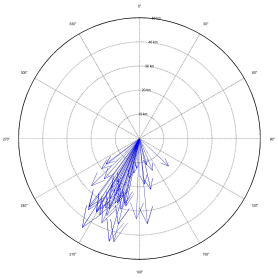

(e) Distance & direction travelled 31 August - 2 Sept

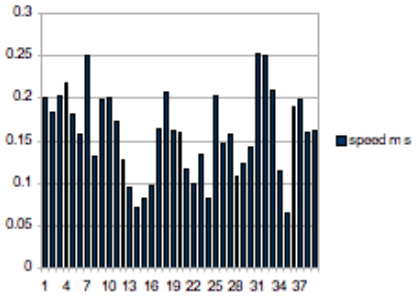

(f) Speed 31 August - 2 September

Figure A.3: Speed, distance & direction of travel between the 26 - 30 August, 30-31 August, 31August - 2 September. Between 26 - 30 August the objects tracked are moving towards the South East at relatively low speeds. Between 30 - 31 August movement is again towards the North East and speeds up to 0.5 m s $^{-1}$. This reverses again towards South South West and slows to 0.2 m s $^{-1}$ between 31August - 2 September.

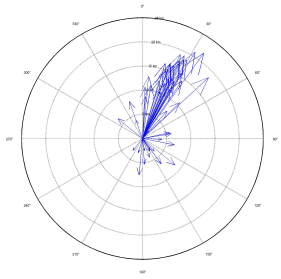

(a) Distance & direction travelled 2 - 3 September

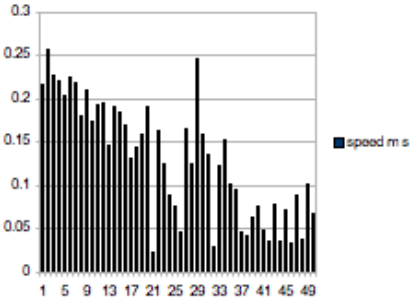

(b) Speed 2 - 3 September

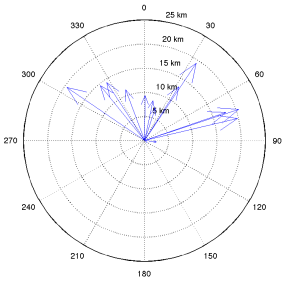

(c) Distance & direction travelled 12:00 - 20:17 1 September

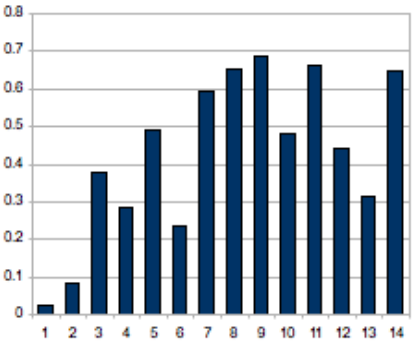

(d) Speed 12:00 - 20:17 September

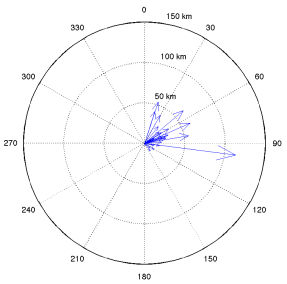

(e) Distance & direction travelled 1 - 2 September

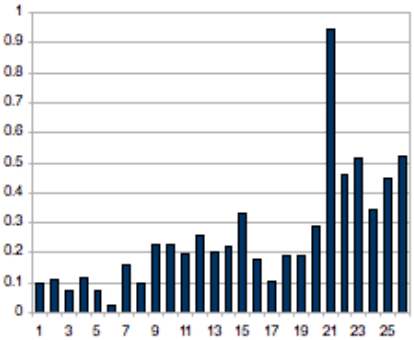

(f) Speed 1 - 2 September

Figure A.4: Speed, distance & direction of travel between: a) & b) 02 - 03 Sept, c)& d) 1 Sept 12:00 - 20:17, e) & f) 1 Sept 12:00 - 2 Sept 21:26. This is a slightly odd set of graphs. The first pair is from a pair of Radarsat images that follow from the previous set (Figure reffig:5b:9) Here movement is strong towards the North East. Those in the centre are from a pair of Envisat wide swath images acquired 8 hours apart on 1 September. They fall within the time step shown in Figures A.3e and A.3f. Interestingly on the shorter time steps movement appears to be in the opposite direction to that measured within the longer time step they sit within.

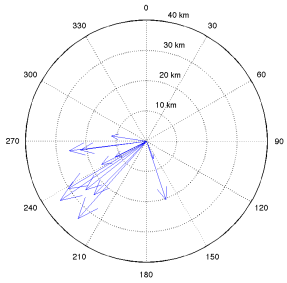

(a) Distance & direction travelled 2 - 3 September

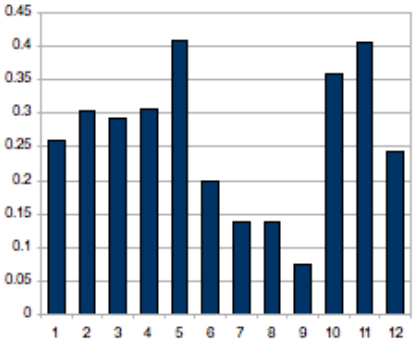

(b) Speed 2 - 3 September

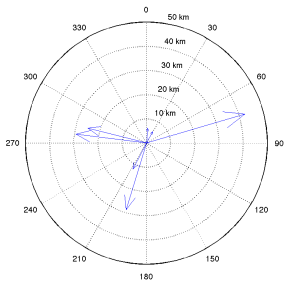

(c) Distance & direction travelled 3 -4 September

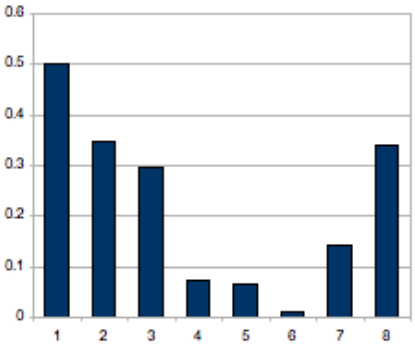

(d) Speed 3 -4 September

Figure A.5: Speed, distance & direction of travel between: a) & b) 2 - 3 Sept, c) & d) 3 - 4 Sept. Between 2 - 3 September movement towards the south west has resumed. Between 3 - 4 September there is no clear pattern

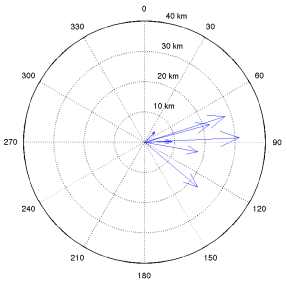

(a) Distance & direction travelled 4 - 5 September

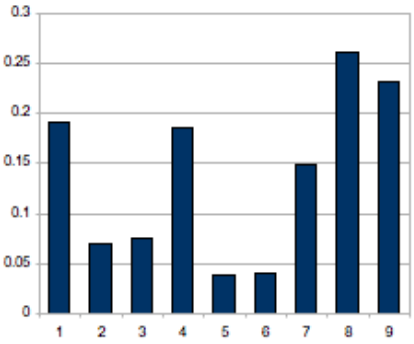

(b) Speed 4 -5 September

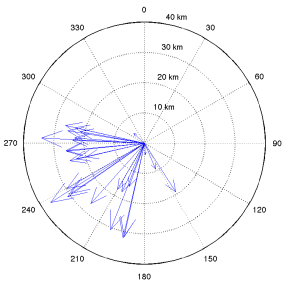

(c) Distance & direction travelled 5 - 6 September

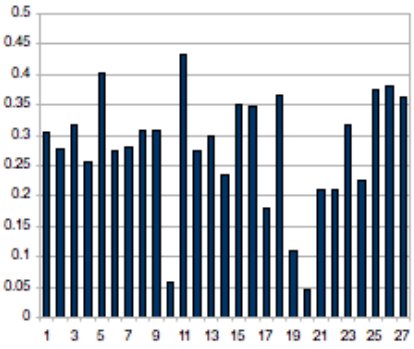

(d) Speed 5 - 6 September

Figure A.6: Speed, distance & direction of travel between: a) & b) 4 - 5 Sept; c) & d)) 5-6 Sept. Between 4 - 5 September movement is towards the East, reversing to the South West between 5 -6 September. Contrary to previous pairings the faster movement here is associated with movement towards the south west.

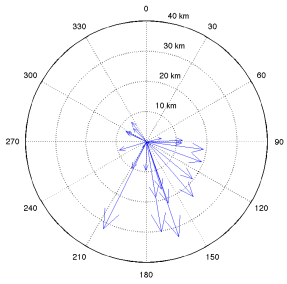

(a) Distance & direction travelled 6 -7 September

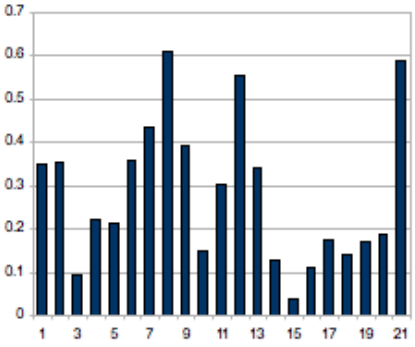

(b) Speed 6 -7 September

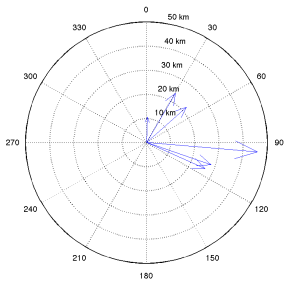

(c) Distance & direction travelled 6 - 8 September

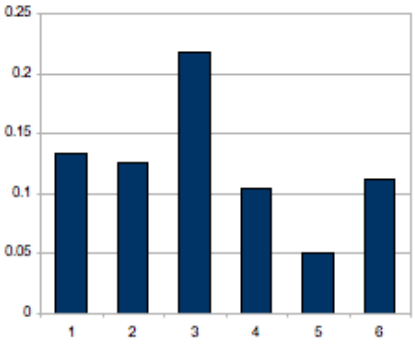

(d) Speed 6 - 8 September

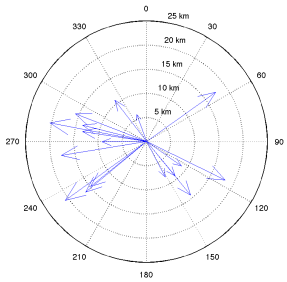

(e) Distance & direction travelled 8 - 9 September

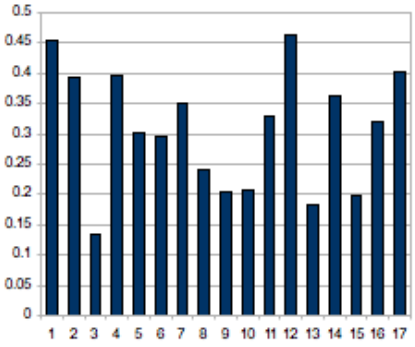

(f) Speed 8 - 9 September

Figure A.7: Speed, distance & direction of travel between: a: & b) 6-7 Sept; c) & d) 6- 8 Sept; e) & f) 8-9 Sept. The vectors here have a wider spread in direction than some of those that came before. Between the 6 -7 movement is broadly south, moving towards the east between 6-8. On the 8 - 9 the majority of tracked objects are moving west, with a few going in the opposite direction. Speeds are lowest where objects are moving west.

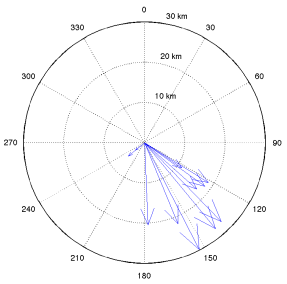

(a) Distance & direction travelled 9 - 10 September

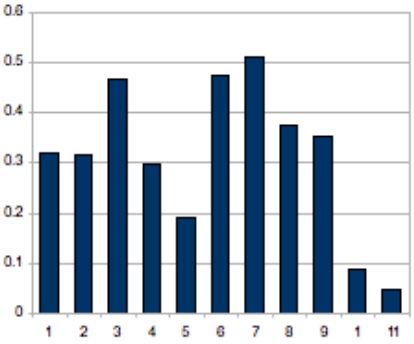

(b) Speed 9 - 10 September

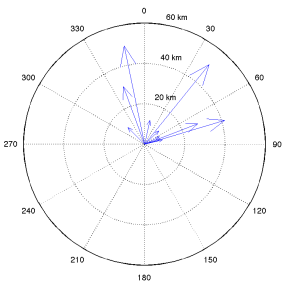

(c) Distance & direction travelled 10 - 11 September

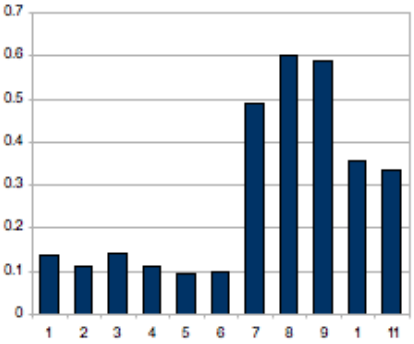

(d) Speed 10 - 11 September

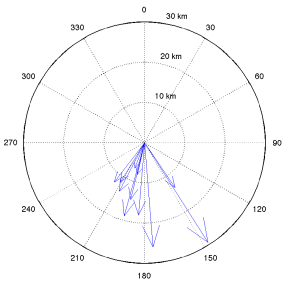

(e) Distance & direction travelled 11-13 September

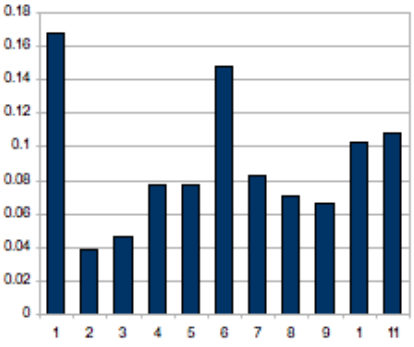

(f) Speed 11 - 13 September

Figure A.8: Speed, distance & direction of travel between a) & b) 9-10 Sept; c) & d) 10-11 Sept; e) & f) 11-13 Sept. Here again we see alternation in the direction and speed of travel.

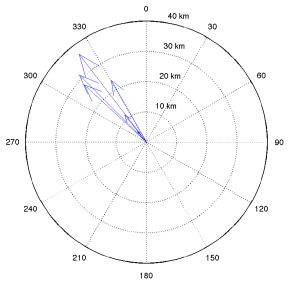

(a) Distance & direction travelled 13 - 14 September

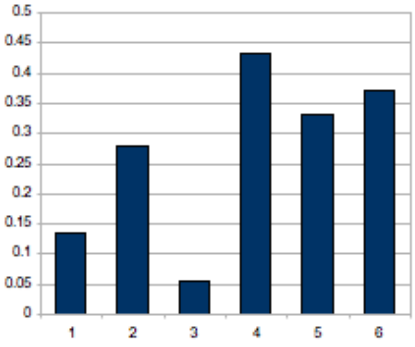

(b) Speed 13 - 14 September

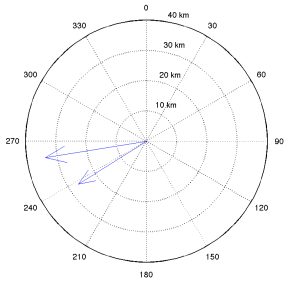

(c) Distance & direction travelled 14 - 15 September

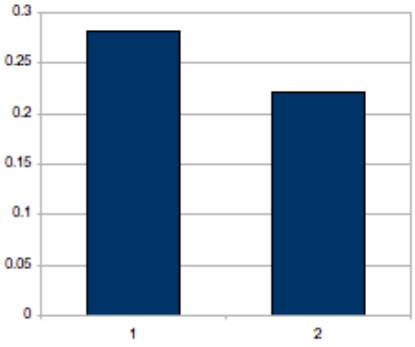

(d) Speed 14 -15 September

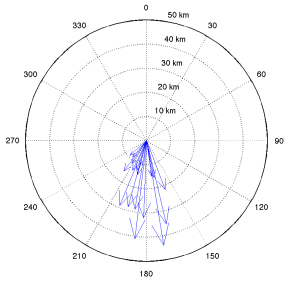

(e) Distance & direction travelled 15 - 26 September

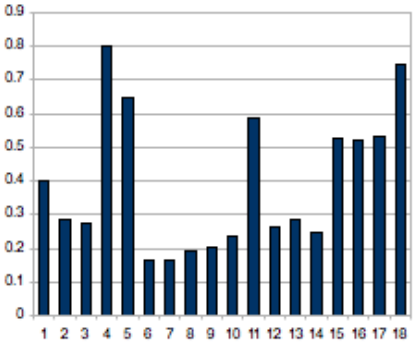

(f) Speed 15 -16 September

Figure A.9: Speed, distance & direction of travel between a) & b) 13- 14 Sept; c) & d) 14- 15 Sept; e) & f) 15-16 Sept